Final Report

FDOT Contract No: BDV31-977-66
UF Project No: 31216

Bearing Capacity Factors for Shallow Foundations Subjected to Combined Lateral and Axial Loading

Principal Investigators: Scott J. Wasman (PI)
Michael C. McVay (Co-PI)

Graduate Student: Stephen Crawford

Department of Civil and Coastal Engineering

Engineering School of Sustainable Infrastructure and Environment

University of Florida

P.O. Box 116580

Gainesville, Florida 32611-6580

Developed for the

Larry Jones, Project Manager

June 30, 2020

DISCLAIMER

The opinions, findings, and conclusions expressed in this publication are those of the authors and not necessarily those of the Florida Department of Transportation or the U.S. Department of Transportation.

Prepared in cooperation with the State of Florida Department of Transportation and the U.S. Department of Transportation.

SI (MODERN METRIC) CONVERSION FACTORS (from FHWA)

APPROXIMATE CONVERSIONS TO SI UNITS

SYMBOL	WHEN YOU KNOW	MULTIPLY BY	TO FIND	SYMBOL
		LENGTH		
in	inches	25.4	millimeters	mm
ft	feet	0.305	meters	m
yd	yards	0.914	meters	m
mi	miles	1.61	kilometers	km

SYMBOL	WHEN YOU KNOW	MULTIPLY BY	TO FIND	SYMBOL
		AREA		
in^2	square inches	645.2	square millimeters	mm^2
ft^2	square feet	0.093	square meters	m^2
yd^2	square yard	0.836	square meters	m^2
ac	acres	0.405	hectares	ha
mi^2	square miles	2.59	square kilometers	km^2

SYMBOL	WHEN YOU KNOW	MULTIPLY BY	TO FIND	SYMBOL
		VOLUME		
fl oz	fluid ounces	29.57	milliliters	mL
gal	gallons	3.785	liters	L
ft^3	cubic feet	0.028	cubic meters	m^3
yd^3	cubic yards	0.765	cubic meters	m^3
NOTE: volumes greater than 1000 L shall be shown in m^3				

SYMBOL	WHEN YOU KNOW	MULTIPLY BY	TO FIND	SYMBOL
		MASS		
oz	ounces	28.35	grams	g
lb	pounds	0.454	kilograms	kg
T	short tons (2000 lb)	0.907	megagrams (or "metric ton")	Mg (or "t")

SYMBOL	WHEN YOU KNOW	MULTIPLY BY	TO FIND	SYMBOL
		TEMPERATURE (exact degrees)		
°F	Fahrenheit	5 (F-32)/9 or (F-32)/1.8	Celsius	°C

SYMBOL	WHEN YOU KNOW	MULTIPLY BY	TO FIND	SYMBOL
		ILLUMINATION		
fc	foot-candles	10.76	lux	lx
fl	foot-Lamberts	3.426	candela/m^2	cd/m^2

SYMBOL	WHEN YOU KNOW	MULTIPLY BY	TO FIND	SYMBOL
		FORCE and PRESSURE or STRESS		
Lbf *	poundforce	4.45	newtons	N
kip	kip force	1000	pounds	lbf
lbf/in^2	poundforce per square inch	6.89	kilopascals	kPa

APPROXIMATE CONVERSIONS TO SI UNITS

SYMBOL	WHEN YOU KNOW	MULTIPLY BY	TO FIND	SYMBOL
		LENGTH		
mm	millimeters	0.039	inches	in
m	meters	3.28	feet	ft
m	meters	1.09	yards	yd
km	kilometers	0.621	miles	mi

SYMBOL	WHEN YOU KNOW	MULTIPLY BY	TO FIND	SYMBOL
		AREA		
mm^2	square millimeters	0.0016	square inches	in^2
m^2	square meters	10.764	square feet	ft^2
m^2	square meters	1.195	square yards	yd^2
ha	hectares	2.47	acres	ac
km^2	square kilometers	0.386	square miles	mi^2

SYMBOL	WHEN YOU KNOW	MULTIPLY BY	TO FIND	SYMBOL
		VOLUME		
mL	milliliters	0.034	fluid ounces	fl oz
L	liters	0.264	gallons	gal
m^3	cubic meters	35.314	cubic feet	ft^3
m^3	cubic meters	1.307	cubic yards	yd^3

SYMBOL	WHEN YOU KNOW	MULTIPLY BY	TO FIND	SYMBOL
		MASS		
g	grams	0.035	ounces	oz
kg	kilograms	2.202	pounds	lb
Mg (or "t")	megagrams (or "metric ton")	1.103	short tons (2000 lb)	T

SYMBOL	WHEN YOU KNOW	MULTIPLY BY	TO FIND	SYMBOL
		TEMPERATURE (exact degrees)		
°C	Celsius	1.8C+32	Fahrenheit	°F

SYMBOL	WHEN YOU KNOW	MULTIPLY BY	TO FIND	SYMBOL
		ILLUMINATION		
lx	lux	0.0929	foot-candles	fc
cd/m^2	$candela/m^2$	0.2919	foot-Lamberts	fl

SYMBOL	WHEN YOU KNOW	MULTIPLY BY	TO FIND	SYMBOL
		FORCE and PRESSURE or STRESS		
N	newtons	0.225	poundforce	lbf
kPa	kilopascals	0.145	poundforce per square inch	lbf/in^2

*SI is the symbol for International System of Units. Appropriate rounding should be made to comply with Section 4 of ASTM E380.
(Revised March 2003)

TECHNICAL REPORT DOCUMENTATION PAGE

1. Report No.	2. Government Accession No.	3. Recipient's Catalog No.
4. Title and Subtitle Bearing Capacity Factors for Shallow Foundations Subjected to Combined Lateral and Axial Loading		5. Report Date June 2020 6. Performing Organization Code
7. Author(s) Scott Wasman, Michael McVay, and Stephen Crawford		8. Performing Organization Report No.
9. Performing Organization Name and Address University of Florida – Dept. of Civil and Coastal Engineering Engineering School of Sustainable Infrastructure and Environment 365 Weil Hall – P.O. Box 116580 Gainesville, FL 32611-6580		10. Work Unit No. (TRAIS) 11. Contract or Grant No. BDV31-977-66
12. Sponsoring Agency Name and Address Florida Department of Transportation 605 Suwannee Street, MS 30 Tallahassee, FL 32399		13. Type of Report and Period Covered Final Report 1/1/17 – 6/30/20 14. Sponsoring Agency Code
15. Supplementary Notes		

16. Abstract: In this study, a series of centrifuge tests of strip, rectangular, and square footings was constructed to model prototype footings on very dense and medium dense sand subjected to concentric and inclined-eccentric loads. The experimental program was designed to test parameters representative of engineering practice in Florida for shallow foundation design and construction; materials and conditions included very dense and medium dense A3 poorly graded sand with less than 3% fines; embedment depths of zero, 0.5B, and B; prototype footing widths of 3.25 ft (L/B = 20) and 5 ft (L/B = 10 and 1); lateral-to-axial load ratios of 0.10 and 0.25; and load eccentricity of B/6.

A total of 185 centrifuge tests of combinations of the above materials and conditions were tested, and load, displacement, and soil pressure were measured. Bearing pressure versus displacement curves were developed until general shear failure occurred. Measured soil pressure beneath the footings provided a confirmation of pressure distribution of a rigid footing on sand, measured eccentricity of resultant load, and observed effect of inclined load to enhance or diminish the eccentricity.

The case of eccentric-inclined loading where the load was inclined in the direction of eccentricity (Load Case-3) was the most critical case for all footings. For the rectangular footings (L/B = 10), bearing capacities were up to 82% less than the concentrically loaded footing for the lateral-to-axial load ratio of 0.25 and in dense sand. Embedding the footing 0.5B in this case had a marked effect, increasing bearing capacity up to 90% in dense sand. For the case of the inclined load at the center of the footing (Load Case-4), bearing capacity was up to 72% less than the concentrically loaded footing for the lateral-to-axial load ratio of 0.25 and in medium dense sand. Embedding the footing 0.5B in this case also had a marked effect, increasing the bearing capacity up to 100% in medium dense sand. For the square footings (L/B = 1), bearing capacities were up to 68% less than the concentrically loaded footing for the lateral-to-axial load ratio of 0.25 and in medium dense sand. Embedding the footing 0.5B in this case had a marked effect, increasing bearing capacity up to 87% in medium dense sand. For the case of the inclined load at the center of the footing (Load Case-4), bearing capacity was up to 67% less than the concentrically loaded footing for the lateral-to-axial load ratio of 0.25 and in medium dense sand. Embedding the footing 0.5B in this case also had a marked effect, increasing the bearing capacity up to 95% in medium dense sand.

Methods to estimate the bearing capacity included those in the AASHTO specifications and existing methods in the literature. Depth of embedment factors from Meyerhof and multiple shape factors compared well with the results and were used in the analysis. For the rectangular footing (L/B = 10) on very dense sand, the Hansen N_γ with Hansen i_q and i_γ, the Vesić and Zhu N_γ with Loukidis f_{ie} (factor to account for eccentric-inclined load), and Hansen N_γ with Loukidis f_{ie} resulted in good agreement with most cases tested. For the rectangular footing (L/B = 10) on medium dense sand, the Vesić N_γ with Loukidis f_{ie} and Zhu N_γ with Loukidis f_{ie} resulted in good agreement with most cases tested. For the square footing (L/B = 1) on very dense sand, the Hansen N_γ with Hansen i_q and i_γ, Hansen N_γ with Vesić i_q and i_γ, and Zhu N_γ with Loukidis f_{ie} resulted in good agreement with most cases tested. For the square footing (L/B = 1) on medium dense sand, the Vesić N_γ with Hansen i_q and i_γ, Hansen N_γ with Vesić i_q and i_γ, Zhu N_γ with Loukidis f_{ie} resulted in good agreement with most cases tested.

17. Key Words	18. Distribution Statement
Bearing Capacity, Shallow Foundations, Inclined Load, Eccentric-Inclined Load, Centrifuge Tests, Depth of Embedment	No restrictions.

19. Security Classif. (of this report)	20. Security Classif. (of this page)	21. No. of Pages: 308	22. Price
Unclassified	Unclassified		

Form DOT F 1700.7 (8-72) Reproduction of completed page authorized

ACKNOWLEDGMENTS

The researchers would like to thank the Florida Department of Transportation (FDOT) for the financial support to carry out this research, as well as the assistance of the FDOT State Materials Office in obtaining the sand and performing laboratory tests. They would also like to thank the engineers at the FDOT district offices and the State Materials Office for participating in the survey on the state of practice for shallow foundation design in Florida.

EXECUTIVE SUMMARY

In Florida, bridges, Mechanically Stabilized Earth (MSE) walls, cast-in-place walls, sign structures, and gantries are built on shallow foundations and may subject the foundations to combined axial and lateral loads. Previous studies have found that the bearing capacity can be reduced by up to 75% for some laterally loaded walls. Currently, there isn't a consensus among engineers about how to estimate the bearing capacity of footings subjected to combined axial and lateral loads. The NCHRP Report 651, "LRFD Design and Construction of Shallow Foundations for Highway Bridge Structures," surveyed officials from 39 states and found that 17% of the foundations used in their states were shallow foundations, but that 53% of the officials do not use load inclination factors in their designs. Furthermore, for inclined-eccentric loads, there isn't a recommendation on how to differentiate between loads inclined in the direction or in the opposite direction of the eccentricity. At the same time, AASHTO Bridge Design Specifications include commentary suggesting that using load inclination factors may be overly conservative when footings are embedded 1B or deeper. This is attributed to the development of inclination factors for footings not embedded and resting on the ground surface.

In this study, a series of centrifuge tests of strip, rectangular, and square footings was conducted to model prototype footings on very dense and medium dense sand subjected to concentric and inclined-eccentric loads. The experimental program was designed based on the state of practice in Florida for designing and constructing shallow foundations on sand. The following materials and conditions were tested:

- A3 poorly graded sand with less than 3% fines
- Very dense and medium dense sand
- Embedment depths of zero, 0.5B, and B
- Prototype footing widths of 3 ft (L/B = 20) and 5 ft (L/B = 10 and 1)

- Concentric, eccentric, inclined and inclined-eccentric loads
- Lateral-to-axial load ratios of 0.10 and 0.25
- Load eccentricity of B/6.

A total of 185 centrifuge tests of combinations of the above materials and conditions were tested, and load, displacement, and soil pressure were measured. Bearing pressure versus displacement curves were developed until general shear failure occurred. Measured soil pressure beneath the footings provided a confirmation of pressure distribution of a rigid footing on sand, measured eccentricity of resultant load, and observed effect of inclined load enhance or diminish the eccentricity.

The case of eccentric-inclined loading where the load was inclined in the direction of eccentricity (Load Case-3) was the most critical for all cases and for all footing types. For the rectangular footings (L/B = 10), bearing capacities were up to 82% less than the concentrically loaded footing for the lateral-to-axial load ratio of 0.25 and in dense sand. Embedding the footing 0.5B in this case had a marked effect, increasing bearing capacity up to 90% in dense sand. For the case of the inclined load at the center of the footing (Load Case-4), bearing capacity was up to 72% less than the concentrically loaded footing for the lateral-to-axial load ratio of 0.25 and in medium dense sand. Embedding the footing 0.5B in this case also had a marked effect, increasing the bearing capacity up to 100% in medium dense sand. For the square footings (L/B = 1), bearing capacities were up to 68% less than the concentrically loaded footing for the lateral-to-axial load ratio of 0.25 and in medium dense sand. Embedding the footing 0.5B in this case had a marked effect, increasing bearing capacity up to 87% in medium dense sand. For the case of the inclined load at the center of the footing (Load Case-4), bearing capacity was up to 67% less than the concentrically loaded footing for the lateral-to-axial load ratio of 0.25 and in medium dense sand. Embedding the footing 0.5B in this case also had a marked effect, increasing the bearing capacity

up to 95% in medium dense sand.

Methods to estimate the bearing capacity of the footings tested in this study include those recommended by AASHTO Bridge Design Specifications and existing methods in the literature. These mostly vary on the soil self-weight factor, N_γ, and the inclination factors i_q and i_γ. Depth of embedment factors from Meyerhof and multiple shape factors compared well with the results and were used in the bearing capacity analysis. For the rectangular footing (L/B = 10) on very dense sand, the Hansen N_γ with Hansen i_q and i_γ, the Vesić and Zhu N_γ with Loukidis f_{ie} (factor to account for eccentric-inclined load), and Hansen N_γ with Loukidis f_{ie} resulted in good agreement with most cases tested. For the rectangular footing (L/B = 10) on medium dense sand, the Vesić N_γ with Loukidis f_{ie} and Zhu N_γ with Loukidis f_{ie} resulted in good agreement with most cases tested. For the square footing (L/B = 1) on very dense sand, the Hansen N_γ with Hansen i_q and i_γ, Hansen N_γ with Vesić i_q and i_γ, and Zhu N_γ with Loukidis f_{ie} resulted in good agreement with most cases tested. For the square footing (L/B = 1) on medium dense sand, the Vesić N_γ with Hansen i_q and i_γ, Hansen N_γ with Vesić i_q and i_γ, Zhu N_γ with Loukidis f_{ie} resulted in good agreement with most cases tested.

TABLE OF CONTENTS

LIST OF TABLES

Table page

LIST OF FIGURES

Figure page

1.0 INTRODUCTION

1.1 Background

The FDOT has number of structures that are designed and constructed on shallow foundations subject to combined axial and lateral loads (bridges, MSE walls, cast-in-place walls, etc.). Current AASHTO Specifications (10.6.3.1.2) make allowance for the consideration of load inclination (combined axial and lateral load) when estimating nominal bearing resistance of spread footings. For instance, the reductions in axial bearing capacity due to Meyerhof (1953), Vesić (1973) and Hansen (1973) were considered. However, the commentary (C10.6.3.1.2a) in the code suggests "…. resistance and load inclination factors may be overly conservative for footings with an embedment of approximately $D_f/B = 1$ or deeper because the load inclination factors were derived for footings without embedment. In practice, therefore, for footings with modest embedment, consideration may be given to omission of the load inclination factors." It should be noted that the resistance factors included in the AASHTO code were derived for vertical loads, and their applicability to combined lateral-to-axial loads is currently unknown (C10.6.3.1.2a).

Unfortunately, for some laterally loaded walls, reduction of 75% in nominal bearing resistance may be computed with AASHTO recommended load inclination factors. Moreover, the code provides little if any insight into the influence of axial load on the sliding resistance of shallow foundations. Work in Europe and Australia (Perau, 1995) suggest that the ratio of axial load /axial bearing capacity varies in combination Horizontal Load/ Axial Bearing Load.

According to AASHTO C10.6.3.1.2a., the inclination factor equations listed in AASHTO 10.6.3.1.2 are based on small-scale experiments and limited theoretical work from 1950 to the 1970s. Paikowsky et al. (2010) in NCHRP 651 on LRFD Design and Construction of Shallow Foundations for Highway Bridges identified the work by the Europeans and Australians and the

significance of combined lateral and axial loading on the design of shallow foundations. They identified and proposed the concept of a combined failure state (similar to beam-column interaction diagram).

FDOT research project BDK75-977-22 completed in December 2013 was conducted in the centrifuge at the University of Florida considered a limited set of combined vertical and horizontal loads. The results indicate the inclination of resultant load had an experimentally proven effect on the bearing capacity of MSE walls for two different soil densities and one L/B ratio. This work showed for medium dense sand, the bias (measured/predicted) varied from 3.6 (Vesić) to 5.6 (Meyerhof) using Vesić's inclination factors. Whereas for dense sand the bias (measured/predicted) varied from 2.54 to 3.53 using Vesić's inclination factors suggesting Vesić is quite conservative. However, if Hansen's inclination factors were used, the bias (measured/predicted) varied from 1.3 to 1.9 for the medium dense, but only 0.6 to 0.9 for the dense sand suggesting a factor of two or more uncertainty as well as a lack of understanding in the combined influence of lateral and vertical load on a foundation's ultimate limit state.

1.2 Objective and Supporting Tasks

Given the great difference between AASHTO estimated bearing capacity with and without capacity factors (i.e., inclination, eccentricity, etc.), recommendations in AASHTO's commentary and the factors found in the limited reported data (e.g., BDK75-97-22 & NCHRP 651), there is great need to experimentally evaluate the influence of embedment depth, width/length ratio, axial to lateral load ratio, as well as soil density on the bearing capacity of a shallow foundations using the largest scale model practical. A means to accomplish the required testing (>100 tests) as well as reproduce the field conditions is with the centrifuge. Specifically, the centrifuge reproduces the same field stresses in the laboratory experiment as in the full-scale field experiment and allows for control of soil densities, multiple combination of axial and lateral loads, embedment depths for

bearing capacity factors assessment at a reasonable cost. Therefore, the objectives of this research are to:

- Collect Data on current B/L (width/length), embedment (D/B), eccentricity, lateral-to-axial load combination and sand densities beneath shallow foundations in Florida.
- Select one average foundation width, B (e.g., B = 5’ < B <10’) two B/L ratios (e.g., 1 and 3), two embedment depths, (e.g., D = 2’ and 5’), two loading locations, 3.5 axial to lateral load ratio, and two sand densities (e.g., medium dense and dense) for centrifuge testing (56 different cases x 2 repetitions = 112 total tests).
- Based on the results of the first 112 tests, three conditions will be repeated where D is near B.
- Construct a loading frame for shallow foundation testing in the centrifuge which considers, two embedment depths, two load locations on the foundation with 3.5 axial-to-lateral load ratios (i.e., inclinations).
- Conduct all the centrifuge tests with various soil densities, axial-to-lateral load ratios to obtain both the measured nominal bearing capacities as well as the measured axial-to-lateral inclination and eccentricity factors (i.e., measured axial-to-lateral bearing capacity and axial only bearing capacity).
- Compare the measured centrifuge results with current AASHTO bearing equations, as well as European and Australian approaches, and identify which combination of factors (Vesić, Meyerhof, Hansen, etc.) are representative and should be recommended for FDOT use.

1.2.1 Task 1 – Survey of FDOT Shallow Foundation Design and Construction Practices

FDOT Districts were contacted to identify structures (i.e., bridges, MSE walls, etc.) that were designed and constructed on shallow foundations. Of interest are the range of foundation widths (B), L/B, and embedment ranges along with the bearing capacity equations and associated

embedment, inclination, eccentricity factors that were used in the design. Also, of interest are the soil properties that were used for design (e.g., angle of internal friction) as well as the actual constructed values. The SMO was also surveyed to identify the range of sand gradation, and properties found in Florida beneath shallow foundations

1.2.2 Task 2 – Construct Centrifuge Container and Loading Frame for Variable Embedment, Eccentricity, and Load Inclination Tests on Shallow Foundations

To evaluate the bearing capacity factors for shallow foundations in the centrifuge, an experimental box with loading frame had to be designed and constructed. For this research, it was proposed that the box/container from FDOT project BDK75-977-22 should be used. It employs Plexiglas windows which allows observation of rupture surface. A steel frame with attachment for load actuators for inclined loads (multiple axial-to-lateral combinations) needed to be constructed for attachment to bottom of box/container. In addition, an independent frame for measuring vertical deformations at multiple locations on the foundation is required. Actuators for applying loads, and LVDTs for measuring foundation translation and rotation were acquired and attached to the deformation measuring frame. Applied loads were measured with load cells in-line with the actuators, and pressure transducers.

This task also involved the acquisition of the granular soil for the planned centrifuge tests as well as the construction of the different widths (B) and lengths, L, (i.e., L/B) foundations for testing. Each foundation was constructed from aluminum plate with bending stiffness (i.e. thickness), representative of shallow foundations.

1.2.3 Task 3 – Centrifuge Testing of Shallow Foundations

The experimental work utilized the large centrifuge at the University of Florida, as it made feasible the testing of multiple different models to meet the objectives. Table 1.1 shows the variables planned to be tested in the centrifuge.

Table 1.1 Parameters planned to be tested in the centrifuge model tests of bearing capacity

Soil Density	B, Width	L, Lengths	D, Depths	Axial-to-Lateral Load Ratios	Loading Locations	Repetitions
2	1	2	2**	3.5***	2	2*
Med Dense & Very Dense	Average FDOT width	L/B = 1 and L/B>3	Near Surface, Near B/2	See Figure 1.1	See Figure 1.1: Center (A) & Near Edge (B)	Repeat each test

*If 2 repetitions are not same third test will be performed
** Based on the results of the first 100-112 tests, 3 conditions will be repeated near D = B
*** Point A is loaded 3 times and B 4 times; average = 3.5

The selection of eccentricities and axial-to-lateral load ratio is as follows:

- Loading at Point B on the foundation is identical to loading at Point C for all axial load ratios; consequently, only one eccentricity with multiple inclinations considered.
- For cases of loading at Point A, all axial-to-lateral load ratios to left would be symmetric to loads to the right shown.
- All axial load ratios at Point A (1-3) will be used to find the measured eccentricity contributions; axial-to-lateral load ratios (2 and 3) will give the measured axial-to-lateral load influence factors.
- All axial load ratios at Point B will give the measured axial-to-lateral load influence for inclinations in either direction from the vertical (2 and 4) and the axial-to-lateral load ratios (2 and 3), with eccentricity (1 – 4).
- A total of 115 centrifuge tests will be performed from Table 1.1 (2 x 2 x 2 x 3.5 x 2 x 2+3)

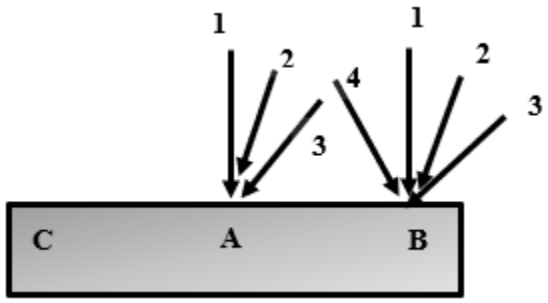

Figure 1.1 Proposed load scenarios

1.2.4 Task 4 – Comparison of AASHTO and Published Bearing Capacity Factors with Centrifuge Results

As identified in the background, Task 4 was planned to answer the question of the use of bearing capacity factors (e.g. AASHTO commentary "…..In practice, therefore, for footings with modest embedment, consideration may be given to omission of the load inclination factors…."). Using both the shallow and deep bearing capacity results (i.e. centrifuge tests), measured individual bearing capacity values may be determined. For instance, the case of centric loading (Vertical) will be divided by centric loading with an axial-to-lateral ratio for cases of both shallow and deep footings (i.e. assessment of load inclination factor). Similar results will be obtained for eccentric loading with and without axial-to-lateral loading.

Finally, AASHTO and published bearing capacity factors were compared with the measured bearing capacity factors. Bearings capacity factors for depth, eccentricity and axial-to-lateral load ratio – inclination based on Meyerhof, Vesić, Hansen and others were investigated. Based on the comparison, Task 4 also recommends bearing capacity factors for use in Florida conditions.

2.0 SURVEYS OF SHALLOW FOOTING DESIGN AND CONSTRUCTION PRACTICE

Surveys of engineers in Florida and across the United States were used to finalize the parameters and footing sizes and embedment depths to be tested in the experimental program. A discussion of a survey of FDOT engineers conducted for this research and a survey as part of the

NCHRP-651 study follow.

2.1 Questionnaire of Practices and Experiences

An online questionnaire on shallow foundation design and construction practices was distributed to all FDOT district offices. The purpose was to elicit information from state engineers and identify foundation and soil parameters that should be modeled in the experimental program (Task 3). Engineers were asked a series of questions about uses of shallow foundations, foundation widths (B), length to width ratios (L/B), foundation embedment depths (D_f), use of load inclination factors and typical factors, and eccentric loads and typical factors. Questions also covered typical bearing soil types, unit weights, and angles of internal friction. A summary of the survey questions and results follows.

The responses indicate shallow foundations are common among single story residential or commercial structures, multiple story residential (condo) or commercial structures, retaining walls, and bridges (Figure 2.1), while they have been used less for sign structures, toll gantry, sound walls, and light poles. Figure 2.2 shows the responses to question two. Among the responses, the largest foundation widths (B) were 12 ft (bridges) and the smallest 3 ft (single story residential or commercial structures). Foundation widths of 8 ft and 3 ft were the most common. The most common L/B was 1 followed by 2, then 6 and 10. A respondent answered "other" to this question, but did not provide what L/B was used. The most common depth of embedment was 4 ft, followed by 3 ft, 2 ft, and 5 ft (Figure 2.4). Of the foundations designed for eccentric loads, the only eccentricity provided was B/6 (Figure 2.5). Four respondents indicated that inclined loads were used in designs; however, only two of those answered with lateral-to-axial load ratio values of 0.1 and 0.25 (Figure 2.6). The most common soil types were A3 and A-2-4 (Figure 2.7). A respondent identified limestone in as the bearing material of shallow foundations in two cases. Note, the FDOT 455 specifications section 30 require soil beneath the foundation to be clean

cohesionless soil and classified as A1, A2, or A3 material. Respondents indicated that the bearing soil was most frequently compacted to 100% of maximum dry density per the AASHTO-T99 specifications and slightly less frequently to 95% of maximum dry density per the AASHTO-T180 specifications (Figure 2.8). Note, the FDOT 455 specifications section 31 require soil beneath the foundation to be compacted to 95% of AASHTO-T180 for a minimum depth of 2 ft. The most common soil angle of internal friction was 34° followed by 32° (Figure 9).

In response to question 14, respondents indicated that load test or plate load test data didn't exist or may exist. In response to question 15, two respondents provided the following:

- In Miami, we avoid use of shallow foundations when footing is to be constructed below groundwater table due to difficulties in dewatering.
- Sinkholes.

Overall, there was 5 respondents that provided answers related to projects across 6 districts and the Turnpike office (Figure 2.10).

1) For what type of structure have you used shallow foundations?

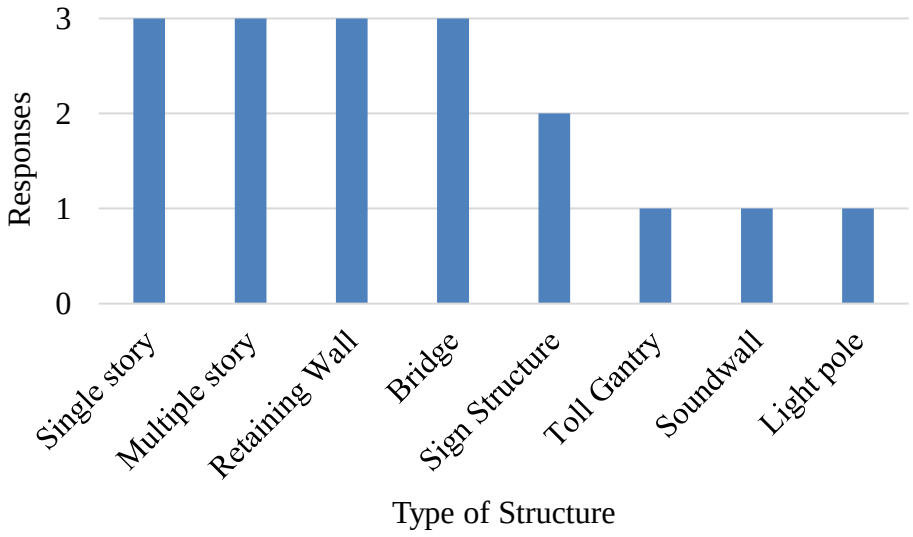

Figure 2.1 Survey responses of structures with shallow foundations

2) For the structures you have designed, what are the most common width of shallow foundations for:

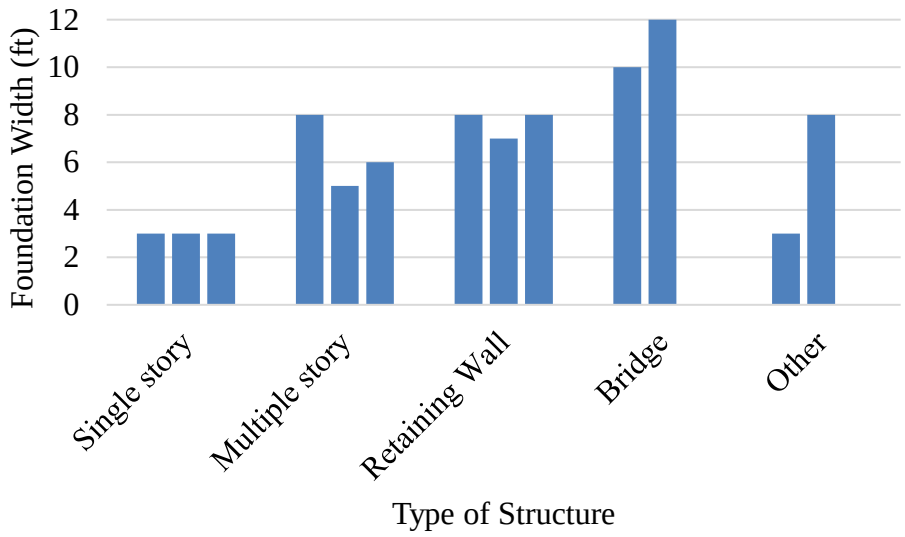

Figure 2.2 Survey responses of foundation widths for structures identified

3) For the structures you have designed, what are the most common foundation length/width (L/B) ratios?

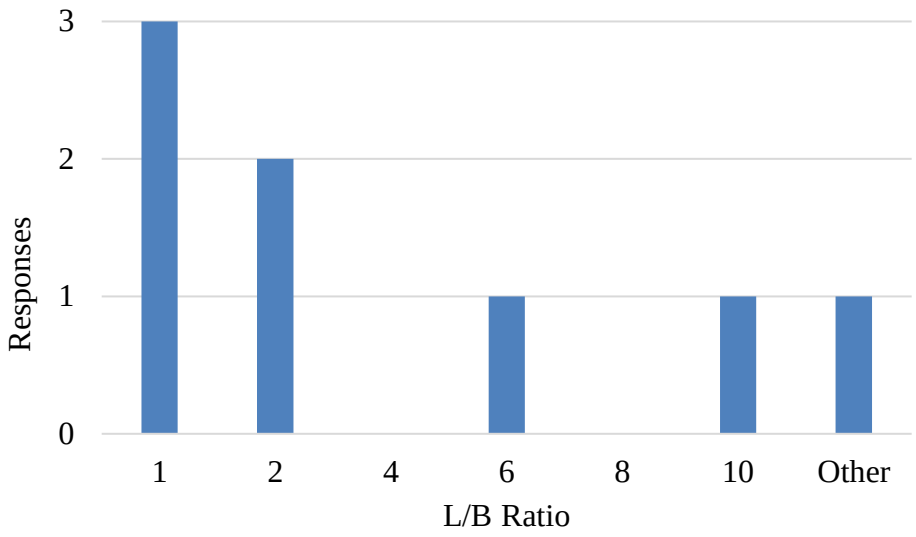

Figure 2.3 Survey responses of L/B ratios for shallow foundations

4) Are the shallow foundations typically embedded?
   a. Yes
   b. No

5) If yes, what are the typical depths?

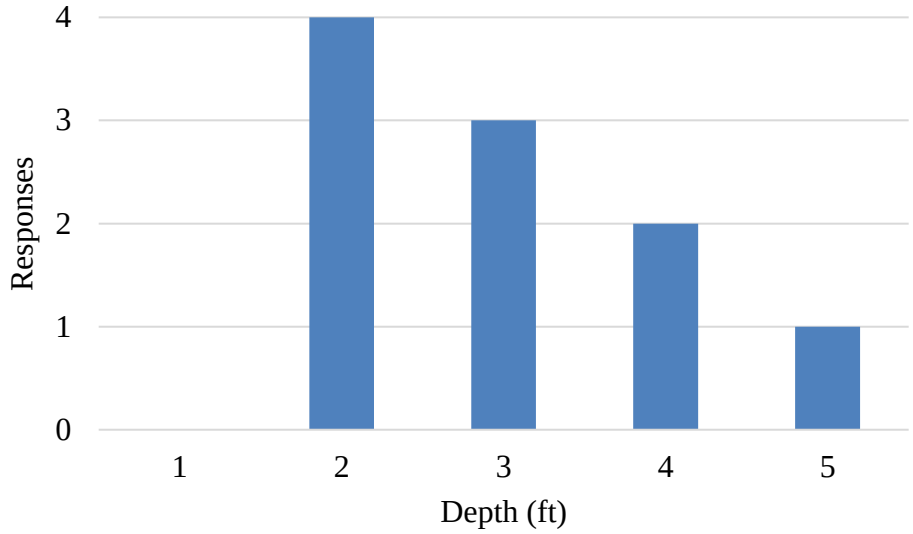

Figure 2.4 Survey responses of shallow foundation depths of embedment

6) Were these shallow foundations designed for eccentric loads?
   a. Yes
   b. No
7) If yes, what are the typical eccentricities

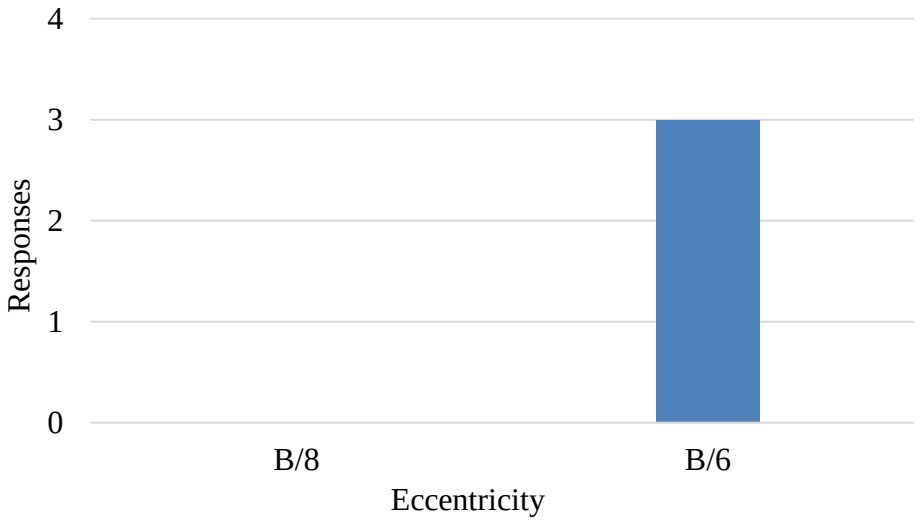

Figure 2.5 Survey responses of load eccentricities

8) Were these shallow foundations designed for inclined loads?
   a. Yes
   b. No
9) What were the typical lateral-to-axial load ratios?

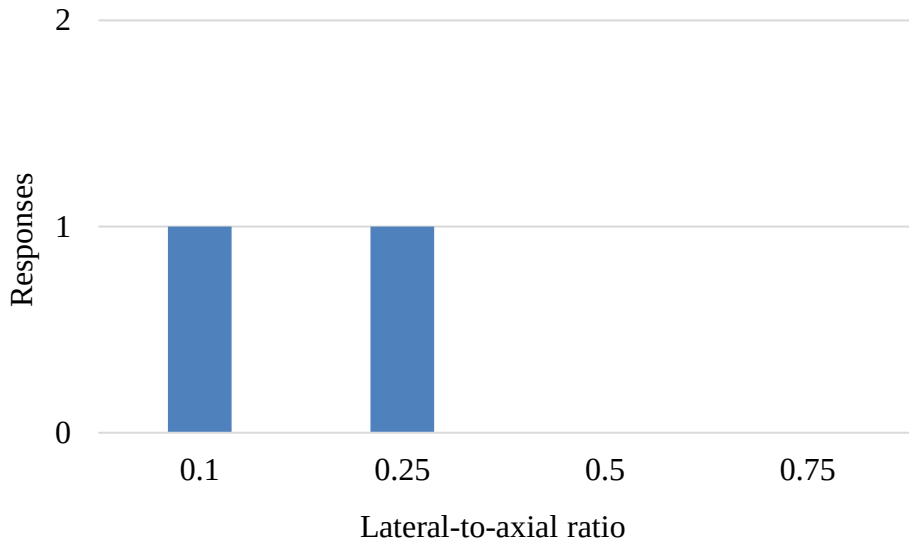

Figure 2.6 Survey responses of lateral-to-axial load ratios

10) Do you typically include load inclination factors when designing shallow foundations with combined lateral-to-axial loads?
    a. Yes
    b. No

11) What are the typical soil types beneath the footings?

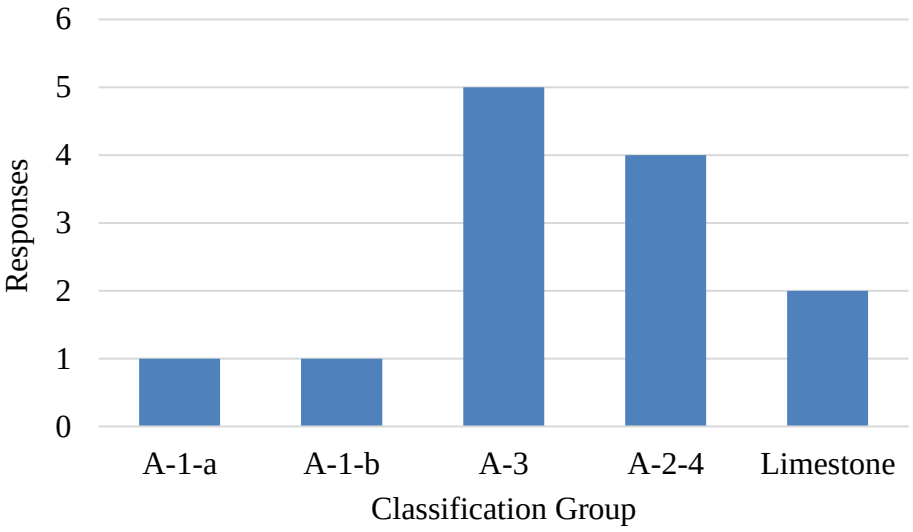

Figure 2.7 Survey responses of soil types classified by AASHTO classification

12) What is the typical soil density requirement beneath footings?

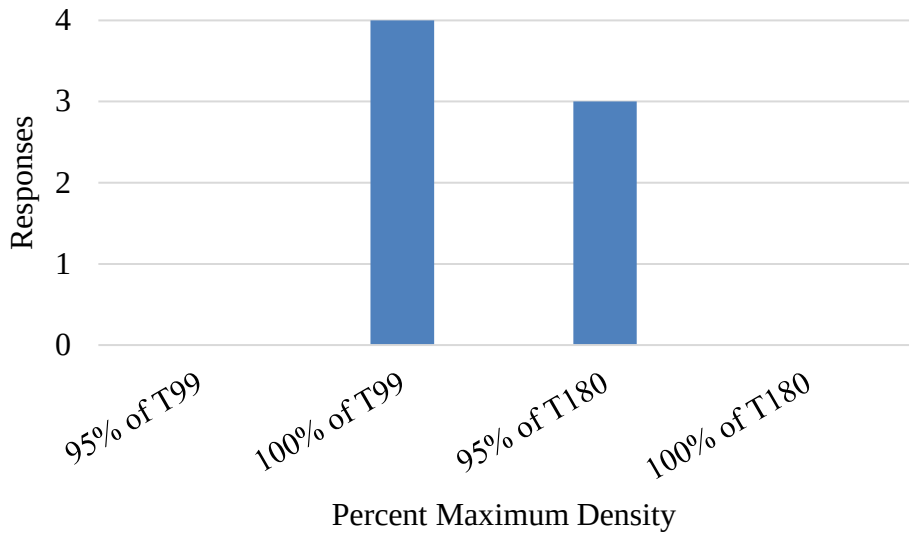

Figure 2.8 Survey results of percent maximum dry density

13) What is the typical expected soil friction angle of the compacted soil beneath the foundations?

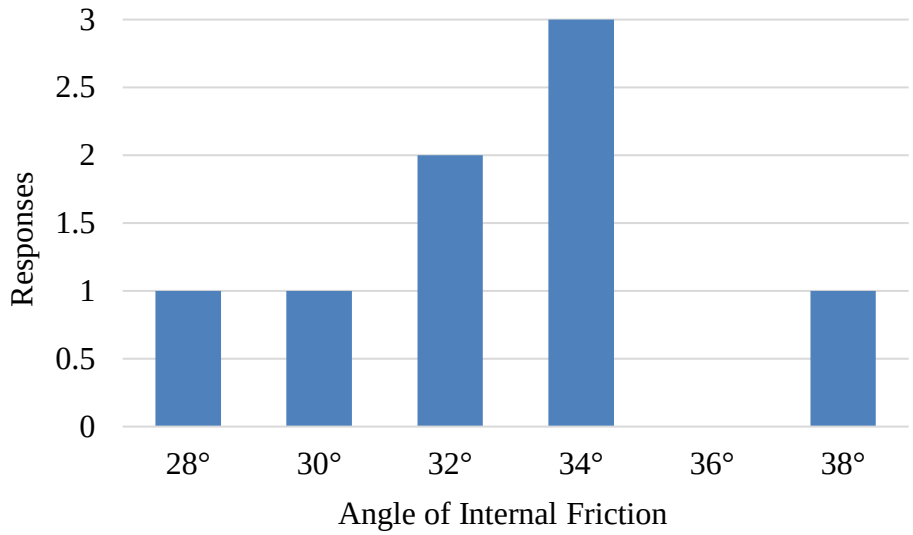

Figure 2.9 Survey results of soil angles of internal friction

14) Does your District Office have any load test or plate load test results used in conjunction with design of spread footings?

15) Are there any specific local considerations when designing shallow foundations in your district?

16) Which FDOT District Offices are responsible for the location of the projects you described in these answers?

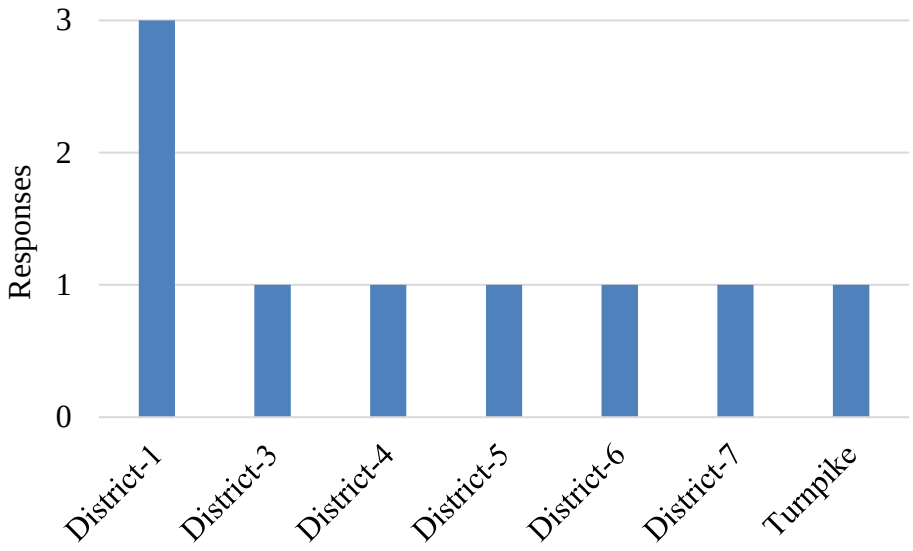

Figure 2.10 District offices that participated in survey and occurrences of participation

2.2 Summary of State of Practice Questionnaire in NCHRP 651

Paikowksy et al. (2010) distributed a questionnaire to all state transportation agencies in the United States as part of the NCHRP Report 651 "LRFD Design and Construction of Shallow Foundations for Highway Bridge Structures". Overall, officials from 39 states responded. The respondents indicated that 17% of the foundations used in their state were shallow foundations. Significant findings from those respondents and that are relevant to this study include:

- The geotechnical design is typically performed prior to the final loads being known and, as a result, the load inclination and/or eccentricity cannot be considered. To resolve this, 1) effective foundation sizes are used in design (i.e., $B' = B - 2e$), 2) greatest eccentricity is assumed, and 3) unit bearing capacity, both nominal and factored (use of resistance factor) are provided.
- 53% of the respondents do not use load inclination factors in their design.
- 70% of respondents evaluate resistance to sliding and most using the gross foundation area (i.e., B x L).

- 13% of the respondents consider the passive resistance on embedded footings, while most indicated concern with its availability long term.
- 63% limit eccentricity to B/6 – B/4.

In the FDOT's Soils and Foundations Handbook (FDOTa, 2017) it is recommended that analysis of shallow foundations should be done in accordance with the AASHTO LRFD Bridge Design Specifications except where otherwise stated in the in the Structures Design Guidelines (FDOTb, 2017).

2.3 Conclusions

The survey responses and review of the NCHRP 651 report suggest provided valuable information from which test parameters and cases could be selected for study. The following were determined to be tested in the centrifuge experiments:

- An A3 poorly graded sand with less than 3% fines will be used.
- Embedment depths of zero, 0.5B, and B will be tested. Only a few selected cases will be tested at embedment of B.
- Prototype footing widths of 3 ft (L/B = 20) and 5 ft (L/B = 10 and 1) will be tested at model scale of N = 34 G and 40 G.
- Lateral-to-axial load rations of 0.10 and 0.25 will be tested.
- Load eccentricity of B/6 will be used.

3.0 CENTRIFUGE EXPERIMENTAL PROGRAM

3.1 Introduction

An experimental program was developed to assess the bearing capacity of shallow footings with concentric, eccentric, inclined and eccentric-inclined loading conditions using centrifuge modeling. A new container was designed and built to accommodate multiple size footings and loading conditions. Based on the size of the container, a model scale was selected for each footing size and test sensors were selected and obtained to monitor stresses beneath the footing and its vertical movement. Finally, granular soil was selected for the shallow foundation study based on the results of the questionnaire distributed to the FDOT districts in Chapter 2. Laboratory tests were performed to assess sand densities (min and max) and angles of internal friction. A discussion for each of the tasks involved in the experimental program follows.

3.2 Centrifuge Test Setup and Models

3.2.1 UF's Large Centrifuge

The UF centrifuge used in this study was constructed in 1987 as part of a project to study the load-deformation response of axially loaded piles and pile groups in sand (Gill, 1988). Throughout the years several modifications have been undertaken to increase the payload capacity of the centrifuge. Previously, electrical access to the centrifuge was only provided by four 24-channel electrical slip-rings. Recently, a National Instruments cRIO data collection system capable of reading strain, voltage, and acceleration was installed on the centrifuge arm. The data is transferred over wireless nodes into a repository exclusive to the centrifuge lab. Pneumatic and hydraulic access is provided by a three-port hydraulic rotary union manufactured by the Deublin Company. The rotating-arm payload on the centrifuge is balanced by fixed counterweights that are placed prior to spinning the centrifuge. Aluminum C channels support both the payload and counterweights in the centrifuge (Figure 3.1).

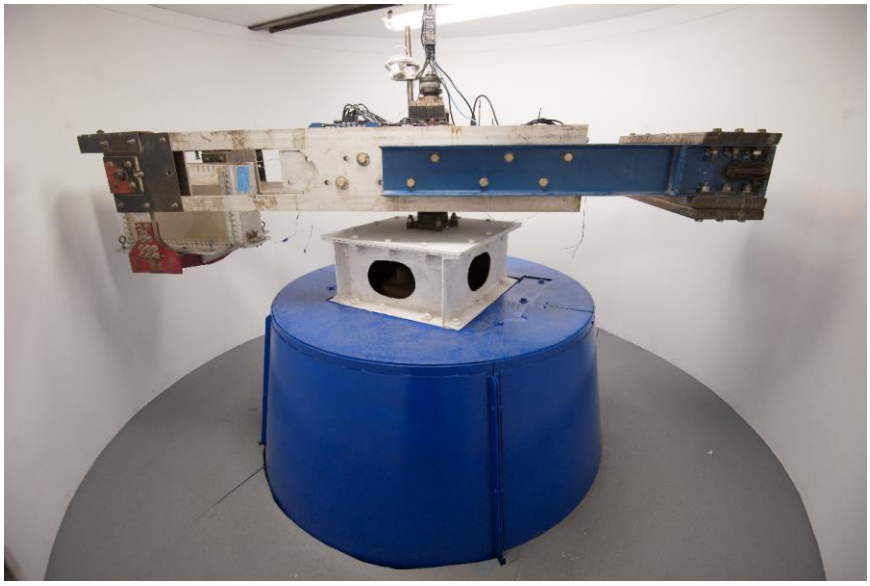

Figure 3.1 University of Florida's large geotechnical centrifuge

On the payload side (Figure 3.1), the aluminum C channels support the swing-up platform, through shear pins. The latter allows the model container to rotate as the centrifugal force increases with increasing rotations per minute (rpm). The platform (constructed from A36 steel) and connecting shear pins were load tested with a hydraulic jack in the centrifuge. The test concluded that both the swing up platform and shear pins were safe against yielding if the overall payload was less than 12.5 tons (Molnit, 1995).

3.2.2 Theory of Similitude

Laboratory modeling of prototype structures has seen several advances over the decades. Of interest, are those which reduce the cost of field-testing as well as reduce the time of testing. Additionally, for geotechnical engineering, the modeling of in situ stresses is extremely important due to soils' stress dependent nature (stiffness and strength). One way to reproduce the latter accurately in the laboratory is with a centrifuge.

A centrifuge generates a centrifugal force, or acceleration based on the angular velocity which a body is traveling. Specifically, when a body rotates about a fixed axis each particle travels in a circular path. The angular velocity, ω, is defined as $d\theta/dt$, where θ is the angular

position, and t is time. From this definition, it can be implied that every point on the body will have the same angular velocity. The period T is the time for one revolution, and the frequency f is the number of revolutions per second (rev/sec). The relation between period and frequency is *f = 1/T*. In one revolution, the body rotates 2π radians or

$$\omega = \frac{2\pi}{T} = 2\pi f \qquad \text{Eq. 3.1}$$

The linear speed of a particle (i.e., v = ds/dt) is related to the angular velocity, ω, by the relationship $\omega = d\theta/dt = (ds/dt)(1/r)$ or

$$v = \omega \mathrm{r} \qquad \text{Eq. 3.2}$$

An important characteristic of centrifuge testing can be deduced from Eqs. 3.1 and 3.2: all particles have the same angular velocity, and their speed increases linearly with distance from the axis of rotation (r). Moreover, the centrifugal force applied to a sample is a function of the revolutions per minute (rpm) and the distance from the center of rotation. In a centrifuge, the angle between the gravitational forces, pulling the sample towards the center of the earth, and outward centrifugal force is 90°. As the revolutions per minute increase so does the centrifugal force. When the centrifugal force is much larger than the gravitational force the normal gravity can be neglected. At this point the model will in essence feel only the "gravitational" pull in the direction of the centrifugal force. The earth's gravitational pull (g) is then replaced by the centrifugal pull (a_c) with the following relationship;

Centrifugal acceleration; $$\mathrm{a}_c = r\left(\frac{\pi \cdot rpm}{30}\right)^2 \qquad \text{Eq. 3.3}$$

where $$rpm = \frac{30}{\pi}\sqrt{\frac{\mathrm{a}_c}{r}} \qquad \text{Eq. 3.4}$$

Scaling factor; $$N = \frac{a}{g} \qquad \text{Eq. 3.5}$$

$$N = \frac{\sqrt{a_c^2 + g^2}}{g^2} \qquad \text{Eq. 3.6}$$

If $a_c >> g$, $$N = \frac{a_c}{g}$$ Eq. 3.7

where a is the total acceleration, g is the normal gravitational acceleration, a_c is the centrifugal acceleration, rpm is the number of revolutions per minute, and r is the distance from center of rotation.

The scaling relationship between the centrifuge model and the prototype can be expressed as a function of the scaling factor, N (Eq. 3-7). It is desirable to test a model that is as large as possible in the centrifuge, to minimize sources of error (boundary effects, etc.), as well as grain size effects with the soil. With the latter in mind, and, requiring the characterization of shallow footings be 3ft. wide for the strip footing and 5ft. wide for the rectangular and square, the following rationale was employed to determine the appropriate centrifuge G-level and angular speed, ω.

The maximum inside width of the sample container was 20 inches, which dictated the footing model width and the permissible lateral extents of shear failure surface without introducing boundary effects on each test. Modeling a 5 ft wide prototype footing with expected lateral extents of the failure surface in a vertical centric loading case (Figure 3.2) at N = 40 results in a model footing 1.5 inches wide and 8 inches on both sides of the footing for a failure surface.

Based on Equation 3.7, several important model (centrifuge) to prototype (field) scaling relationships have been developed (Taylor, 1984). Shown in Table 3.1 are those, which apply to this research. Two significant scaling relationships emerge: (1) Linear Dimension are scaled 1/N (prototype width = N*model width), (2) Stresses are scaled 1:1. The first significantly decreases the size of the experiment, which reduces both the cost and time required to run a test. The second relationship ensures that the in situ field stresses and model stresses are 1:1.

Note, the effective stress controls both the stiffness and strength of the soil.

Table 3.1 Centrifuge scaling relationships (Taylor, 1984)

Property	Prototype	Model
Acceleration (L/T^2)	1	N
Dynamic Time (T)	1	1/N
Linear Dimensions (L)	1	1/N
Area (L^2)	1	$1/N^2$
Volume (L^3)	1	$1/N^3$
Mass (M)	1	$1/N^3$
Force (ML/T^2)	1	$1/N^2$
Unit Weight (M/L^2T^2)	1	N
Density (M/L^3)	1	1
Stress (M/LT^2)	1	1
Strain (L/L)	1	1
Moment (ML^2/T^2)	1	$1/N^3$

3.2.3 Model Containers and Load Frame

As previously mentioned, the large centrifuge at UF has a safe working capacity of 12.5 tons to ensure that the bearing pins on the rotating swing up arm will not yield. Therefore, the maximum design payload for each test apparatus cannot exceed 625 lb at 40 G. The width of the swing up arm, which houses the test apparatus, and the position of the shear pin limit the test apparatus to a maximum width of 21 inches and maximum length of 23 inches. The load frame apparatus and containers presented in Figures 3.3-3.5 were bound by these limitations. The theoretical failure surface was another limiting factor in the container design. Shown in Figure 3.2 is the theoretical bearing capacity failure in soil under ridged strip foundation.

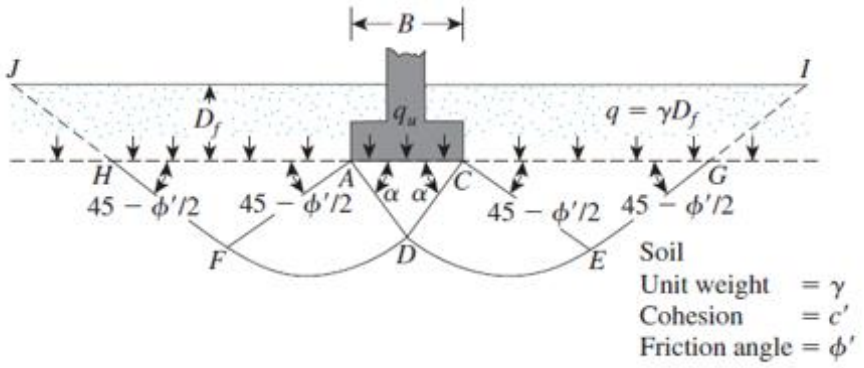

Figure 3.2 Theoretical failure surface

The failure surface is a function of the foundation width, *B*, embedment depth, D_f, and angle of internal friction, ϕ. The theoretical failure surface was calculated to allow for appropriate clearance to ensure that the container walls do not cause any boundary effect on the failure surface. In the case of the inclined loads, the load actuator is positioned out of center of the load frame to allow for additional clearance from the container walls. The inclined load scenarios can be seen in Figures 3.4 and 3.5.

In order to carry the anticipated applied footing loads required to achieve general bearing failure (ultimate bearing capacity), the upper load frame was designed using 2- by 2-in high strength steel tubing with 0.25-inch wall thickness, and the lower load frame columns and bracing were constructed out of 2- by 1-in high strength steel tubing with 0.1875-inch wall thickness. The load frame was designed to withstand two times the design load. The frame can also be configured for inclined and eccentric load cases. The load test frame designs for L/B = 20, 10, and 1 are shown in Figures 3.3-3.5, respectively, and dimensions for each, including the dimensions and loads driving the design of each, are listed in Table 3.2.

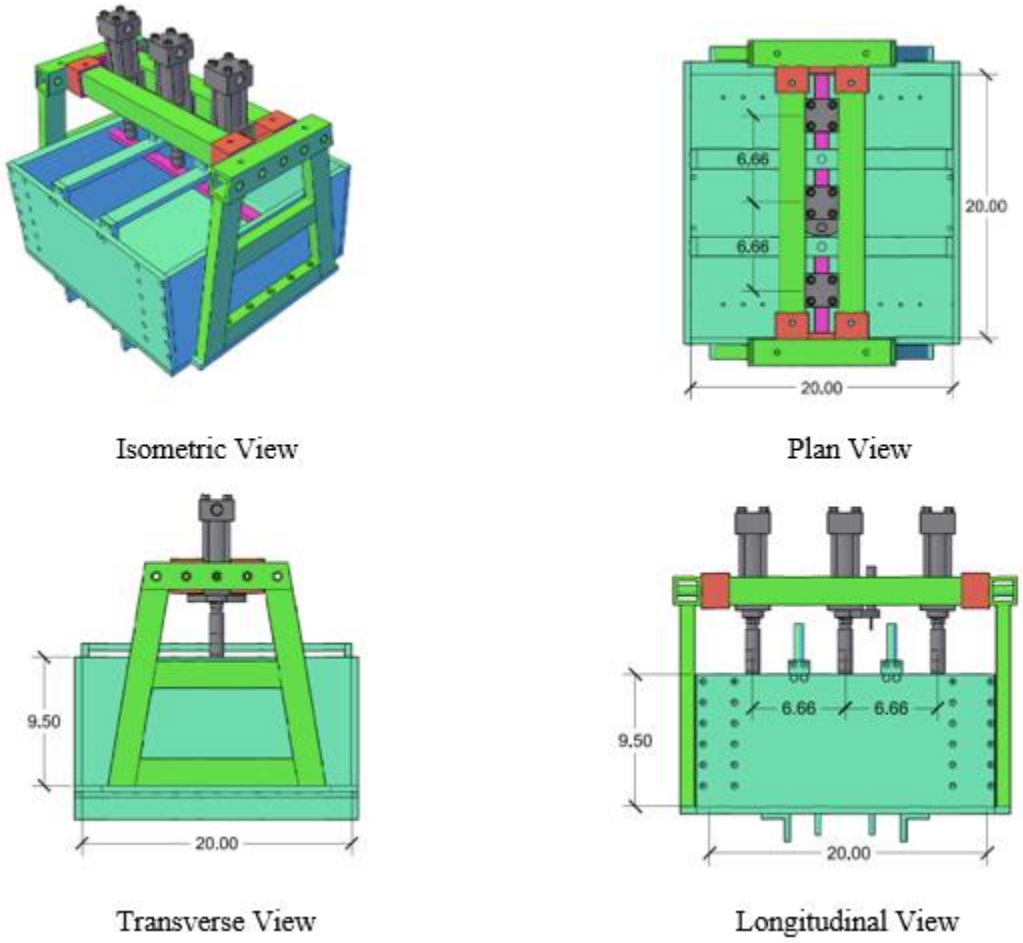

Figure 3.3 Strip footing (L/B = 20) test apparatus

Table 3.2 Container and model dimensions and loads

Container and Model Specifications	Strip Footing: (L/B = 20)	Rectangular Footing: (L/B = 10)	Square Footing: (L/B = 1)
Interior Container Width (in)	20	20	20
Interior Container Length (in)	20	15	20
Interior Container Height (in)	9.5	9.5	9.5
Soil Height (in)	8	8	8
Failure Surface length (in)	9.45	19.5	17.7
Total Load on Foundation (lb)	2290	3767	469
Total design weight of test apparatus (lb)	525	467	514

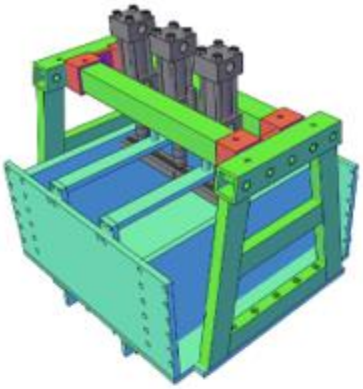

Isometric View (Concentric)

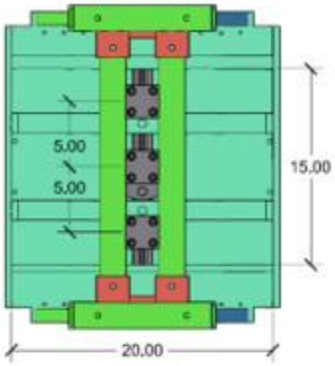

Plan View

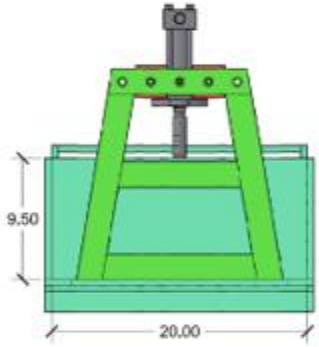

Transverse View (Concentric)

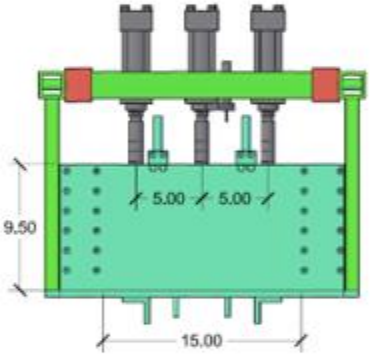

Longitudinal View

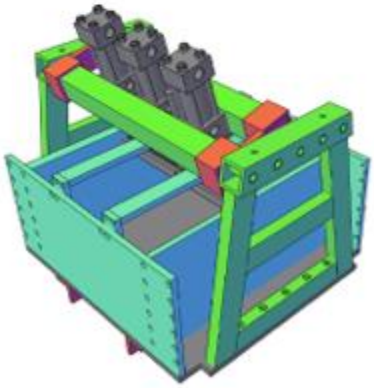

Isometric View (Inclined)

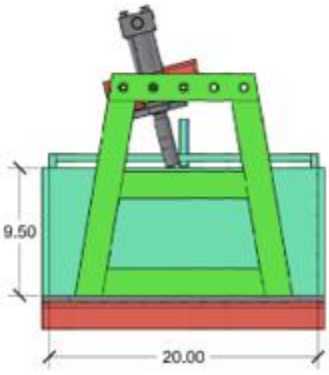

Transverse View (Inclined)

Figure 3.4 Rectangular footing (L/B = 10) test apparatus

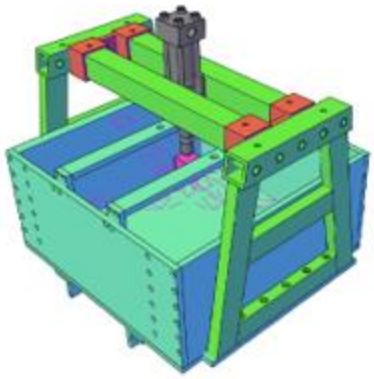

Isometric View (Concentric)

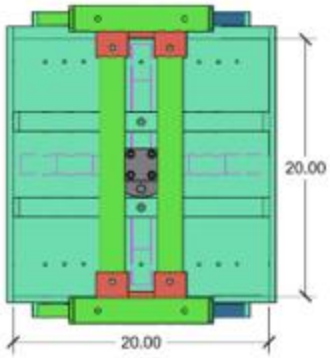

Plan View

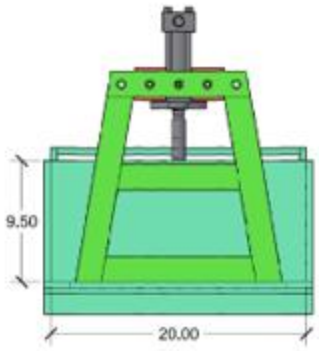

Transverse View (Concentric)

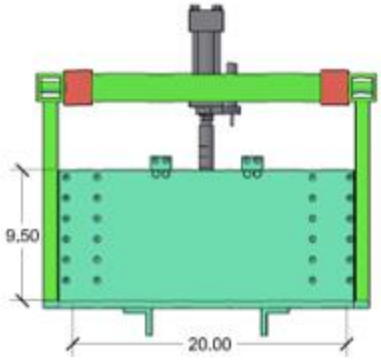

Longitudinal View

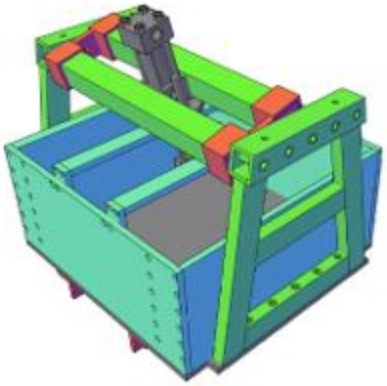

Isometric View (Inclined)

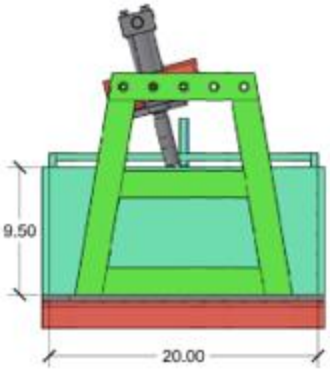

Transverse View (Inclined)

Figure 3.5 Square footing (L/B = 1) test apparatus

3.2.4 Model Footings

To minimize the flexure in the model foundations mock concrete foundations were designed in prototype size using soil pressures equal to 1/3 of the bearing capacity value. The shear and moment diagrams for the rectangular foundation (L/B = 10) with an ultimate bearing capacity of 24 ksf, and a design bearing pressure of 8 ksf are presented in Figure 3.6-3.7 for this load case.

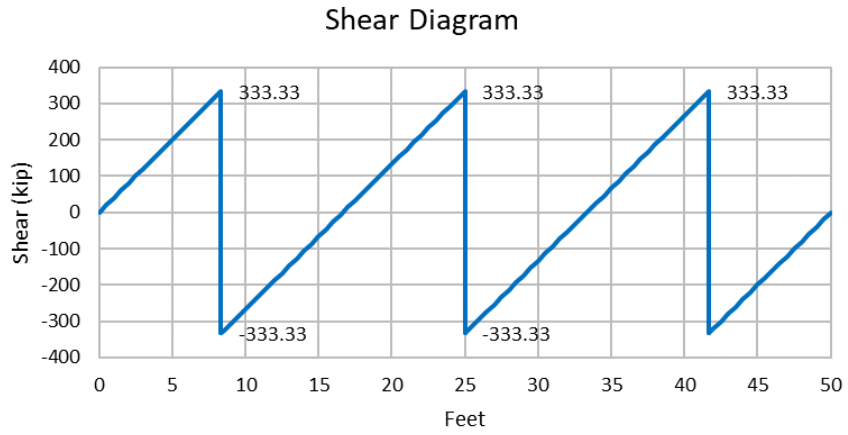

Figure 3.6 Shear diagram for rectangular foundation (8-ksf bearing pressure)

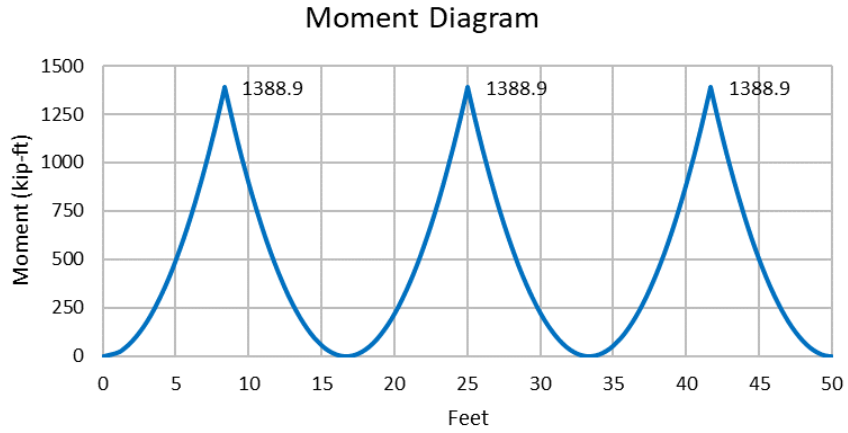

Figure 3.7 Moment diagram for rectangular foundation (8-ksf bearing pressure)

The effective moment of inertia, I, was determined for each concrete foundation scenario. The mock concrete foundation was then transformed to and aluminum foundation in prototype size with an equivalent stiffness, *k*, as related to flexure using Eq. 3.8.

$$E_c I_c = E_A I_A \quad \text{Eq. 3.8}$$

where E_c, is the Young's modulus of concrete, I_c, is the effective moment of inertia for the concrete, E_A, is the Young's modulus of Aluminum, and I_A, is the moment of inertia for aluminum.

The moment of inertia for aluminum is then used to determine the height, h_a of the prototype size aluminum foundation using the gross moment of inertia equation presented in Eq.3.9

$$I_A = \frac{b \cdot h^3}{12} \quad \text{Eq. 3.9}$$

Once the height of the prototype aluminum foundation is determined the height were scaled down to the appropriate model size foundation using the corresponding G-level. The model footings for each scenario are presented in Table 3.3 and shown in Figure 3.8.

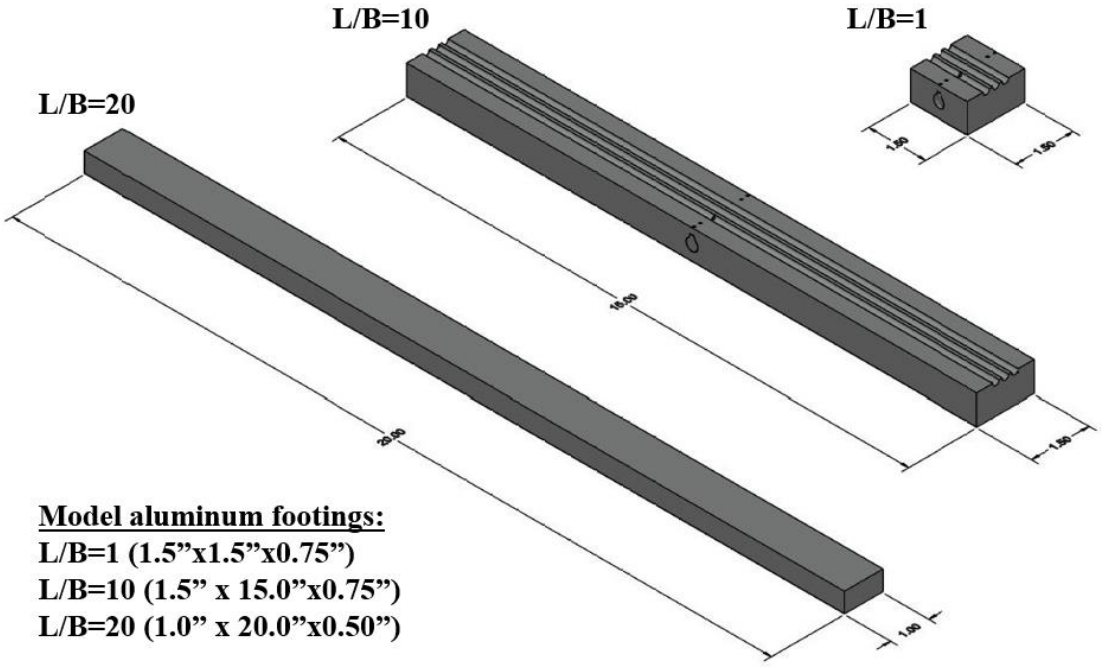

Figure 3.8 Model aluminum footings

Table 3.3 Parameters for strip, rectangular, and square model footings

Model Parameters	Strip Footing: (L/B = 20)	Rectangular Footing: (L/B = 10)	Square Footing: (L/B = 1)
Model Width (in)	1	1.5	1.5
Model Length (in.)	20	15	1.5
Model Thickness (in.)	0.5	0.75	0.75
# of Pressure Transducers	0	4	4

3.2.5 Instrumentation

3.2.5.1 Load Cell

The force applied to the model footing by each actuator is measured using a compression load cell manufactured by Omega show in Figure 3.9. The specifications for the Omega LC202 are listed in Table 3.4.

Figure 3.9 Omega LC 202 load cell (Omega Engineering, Inc.)

Table 3.4 Specifications for the Omega LC202

Excitation	10 VDC, 15 VDC max.
Output	2 mV/V nominal
Accuracy	± 0.25% FSO Linearity, Hysteresis, Repeatability Combined
5-Point Calibration	0%, 50%, 100%, 50%, 0%
Zero Balance	±2% FSO
Operating Temperature Range	-54 to 121°C (-65 to 250°F)
Compensated Temperature Range	16 to 71°C (60 to 160°F)
Thermal Effects	Zero: 0.009% FSO/°C Span: 0.009% FSO/°C
Safe Overload	150% of Capacity
Ultimate Overload	300% of Capacity
Input Resistance	360 Ω Min.

Table 3.4 (continued)

Output Resistance	350 ± 10 Ω
Construction	Stainless Steel
Electrical	1.5 m (5’) 4-Conductor Cable
Protection Class	IP65
MECHANICAL SPECIFICATIONS	
Capacity	3000 lb.
Total length – Dimension A	1.75 in.
Stub Length – Dimension B	0.50 in.
Thread Style – Dimension C	3/8-24 UNF-2A
Diameter- Dimension D	1.00 in.

3.2.5.2 Linear Position Transducers

The footing movement in the vertical direction is monitored during loading using linear position transducers manufactured by BEI shown in Figure 3.10. The specifications for the BEI model 602 transducers are listed in Table 3.5.

Figure 3.10 BEI Linear Position Transducer Model 602

Table 3.5 Specifications for the BEI linear position transducer model 602

Resistance Range	2 KΩ
Resistance Tolerance	±20%
Independent Linearity	±0.35%
Power Rating @ 70□C	0.25 Watts
Output Smoothness	0.10%
Resolution	Infinite
Insulation Resistance @ 500 VDC	1,000 MΩ
Dielectric Strength (VRMS)	500 VRMS
Temperature Range	-55° to +125° C

Table 3.5 (continued)

Mechanical Travel	2 in.
	0.1 in. Min.
Actuation Force	2 Oz. Max.
Repeatability	Within 0.0005 in.
Life	$10X10^6$ cycles

3.2.5.3 Miniature Pressure Transducers

The rectangular and square model footings were instrumented with miniature pressure transducers to measure the soil pressure distribution beneath the bottom footing. The pressure transducers have a capacity of 3 MPa (63 ksf) with a diameter of 7.6 mm (Figure 3.11), the specifications for the miniature pressure transducers are presented in Table 3.6.

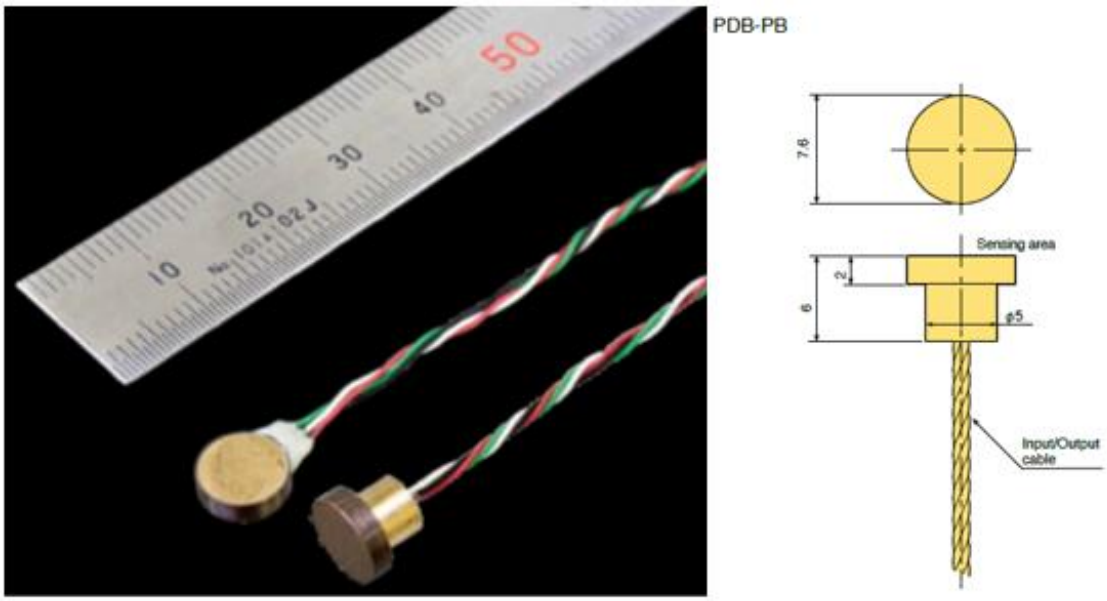

Figure 3.11 Miniature pressure transducers (Tokyo Measuring Instruments Lab)

Table 3.6 Miniature pressure transducers

Manufacture	Tokyo Measuring Instruments Lab.)
Type	PDB-3MPB
Capacity	3 MPa
Rated Output	1 mV/V ($2000x10^{-6}$ strain)
Non-linearity	1% RO
Hysteresis	1% RO

Table 3.6 (continued)

Temperature effect on zero	1% RO/°C
Temperature effect on span	1% /°C
Compensated temperature range	-10 ~ +60°C (no icing)
Allowable temperature range	-20 ~ +70°C (no icing)
Input/output resistance	350 Ω
Recommended exciting voltage	2 V or less
Allowable exciting voltage	5 V
Weight	0.7g

3.2.6 Soil Stress Sensor Calibration

Each sensor's sensitivity (mV/psi) was initially determined by the manufacturer through calibration in a pressure chamber (i.e., uniform fluid pressure). Since, the sensors were to be used in 63% - 95% relative density uniform dry soil, it was decided to calibrate under the same conditions. Labuz and Theroux (2005) designed a calibration apparatus for diaphragm type earth pressure cells that included soil overburden and applied uniform pressures up to 100 psi. The calibration of the sensors in this study utilized the centrifuge and the ability to increase the soil unit weight (increased G-levels) which creates the increased overburden pressures (i.e., $\sigma v = N_s\, g\, \rho s Z$). A series of four test were performed by placing the square model footing on the ground surface and incrementally spinning the centrifuge up to the operating rpm (G-Level). Figure 3.12 shows sensitivity measurements from calibration Test-4. The results for all four-calibration test and the factory calibrated slopes can be seen in Table 3.7. This proved to be an extremely effective and efficient method for laboratory calibration of a pressure sensors.

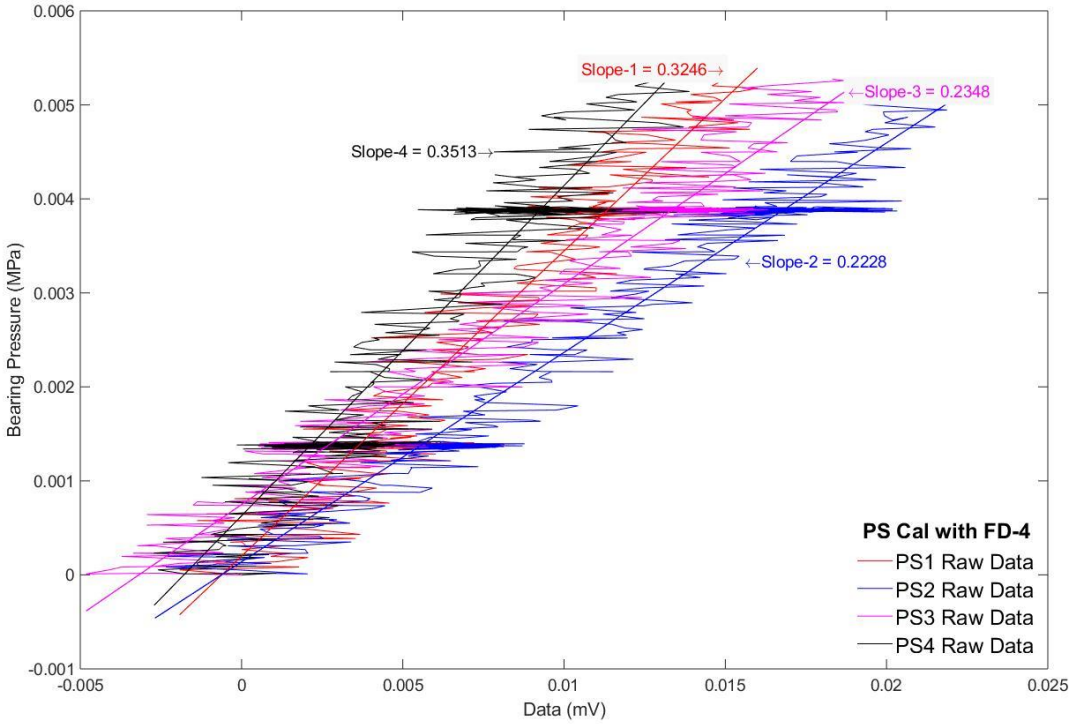

Figure 3.12 Soil stress sensor sensitivities from calibration #4 (slope = sensitivity)

Table 3.7 Soil stress sensor sensitivities from calibrations and factory settings

Title	Rated Output (mV/V)	Capacity (Mpa)	Excitation (V)	Calibration Test #1 (Mpa/mV)	Calibration Test #2 (Mpa/mV)	Calibration Test #3 (Mpa/mV)	Calibration Test #4 (Mpa/mV)
PS-1	1.004	3	5	0.278	0.264	0.317	0.325
PS-2	0.999	3	5	0.303	0.210	0.215	0.223
PS-3	1.034	3	5	0.499	0.267	0.235	0.235
PS-4	0.975	3	5	0.578	0.351	0.380	0.351

3.2.7 Hydraulic Loading Device

Shown in Figure 3.13 is the model container with the hydraulic load actuators attached to the load frame and the cross bars for the linear potentiometers (vertical displacement).

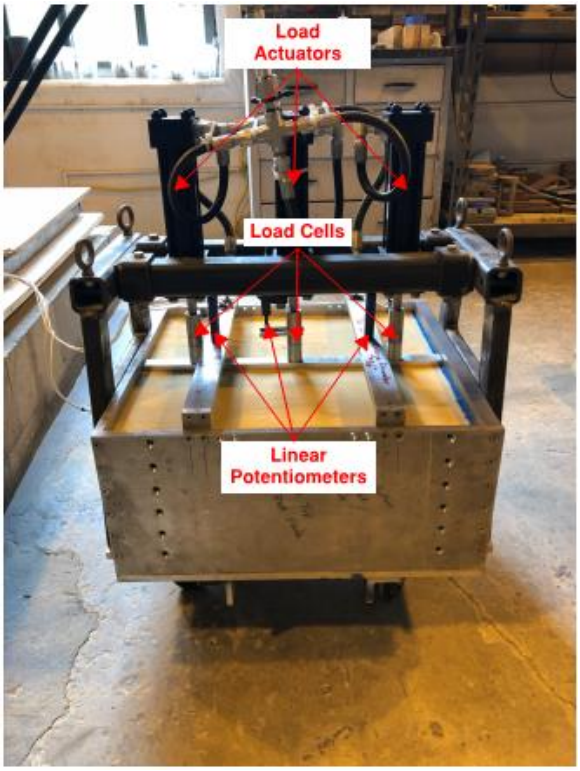

Figure 3.13 Setup of strip footing model with $D_f = 0$

Each load actuator shown in Figure 3.13 has a maximum operation pressure of 3000 psi and a stroke length of 5 inches (specifications in Table 3.8). The load actuators were set in motion using an Enerpac P464 hydraulic hand pump that delivers 0.29 cubic inches of oil per stroke and has a maximum operating pressure of 10,000 psi. The hand pump specifications are in Table 3.9.

Table 3.8 Hydraulic load actuator and performance specifications

Heavy Duty (Max 3000 psi)				Applied pressure (2000 psi)
B (in)	Bore (in)	Rod Dia. (in)	Area (in^2)	Force (lb)
2.5	1.50	0.63	1.77	3,534

Table 3.9 Enerpac hydraulic hand pump

Enerpac Model	P464
Maximum Operating Pressure (psi)	10,000
Cylinder Compatibility	Double-acting
Reservoir Capacity (in^3)	453
Maximum Flow at Rated Pressure (in^3/stroke)	0.29

Table 3.9 (continued)

Oil Displacement per stroke (in^3)	0.29
Piston stroke (in)	1.5

3.3 Loading Conditions

The strip footing solely utilized Load Case-1. For the case of the rectangular and square footing there were a total of five load cases scenarios considered for testing which are shown in Figure 3.14.

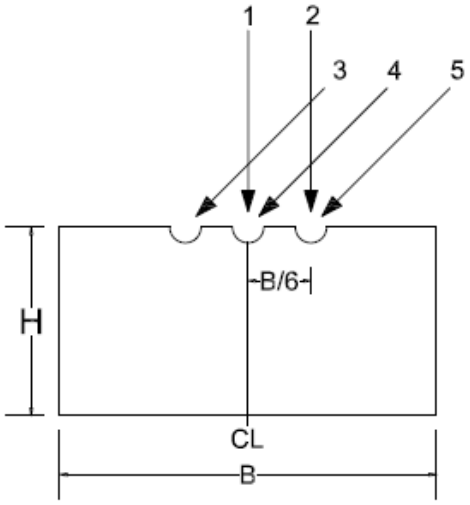

Figure 3.14 Load case scenarios

The load cases measured are characterized by positions one through five, Load Case-1, concentric, Load Case-2, eccentric, Load Case-3, eccentric-inclined, horizontal component positive (+), to the direction of the eccentricity, Load Case-4, inclined and Load Case-5, eccentric-inclined, horizontal component negative (–), to the direction of the eccentricity as presented by Meyerhof (1953).

3.4 Test Setup

3.4.1 Strip Footing Setup

For the strip footing (L/B = 20) tests, the model footing size was 20 inches in length x 1

inch in width and tested at a centrifuge model scale of N = 39, which equates to a prototype footing length of 65 feet by 3.25 feet in width (L/B = 20). Tests of the footing for three different depths of embedment (D_f = 0, 0.5B, and B) and two sand density conditions (medium dense and very dense) were conducted. The model footing is presented in Figure 3.15.

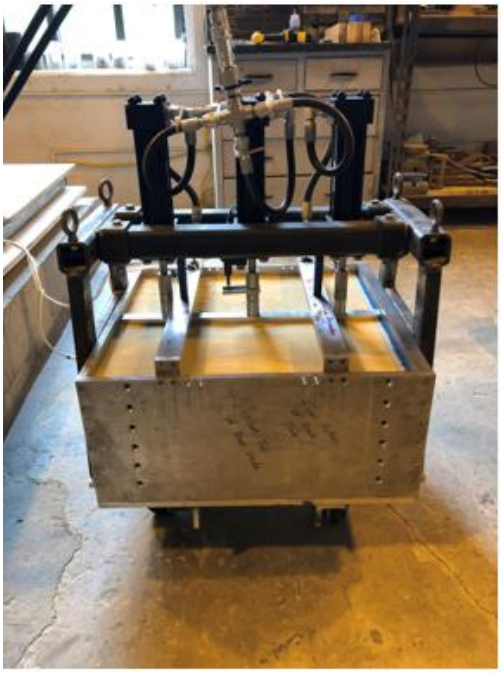

Figure 3.15 Model strip footing (L/B = 20)

3.4.2 Rectangular Setup

For the rectangular footing (L/B = 10) tests, the model footing size was 15 inches in length x 1.5 inches in width and tested at a centrifuge model scale of N = 40, which equates to a prototype footing length of 50 feet by 5 feet in width. The model footing is presented in Figure 3.16. The model footing had A3 sand glued to the bottom and was instrumented with miniature pressure transducers to measure the pressure distribution beneath the bottom footing sequential order (PS-1 through PS-4) at a spacing of 0.36 inches.

Figure 3.16 Model footing (L/B = 10) with miniature pressure transducers

Figure 3.17 illustrates loading conditions for Load Case-3 with L/A = 0.25 and embedment depth equal to 0.5B prior to testing.

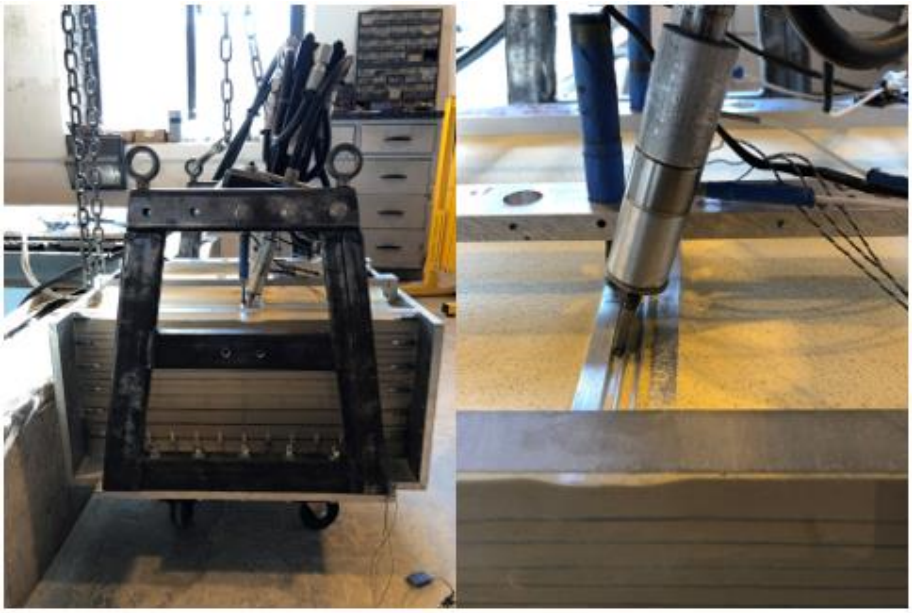

Figure 3.17 Pre-test images of Load Case-3

3.4.3 Square Footing Setup

For the square footing (L/B = 1) tests, the model footing size was 1.5 inches in length x 1.5 inches in width and tested at a centrifuge model scale of N = 40, which equates to a prototype footing length of 5 feet by 5 feet in width. The model footing is presented in Figure 3.18. Similar to the rectangular footing, the square model footing had A3 sand glued to the bottom and was instrumented with miniature pressure transducers to measure the pressure distribution beneath the bottom footing in sequential order (PS-1 through PS-4) at a spacing of 0.36 inches.

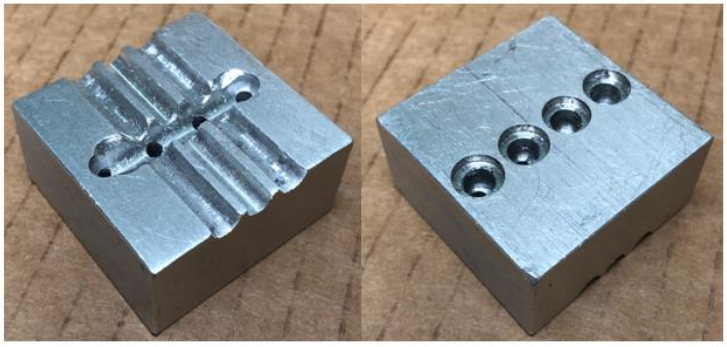

Figure 3.18 Model footing (L/B = 1) with machined locations for miniature pressure transducers

Figure 3.19 illustrates loading conditions for Load Case-4 with L/A = 0.10 and embedment depth equal to zero prior to testing.

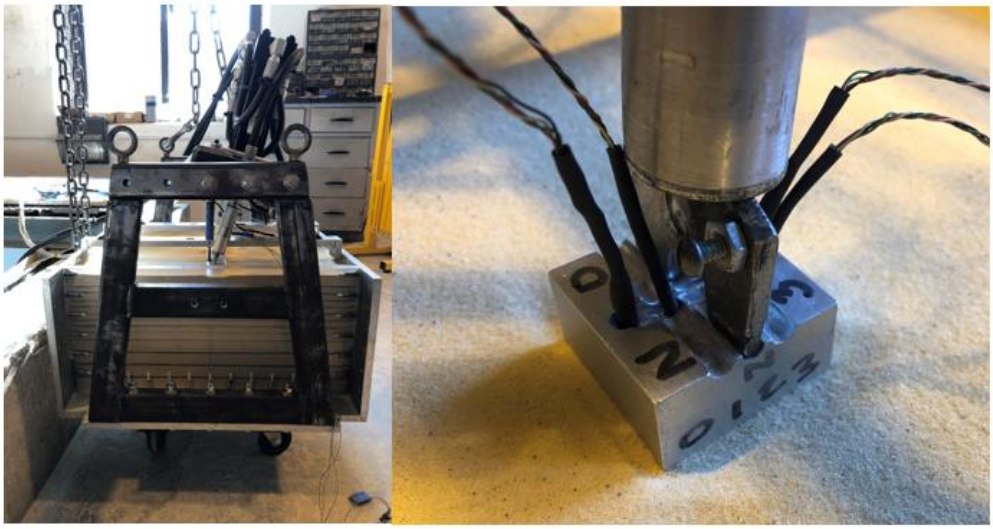

Figure 3.19 Pre-test images of Load Case-4

3.5 Soil

The sand grain size is of a concern in centrifuge modeling. A study of the grain size effect on bearing capacity models has shown that if the model size to mean grain size is 30 or greater, there is no effect (Fuglsang and Ovesen, 1988; Yamaguchi et al., 1976; Kimura et al., 1985; and Ovesen, 1985). The ratio of model width to mean grain size for these tests is 25.4 mm/0.2 mm = 127. Replicates of each case were performed to confirm experimental repeatability.

The footing models are being load tested on an A3 soil which is characterized as a poorly graded sand with less than 3% fines (Figure 3.20). Table 3.10 lists the index properties and classifications of the soil. Shown in Figure 3.21 is the relationship between internal friction angle and relative density, D_r, at peak shearing stress measured using the direct shear (DX) test and the triaxial consolidated drained (TX) test. The results of the DX test indicate for D_r between 47 to 87% (medium to very dense) peak ϕ from 29.7˚ to 34.8˚. The results of the TX test indicate for D_r between 52 to 100% (medium dense to very dense) peak ϕ from 33.3 ˚ to 41.7˚. The friction angle from the TX tests are generally about 3.5° greater than those from the DX tests. Lambe and Whitman (1969) note that the friction angle from the DX test is generally greater than that from the TX test, with the most significant difference in dense sands. Boyle (1995) reported DS and TX test results on very dense Ottawa sand (C_u = 1.7 and sub-rounded to rounded) and very dense Rainer sand (C_u = 2.9 and angular). The TX test's friction angles were 3° to 4° greater than the DS test's friction angle for the Ottawa sand, while the TX and DS test's friction angles for the angular Rainer sand were opposite and showed smaller differences. This suggests the influence of particle shape during the different shearing (shear plane permitted to form while shear plane forced) in the two tests and as the A3 sand used for this research is sub-rounded to sub-angular may explain the difference between the TX and DS test results. The L/B = 20 and 10 models are plain strain experiments and therefore neither the DS nor TX test the sand behavior appropriately; however, experiments have established the general differences in friction angle between all the tests as summarized by Ladd et al. (1977) and Boyle (1995) for Ottawa and Rainer sands. Furthermore, the bearing capacity factors have been derived for plane strain behavior and at a fully developed failure surface, which occurs post peak in stress, at larger strains corresponding to the residual or ultimate stress. For this reason, relationships between the

friction angle and relative density based on residual strength (Figure 3.23) were considered in the analysis of the centrifuge test results.

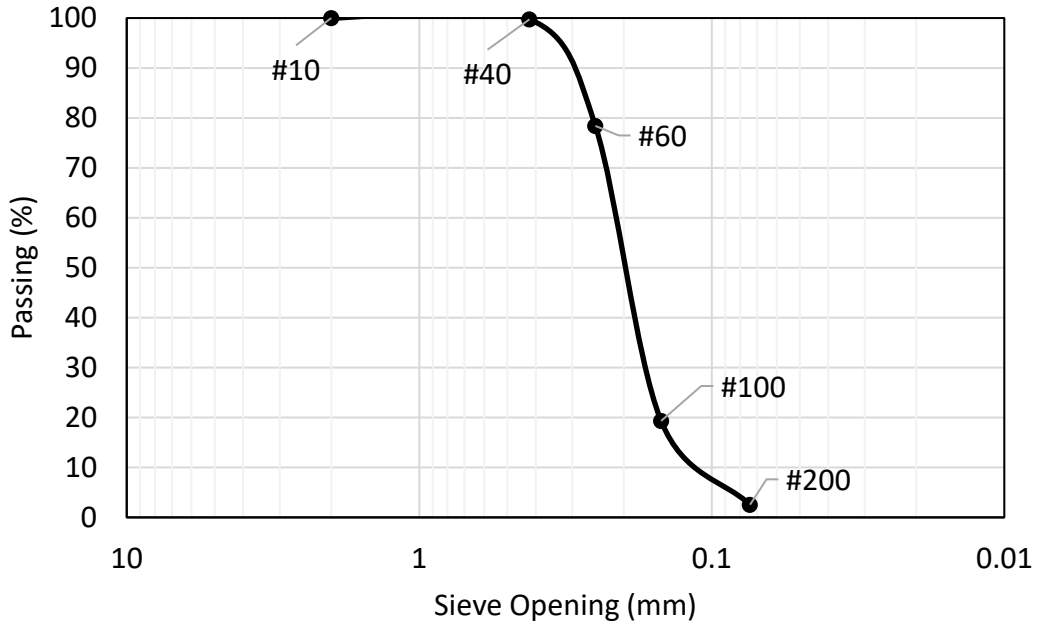

Figure 3.20 Particle size distribution curve for A3 soil

Table 3.10 Properties of A3 soil

Property	**Value**
Sand fraction (%)	97.5
Silt fraction (%)	2
Clay fraction (%)	0.5
Coefficient of Uniformity, C_u	1.67
Coefficient of Curvature, C_c	1.35
AASHTO classification	A3
USCS classification	SP
Specific gravity, G_s	2.67
e_{min}	0.53
e_{max}	0.84
Maximum unit weight, γ_{max}, (lb/ft^3)	108.9
Minimum unit weight, γ_{min}, (lb/ft^3)	90.7
Shape	Sub-rounded to Sub-angular
Liquid limit, LL (%)	NP
Plastic Limit, PL (%)	NP

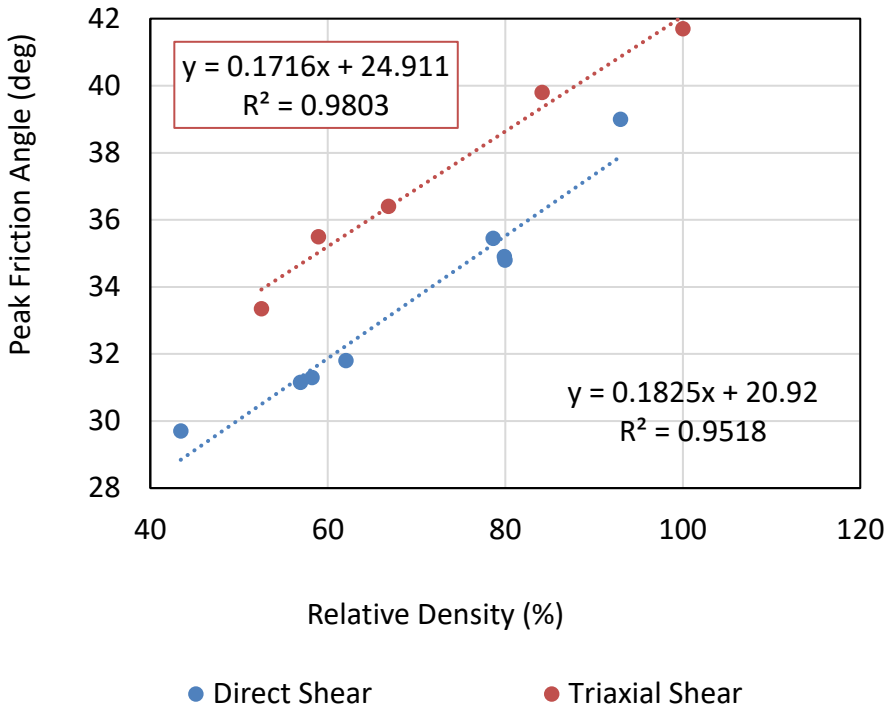

Figure 3.21 Peak friction angle versus relative density for A3 soil

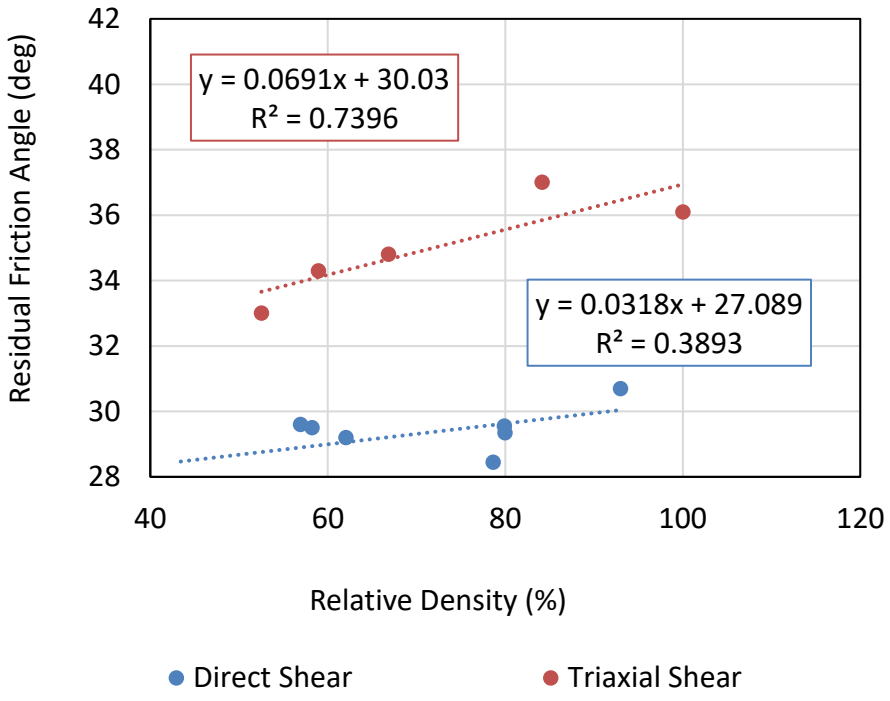

Figure 3.22 Residual friction angle versus relative density for A3 soil

3.6 Model Preparation

To prepare homogenous soil layers, sand grains were air-pluviated to target relative densities and void ratios which could be achieved. The pluviator consisting of a hopper, a shutter, and a moveable diffuser screen (Figure 3.23) and was used to deposit the sand into homogenous layers (Figure 3.27). The diffuser screen was made of #6 sieve screen (3.36 mm opening). Layer densities were controlled by maintaining a nearly constant drop height and flow rate. To achieve the desired density the drop height was determined to be 26 inches. The canopy was covered with a second diffuser screen made of #8 sieve screen (2.38 mm opening) in an effort to distribute the soil more evenly during the pluviation process.

The drop height was controlled for each successive layer using the drop height adjusters shown in Figure 3.23. Table 3.11 lists the pluviator settings to achieve medium dense and very dense relative densities of 63% and 97%, respectively, of the A3 sand.

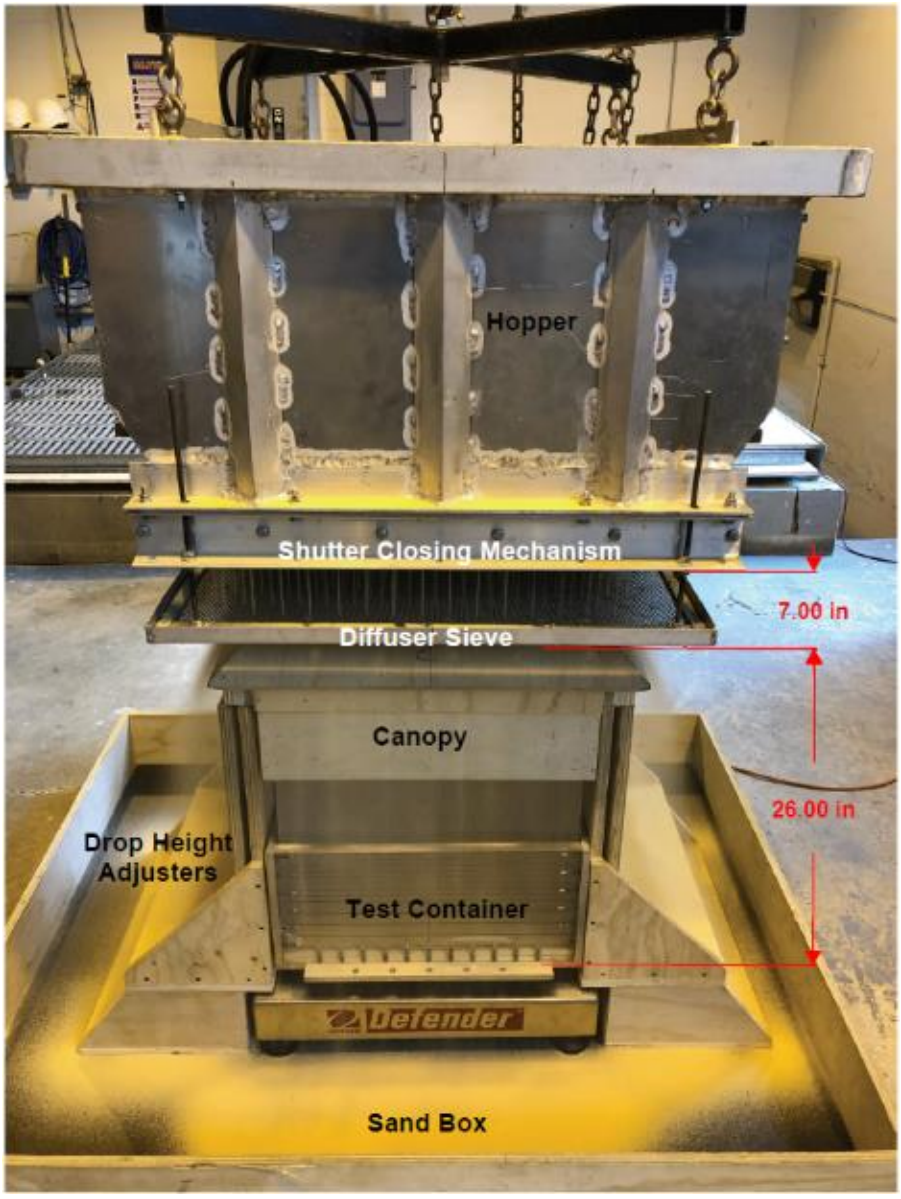

Figure 3.23 Elevation view of pluviator (dimensions in inches)


Figure 3.24 A3 soil falling through diffuser screen

The desired relative densities can be achieved by changing the flow rate of the sand, which is a function of the shutter hole area and hole spacing as shown in Figures 3.25 and 3.26.

Table 3.11 Achievable relative densities through dry pluviation of the A3 soil

Parameter	Medium Dense	Very Dense-Initial	Very Dense-Final
Relative Density – (D_r)	63%	90%	95%
Range of Relative Density condition	35-65%	85-90%	90-97%
Drop height of A3 soil	26 in.	26 in.	26 in.
Shutter hole area	0.065 in^2	0.024 in^2	0.024 in^2
Flow Rate of A3 soil	0.12 ft^3/min	0.015 ft^3/min	0.008 ft^3/min
Hole Spacing	1.57 inches	1.57 inches	3.15 inches

Initial soil models with relative densities greater than 85% were prepared with a shutter hole spacing of 1.57 inches, which could only achieve a maximum relative density of 90%. The hole spacing was subsequently increased to 3.15 inches which achieved relative densities between 90 to 95%.

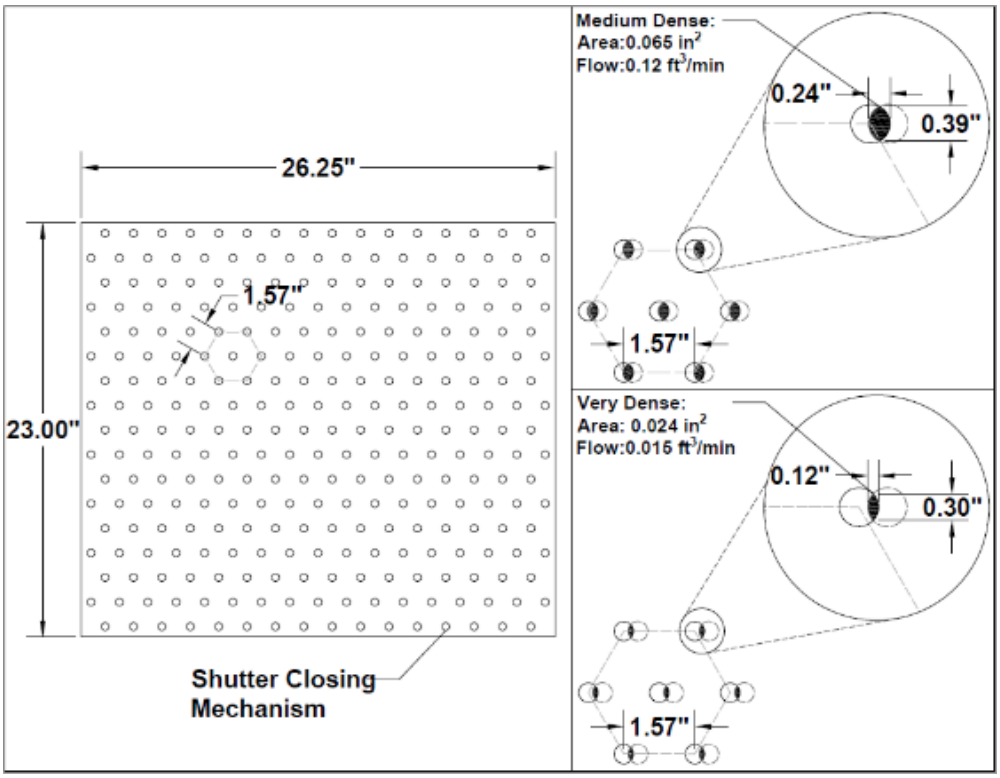

Figure 3.25 Shutter closing mechanism 1.57-inch spacing

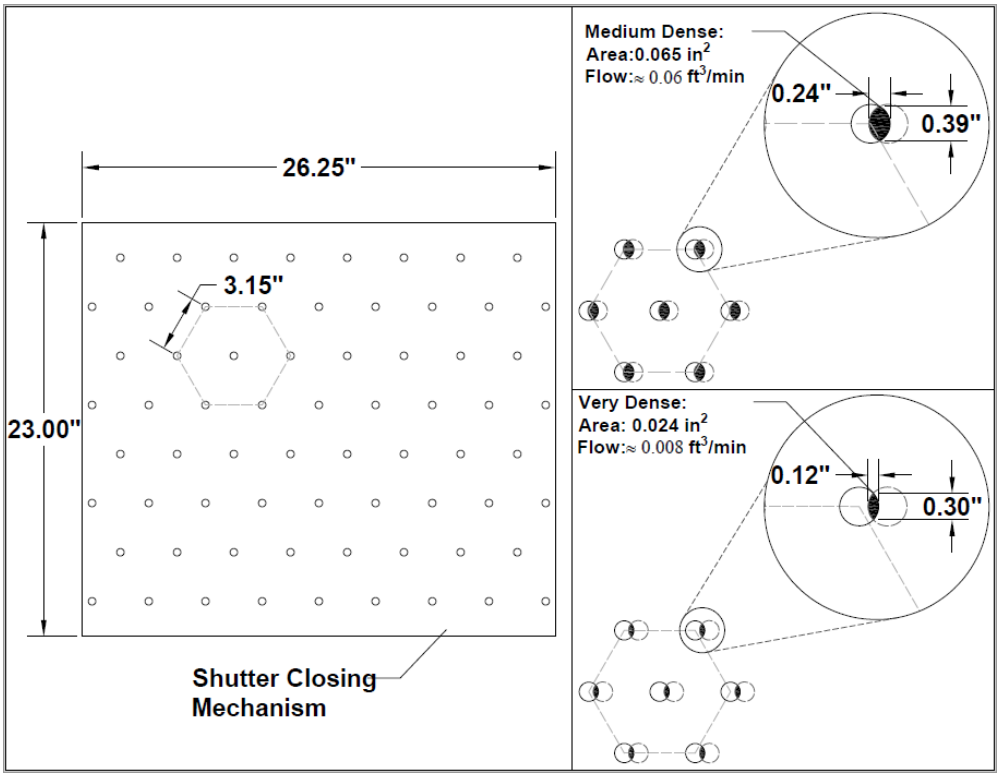

Figure 3.26 Shutter closing mechanism 3.15-inch spacing

Building the soil models using the A3 soil consists of pluviating one-inch lifts for the first five consecutive lifts, then ½ inch lifts for the remaining 7 lifts (total of 12 lifts). The upper lifts were reduced to ½ inch lifts to improve the mesh size in order to capture the expected failure surface. A thin line of blue colored soil with similar properties to the A3 soil was installed at the top of each lift to aid in identifying the failure surface in each test. The density of each layer was documented as the model was being prepared. To measure the mass of each soil layer, the model was prepared on a scale (shown in Figure 3.27). The thickness of each layer was calculated based on consecutive dial gauge measurements from a reference point to the top of each pluviated soil layer, as shown in Figure 3.27.

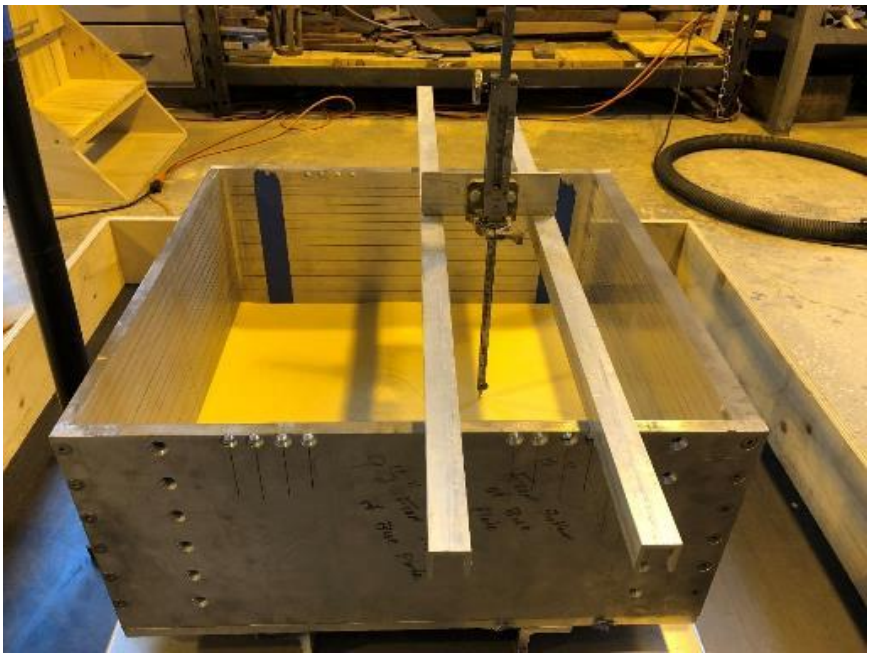

Figure 3.27 Dial gauge measurement

4.0 STRIP FOOTING (L/B = 20) TESTS

4.1 Model Load Tests – Concentric Loading on Strip Footing

The purpose of this series of tests was to validate and select bearing capacity factors for self-weight, N_γ ,overburden, N_q and depth correction factors, d_γ and d_q to be used in subsequent analysis. Load Case-1 was tested at three embedment depths (D_f = 0, 0.5B, and B) for two relative density conditions (medium dense and very dense (D_f = B only). Replicates of each case were performed to check for experimental repeatability. Table 4.1 lists the identifiers for each test with their dates, sand conditions, and footing depth of embedment.

Table 4.1 List of load tests for L/B = 20

Name	Date	Relative Density (D_r)	Embedment Depth (D_f)	Series #
LT-01*	07/05/2018	Very Dense	0	1
LT-02*	07/07/2018	Very Dense	0	2
LT-03	07/12/2018	Medium Dense	0	1
LT-04	07/13/2018	Medium Dense	0	2
LT-05	07/14/2018	Medium Dense	0.5B	1
LT-06	07/16/2018	Medium Dense	0.5B	2
LT-07*	07/17/2018	Very Dense	0.5B	1
LT-08*	07/18/2018	Very Dense	0.5B	2
LT-09	08/20/2018	Medium Dense	0.5B	3
LT-10*	08/28/2018	Very Dense	0.5B	3
LT-11*	09/06/2018	Very Dense	0.5B	4
LT-12*	10/01/2018	Very Dense	0.5B	5
LT-13**	10/10/2018	Very Dense	0.5B	6
LT-14**	10/29/2018	Very Dense	0.5B	7
LT-15†	11/05/2018	Very Dense	0	3
LT-16**	11/12/2018	Very Dense	B	1
LT-17**	11/13/2018	Very Dense	0	4
LT-18**	11/14/2018	Very Dense	0	5
LT-19†	11/16/2018	Very Dense	0.5B	8
LT-20**	11/20/2018	Very Dense	0.5B	9
LT-21**	11/26/2018	Very Dense	B	2
* D_r = 85-90%, ** D_r = 91-96%				
** Load test excluded from analysis due to instrumentation malfunction				

The centrifuge loading was performed in accordance with ASTM D1194-94. The load was applied to the soil in cumulative equal increments of approximately 450 psf each which is less than one tenth of the estimated bearing capacity.

4.1.1 Concentric Loading Condition with Depth of Embedment Equal to Zero

In this series of tests, the footing was loaded concentrically with depth of embedment equal to zero for two medium dense samples and four very dense samples. The A3 soil used in the test had an average dry unit weight, $\gamma_{dry,}$ in the range of 101.36 lb/ft^3 to 107.90 lb/ft^3 and average relative density, D_r in the range of 62.94% to 95.37% for the soil layers where the failure surface was observed. The average peak friction angle from the direct shear test was estimated to be in the range of 32.38° to 38.33°. The model footing was tested at N = 39 G with the L/B ratio of 20, which results in a prototype width and length of 3.25 feet by 65 feet. Table 4.2 presents the post-test plan view and failure surface views of the soil stratigraphy, which indicate general shear failure did occur. The failure surface ruptured the ground surface in all cases.

Table 4.2 Post-test failure surface for concentric loading condition at embedment depth equal to zero

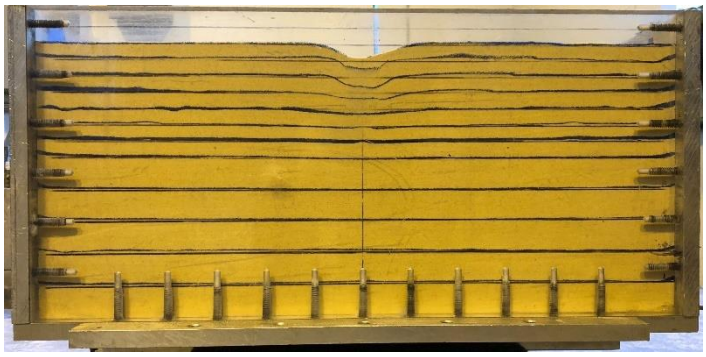 LT-01	

 LT-02	
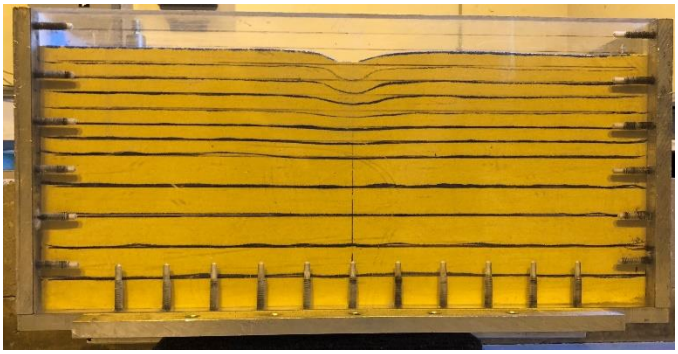 LT-03	
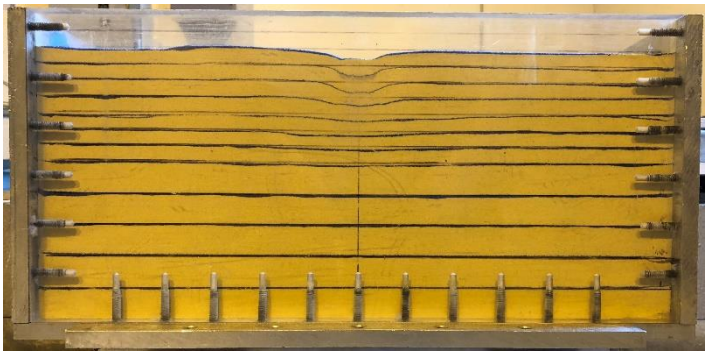 LT-04	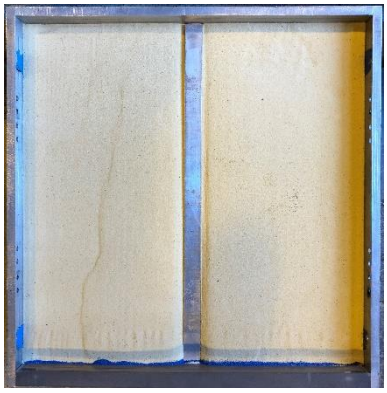
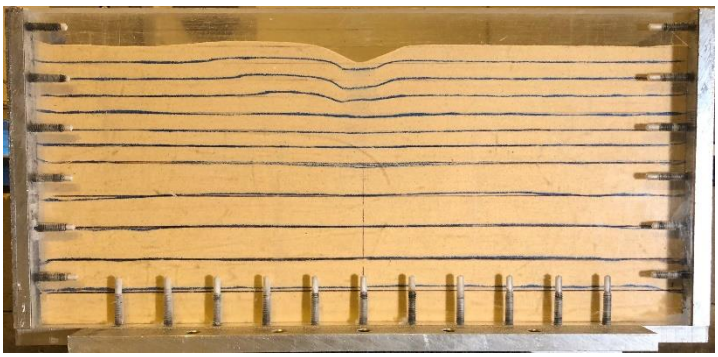 LT-17	

LT-18

Summary of the post-test images of rupture surfaces:

- Very dense sand (LT-01, LT-02, LT-17 and LT-18): The observed rupture surface for LT-01 shows a maximum depth and length of 2.50 inches and 7.99 inches. The failure surface ruptured the top layer of soil on the left side of the footing and over approximately 50% the length as the test underwent concentric loading at the center of the footing.
- Medium dense sand (LT-03 and LT-04): The observed rupture surface for LT-04 shows a maximum depth and length of 2.48 inches and 6.25 inches. The failure surface ruptured the top layer of soil on the left side of the footing the full length as the test underwent concentric loading at the center of the footing.

There have been several observations about when the failure surface will reach the ground surface relative to the ultimate bearing capacity. Vesić (1973) claimed, in the case of general shear failure, “the peak, ultimate load is reached simultaneously with the appearance of slip lines at the ground surface”, while Meyerhof (1948) differentiated between ultimate and final bearing capacity, ultimate being the load value corresponding to peak of load settlement curve and second, final being the value at which the shear failure slip lines fully form. Meyerhof (1948) further observed the final bearing capacity “by which time a failure surface usually becomes noticeable at the ground level” occurred at approximately twice the settlement at which

the peak load develops. These observations have been witnessed by other researchers. Ko and Davidson (1973) showed "at the footing penetration corresponding to ultimate bearing capacity, no distinct failure surface was visible. At a penetration of approximately 60% to 100% greater than that at which the ultimate bearing capacity occurred; a definite failure surface became observable". This behavior is consistent with load tests when the footing was pushed the maximum extent that could be measured by the linear potentiometer and not stopped when ultimate bearing capacity was observed in the load displacement plots during the tests.

Shown in Figure 4.1 are the prototypical bearing pressures and loads for LT-1 through LT-4, and LT-17 through LT-18 combined. The net ultimate bearing pressure q_u, achieved during each test is shown in Table 4.3 with corresponding relative density, D_r, dry unit weight, γ_{dry}, internal friction angle, ϕ, prototype load, normalized displacement Δ/B, and prototype displacement, Δ .

Table 4.3 Net ultimate bearing pressure q_u for concentric loading condition with depth of embedment equal to zero ($D_f = 0$)

Name	D_r (%)	γ_{dry} (lb/ft^3)	ϕ (degree)	Measured-q_u (psf)	Measured-Load (kip)	Δ/B	Δ (inch)
LT-01	86.82	106.09	36.77	12,384	2662	0.1859	7.44
LT-02	86.71	106.07	36.75	12,000	2558	0.1693	6.60
LT-03	63.97	101.56	32.60	6,227	1338	0.1492	5.81
LT-04	62.81	101.34	32.38	6,097	1309	0.1478	5.76
LT-17	95.37	107.90	38.33	13,000	2329	0.1911	7.45
LT-18	94.88	107.79	38.24	12,844	2300	0.1744	6.80

For load tests 1-4 there was an increase in bearing capacity proportional to an increase in relative density, as expected. However, for LT-17 and LT-18, which display higher density soil than LT-1 and LT-2, the bearing capacities were less. Load test 17 and 18 displayed a failure surface acting solely on the left side of the footing, indicating that eccentricity may have developed during loading.

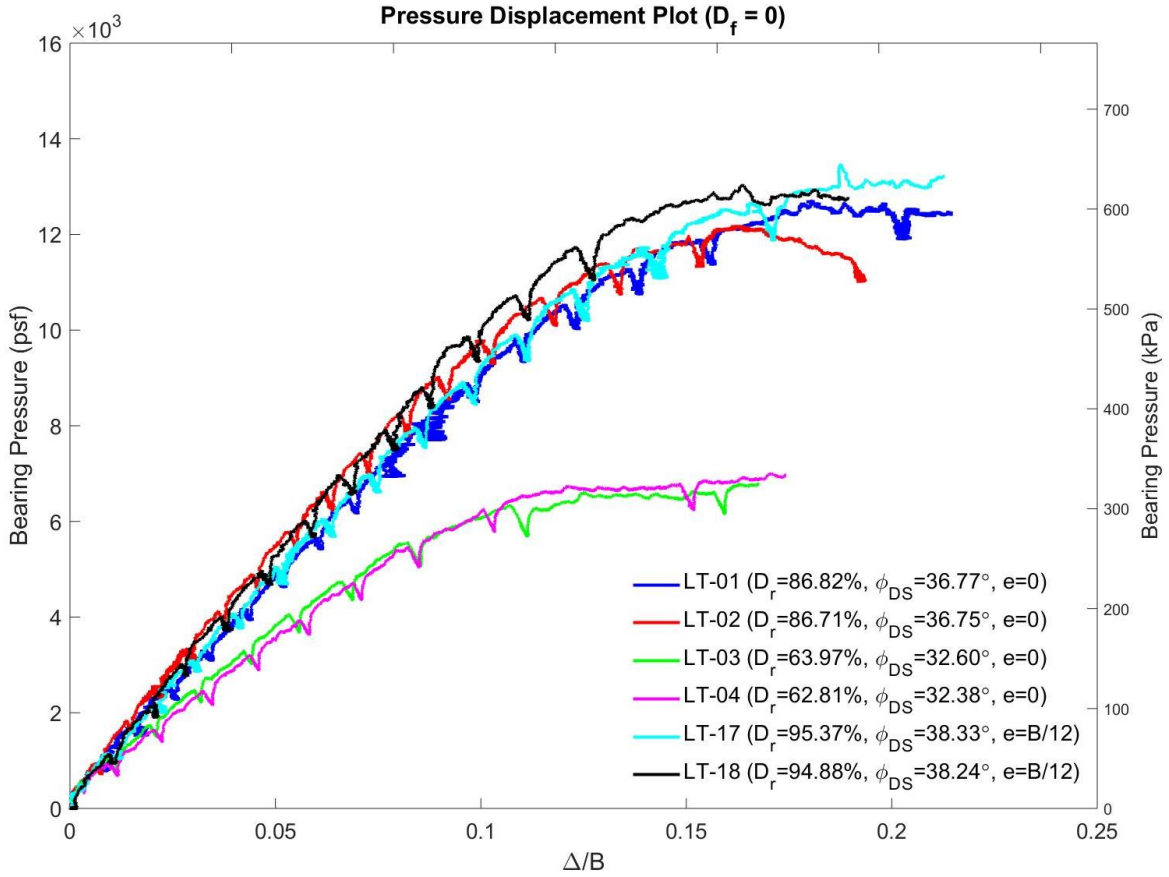

Figure 4.1 LT-1-4, LT-17, and LT-18 (D_f = 0) prototype net ultimate bearing pressure and load displacement plots

For these tests, the eccentricity was back-calculated by adjusting the effective area for each load test until the bearing pressure aligned with other load test with similar soil and loading parameters. The effective area is calculated using the effective width of the footing, B' shown in Eq. 4.1.

$$B' = B\text{-}2e_b \quad \text{Eq. 4.1}$$

where B = footing width and e_b = eccentricity along the footing width.

In the case of LT-17 and LT-18, the eccentricity was calculated to be B/12, or 0.08 ft. The bearing pressures presented in Figure 4.1 are after applying the eccentricity to LT-17 and LT-18. Initially, higher values of eccentricity were explored for LT-17 and LT-18, with negative effects to the measured N_γ and N_q values.

The minimum slopes for each test shown in Figure 4.1 clearly illustrate soil failure during the load tests. However, all load tests showed a slight discrepancy between the experimental ultimate bearing capacity (q_u) achieved during the test and the theoretical ultimate bearing capacity determined by the design bearing capacity formulas.

While effort was made to minimize the boundary effects from the container walls by using smooth acrylic and aluminum sheets, it was thought that the discrepancy in bearing pressure was, in part, due to friction developed at the container boundaries. The boundary effects can be seen in Figure 4.2. The length of the failure surface at the Plexiglas is 6.07 inches, and the maximum length of the failure surface was measured to be 7.99 inches, about 5 inches inward from the acrylic. An estimate of the shear over the area of the failure wedge in Figure 4.2 was required. The acrylic boundary was instrumented with Tokyo Measuring Instruments PDB-3MPB miniature pressure transducers (Figure 3.12) to measure the pressure distribution along the failure wedge, as shown in Figure 4.4. The maximum pressure measured was 1,067 psf, which

was located at the center directly under the footing.

To obtain the shear stress, τ, at the container boundaries, the failure wedges for each test were scaled and traced using AutoCAD. The failure surface was divided into slices of equal width, after which the individual slice areas and midpoint heights were determined, as shown in Figure 4.5.

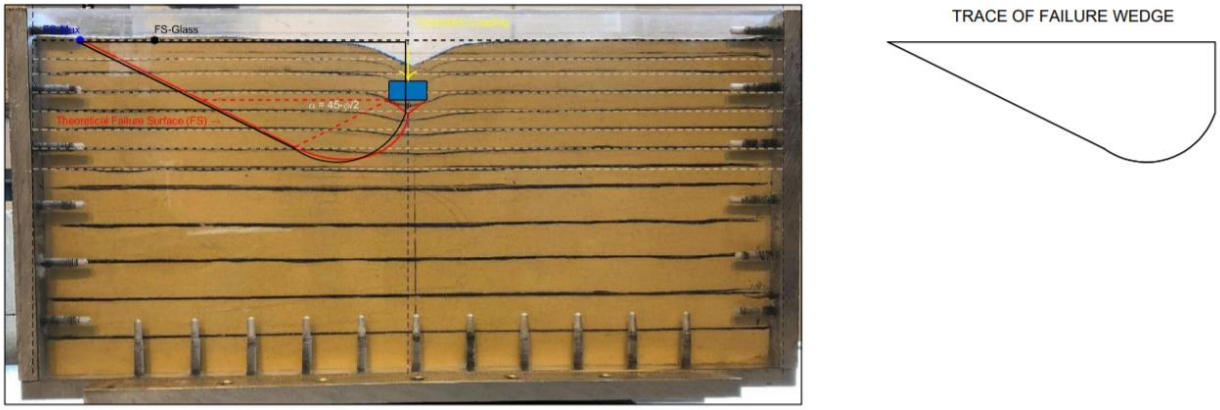

Figure 4.2 Depiction of the area contained within the failure wedge (LT-01)

Figure 4.3 Pre and post-test failure surface for boundary condition experiment

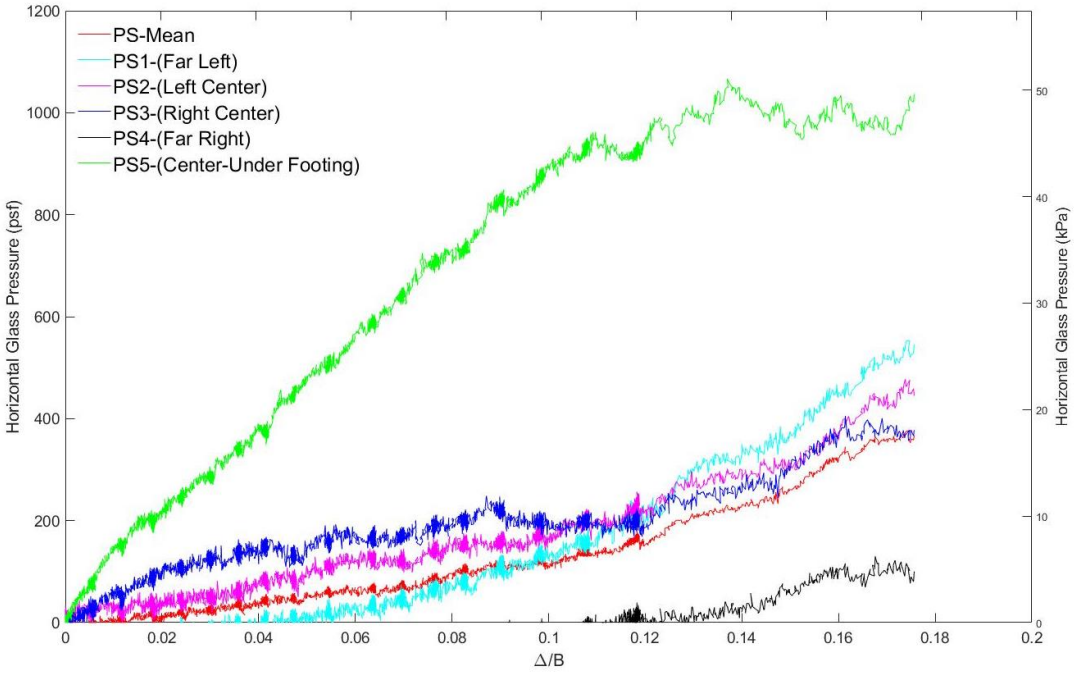

Figure 4.4 Horizontal pressure on acrylic wall during loading

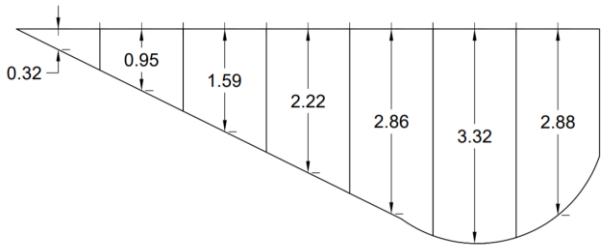

Figure 4.5 Example of failure wedge divided into slices (LT-01)

Using the areas and heights determined from the traced image, the horizontal shear stress, τ, was determined for each slice using the following equations (Eq. 4.2 and 4.3) and the lateral earth coefficient determined through the boundary condition experiment.

$$\tau = \sigma_h tan(\delta) \qquad \text{Eq. 4.2}$$

$$\sigma_h = K_o \gamma h \qquad \text{Eq. 4.3}$$

where δ = interface friction angle, σ_h = horizontal earth pressure on container boundaries, K_o = (≈0.80-1.0)

The horizontal shear force acting on each slice was weighted by the area of the slice and averaged to determine the total shear force, τ, acting on the failure wedge. The horizontal shear stress was recalculated using δ = 1/2 ϕ, δ = 2/3 ϕ and δ = 1/6 ϕ to account for the reduced friction

between the container and the sand. This was based on previous direct shear tests which indicated that the friction angle between the sand and Plexiglas used in the container was approximately 1/6 ϕ while shear tests between sand and aluminum showed a friction angle of approximately 1/2 ϕ to 2/3 ϕ.

Theoretically this failure wedge would occur equally at each of the four corners of the footing, with two wedges in contact with the Plexiglas and two wedges in contact with the rear aluminum plate. Therefore, the total shear stress, τ, of the sides of the container is represented by Eq. 4.4. However, the observed failure surface for each load was examined to determine the appropriate amount of shear stress measured (e.g., failure surface developed on one side or both side of footing).

$$\tau_{total} = 2\tau_{Plexiglass} + 2\tau_{Aluminum} \qquad \text{Eq. 4.4}$$

The calculated shear forces were subtracted from the experimental bearing capacity values to determine how they lowered the percent difference between the experimental and theoretical bearing capacities. Boussinesq analyses in prototype scale were also performed to confirm the observed pressure along the face of the acrylic. The results were similar to the observed values in the boundary condition experiment (Figure 4.4).

Combining the reduced bearing capacity equation for surface strip footings and Eq. 4.4, N_γ could be calculated as shown in Eq. 4.5.

$$N_\gamma = \frac{q_{u-\tau_{total}}}{0.5\gamma B s_\gamma} \qquad \text{Eq.4.5}$$

The bias (measured/predicted) for the Vesić (AASHTO recommended) and Zhu et al. method N_γ (calculated using ϕ from the direct shear test) is shown in Figure 4.6. The Vesić and Zhu et al. methods appear to be representative for the medium dense and the very dense conditions. Vesić's method tends to slightly under predict the bearing capacity factor. The Zhu et

al. method is based on centrifuge tests of strip footings with L/B = 5 and had slightly better predictions of the tests performed here. Vesić method provides slightly more conservative values and is recommended by AASHTO. Analysis of all centrifuge test result in Ch. 7 will consider other existing methods for N_γ.

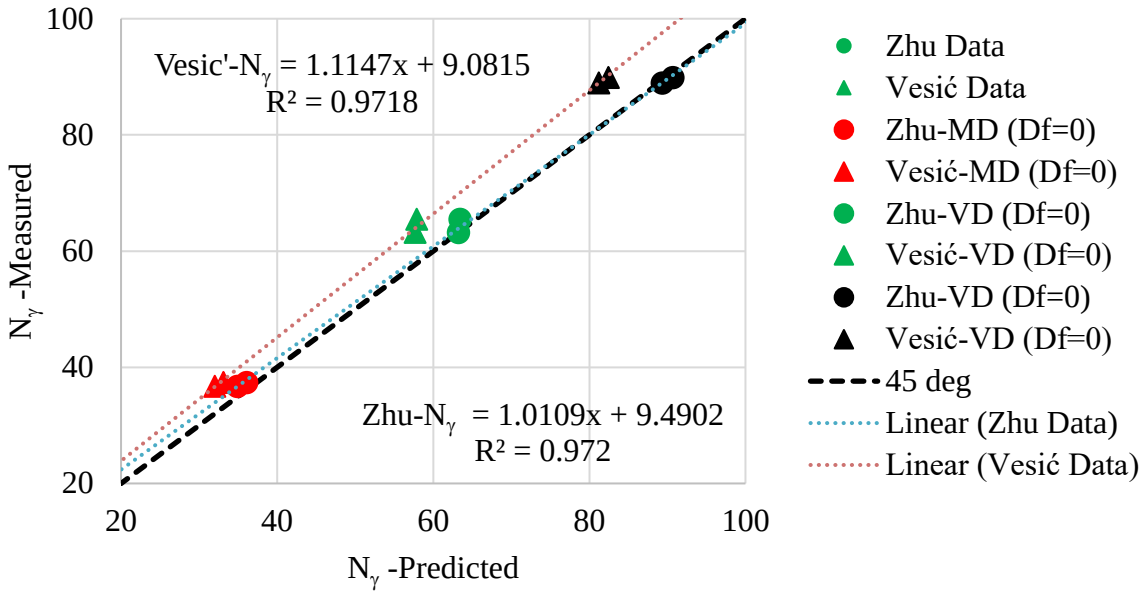

Figure 4.6 Bearing capacity factor N_γ (Bias) plot

4.1.2 Concentric Loading Condition with Depth of Embedment Equal to 0.5B

In this series of experiments, a total of 11 load tests on footings embedded 0.5B were performed at a centrifuge model scale of approximately N = 39, which is equivalent to a prototype size footing 3.25 feet wide and 65 feet long. The A3 sand was tested in a medium dense and very dense state and had an average dry unit weight, γ_{dry}, in the range of 101.51 lb/ft^3 to 107.94 lb/ft^3 and average relative density, D_r, in the range of 63.72% to 95.55% for the top soil layers where the failure surface was observed. The average peak friction angle from the direct shear test was estimated to be in the range of 32.55° to 38.36°. The purpose of the tests was to assess the influence of the embedment term, N_q on the bearing capacity of an embedded

strip footing. The net ultimate bearing capacity, q_n, is the ultimate pressure per unit area of the footing which can be supported by the soil in excess of the existing vertical effective stress at the depth of the footing ($q = \gamma D_f$). In the experiments with $D_f > 0$, the only measurement of bearing pressure is through the load measured in each of the pistons loading the model footing, which is q_n in Eq. 4.6.

$$q_n = q_u - q \qquad \text{Eq. 4.6}$$

After each test, pictures of profile and plan view of the models were taken to measure the depths, shape and extent of the rupture surface after general shear failure. The measurements were helpful in studying the internal friction angle at failure and estimating N_γ and N_q. Table 4.4 presents the post-test profile and plan views of the models, which indicate the failure surface ruptured the ground surface in all cases, except for LT-07, LT-12 and LT-14.

Table 4.4 Post-test failure surface for concentric loading condition at embedment depth equal to 0.5B

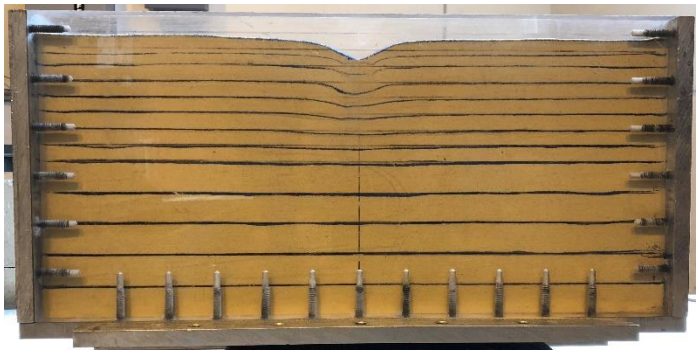 LT-05	

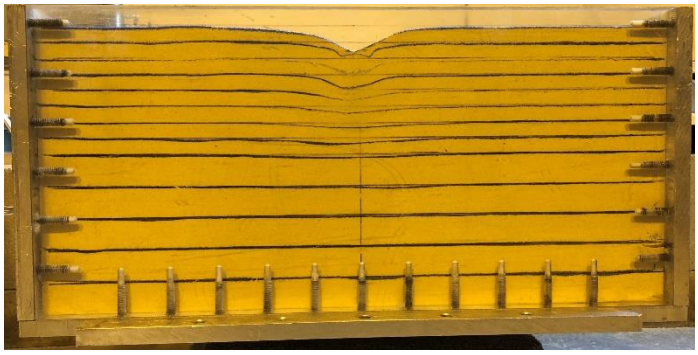

LT-06

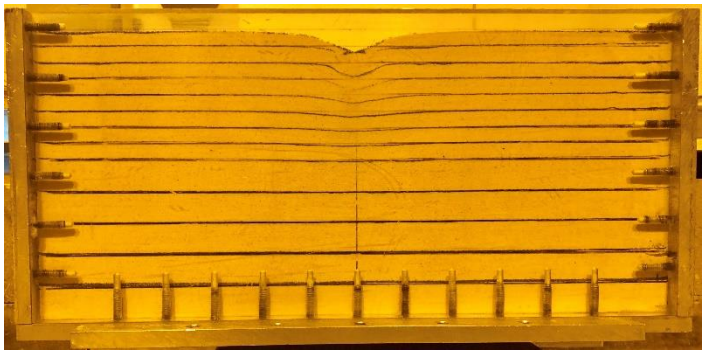

LT-07

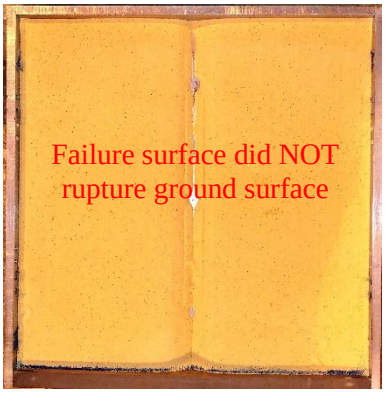

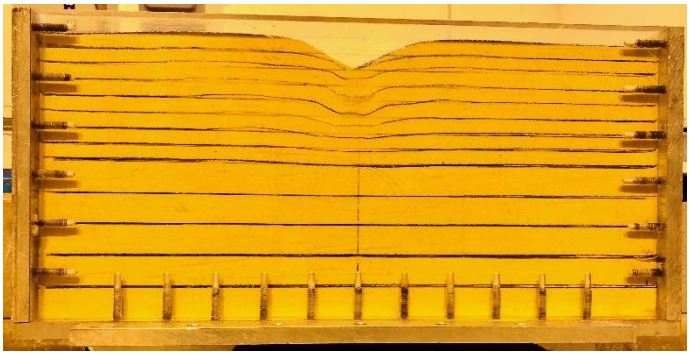

LT-08

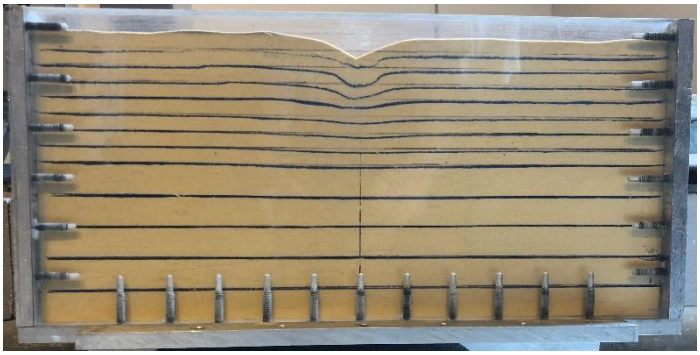

LT-09

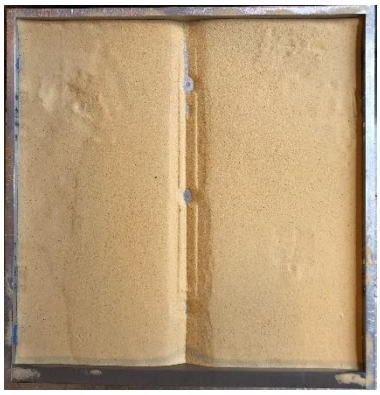

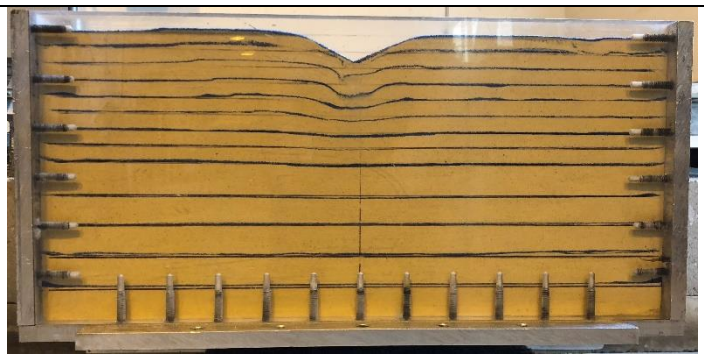 LT-10	
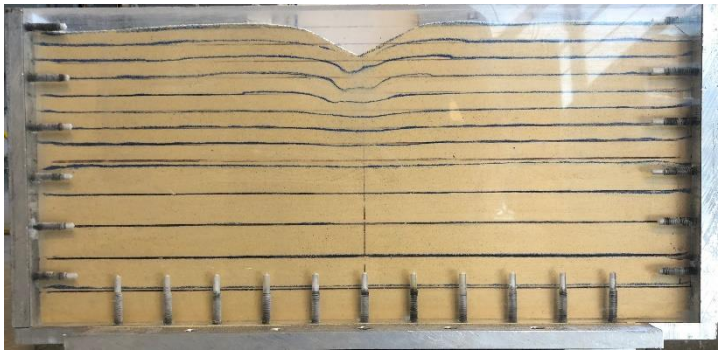 LT-11	
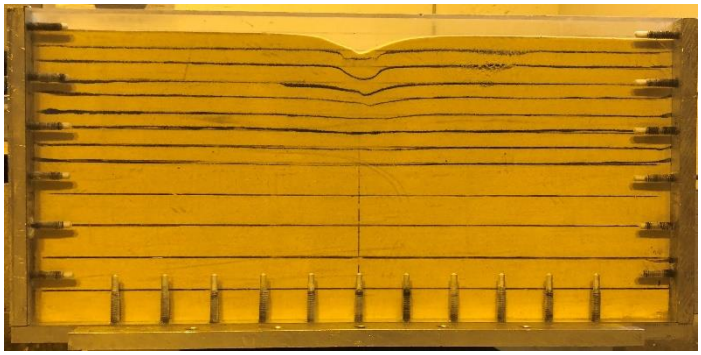 LT-12	 Failure surface did NOT rupture ground surface
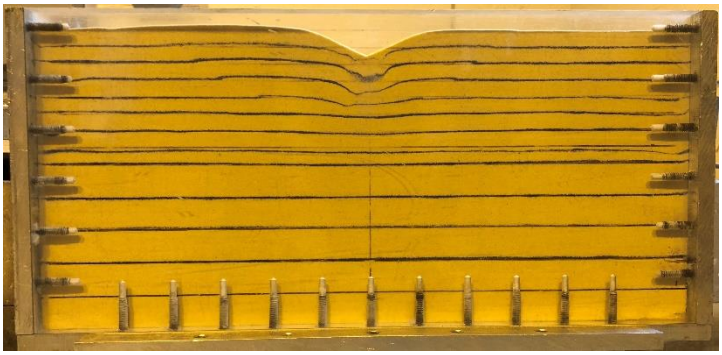 LT-13	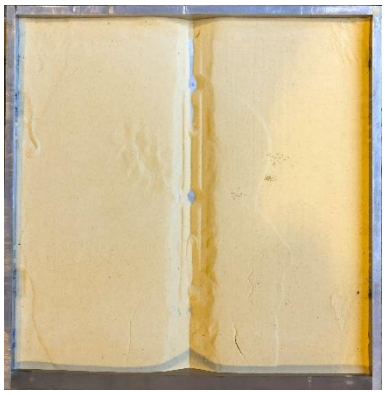

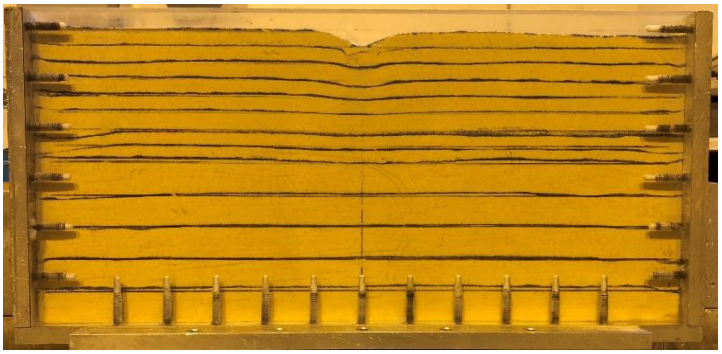

LT-14

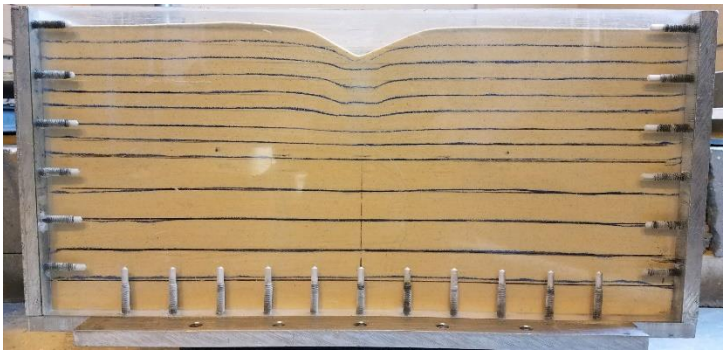

LT-20

Summary of the post-test images of rupture surfaces:

- Very dense sand (LT-07, LT-08, LT-10 – LT-14, and LT-20): The observed rupture surface for LT-13 shows a maximum depth and length of 3.40 inches and 9.47 inches. The failure surface for LT-13 ruptured the ground surface the full length of the footing (20 inches) on the left side of the footing and approximately 75% the length of the footing (+/- 16 inches) on the right side as shown in Table 4.4. LT-08 is the only test with a failure surface solely on the right side which is the full length of the 20-inch footing. LT-20 is the only test with a failure surface solely on the left side which is the full length of the 20-inch footing. The observed failure surface ruptured the ground surface on the left and right sides of LT-10, LT-11 and LT-13.
- Medium dense sand (LT-05, LT-06 and LT-09): The observed rupture surface for LT-05

shows a maximum depth and length of 2.78 inches and 8.74 inches. The failure surface ruptured the ground surface approximately ¾ the length of the footing (+/-16 inches) on the left side of the footing as shown in Table 4.4. The observed failure surface ruptured the ground surface on the left and right sides for LT-06.

Shown in Figure 4.7 are the prototypical bearing pressures for LT-5 through LT-14, and LT-20 combined. Load test 5-14 showed an increase in bearing capacity with increase in relative density as expected. However, LT- 20 had slightly lower bearing capacity (17,426 psf) than LT-14 (19,700 psf), while having a higher relative density (12.25% difference).

In this series of testing, it was determined that LT-07, LT-12, LT-13, and LT-20 experienced unexpected eccentricity during loading. LT-07, LT-12, and LT-20 displayed a failure surface solely on one side of the footing and exhibited less bearing pressure than in similar load tests with lower relative densities.

While LT-13 displayed a failure surface primarily on the left side with a partial failure surface on the right side of the footing, the bearing pressure was less than in similar load tests. To assess possible eccentricity developed during loading, bearing pressure was back-calculated by adjusting the effective area for each load test until the bearing pressure aligned with other load tests conducted with similar soil and loading parameters. The effective area was calculated using the effective width of the footing, B' shown in Eq. 3.3.

In the case of LT-07, LT-12, LT-13 and LT-20 the eccentricity was calculated to be B/14 or 0.07 ft. The bearing pressures for LT-07, LT-12, LT-13 and LT-20 presented in Figure 4.7 are the adjusted values after applying the new eccentricities.

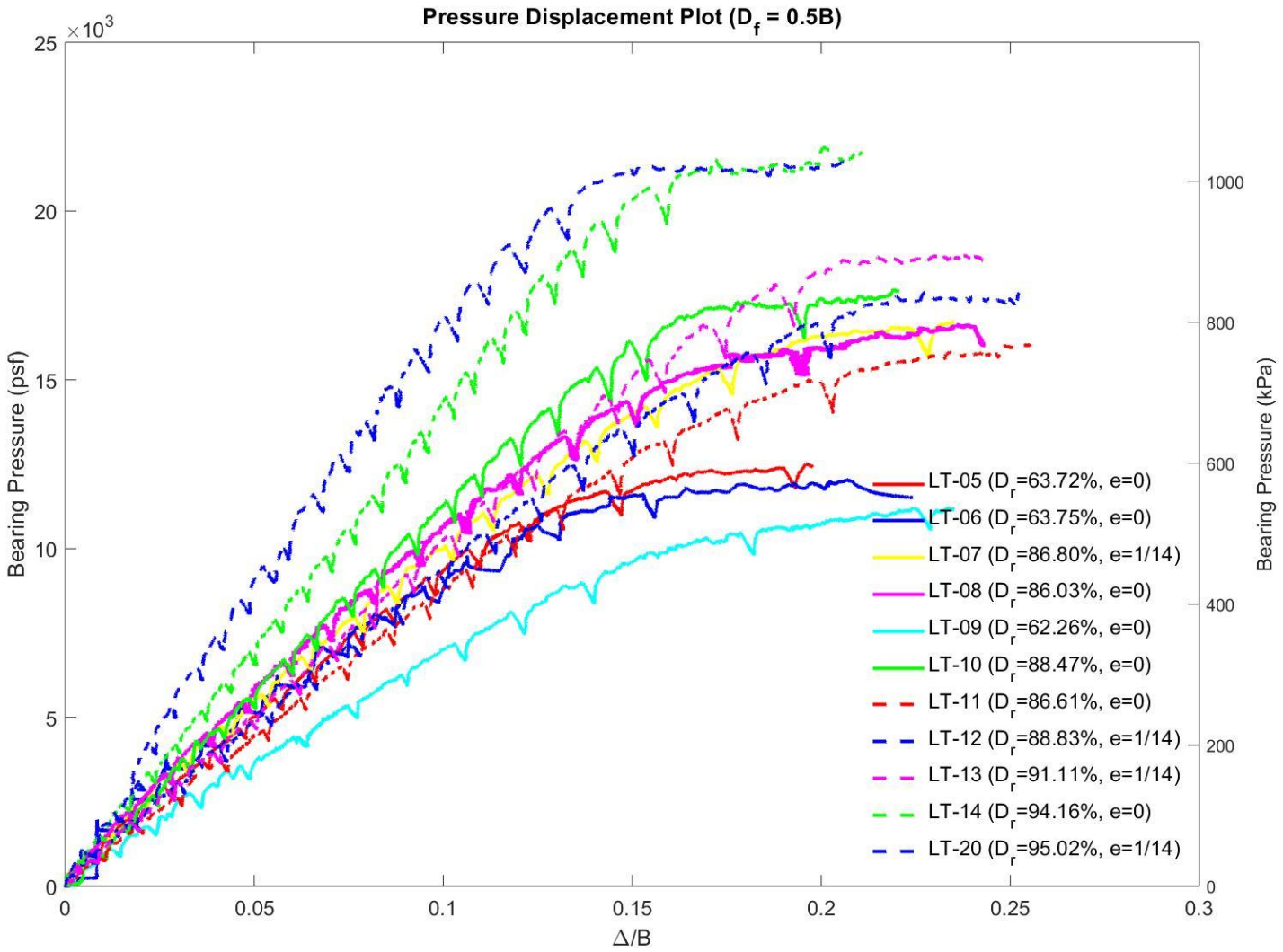

Figure 4.7 LT-5-14, and LT-20 (D_f = 0.5B) prototype net ultimate bearing pressure and load displacement plots

The net ultimate bearing pressure, q_u, achieved during each test is shown in Table 4.5 with corresponding relative density, D_r, dry unit weight, γ, internal friction angle, ϕ, normalized displacement, Δ/B, and prototype displacement, Δ.

Table 4.5 Ultimate bearing pressure q_u for concentric loading condition with depth of embedment equal to zero (D_f = 0.5B)

Name	D_r (%)	γ_{dry} (lb/ft^3)	ϕ (degree)	Measured-q_u (psf)	Measured-Load (kip)	Δ/B	Δ (inch)
LT-05	63.72	101.51	32.55	11,630	2,472	0.1758	6.85
LT-06	63.75	101.52	32.55	11,122	2,364	0.1883	7.34
LT-07	86.80	106.09	36.76	15,970	3,530	0.2217	8.64
LT-08	86.07	105.94	36.62	16,702	3,561	0.2294	8.94
LT-09	62.26	101.23	32.28	10,992	2,332	0.2245	8.75
LT-10	88.47	106.44	37.07	17,503	3,728	0.2029	7.91
LT-11	86.61	106.05	36.73	15,777	3,357	0.2464	9.61
LT-12	88.83	106.51	37.13	17,701	3,231	0.2257	8.80
LT-13	91.11	106.99	37.55	18,406	3,367	0.2220	8.66
LT-14	94.16	107.64	38.10	22,120	4,697	0.1839	7.17
LT-20	95.02	107.82	38.26	21,262	3,872	0.1651	6.44

4.1.3 Concentric Loading Condition with Depth of Embedment Equal to 1B

In this series of experiments, a total of 2 load tests on footings embedded 1B were performed at a centrifuge model scale of approximately N = 39, which is equivalent to a prototype size footing 3.25 feet wide and 65 feet long. The A3 sand was prepared in a very dense state with an average dry unit weight, $\gamma_{dry,}$ of 107.67 lb/ft^3 and 107.94 lb/ft^3 and average relative density, D_r of 94.31% and 95.55% for the sand layers where the failure surface was observed. The average peak friction angle from the direct shear test was estimated to be in the range of 38.13° and 38.36°. The purpose of the tests was to assess the influence of the embedment term, N_q on the bearing capacity for depth of embedment equal to B.

Table 4.6 presents the post-test plan view and failure surface views of the soil stratigraphy, which indicate general shear failure did occur. The failure surface ruptured the

ground surface for LT-21 but did not for LT-16.

Table 4.6 Post-test failure surface for concentric loading condition at embedment depth equal to the footing width, B

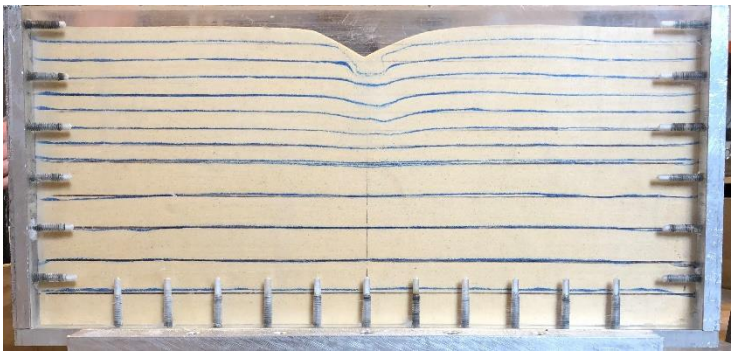 LT-16	
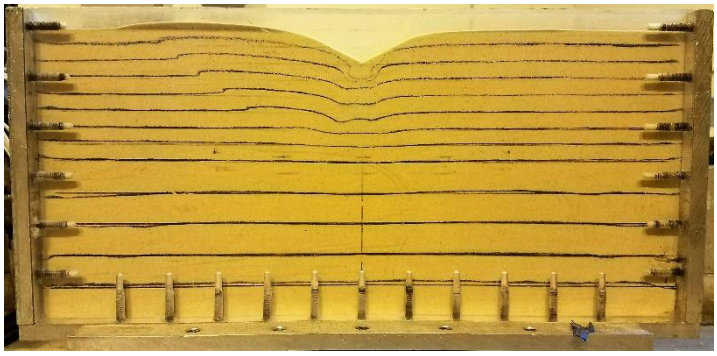 LT-21	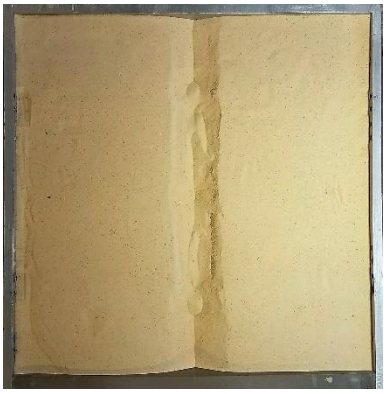

The observed rupture surface for LT-21 shows a maximum depth and length of 2.97 inches and 9.63 inches. The failure surface for LT-21 ruptured the ground surface the full length of the footing (20 inches) on the left side of the footing as shown in Table 4.6.

Shown in Figure 4.8 are the prototypical bearing pressures for LT-16 and LT-21 combined. Load tests 16 and 21 show an increase in bearing capacity with increase in relative density as expected. However, when compared to the design values the measured values were considerably lower. After further examination of the failure surface plots, it was concluded LT-16 and LT-21 incurred unexpected eccentricity during loading.

LT-16 and LT-21 displayed a failure surface acting solely on one side of the footing and

exhibited less bearing pressure. Eccentricity was back-calculated by adjusting the effective area for each load test until the bearing pressure aligned with other load test with similar soil and loading parameters, in this case the design values were used as a reference. The effective area was calculated using the effective width of the footing, B' in Eq. 3.3.

In the case of LT-16 and LT-21 the eccentricity was calculated to be B/14 or 0.07 ft. The bearing pressures presented in Figure 4.8 are after applying the eccentricity to LT-16 and LT-21. The net ultimate bearing pressure q_u, achieved during each test is shown in Table 4.7 with corresponding relative density, D_r, dry unit weight, γ_{dry}, internal friction angle, ϕ, prototype load, normalized displacement Δ/B, and prototype displacement, Δ .

Table 4.7 Net ultimate bearing pressure q_u for concentric loading condition with depth of embedment equal to footing width (D_f = B)

Name	D_r (%)	γ_{dry} (lb/ft^3)	ϕ (degree)	Measured-q_u (psf)	Measured-Load (kip)	Δ/B	Δ (inch)
LT-16	94.31	107.67	38.13	30,976	5,652	0.1475	5.90
LT-21	95.55	107.94	38.36	32,484	5,921	0.1393	5.57

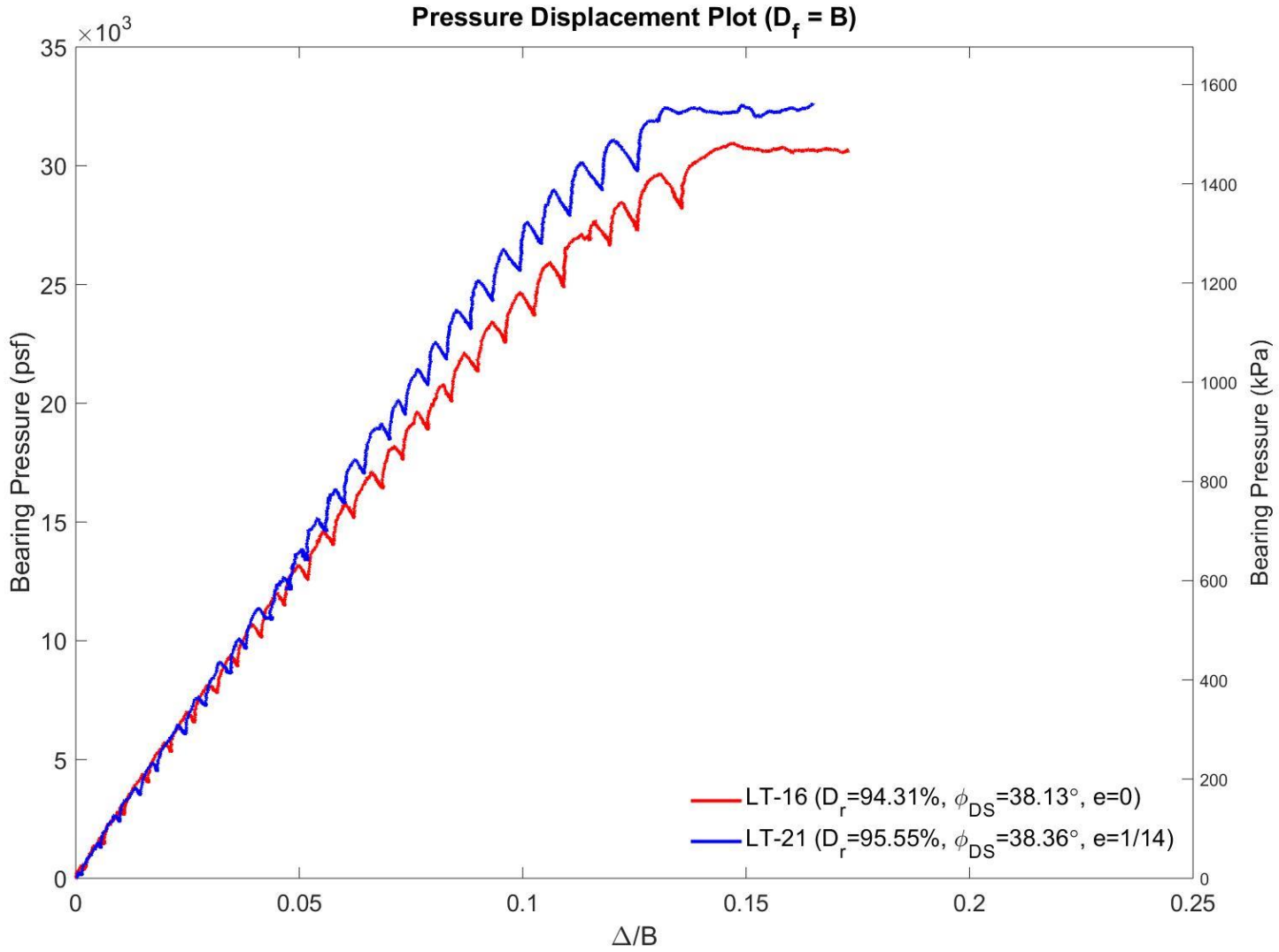

Figure 4.8 LT-16 and LT-21 (D_f = B) prototype net ultimate bearing pressure and load displacement plots

5.0 RECTANGULAR FOOTING (L/B = 10) TESTS

5.1 Model Load Tests on Rectangular Footing (L/B=10) for Very Dense Condition

Each load case was tested at $D_f = 0$ and $D_f = 0.5B$ for lateral to axial load ratios of 0.10 and 0.25, and on medium dense and very dense sand. All eccentric loads were applied B/6 from the centerline of the footing. Replicates of each case were performed to check for experimental repeatability. Table 5.1 lists the identifiers for each test with their date, load case, sand conditions, and footing embedment depth.

Table 5.1 List of load tests for rectangular footing

Name	Date	Load Case	Density (D_r)	Embedment Depth (D_f)	Eccentricity	Inclination L/A ratio	Series #
LT-22*	3/08/19	1	Very Dense	0	0	0	1
LT-23	3/25/19	1	Very Dense	0	0	0	2
LT-24	3/27/19	1	Very Dense	0	0	0	3
LT-25	3/29/19	4	Very Dense	0	B/6	0.10	1
LT-26	4/05/19	4	Very Dense	0	B/6	0.10	2
LT-27	4/08/19	5	Very Dense	0	B/6	0.10	1
LT-28	4/09/19	5	Very Dense	0	B/6	0.10	2
LT-29	4/09/19	3	Very Dense	0	B/6	0.10	1
LT-30	4/12/19	3	Very Dense	0	B/6	0.10	2
LT-31	4/15/19	2	Very Dense	0	B/6	0	1
LT-32	4/16/19	2	Very Dense	0	B/6	0	2
LT-33	4/17/19	2	Very Dense	0.5B	B/6	0	1
LT-34	4/18/19	2	Very Dense	0.5B	B/6	0	2
LT-35	4/19/19	1	Very Dense	0.5B	0	0	1
LT-36	4/22/19	1	Very Dense	0.5B	0	0.10	2
LT-37	4/23/19	4	Very Dense	0.5B	0	0.10	1
LT-38	4/24/19	4	Very Dense	0.5B	0	0.10	2
LT-39	4/25/19	5	Very Dense	0.5B	B/6	0.10	1
LT-40	4/25/19	5	Very Dense	0.5B	B/6	0.10	2
LT-41	4/26/19	3	Very Dense	0.5B	B/6	0.10	1
LT-42	4/27/19	3	Very Dense	0.5B	B/6	0.10	2
LT-43	4/29/19	2	Very Dense	0	B/6	0	3
LT-44	5/06/19	1	Very Dense	0.5B	0	0	3
LT-45	5/07/19	4	Very Dense	0	0	0.25	1
LT-46	5/07/19	4	Very Dense	0	B/6	0.25	2
LT-47	5/08/19	5	Very Dense	0	B/6	0.25	1
LT-48	5/08/19	5	Very Dense	0	B/6	0.25	2

Table 5.1 (continued)

LT-49	5/08/19	3	Very Dense	0	B/6	0.25	1
LT-50*	5/08/19	3	Very Dense	0	B/6	0.25	2
LT-51	5/09/19	4	Very Dense	0.5B	B/6	0.25	1
LT-52	5/09/19	4	Very Dense	0.5B	B/6	0.25	2
LT-53	5/09/19	5	Very Dense	0.5B	B/6	0.25	1
LT-54	5/10/19	5	Very Dense	0.5B	B/6	0.25	2
LT-55	5/10/19	3	Very Dense	0.5B	B/6	0.25	1
LT-56	5/10/19	3	Very Dense	0.5B	B/6	0.25	2
LT-57	5/24/19	3	Very Dense	0	B/6	0.25	3
* Load test excluded from analysis due to unrepeatable results or instrumentation malfunction							

5.1.1 Lateral-to-Axial Ratio of 0.10 with Depth of Embedment Equal to Zero

In this series of tests, the rectangular footing was loaded for Load Cases 1–5 with depth of embedment equal to zero. The AASHTO A3 soil used in the test had an average dry unit weight, $\gamma_{dry,}$ in the range of 106.90 lb/ft^3 to 108.66 lb/ft^3 and average relative density, D_r in the range of 90.63% to 98.89% for the sand layers where the failure surface was observed. The average peak friction angle from the direct shear test was estimated to be in the range of 37.46° to 38.86°. The model footing was tested at N = 40 G which results in a prototype footing width and length of 5 feet by 50 feet with the L/B ratio of 10. All eccentric loads were applied B/6 (0.25 inches) from the center of the footing and inclined loads were applied at a lateral-to-axial ratio of 0.10 (5.7°). The combined eccentric-inclined loads were applied in the same geometric loading conditions as the individual parts.

The net bearing capacity plots for each test are presented in Figure 5.1. All eccentric and eccentric-inclined loading conditions used the effective width B' to determine the bearing pressure. Listed in Table 5.2 are the internal friction angles, unit weight, relative density, and net measured bearing capacities, q_{net}, with percent differences to demonstrate repeatability for each test.

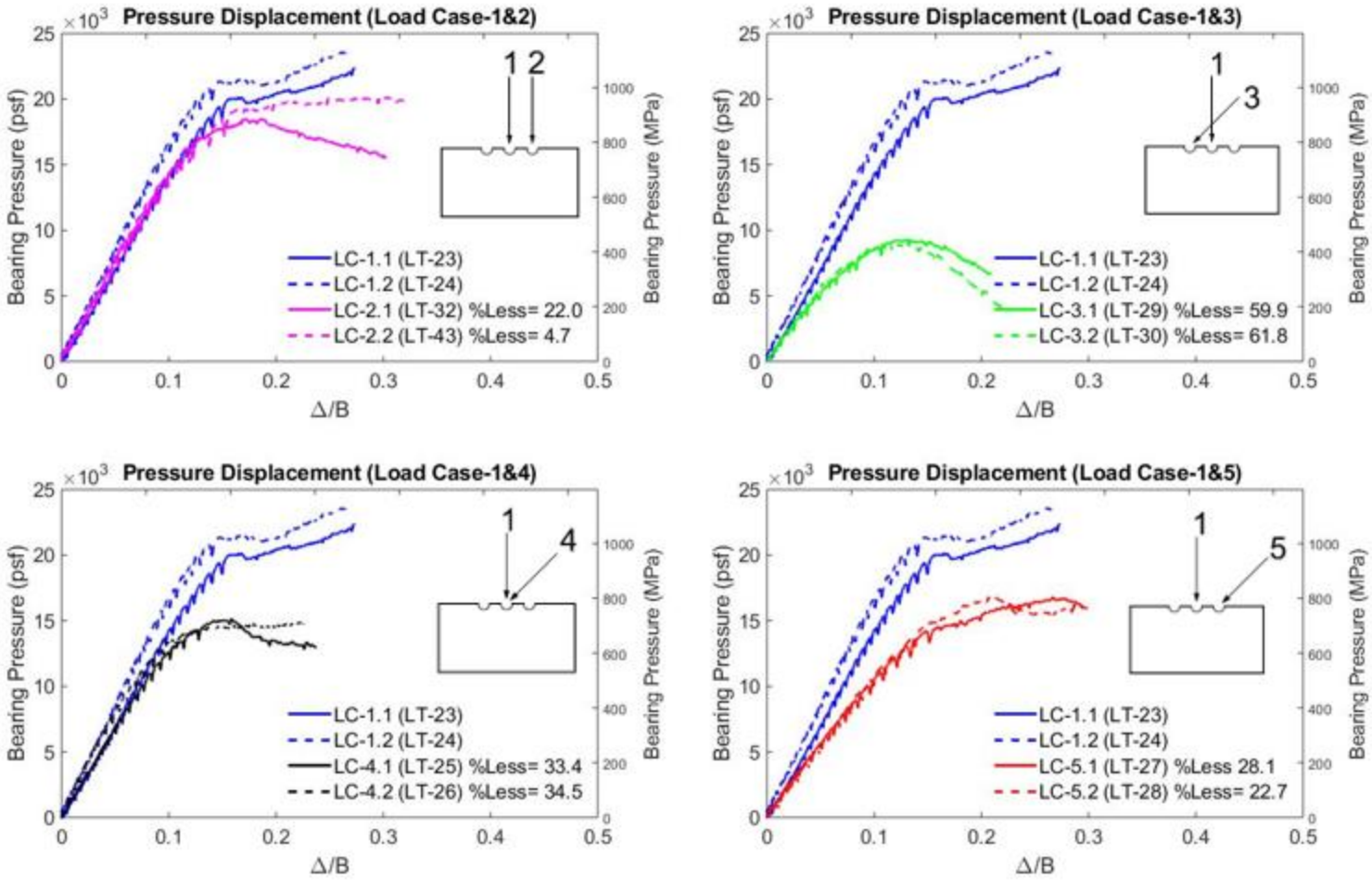

Figure 5.1 Net bearing pressure vs. displacement for Load Cases 1–5 with lateral-to-axial ratio = 0.1 and $D_f = 0$

Table 5.2 Summary of measured test parameters and results for L/B = 10 with lateral-to-axial ratio = 0.1 and D_f = 0 (VD)

Load Test	Load Case	ϕ (deg)	γ_{dry} (lb/ft^3)	D_r (%)	Δ/B	q_{net} Measured (psf)	Percent Difference (%)
LT-23	1	38.41	108.00	95.82	0.175	19,954	6.97
LT-24	1	38.57	108.20	96.73	0.160	21,396	
LT-32	2	38.86	108.66	98.89	0.176	19,102	3.98
LT-43	2	38.57	108.53	98.29	0.180	19,878	
LT-29	3	38.24	107.84	95.07	0.138	9,921	6.06
LT-30	3	38.28	107.84	95.10	0.126	9,337	
LT-25	4	37.46	106.90	90.63	0.154	15,662	3.67
LT-26	4	38.11	107.65	94.20	0.143	15,098	
LT-27	5	38.20	107.75	94.67	0.208	15,526	8.17
LT-28	5	38.55	108.16	96.60	0.204	16,849	

Table 5.3 presents the post-test plan view and failure surface views of the soil stratigraphy, which indicate general shear failure did occur. The failure surface ruptured the ground surface in all cases except for LT-23 (Load Case-1.1).

Table 5.3 Post-test failure surface for lateral-to-axial ratio equal to 0.10 at embedment depth equal to zero

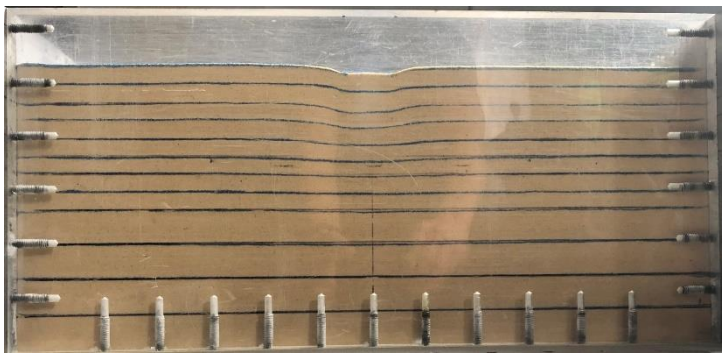

Load Case-1 (LT-23)

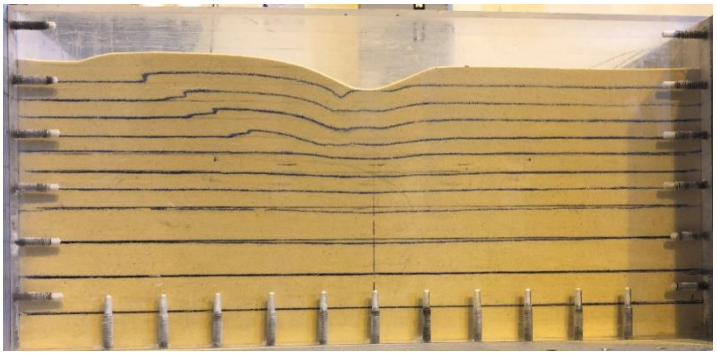 Load Case-1 (LT-24) $D_f = 0$	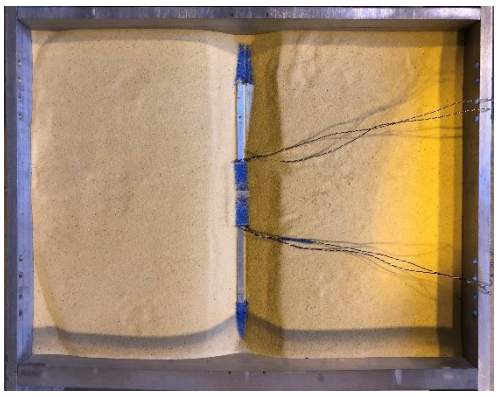
NO IMAGE Load Case-4 (LT-25)	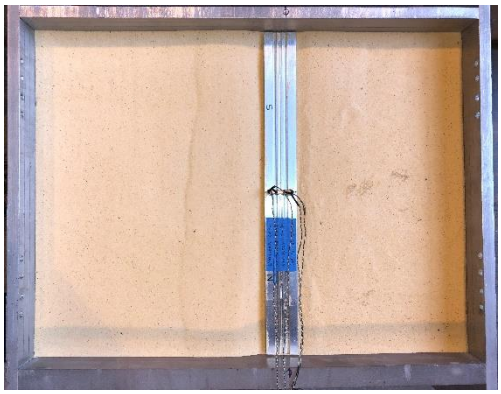
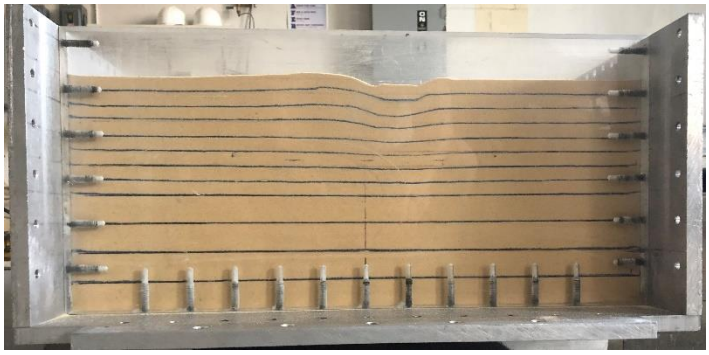 Load Case-4 (LT-26)	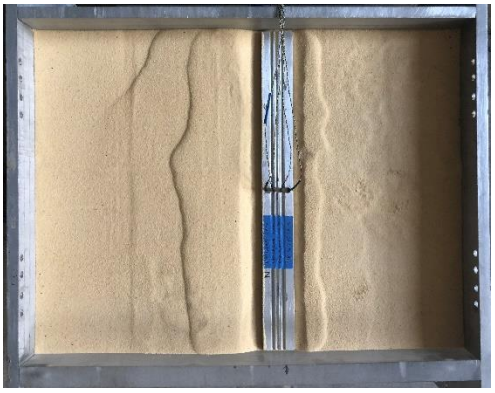
 Load Case-5 (LT-27)	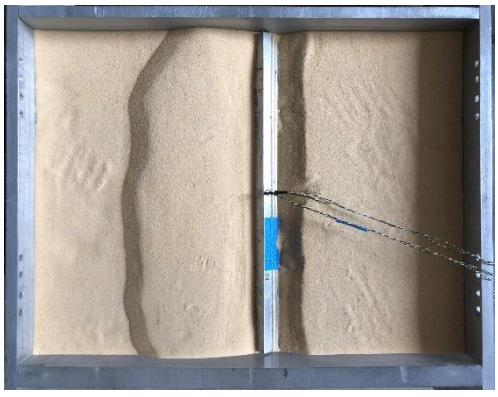

 Load Case-5 (LT-28)	
 Load Case-3 (LT-29)	
 Load Case-3 (LT-30)	
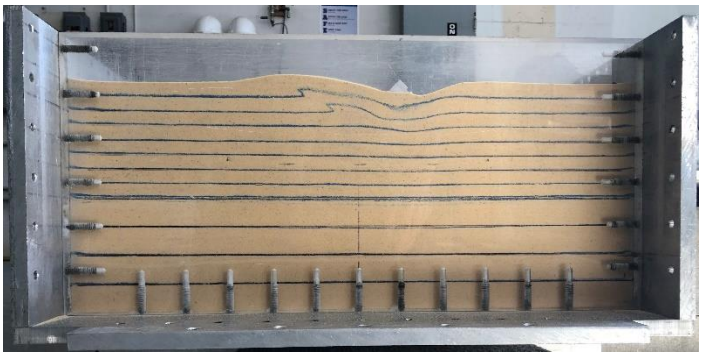 Load Case-2 (LT-31)	

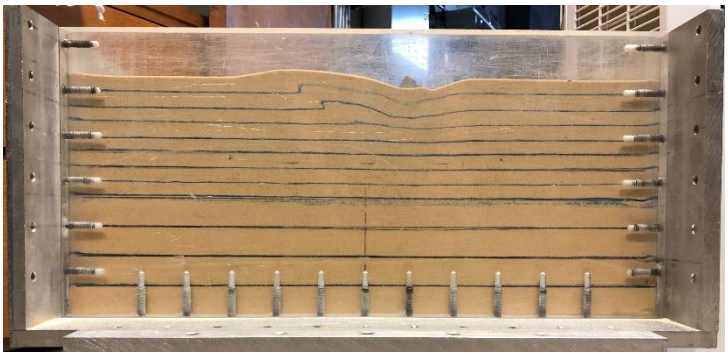

Load Case-2 (LT-32)

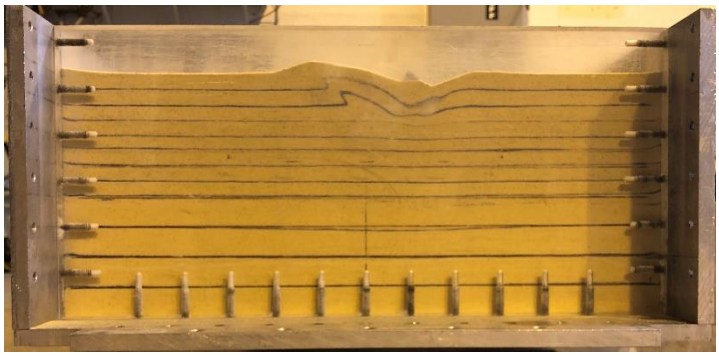

Load Case-2 (LT-43)

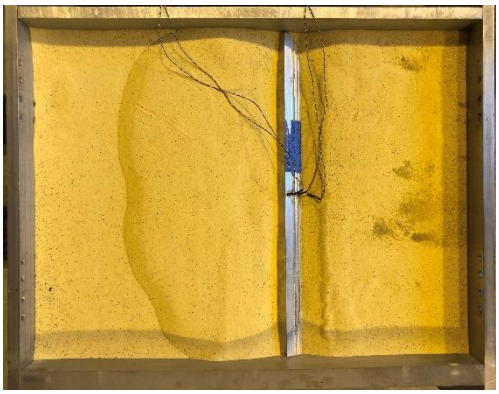

Summary of the post-test images of rupture surfaces:

- The observed rupture surface for Load Case-1 (LT-24) shows the maximum depth and length of the failure surface. LT-24 had a failure surface depth and length of 5 inches and 9.42 inches. The failure surface ruptured the top layer of soil on the left side of the footing as the test underwent concentric loading at the center of the footing.
- Load Case-2 (LT-31, LT-32 and LT-43) had failure surface depths of 3.03, 2.97 and 3.01 inches with lengths of 7.97, 8.75 and 7.70 inches. Load Case-2 applies an eccentric load B/6 from the center of the footing.
- Load Case-3 (LT-29 and LT-30) shows the minimum failure surface depth and length. LT-29 and LT-30 had failure surface depths of 2.00 and 2.53 inches. LT-29 had a failure surface length of 2.63 inches. LT-30 had a failure surface length of 7.97 inches. Both LT-29 and LT-

30 observed a failure surface on the right side of the footing as the footing underwent inclined-eccentric loading outward (+) to the direction of the eccentricity.

- The profile view of the failure surface for Load Case-4 (LT-25) was lost. Load Case- 4 (LT-26) reports a failure surface depth and length of 3.05 inches and 4.68 inches as the footing underwent inclined loading at the center of the footing. Similar to LT-29, continued loading after initial bearing capacity failure would have resulted in a more pronounced failure surface.
- Load Case-5 (LT-27 and LT-28) observed well-formed failure surfaces. The measured depth and length of LT-27 was 2.99 inches and 6.61 inches while LT-28 had failure surface depth and length of 3.04 inches and 8.08 inches.

Wack (1961) and Sokolovski (1960) showed the effect of eccentric inclined loads through a theoretical framework. Wack (1961) showed that for the case of an eccentric inclined load in the direction of the eccentricity (Load Case-5) the failure surface would be shallower and thus the capacity of the soil would be reduced (Figure 5.2). Alternatively, where the eccentric load was inclined opposite the direction of eccentricity (Load Case-3), Wack (1961) suggested that the failure surface would be deeper and the capacity of the soil would be greater than the eccentric case (Figure 5.3).

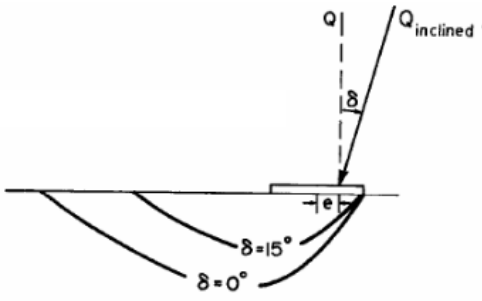

Figure 5.2 Effect of load inclined in direction of eccentricity (from Perloff and Baron, 1976)

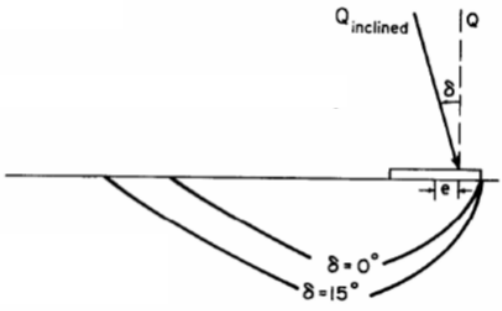

Figure 5.3 Effect of load inclined opposite of eccentricity (from Perloff and Baron, 1976)

The direction of the observed failure surfaces for Load Cases-3, 4, and 5 are similar to what Wack (1961) proposed (Figures 5.2 and 5.3). However, the depth of the failure surface is opposite in Perloff and Baron, (1976) (based on Wack, 1961), as seen in Table 5.3 and Figures 5.2 and 5.3. This difference in depth of the failure surface translates to the bearing capacities (mobilized shear stress over the length of the failure surface). The results in Table 5.2 are opposite of the trend in capacities suggested Wack (1961) for Load Cases 3 and 5. Observations of bearing capacities of footings on saturated clays ($\phi = 0$) that are subjected to inclined-eccentric loads agree with Figures 5.2 and 5.3 (Bransby and Randolph, 1998; Gourvenec and Randolph, 2003). Gottardi and Butterfield (1993), Loukidis et al. (2008), and Patra et al. (2012) show trends in capacities for Load Cases 3 and 5 of studies of footings on granular material subjected to Load Cases 3 and 5 that agree with results in Table 5.2.

The bearing pressure distribution observed by the miniature pressure transducers is presented for each load test in Figures 5.4 and 5.5. The loading position and orientation is displayed in each plot to illustrate how the pressure distribution is developed. The pressure sensors were position beneath the footing in sequential order (PS-1 through PS-4) from left to right at a spacing of 0.36 inches in model scale as previously stated.

Load Case-1 (LT-23 and LT-24) demonstrates a pressure distribution with an increasing

radial shape towards the center of the footing. This pressure profile is consistent with Loukidis et al. (2008) for sand, as shown in Figure 5.6. Note, Loukidis et al. (2008) assigned positive eccentricity in the negative direction from the footing centerline. Load Case-2 (LT-32 and LT-43), Load Case-3 (LT-29 and LT-30), Load Case-4 (LT-25 and LT-26), and Load Case-5 (LT-27 and LT-28) demonstrates a trapezoidal shape with increasing pressure on the side of eccentricity, inclination or eccentric-inclined loading.

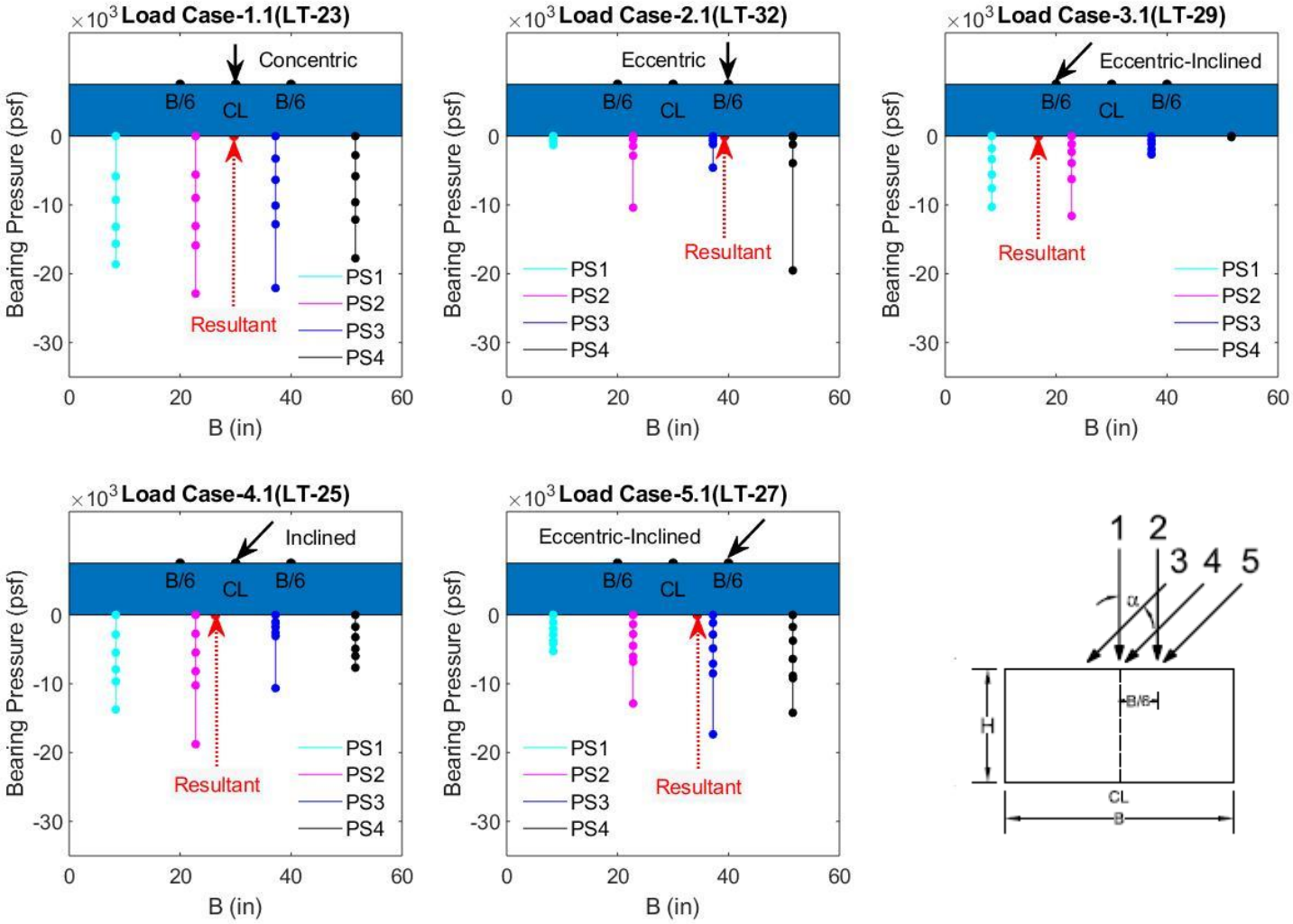

Figure 5.4 Bearing pressure distribution for Load Cases 1–5 with lateral-to-axial ratio = 0.1 and D_f = 0

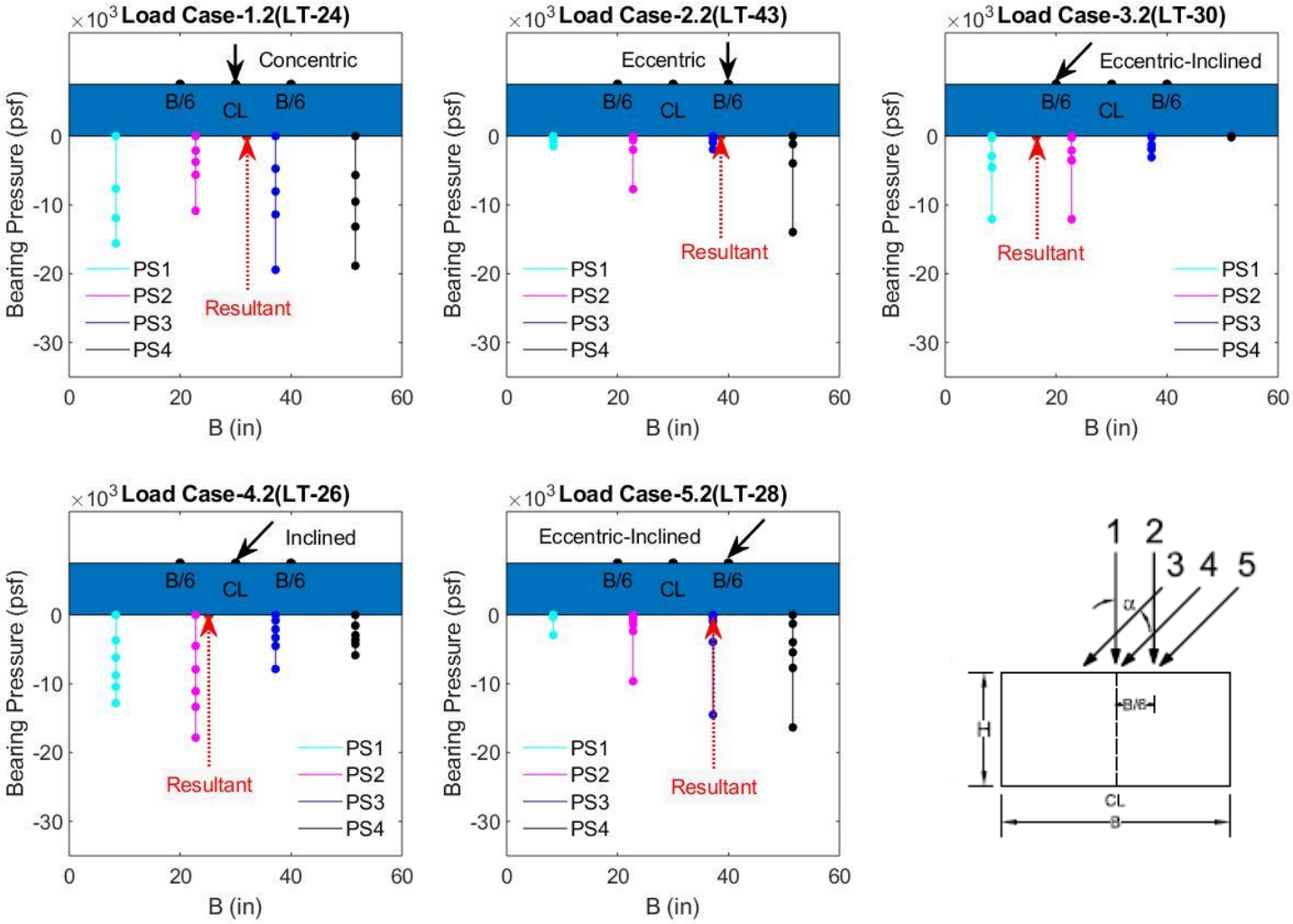

Figure 5.5 Bearing pressure distribution for Load Cases 1–5 with lateral-to-axial ratio = 0.1 and D_f = 0

Like the results presented in the pressure displacement plots (Fig. 5.1), Load Case-1 reports the highest bearing pressure and Load Case-3 reports the lowest bearing pressures. Comparing Load Case-3 with Load Case-5, the latter shows an increase in bearing pressure over Load-Case-3 as evidenced by the observed failure surfaces in Table 5.3 (shallower and shorter surface in Load Case 3 compared to Load Case 5).

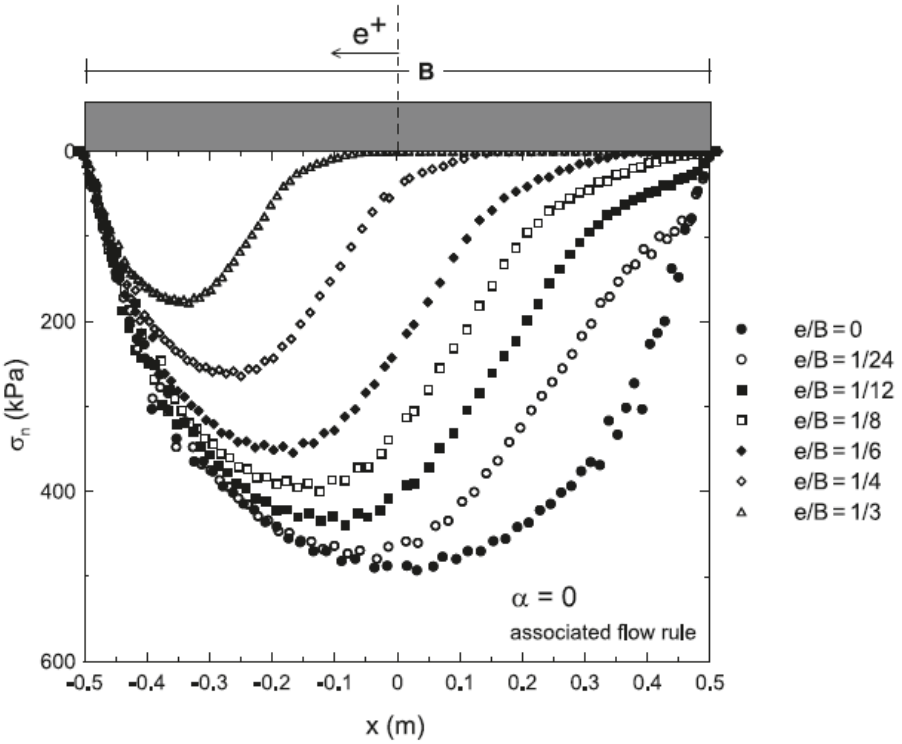

Figure 5.6 Pressure distributions from numerical models of eccentrically loaded footing on granular soil (Loukidis et al., 2008)

5.1.2 Lateral-to-Axial Ratio of 0.10 with Depth of Embedment Equal to 0.5B

In this series of tests, the rectangular footing was loaded for Load Cases 1–5 with depth of embedment equal to 0.5B. The AASHTO A3 soil used in the tests had an average dry unit weight, $\gamma_{dry,}$ in the range of 107.91 lb/ft^3 to 108.38 lb/ft^3 and average relative density, D_r in the range of 95.40% to 97.58% for the top soil layers where the failure surface was observed. The average peak friction angle from the direct shear testing was estimated to be in the range of

38.33° to 38.73°. The model footing was tested at N = 40 G which represents a prototype footing width and length of 5 feet by 50 feet (L/B = 10) and embedment depth equal to 0.5B. All eccentric loads were B/6 (0.25 inches) from the center of the footing and inclined loads were applied at a lateral-to-axial ratio of 0.10 (5.7°). The combined eccentric-inclined load test will apply the same geometric loading conditions as the individual parts.

The net bearing capacity for each test are presented in Figure 5.7. All eccentric and eccentric-inclined loading conditions used the effective width B' to determine the bearing pressure. Listed in Table 5.4 are the internal friction angles, unit weight, relative density, and net measured bearing capacities with percent differences to demonstrate repeatability for each test.

Table 5.4 Summary of measured test parameters and results for L/B = 10 with lateral-to-axial ratio = 0.1 and D_f = 0.5B (VD)

Load Test	Load Case	ϕ (deg)	γ_{dry} (lb/ft^3)	D_r (%)	Δ/B	q_{net} Measured (psf)	Percent Difference (%)
LT-36	1	38.37	107.95	95.60	0.215	31,049	8.49
LT-44	1	38.38	107.97	95.70	0.223	33,802	
LT-33	2	38.33	107.91	95.40	0.194	24,261	3.83
LT-34	2	38.38	107.96	95.65	0.193	25,208	
LT-41	3	38.63	108.17	96.65	0.169	13,873	10.11
LT-42	3	38.64	108.27	97.10	0.153	15,351	
LT-37	4	38.54	108.15	96.54	0.173	26,102	4.98
LT-38	4	38.42	108.01	95.89	0.175	24,834	
LT-39	5	38.63	108.25	97.02	0.196	26,292	2.90
LT-40	5	38.73	108.38	97.58	0.206	25,539	

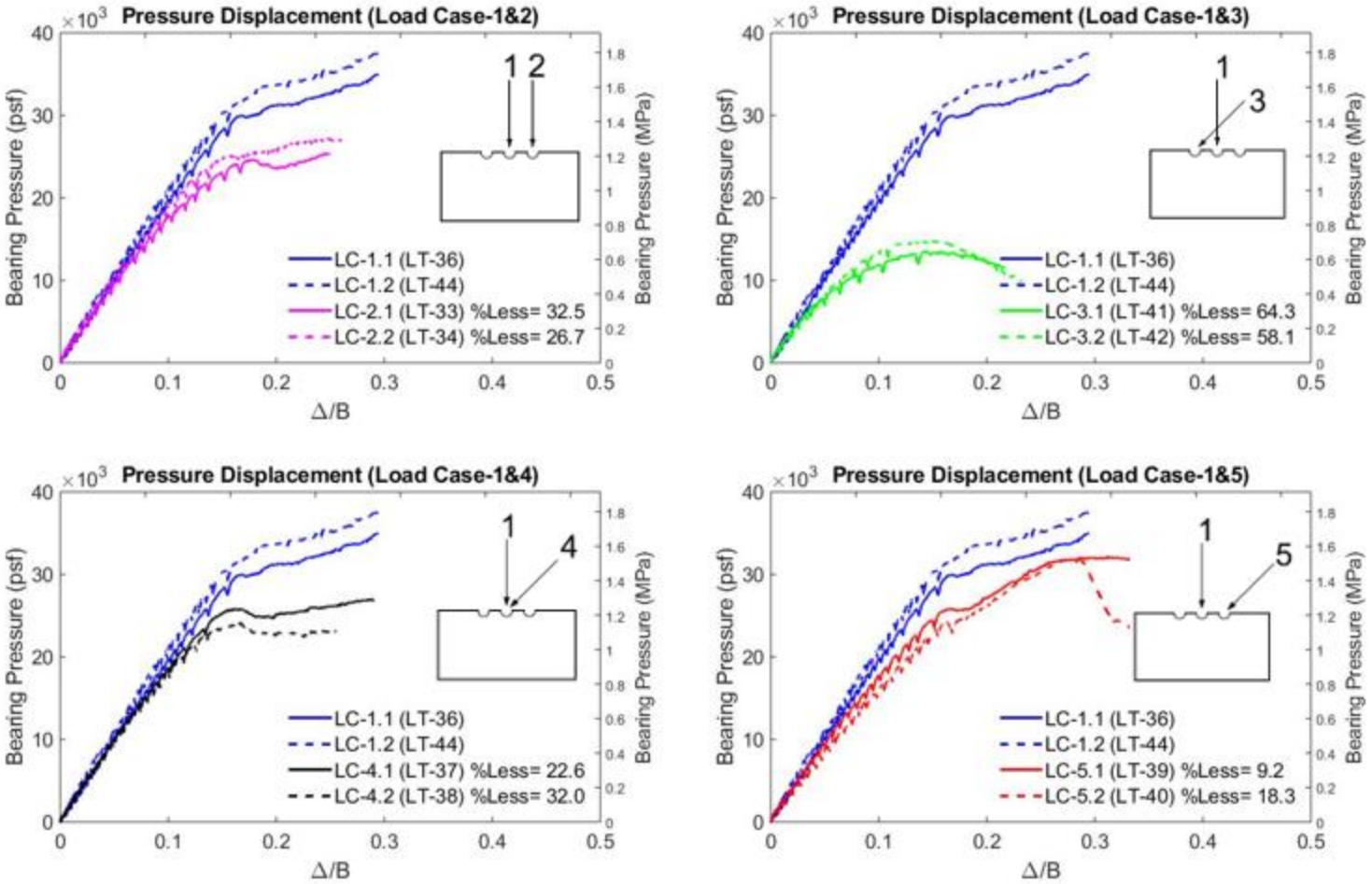

Figure 5.7 Net bearing pressure vs. displacement for Load Cases 1–5 with lateral-to-axial ratio = 0.1 and D_f = 0.5B

Table 5.5 presents the post-test plan view and failure surface views of the soil stratigraphy, which indicate general shear failure did occur. The failure surface ruptured the ground surface in all cases

Table 5.5 Post-test failure surface for lateral-to-axial ratio equal to 0.10 at embedment depth equal to 0.5B

 Load Case-1 (LT-35)	
 Load Case-1 (LT-36)	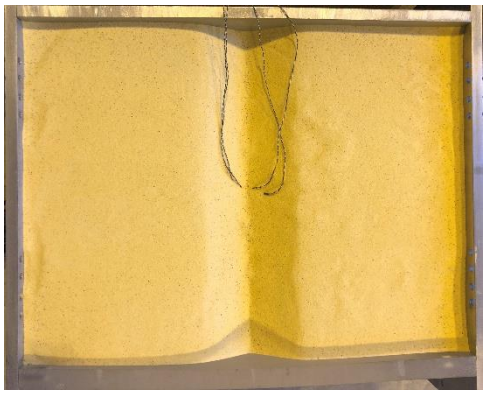
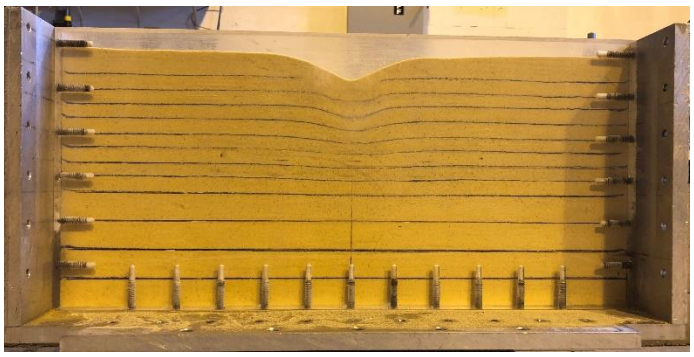 Load Case-1 (LT-44)	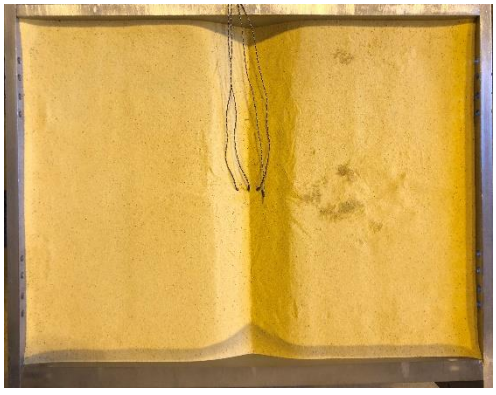

Load Case-2 (LT-33)

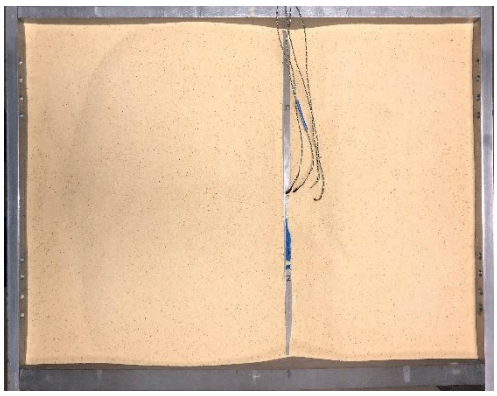

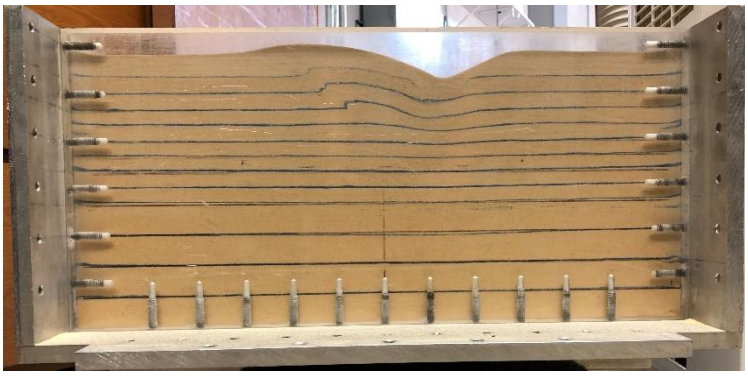

Load Case-2 (LT-34)

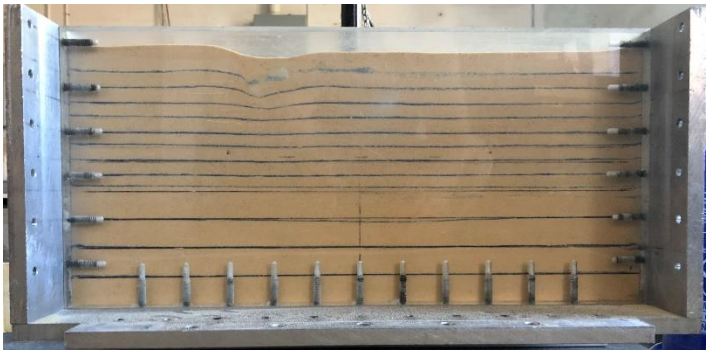

Load Case-3 (LT-41)

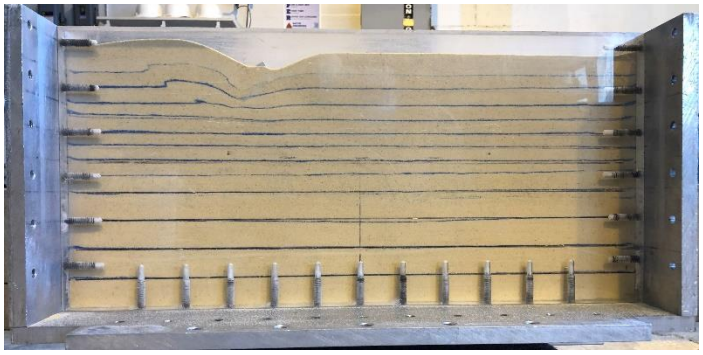

Load Case-3 (LT-42)

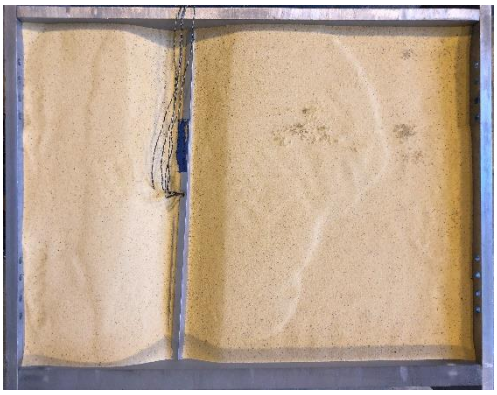

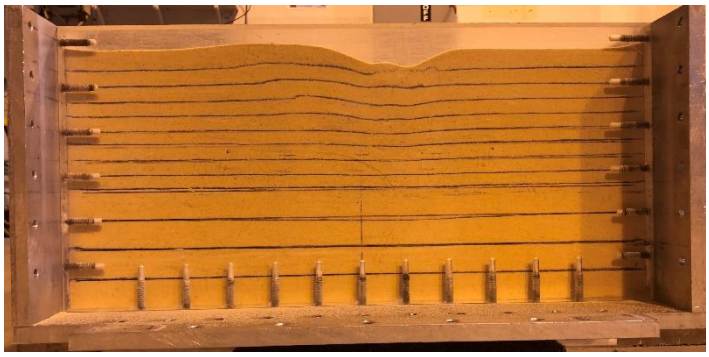

Load Case-4 (LT-37)

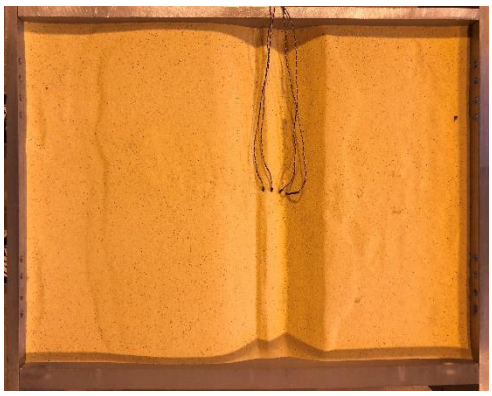

Load Case-4 (LT-38)

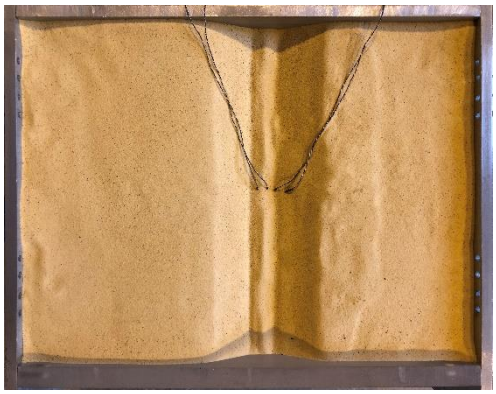

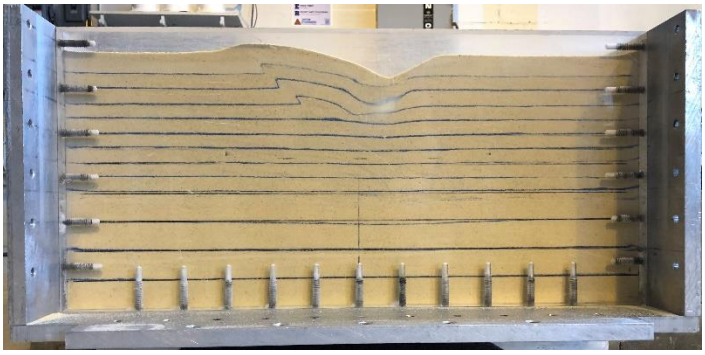

Load Case-5 (LT-39)

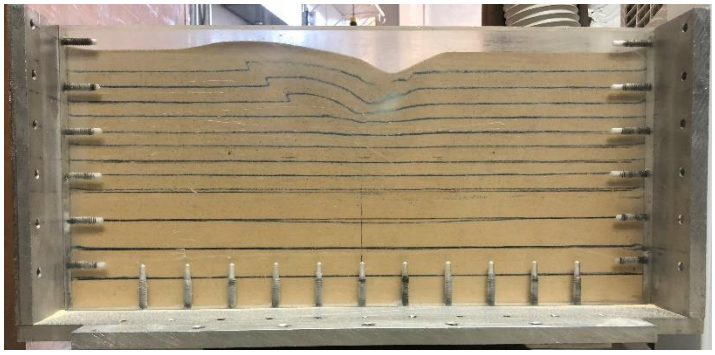

Load Case-5 (LT-40)

Summary of the post-test images of rupture surfaces:

- The observed rupture surface for Load Case-1 (LT-35, LT-36, and LT-44) shows the maximum depth and length of the failure surface. LT-35, LT-36, and LT-44 had showed well-formed failure surfaces (Table 5.5) with depths of 4.19, 4.76, and 4.22 inches with lengths of 9.61, 9.60, and 9.41 inches. The failure surface ruptured the top layer of soil on the left side of the footing as the test underwent concentric loading at the center of the footing.
- Load Case-2 (LT-33 and LT-34) had well-formed failure surface depths of 3.17 and 3.24 inches with lengths of 9.31 and 9.26 inches. The failure surface ruptured the top layer of soil on the left side of the footing as the test underwent eccentric loading at distance of B/6 from the center of the footing.
- Load Case-3 (LT-41 and LT-42) shows the minimum failure surface depth and length. LT-41 and LT-42 had failure surface depths of 2.75 and 2.73 inches with lengths of 5.42 and 6.38 inches. LT-41 and LT-42 unexpectedly observed a failure surface on the left side of the footing as the footing underwent inclined-eccentric loading outward (–) to the direction of the eccentricity.
- Load Case- 4 (LT-37 and LT-38) observed well-formed failure surface depth of 3.69 and 3.74 inches with lengths of 7.9 inches and 10.44 inches as the footing underwent inclined loading at the center of the footing.
- Load Case-5 (LT-39 and LT-40) observed well-formed failure surfaces. The measured depth and length of LT-39 was 3.23 inches and 9.96 inches while LT-40 had failure surface depth and length of 3.22 inches and 10.57 inches. The failure surface ruptured the top layer of soil on the left side of the footing as the test underwent eccentric-inclined loading inward (+) to

the direction of the eccentricity.

The bearing pressure distribution observed by the miniature pressure transducers is presented for each load test in Figures 5.8 and 5.9. The loading position and orientation is displayed in each plot to illustrate how the pressure distribution is developed. The pressure sensors were positioned beneath the footing in sequential order (PS-1 through PS-4) from left to right at a spacing of 0.36 inches in model scale as previously stated.

Load Case-1 (LT-36 and LT-44) demonstrates a pressure distribution with an increasing radial shape towards the center of the footing. This pressure profile is consistent with previous numerical modeling research presented by Loukidis et al. (2008) for sand as shown in Figure 5.6. Load Case-2 (LT-33 and LT-34), Load Case-3 (LT-41 and LT-42), Load Case-4 (LT-37 and LT-38), and Load Case-5 (LT-39 and LT-40) demonstrates a trapezoidal shape with increasing pressure on the side of eccentricity, inclination or eccentric-inclined loading. The trapezoidal shift in pressure towards the side of eccentric or inclined loading is also present in Loukidis et al. (2008) analysis.

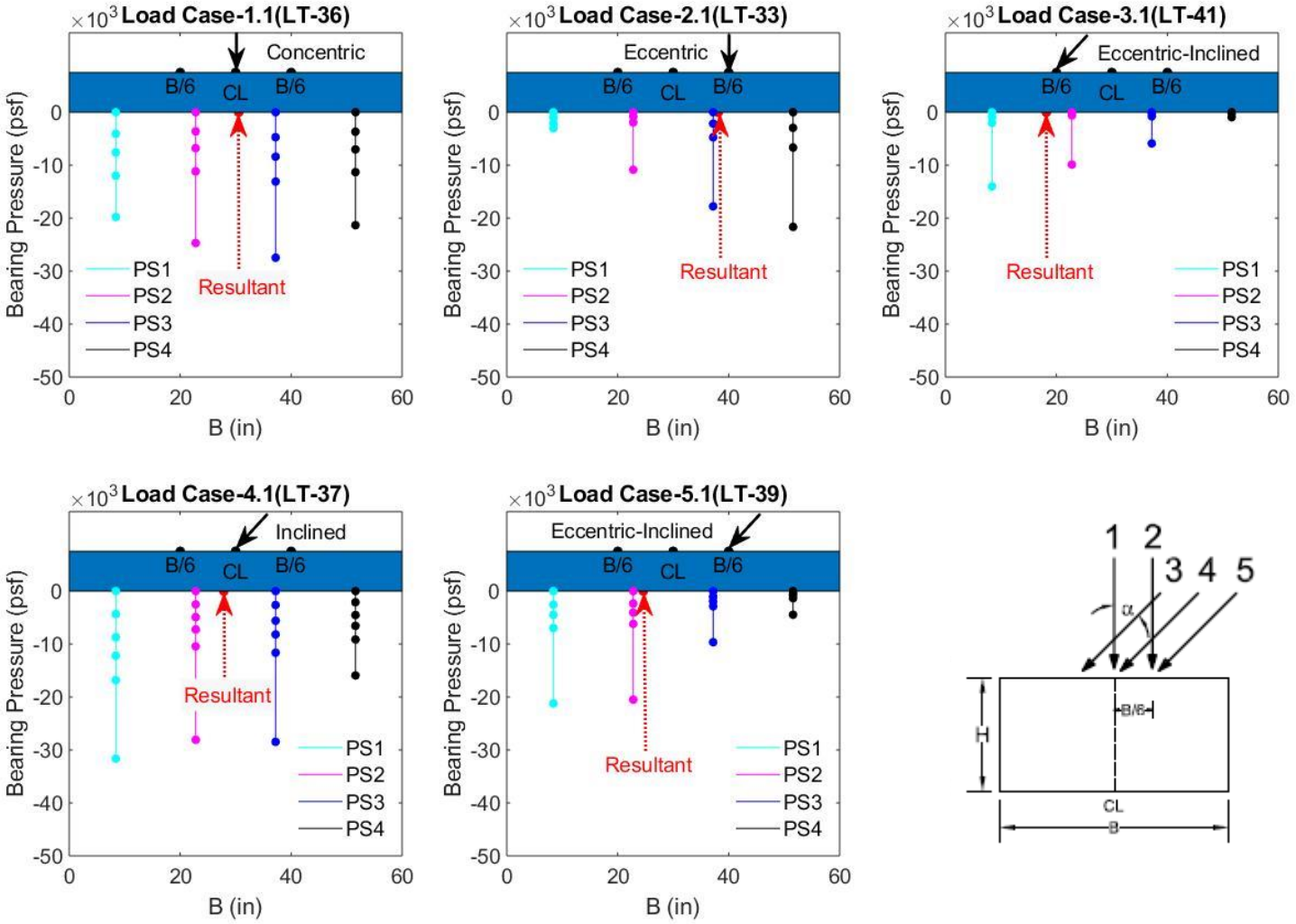

Figure 5.8 Bearing pressure distribution for Load Cases 1–5 with lateral-to-axial ratio = 0.1 and D_f = 0.5B

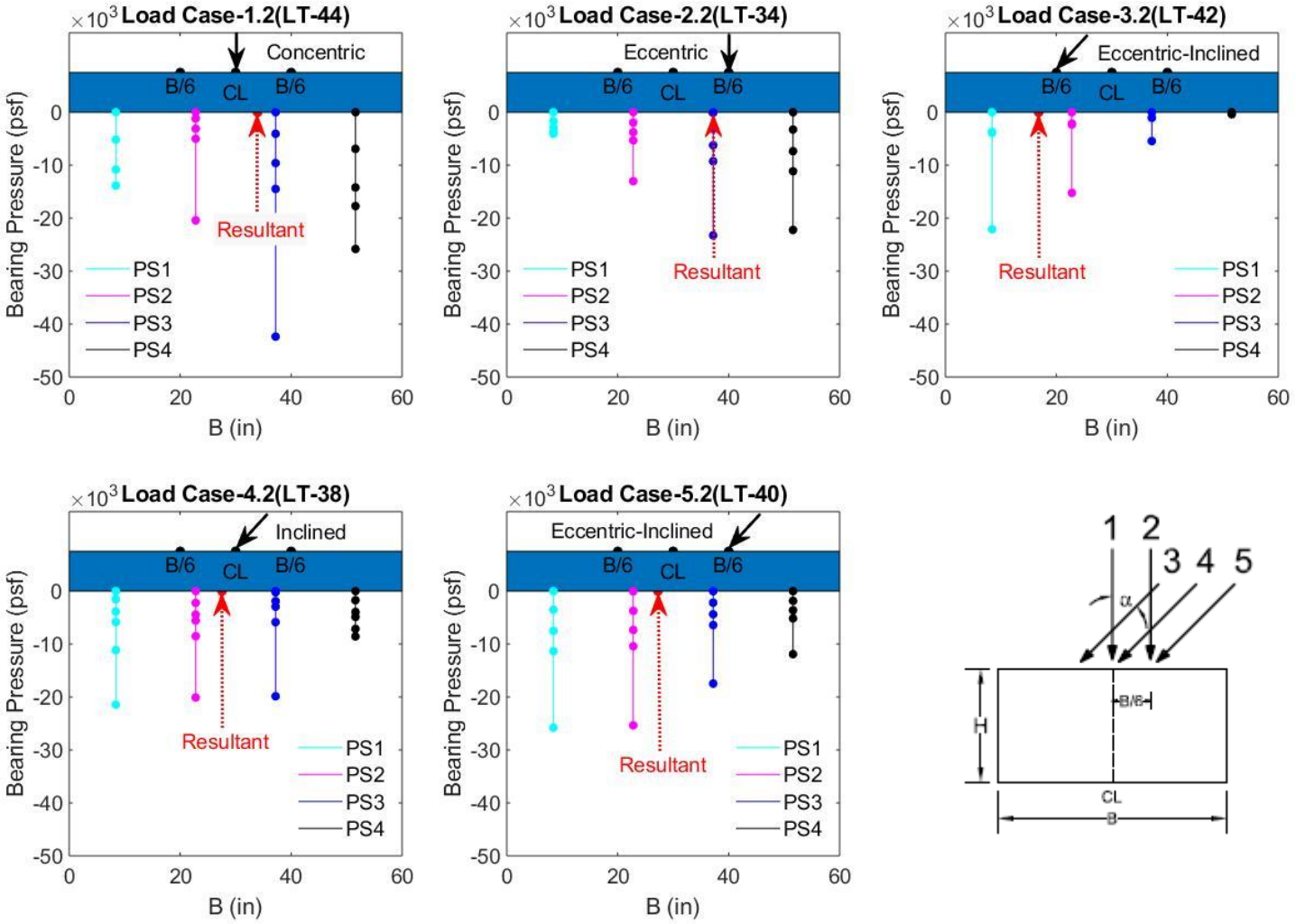

Figure 5.9 Bearing pressure distribution for Load Cases 1–5 with lateral-to-axial ratio = 0.1 and D_f = 0.5B

5.1.3 Lateral-to-Axial Ratio of 0.25 with Depth of Embedment Equal to Zero

In this series of tests, the rectangular footing was loaded for Load Cases 1–5 with depth of embedment equal to zero. The AASHTO A3 soil used in the tests had an average dry unit weight, $\gamma_{dry,}$ in the range of 107.82 lb/ft^3 to 108.66 lb/ft^3 and average relative density, D_r in the range of 94.99% to 98.89% for the top soil layers where the failure surface was observed. The average peak friction angle from the direct shear test was estimated to be in the range of 38.26° to 38.86°. The model footing was tested at N = 40 G which results in a prototype footing width and length of 5 feet by 50 feet with the L/B ratio of 10. All eccentric loads were applied at a distance of B/6 (0.25 inches) from the center of the footing and inclined loads were applied at a lateral-to-axial ratio of 0.25 (14°). The combined eccentric-inclined load test applied the same geometric loading conditions as the individual parts.

The net bearing capacity for each test is presented in Figure 5.10. Listed in Table 5.6 are the internal friction angles, unit weight, relative density, and net measured bearing capacities with percent differences to demonstrate repeatability for each test.

Table 5.6 Summary of measured test parameters and results for L/B = 10 with lateral-to-axial ratio = 0.25 and D_f = 0 (VD)

Load Test	Load Case	ϕ (deg)	γ_{dry} (lb/ft^3)	D_r (%)	Δ/B	q_{net} Measured (psf)	Percent Difference (%)
LT-23	1	38.41	108.00	95.82	0.175	19,954	6.97
LT-24	1	38.57	108.20	96.73	0.160	21,396	
LT-32	2	38.86	108.66	98.89	0.176	19,102	3.98
LT-43	2	38.57	108.53	98.29	0.180	19,878	
LT-49	3	38.42	108.01	95.89	0.067	3,725	4.59
LT-57	3	38.26	107.82	95.00	0.084	3,900	
LT-45	4	38.39	107.97	95.70	0.077	7,542	6.55
LT-46	4	38.52	108.12	96.41	0.068	7,064	
LT-47	5	38.30	107.87	95.22	0.200	13,390	3.81
LT-48	5	38.26	107.82	94.99	0.178	12,889	

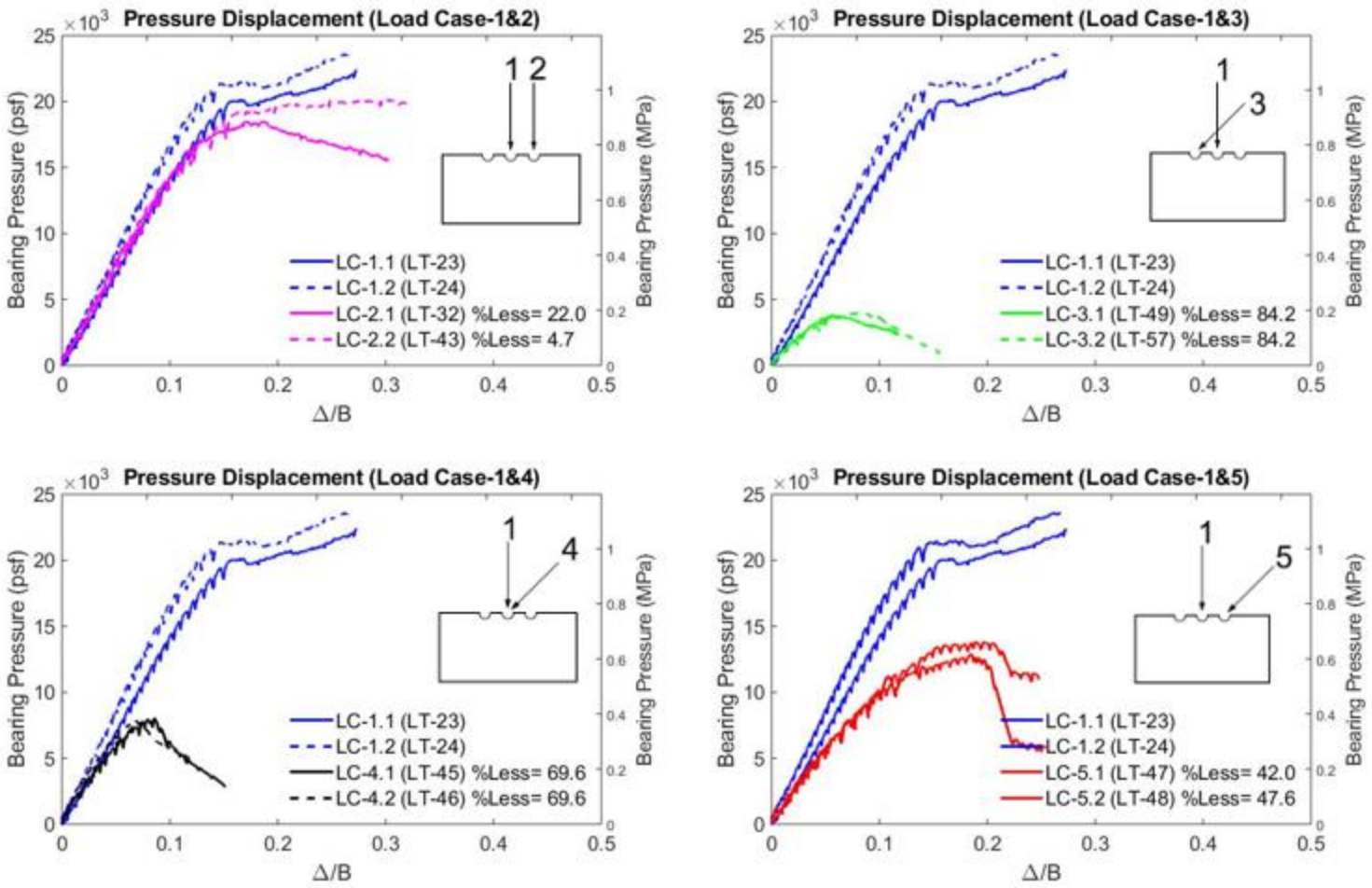

Figure 5.10 Net bearing pressure vs. displacement for Load Cases 1–5 with lateral-to-axial ratio = 0.25 and $D_f = 0$

Table 5.7 presents the post-test plan view and failure surface views of the soil stratigraphy, which indicate general shear failure did occur. The failure surface ruptured the ground surface in all cases.

Table 5.7 Post-test failure surface for lateral-to-axial ratio equal to 0.25 at embedment depth equal to zero

 Load Case-4 (LT-45)	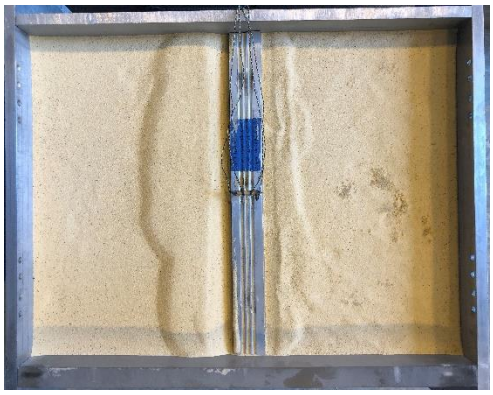
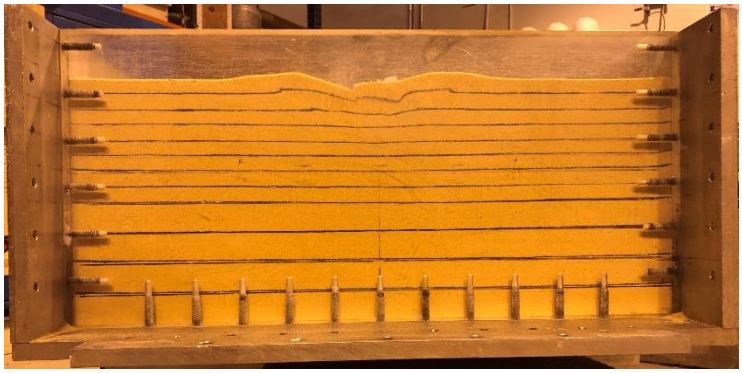 Load Case-4 (LT-46)	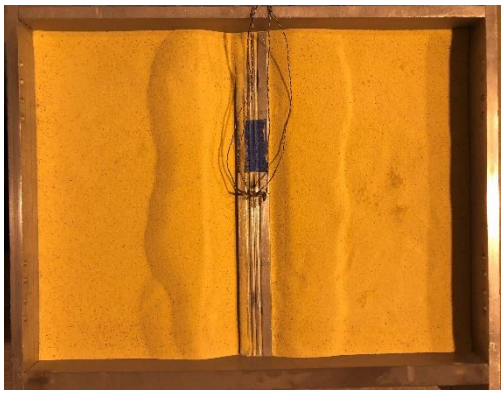
 Load Case-5 (LT-47)	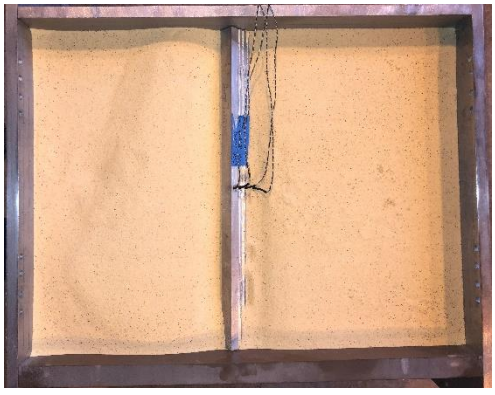

Load Case-5 (LT-48)

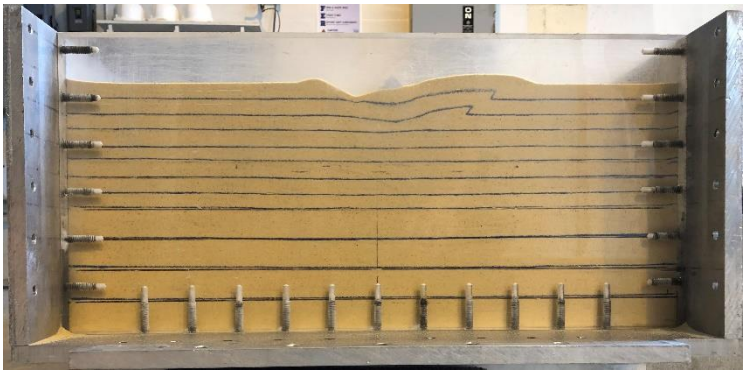

Load Case-3 (LT-49)

Load Case-3 (LT-57)

Summary of the post-test images of rupture surfaces:

- The observed rupture surface for Load Case-1 (LT-23 and LT-24) was previously discussed in section 1.5.1 Load Test for lateral-to-axial ratios of 0.10 with embedment depth equal to zero and were used as the baseline for comparison for the test with lateral-to-axial ration of 0.25 with $D_f = 0$.
- The observed rupture surface for Load Case-2 (LT-31, LT-32 and LT-43) was previously

discussed in section 1.5.1 Load Test for lateral-to-axial ratios of 0.10 with Embedment Depth equal to zero and will also be used for comparison for the test with lateral-to-axial ration of 0.25 with $D_f = 0$.

- Load Case-3 (LT-49 and LT-57) shows the minimum failure surface depth and length. LT-49 and LT-57 had failure surface depths of 2.02 inches each with lengths of 8.21 and 6.49 inches. LT-49 and LT 57 observed a failure surface on the right side of the footing as expected while the footing underwent inclined-eccentric loading outward (–) to the direction of the eccentricity.
- Load Case- 4 (LT-45 and LT-46) observed well-formed failure surface depth of 2.03 and 2.02 inches and lengths of 4.64 inches and 4.73 inches as the footing underwent inclined loading at the center of the footing.
- Load Case-5 (LT-47 and LT-48) observed well-formed failure surfaces. The measured depth and length of LT-47 was 3.01 inches and 7.57 inches while LT-48 had failure surface depth and length of 2.49 inches and 6.99 inches. The failure surface ruptured the top layer of soil on the left side of the footing as the test underwent eccentric-inclined loading inward (+) to the direction of the eccentricity.

The bearing pressure distribution observed by the miniature pressure transducers is presented for each load test in Figures 5.11 and 5.12. The loading position and orientation is displayed in each plot to illustrate how the pressure distribution is developed. The pressure sensors were positioned beneath the footing in sequential order (PS-1 through PS-4) from left to right at a spacing of 0.36 inches in model scale as previously stated.

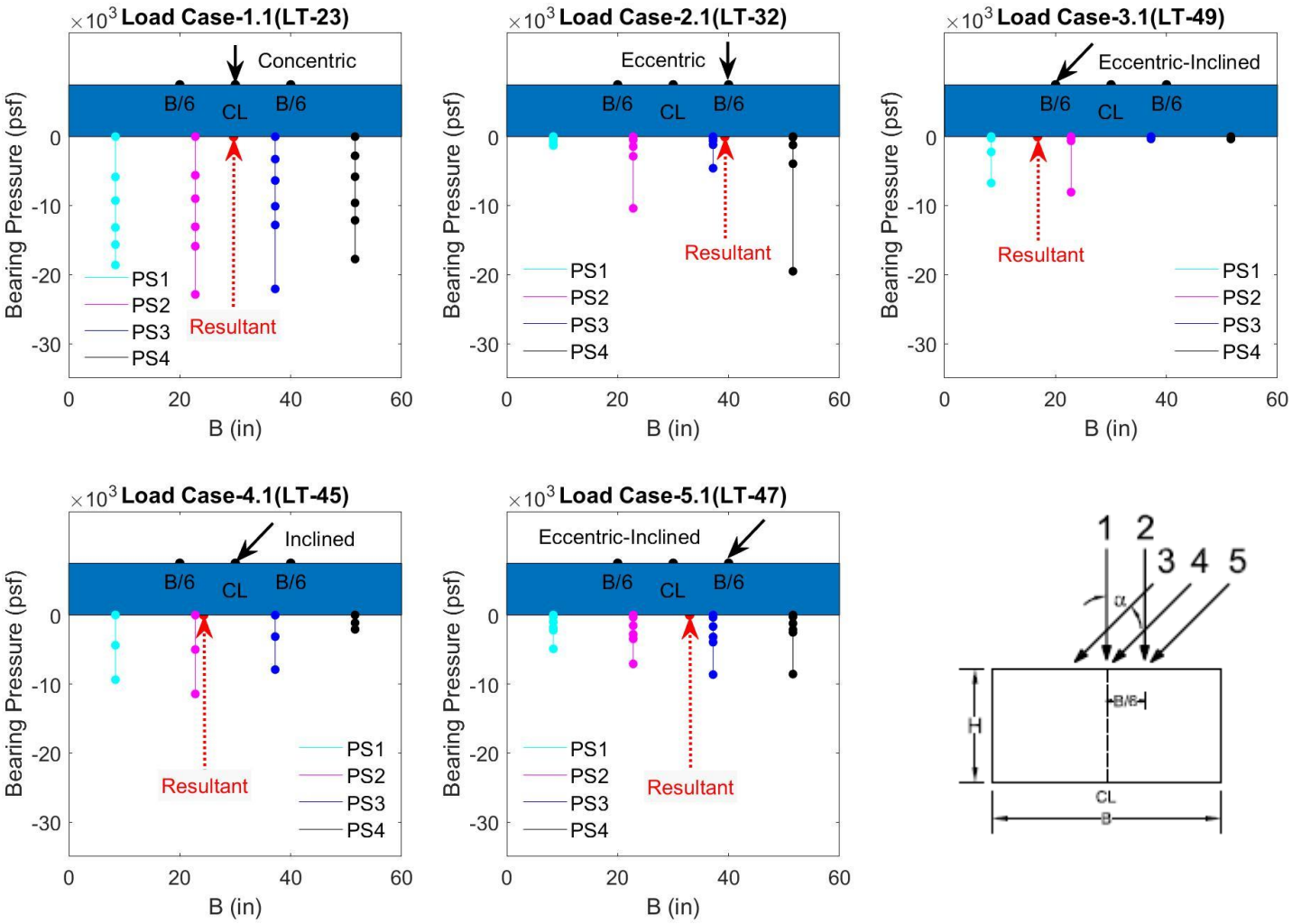

Figure 5.11 Bearing pressure distribution for Load Cases 1–5 with lateral-to-axial ratio = 0.25 and D_f = 0

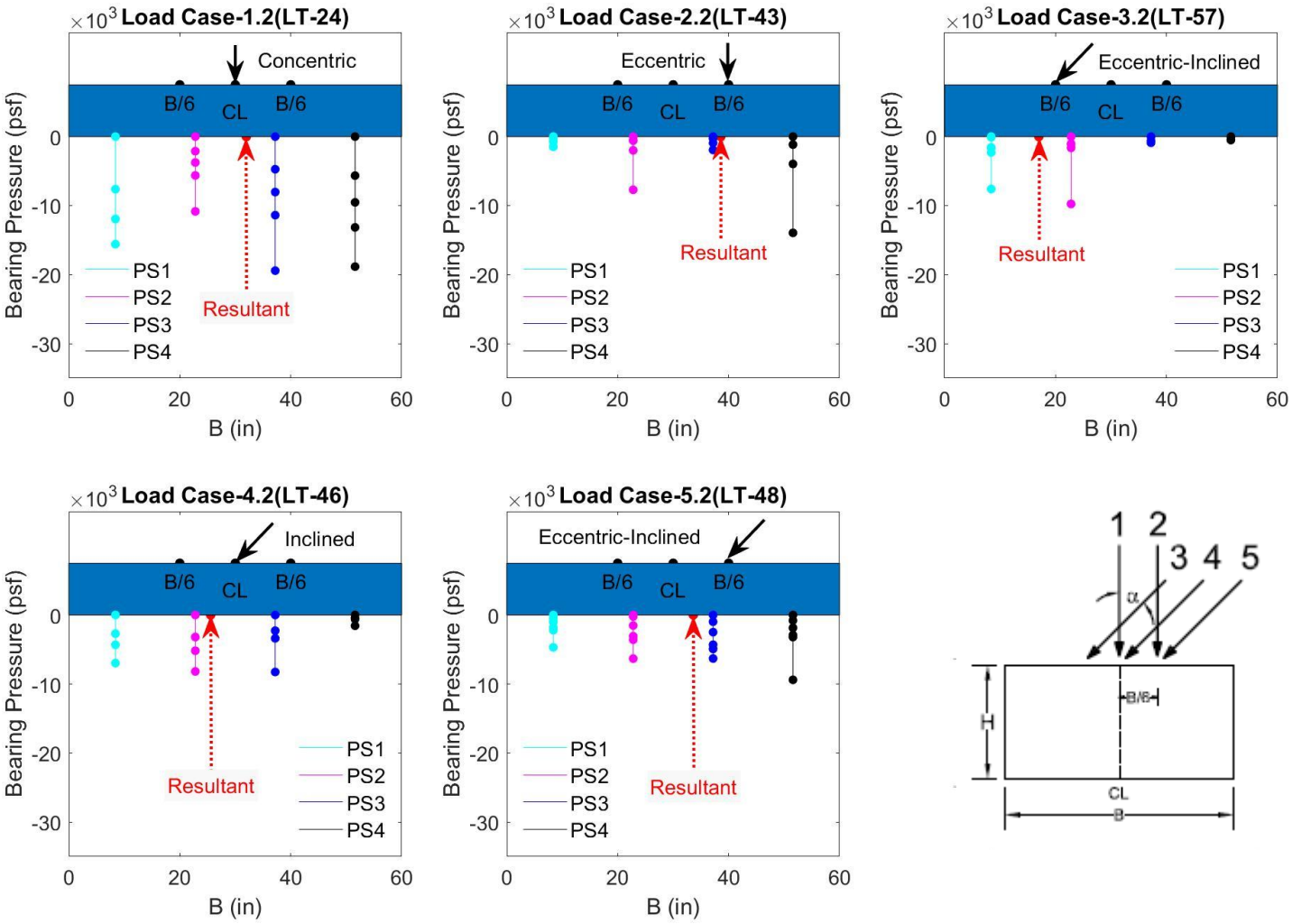

Figure 5.12 Bearing pressure distribution for Load Cases 1–5 with lateral-to-axial ratio = 0.25 and D_f = 0

Load Case-1 (LT-23 and LT-24) demonstrates a pressure distribution with an increasing radial shape towards the center of the footing. This pressure profile is consistent with previous numerical modeling research presented by Loukidis et al. (2008) for sand as shown in Figure 5.6. Load Case-2 (LT-32 and LT-43), Load Case-3 (LT-49 and LT-57), Load Case-4 (LT-45 and LT-46), and Load Case-5 (LT-47 and LT-48) demonstrates a trapezoidal shape with increasing pressure on the side of eccentricity, inclination or eccentric-inclined loading. The trapezoidal shift in pressure towards the side of eccentric or inclined loading is also present in Loukidis et al. (2008) analysis.

Like the results presented in the pressure displacement plots, Load Case-1 reports the highest bearing pressure and Load Case-3 reports the lowest bearing pressures. Comparing Load Case-3 with Load Case-5, the latter shows an increase in bearing pressure over Load-Case-3 which supports the increased failure surface depth previously discussed.

5.1.4 Lateral-to-Axial Ratio of 0.25 with Depth of Embedment Equal to 0.5B

In this series of tests, the rectangular footing was loaded for Load Cases 1–5 with depth of embedment equal to 0.5B. The AASHTO A3 soil used in the tests had an average dry unit weight, $\gamma_{dry,}$ in the range of 107.74 lb/ft^3 to 108.26 lb/ft^3 and average relative density, D_r in the range of 94.63% to 97.06% for the top soil layers where the failure surface was observed. The average peak friction angle from the direct shear test was estimated to be in the range of 38.19° to 38.63°. The model footing was tested at N = 40 G which results in a prototype footing width and length of 5 feet by 50 feet with the L/B ratio of 10 and embedment depth equal to 0.5B. All eccentric loads were applied B/6 (0.25 inches) from the center of the footing and inclined loads were applied at a lateral-to-axial ratio of 0.25 (14°). The combined eccentric-inclined load test applied the same geometric loading conditions as the individual parts. The net bearing capacity

for each test are presented in Figure 5.13. All eccentric and eccentric-inclined loading conditions used the effective width B' to determine the bearing pressure. Listed in Table 5.8 are the internal friction angles, unit weight, relative density, and net measured bearing capacities with percent differences to demonstrate repeatability for each test.

Table 5.8 Summary of measured test parameters and results for L/B = 10 with lateral-to-axial ratio = 0.25 and D_f = 0.5B (VD)

Load Test	Load Case	ϕ (deg)	γ_{dry} (lb/ft^3)	D_r (%)	Δ/B	q_{net} Measured (psf)	Percent Difference (%)
LT-36	1	38.37	107.95	95.60	0.215	31,049	8.49
LT-44	1	38.38	107.97	95.70	0.223	33,802	
LT-33	2	38.33	107.91	95.40	0.194	24,261	3.83
LT-34	2	38.38	107.96	95.65	0.193	25,208	
LT-55	3	38.40	107.98	95.77	0.123	9,628	8.93
LT-56	3	38.25	107.81	94.94	0.135	10,528	
LT-51	4	38.19	107.74	94.63	0.113	13,509	3.69
LT-52	4	38.63	108.26	97.06	0.122	14,017	
LT-53	5	38.36	107.94	95.56	0.254	23,412	0.42
LT-54	5	38.30	107.87	95.22	0.212	23,510	

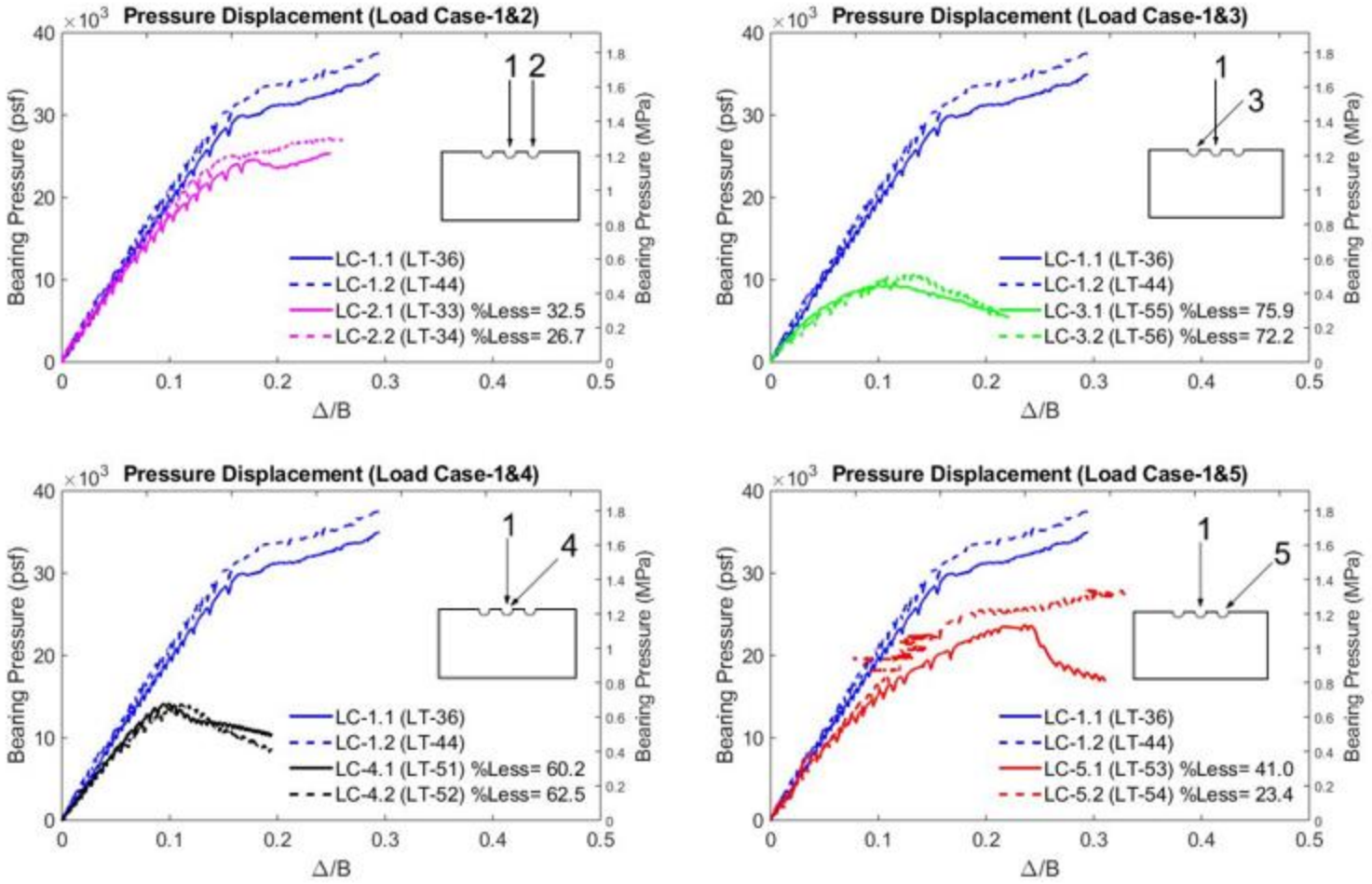

Figure 5.13 Net bearing pressure vs. displacement for Load Cases 1–5 with lateral-to-axial ratio = 0.25 and D_f = 0.5B

Table 5.9 presents the post-test plan view and failure surface views of the soil stratigraphy, which indicate general shear failure did occur. The failure surface ruptured the ground surface in all cases.

Table 5.9 Post-test failure surface for lateral-to-axial ratio equal to 0.25 at embedment depth equal to 0.5B

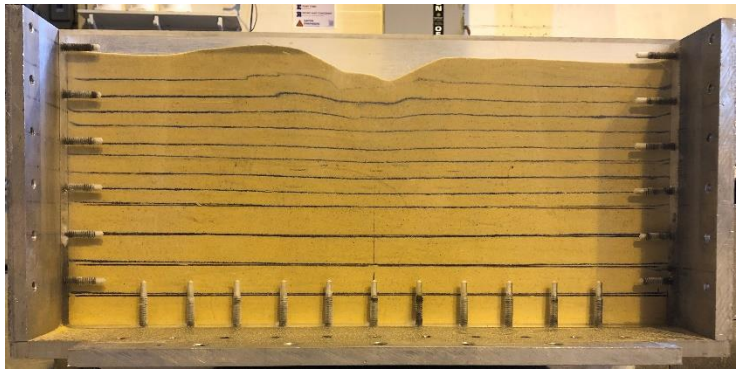 Load Case-4 (LT-51)	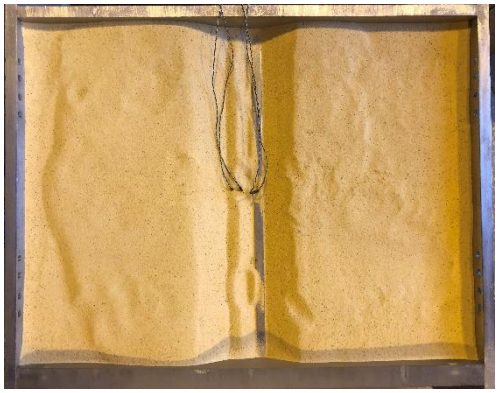
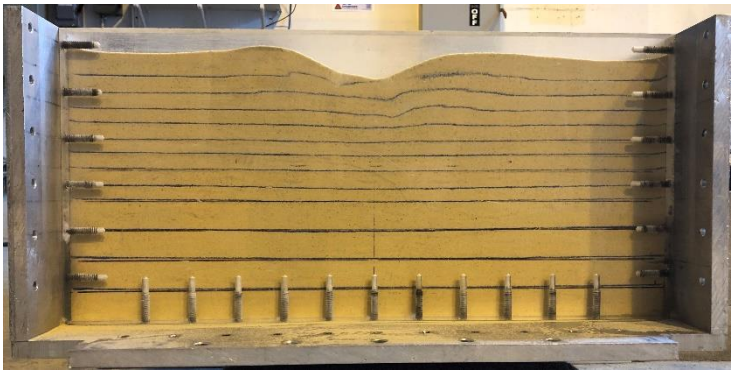 Load Case-4 (LT-52)	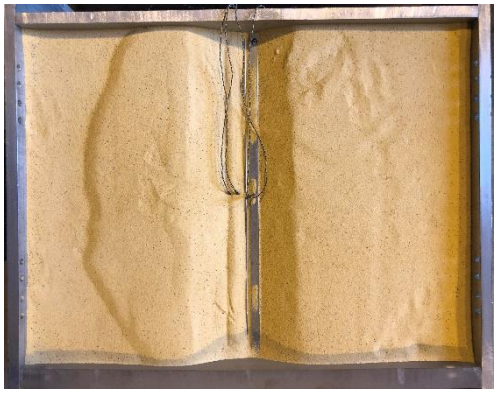
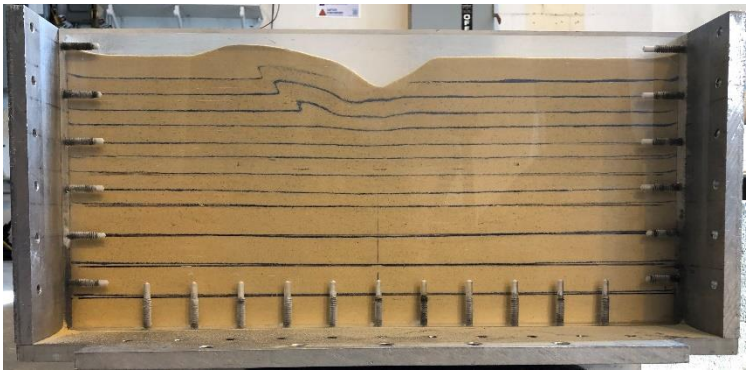 Load Case-5 (LT-53)	

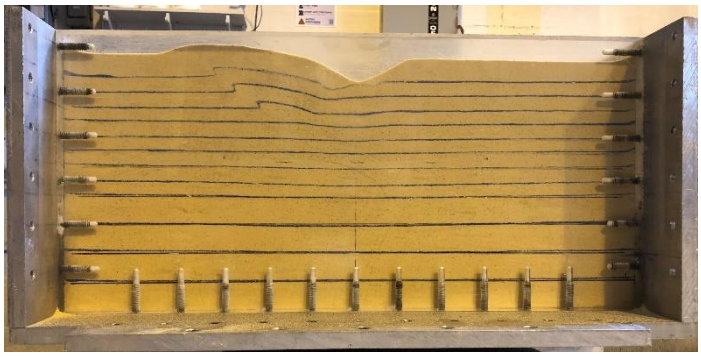

Load Case-5 (LT-54)

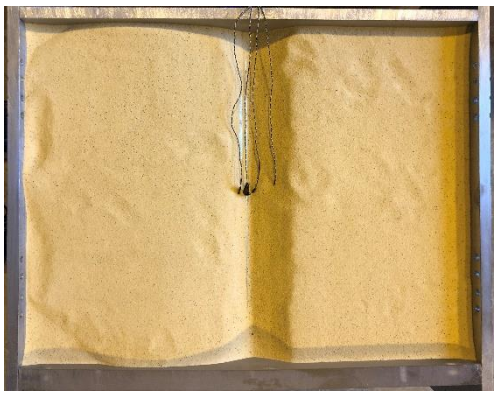

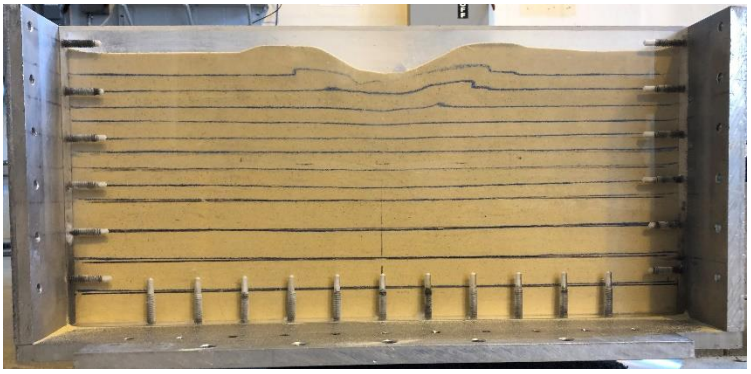

Load Case-3 (LT-55)

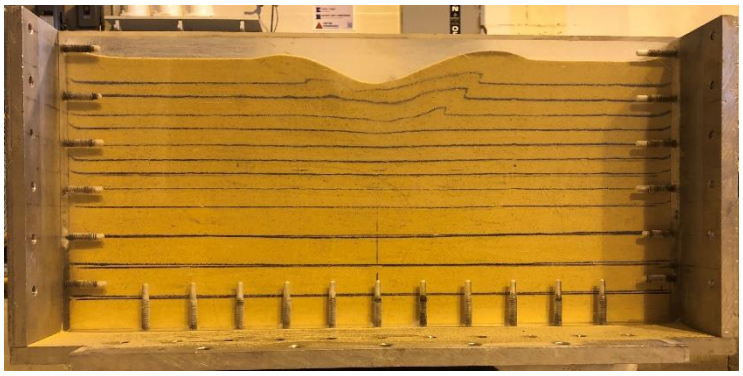

Load Case-3 (LT-56)

Summary of the post-test images of rupture surfaces:

- The observed rupture surface for Load Case-1 (LT-35, LT-36 and LT-44) was previously discussed in section 1.5.2 Load Test for lateral-to-axial ratios of 0.10 with Embedment Depth equal to 0.5B and were used as the baseline for comparison for the test with lateral-to-axial ration of 0.25 with $D_f = 0$.

- Load Case-2 (LT-33 and LT-34) was previously discussed in section 1.5.2 Load Test for lateral-to-axial ratios of 0.10 with embedment depth equal to 0.5B and will also be used for comparison for the test with lateral-to-axial ration of 0.25 with $D_f = 0$.
- Load Case-3 (LT-55 and LT-56) shows the minimum failure surface depth and length. LT-55 and LT-56 had failure surface depths of 2.23 and 2.21 inches with lengths of 6.62 and 6.41 inches. LT- Unlike LT-41 and LT-42, 55 and LT-55 observed a failure surface on the right side of the footing as expected while the footing underwent inclined-eccentric loading outward (–) to the direction of the eccentricity.
- Load Case- 4 (LT-51 and LT-52) observed well-formed failure surface depths of 3.76 and 3.18 inches and lengths of 8.72 inches and 6.92 inches as the footing underwent inclined loading at the center of the footing.
- Load Case-5 (LT-53 and LT-54) observed well-formed failure surfaces. The measured depth and length of LT-53 was 2.72 inches and 7.67 inches while LT-54 had failure surface depth and length of 3.17 inches and 9.48 inches. The failure surface ruptured the top layer of soil on the left side of the footing as the test underwent eccentric-inclined loading inward (+) to the direction of the eccentricity.

The bearing pressure distribution observed by the miniature pressure transducers is presented for each load test in Figures 5.14 and 5.15. The loading position and orientation is displayed in each plot to illustrate how the pressure distribution is developed. The pressure sensors were positioned beneath the footing in sequential order (PS-1 through PS-4) from left to right at a spacing of 0.36 inches in model scale as previously stated.

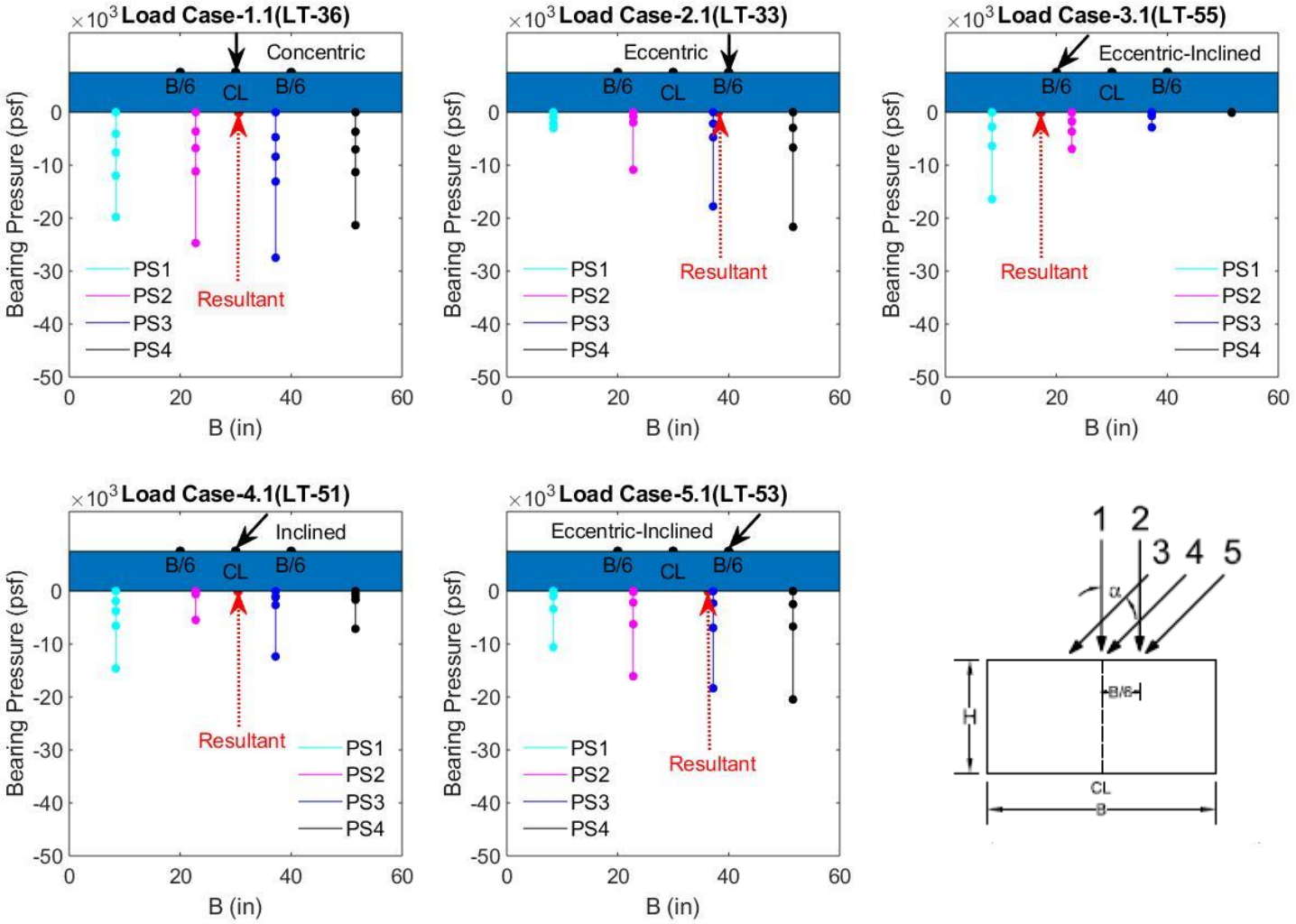

Figure 5.14 Bearing pressure distribution for Load Cases 1–5 with lateral-to-axial ratio = 0.25 and D_f = 0.5B

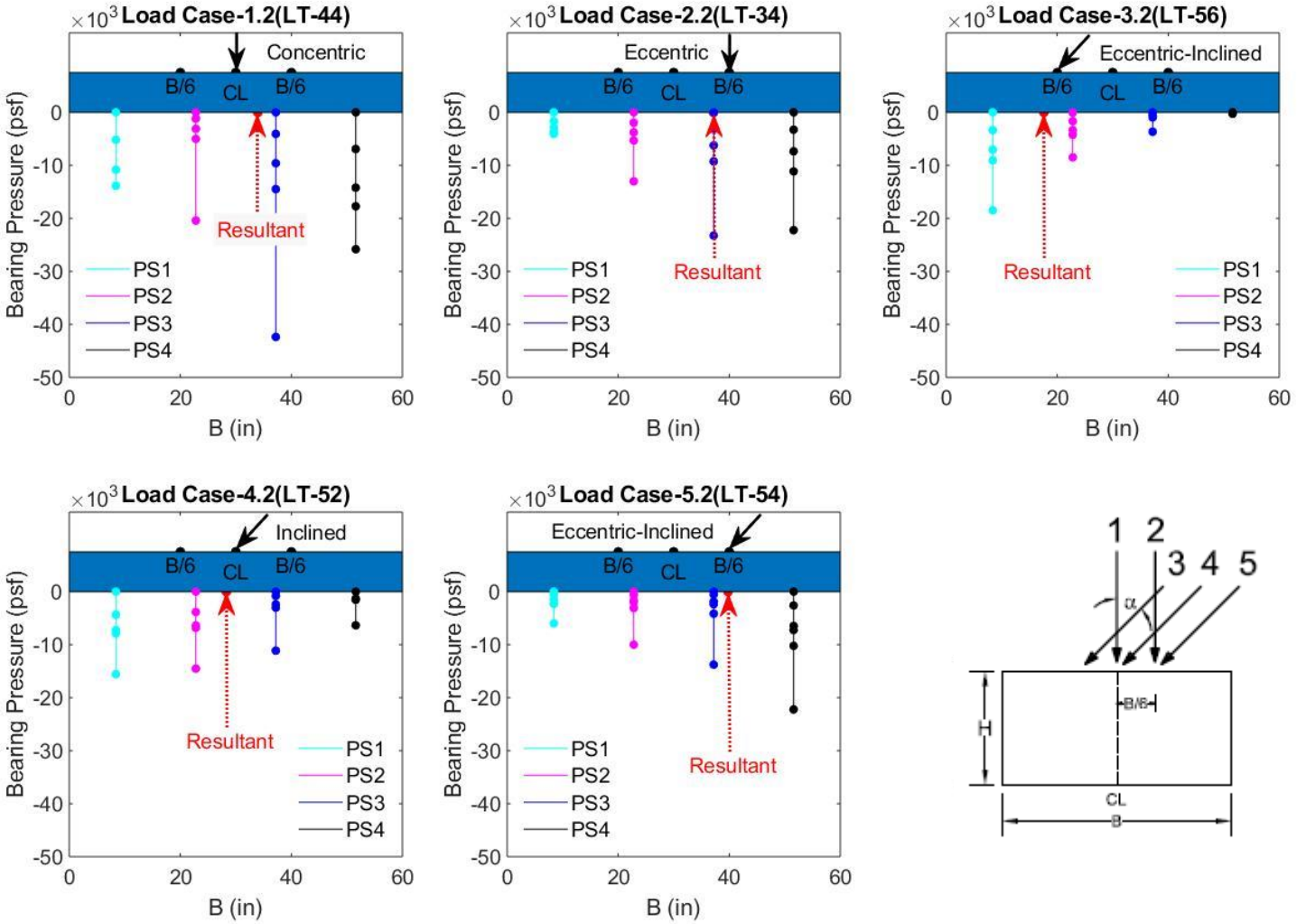

Figure 5.15 Bearing pressure distribution for Load Cases 1–5 with lateral-to-axial ratio = 0.25 and D_f = 0.5B

Load Case-1 (LT-36 and LT-44) demonstrates a pressure distribution with an increasing radial shape towards the center of the footing. Load Case-2 (LT-33 and LT-34), Load Case-3 (LT-55 and LT-56), Load Case-4 (LT-51 and LT-52), and Load Case-5 (LT-53 and LT-54) demonstrates a trapezoidal shape with increasing pressure on the side of eccentricity, inclination or eccentric-inclined loading. The trapezoidal shift in pressure towards the side of eccentric or inclined loading is also present in Loukidis et al. (2008) analysis.

Comparing Load Case-3 and Load Case-5, the latter shows an increase in bearing pressure over Load-Case-3, as evidenced by the observed failure surfaces in Table 5.3 (shorter surface in Load Case 3 compared to Load Case 5).

A summary of the measured test results is presented in Table 5.10 which provides the load case, relative density, D_r, friction angle, ϕ, embedment depth, D_f, L/A ratio, inclination angle, eccentricity, measured bearing capacity, q_u, load and corresponding failure surface direction, failure surface depth, and failure surface length.

Table 5.10 List of load tests on very dense soil (L/B = 10)

Load Test	Load Case	D_r (%)	ϕ_{DS} (deg)	D_f (ft)	L/A Ratio	Inclination Angle (deg)	e	q_{ult} Measured (psf)	Load & Failure Surface Direction	Failure Surface Depth (in)	Failure Surface Length (in)
LT-23	1	95.82	38.41	0.00	0.00	0.0	0	19,954	↓←	3.03	N/A
LT-24	1	96.73	38.57	0.00	0.00	0.0	0	21,396	↓←	5.00	9.42
LT-25	4	90.63	37.46	0.00	0.10	5.7	0	15,662	↙←	N/A	4.05
LT-26	4	94.20	38.11	0.00	0.10	5.7	0	15,098	↙←	3.05	4.68
LT-27	5	94.67	38.20	0.00	0.10	5.7 (–)	0.25	15,526	↙←	2.99	6.61
LT-28	5	96.60	38.55	0.00	0.10	5.7 (–)	0.25	16,849	↙←	3.04	8.08
LT-29	3	95.07	38.24	0.00	0.10	5.7 (+)	0.25	9,921	↙→	2.00	2.63
LT-30	3	95.10	38.28	0.00	0.10	5.7 (+)	0.25	9,337	↙→	2.53	7.97
LT-32	2	98.29	38.86	0.00	0.00	0.0	0.25	19,102	↓←	2.97	7.38
LT-33	2	95.40	38.33	2.45	0.00	0.0	0.25	24,261	↓←	3.17	9.31
LT-34	2	95.65	38.38	2.45	0.00	0.0	0.25	25,208	↓←	3.24	9.26
LT-36	1	95.60	38.37	2.45	0.00	0.0	0	31,049	↓←	4.76	9.6
LT-37	4	96.54	38.54	2.45	0.10	5.7	0	26,102	↙←	3.69	7.9
LT-38	4	95.89	38.42	2.45	0.10	5.7	0	24,834	↙←	3.74	10.44
LT-39	5	97.02	38.63	2.45	0.10	5.7 (–)	0.25	26,292	↙←	3.23	9.96
LT-40	5	97.58	38.73	2.45	0.10	5.7 (–)	0.25	25,539	↙←	3.22	10.57

Table 5.10 (continued)

LT-41	3	96.65	38.63	2.45	0.10	5.7 (+)	0.25	13,873	↙→	2.75	5.42
LT-42	3	97.10	38.64	2.45	0.10	5.7 (+)	0.25	15,351	↙→	2.73	6.38
LT-43	2	96.71	36.43	2.47	0.00	0.0	0.25	19,878	↓←	3.01	7.7
LT-44	1	95.70	38.38	2.45	0.00	0.0	0.25	29,540	↓←	4.22	9.41
LT-45	4	95.70	38.39	0.00	0.25	14.6	0	7,542	↙←	2.03	4.64
LT-46	4	96.41	38.52	0.00	0.25	14.6	0	7,064	↙←	2.02	4.73
LT-47	5	95.22	38.30	0.00	0.25	14.6 (–)	0.25	13,390	↙←	3.01	7.57
LT-48	5	94.99	38.26	0.00	0.25	14.6 (–)	0.25	12,889	↙←	2.49	6.99
LT-49	3	95.89	38.42	0.00	0.25	14.6 (+)	0.25	3,725	↙→	2.02	8.21
LT-51	4	94.63	38.19	2.45	0.25	14.6	0	13,509	↙←	3.76	8.72
LT-52	4	97.06	38.63	2.45	0.25	14.6	0	14,017	↙←	3.18	6.92
LT-53	5	95.56	38.36	2.45	0.25	14.6 (–)	0.25	23,412	↙←	2.72	7.67
LT-54	5	95.22	38.30	2.45	0.25	14.6 (–)	0.25	23,510	↙←	3.17	9.48
LT-55	3	95.77	38.40	2.45	0.25	14.6 (+)	0.25	9,628	↙→	2.23	6.62
LT-56	3	94.94	38.25	2.45	0.25	14.6 (+)	0.25	10,528	↙→	2.21	6.41
LT-57	3	95.00	38.26	0.00	0.25	14.6 (+)	0.25	3,900	↙→	2.02	6.49

(-) indicates the load is inclined against the direction of eccentricity. (+) indicates the load is inclined in the direction of eccentricity.

5.2 Model Load Tests — Concentric Loading on Rectangular Footing (L/B = 10) for Medium Dense Condition

Each load case was tested at two separate embedment depths (D_f = 0 and D_f = 0.5B) for lateral axial ratios of 0.10 and 0.25 for two relative density conditions (medium dense and very dense). All eccentric loads were applied at a distance of B/6 from centerline of the footing. Replicates of each case were performed to check for experimental repeatability. A total of 32 tests were performed in this series. The test procedure presented in sections 5.2 was repeated for the rectangular footing with medium dense soil conditions.

Table 5.11 lists the identifiers for each test with the date, sand condition, load case and footing configuration.

Table 5.11 List of load test for rectangular footing for medium dense condition

Name	Date	Load Case	Density (D_r)	Embedment Depth (D_f)	Eccentricity	Inclination L/A ratio	Series #
LT-58	7/09/19	1	Medium Dense	0	0	0	1
LT-59	7/11/19	1	Medium Dense	0	0	0	2
LT-60	7/12/19	1	Medium Dense	0.5B	0	0	1
LT-61	7/14/19	1	Medium Dense	0.5B	0	0	2
LT-62	7/16/19	2	Medium Dense	0	B/6	0	1
LT-63	7/16/19	2	Medium Dense	0	B/6	0	2
LT-64	7/18/19	2	Medium Dense	0.5B	B/6	0	1
LT-65	7/18/19	2	Medium Dense	0.5B	B/6	0	2
LT-66	7/21/19	3	Medium Dense	0	B/6	0.10	1
LT-67	7/21/19	3	Medium Dense	0	B/6	0.10	2
LT-68	7/23/19	3	Medium Dense	0.5B	B/6	0.10	1
LT-69	7/27/19	3	Medium Dense	0.5B	B/6	0.10	2
LT-70	7/25/19	4	Medium Dense	0	0	0.10	1
LT-71	7/25/19	4	Medium Dense	0	0	0.10	2
LT-72	7/27/19	4	Medium Dense	0.5B	0	0.10	1
LT-73	7/28/19	4	Medium Dense	0.5B	0	0.10	2
LT-74	7/28/19	5	Medium Dense	0	B/6	0.10	1
LT-75	7/29/19	5	Medium Dense	0	B/6	0.10	2
LT-76	7/30/19	5	Medium Dense	0.5B	B/6	0.10	1
LT-77	7/30/19	5	Medium Dense	0.5B	B/6	0.10	2
LT-78	7/31/19	3	Medium Dense	0	B/6	0.25	1
LT-79	8/01/19	3	Medium Dense	0	B/6	0.25	2

Table 5.11 (continued)

LT-80	8/01/19	3	Medium Dense	0.5B	B/6	0.25	1
LT-81	8/02/19	3	Medium Dense	0.5B	B/6	0.25	2
LT-82	8/03/19	4	Medium Dense	0	0	0.25	1
LT-83	8/03/19	4	Medium Dense	0	0	0.25	2
LT-84	8/04/19	4	Medium Dense	0.5B	0	0.25	1
LT-85	8/04/19	4	Medium Dense	0.5B	0	0.25	2
LT-86	8/09/19	5	Medium Dense	0	B/6	0.25	1
LT-87	8/11/19	5	Medium Dense	0	B/6	0.25	2
LT-88	8/11/19	5	Medium Dense	0.5B	B/6	0.25	1
LT-89	8/11/19	5	Medium Dense	0.5B	B/6	0.25	2

5.2.1 Lateral-to-Axial Ratio of 0.10 with Depth of Embedment Equal to Zero

In this series of tests, the rectangular footing was loaded for Load Cases 1–5 with depth of embedment equal to zero. The AASHTO A3 soil used in the tests had an average dry unit weight, $\gamma_{dry,}$ in the range of 101.42 lb/ft^3 to 101.67 lb/ft^3 and average relative density, D_r in the range of 63.27% to 64.56% for the top soil layers where the failure surface was observed. The average peak friction angle from the direct shear test was estimated to be in the range of 32.47° to 32.70°. The model footing was tested at N = 40 G which results in a prototype footing width and length of 5 feet by 50 feet with the L/B ratio of 10. All eccentric loads were applied at a distance of B/6 (0.25 inches) from the center of the footing and inclined loads were applied at a lateral-to-axial ratio of 0.10 (5.7°). Each combined eccentric-inclined load test applied the same geometric loading conditions at the individual parts. The net bearing capacity for each test is presented in Figure 5.16. All eccentric and eccentric-inclined loading conditions used the effective width B' to determine the bearing pressure. Listed in Table 5.12 are the internal friction angles, unit weight, relative density, and net measured bearing capacities with percent differences to demonstrate repeatability for each test.

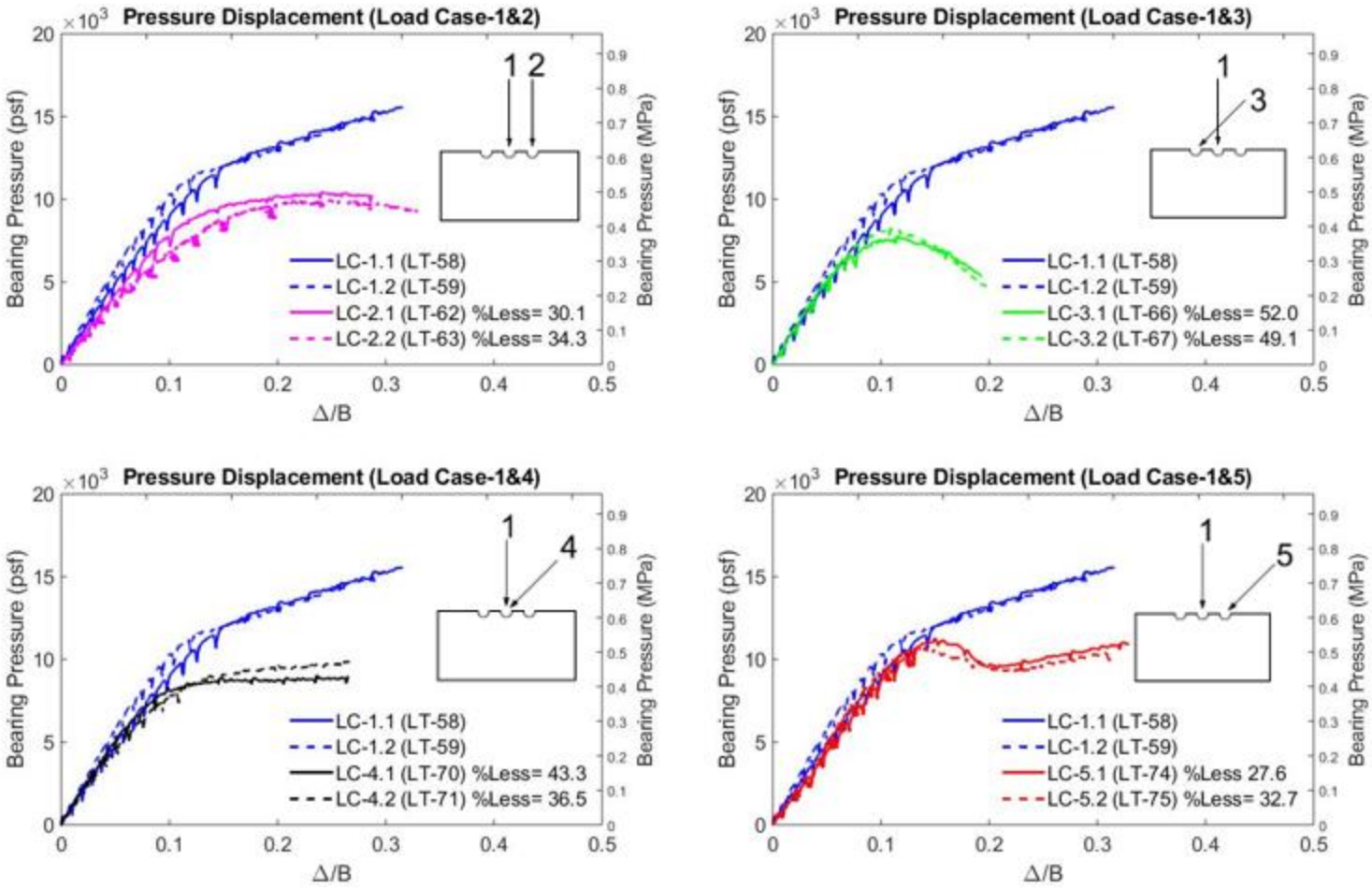

Figure 5.16 Net bearing pressure vs. displacement for Load Cases 1–5 with lateral-to-axial ratio = 0.1 and D_f = 0

Table 5.12 Summary of measured test parameters and results for L/B = 10 with lateral-to-axial ratio = 0.1 and D_f = 0 (MD)

Load Test	Load Case	ϕ (deg)	γ_{dry} (lb/ft^3)	D_r (%)	Δ/B	q_{net} Measured (psf)	Percent Difference (%)
LT-58	1	32.54	101.50	63.65	0.2315	13,303	7.41
LT-59	1	32.61	101.58	64.08	0.2105	12,352	
LT-62	2	32.56	101.53	63.8	0.2003	10,103	4.05
LT-63	2	32.63	101.59	64.16	0.2313	9,702	
LT-66	3	32.70	101.67	64.56	0.1207	7,502	1.74
LT-67	3	32.65	101.61	64.26	0.1155	7,634	
LT-70	4	32.65	101.61	64.25	0.1531	8,564	7.72
LT-71	4	32.47	101.42	63.27	0.1807	9,252	
LT-74	5	32.67	101.64	64.39	0.1689	10,918	8.17
LT-75	5	32.61	101.58	64.08	0.1478	10,061	

Table 5.13 presents the post-test plan view and failure surface views of the soil stratigraphy, which indicate general shear failure did occur.

Table 5.13 Post-test failure surface for lateral-to-axial ratio equal to 0.10 at embedment depth equal to zero

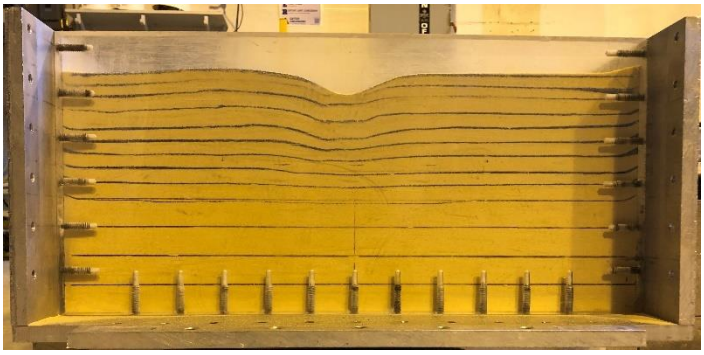

Load Case-1 (LT-58)

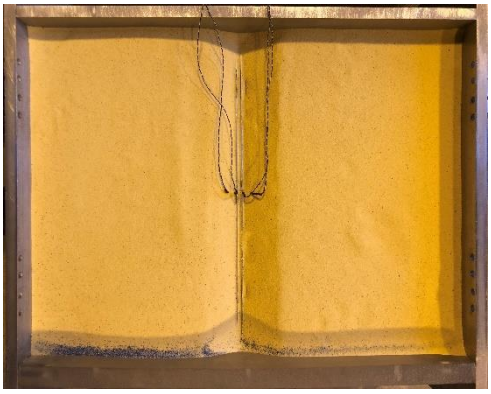

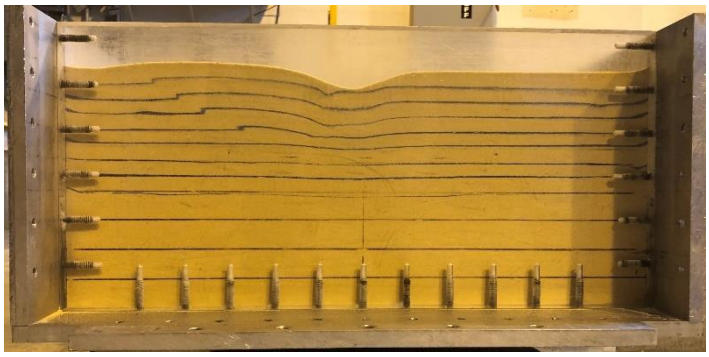

Load Case-1 (LT-59) $D_f = 0$

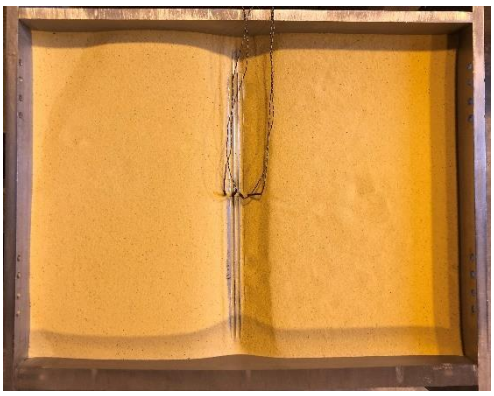

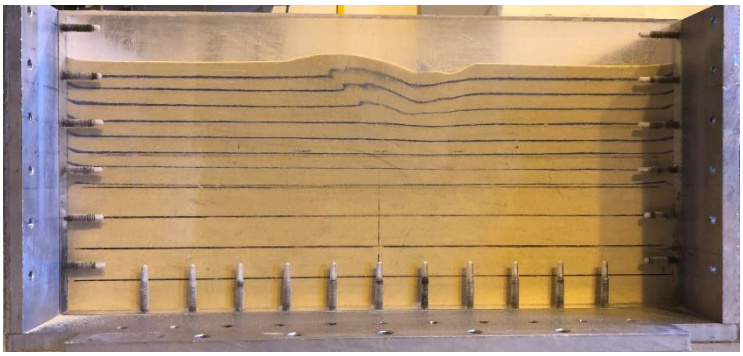

Load Case-2 (LT-62)

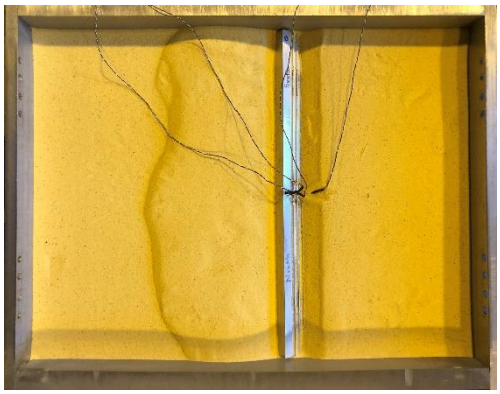

Load Case-2 (LT-63)

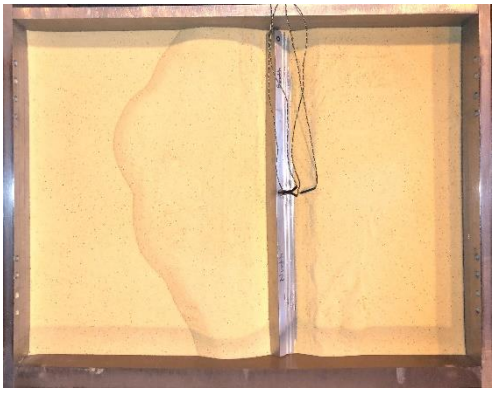

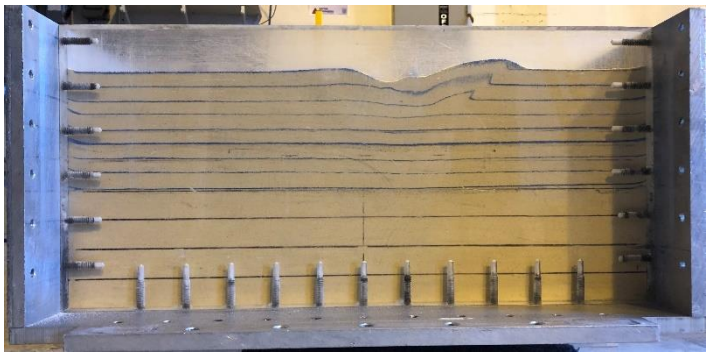

Load Case-3 (LT-66)

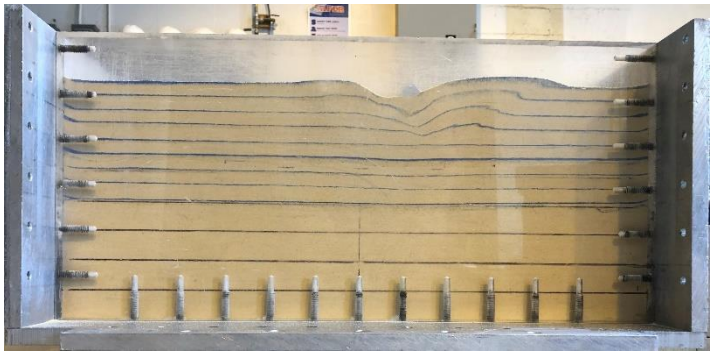

Load Case-3 (LT-67)

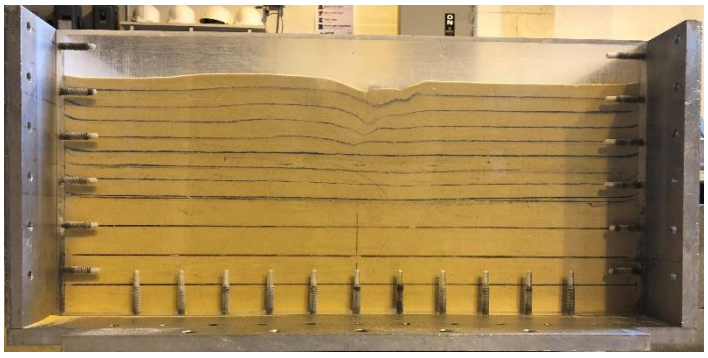

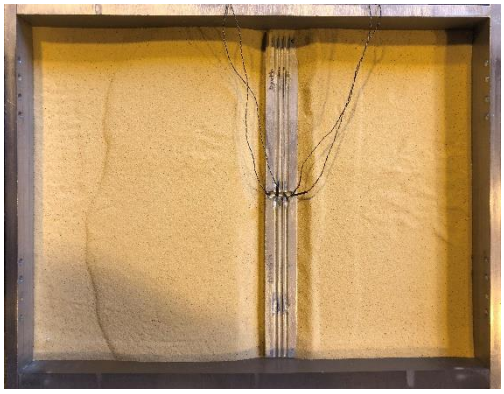

Load Case-4 (LT-70)

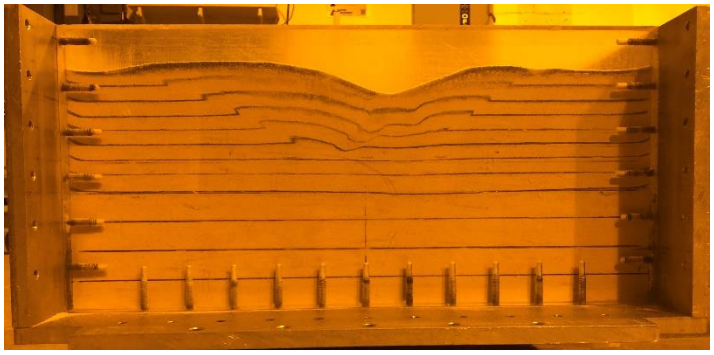

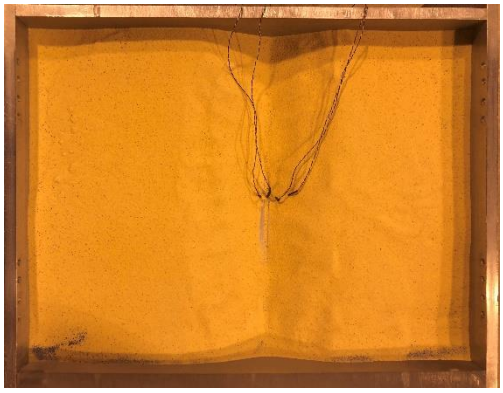

Load Case-4 (LT-71)

Load Case-5 (LT-74)

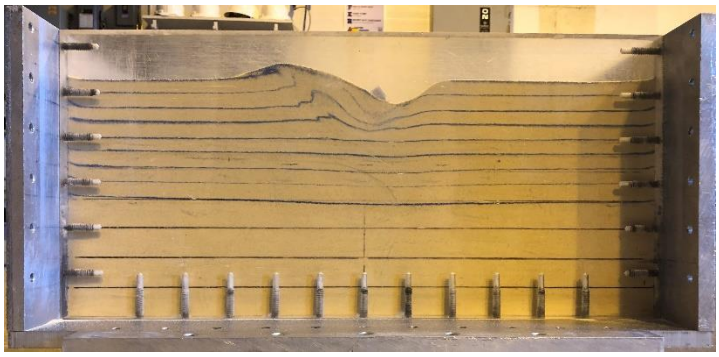

Load Case-5 (LT-75)

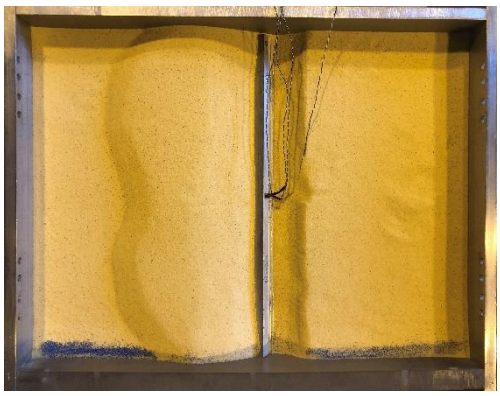

Summary of the post-test images of rupture surfaces:

- The observed rupture surface for Load Case-1 (LT-58 and LT-59) shows the maximum depth and length of the failure surface. Load Case-1 (LT-58 and LT-59) had a failure surface depth of 3.79 and 4.16 inches and lengths of 8.88 and 8.75 inches. The failure surface ruptured the top layer of soil on the left side of the footing as the test underwent concentric loading at the center of the footing.
- Load Case-2 (LT-62 and LT-63) had failure surface depth of 2.57 and 2.53 inches with lengths of 6.43 and 6.72 inches. Load Case-2 applies an eccentric load at a distance of B/6 from the center of the footing.
- Load Case-3 (LT-66 and LT-67) had failure surface depth of 2.07 and 2.09 inches with lengths of 7.44 and 7.60 inches. Both LT-66 and LT-67 observed a failure surface on the right side of the footing as the footing underwent inclined-eccentric loading (+) to the direction of the eccentricity.
- Load Case-4 (LT-70 and LT-71) had failure surface depth of 2.55 and 3.03 inches with lengths of 8.21 and 9.69 inches as the footing underwent inclined loading at the center of the footing. LT-71 mistakenly received additional loading at 1 G after the test was over. The hydraulic pump control valve was in the advance position instead of the retract position as

the test apparatus was being dissembled. This is the reason for the larger failure surface depth and length.

- Load Case-5 (LT-74 and LT-75) had failure surface depth of 2.54 and 2.52 inches with lengths of 7.51 and 7.17 inches. Both LT-74 and LT-75 observed a failure surface on the left side of the footing as the footing underwent inclined-eccentric loading (–) to the direction of the eccentricity.

The bearing pressure distribution observed by the miniature pressure transducers is presented for each load test in Figures 5.17 and 5.18. The loading position and orientation is displayed in each plot to illustrate how the pressure distribution is developed. The pressure sensors were position beneath the footing in sequential order (PS-1 through PS-4) from left to right at a spacing of 0.36 inches in model scale as previously stated.

Load Case-1 (LT-58 and LT-59) demonstrates a non-uniform pressure distribution with an increasing radial shape towards the center of the footing. This pressure profile is consistent with previous numerical modeling research presented by Loukidis et al. (2008) for sand as shown in Figure 5.6. Load Case-2 (LT-62 and LT-63), Load Case-3 (LT-66 and LT-67), Load Case-4 (LT-71), and Load Case-5 (LT-74 and LT-75) demonstrates a trapezoidal shape with increasing pressure on the side of eccentricity, inclination or eccentric-inclined loading. The trapezoidal shift in pressure towards the side of eccentric or inclined loading is also present in Loukidis et al. (2008) analysis. Load Case-4 (LT-70) demonstrates a non-uniform pressure distribution with an increasing radial shape towards the center of the footing similar to Load Case-1. Similar to the results presented in the pressure displacement plots, Load Case-1 reports the highest bearing pressure and Load Case-3 reports the lowest bearing pressures.

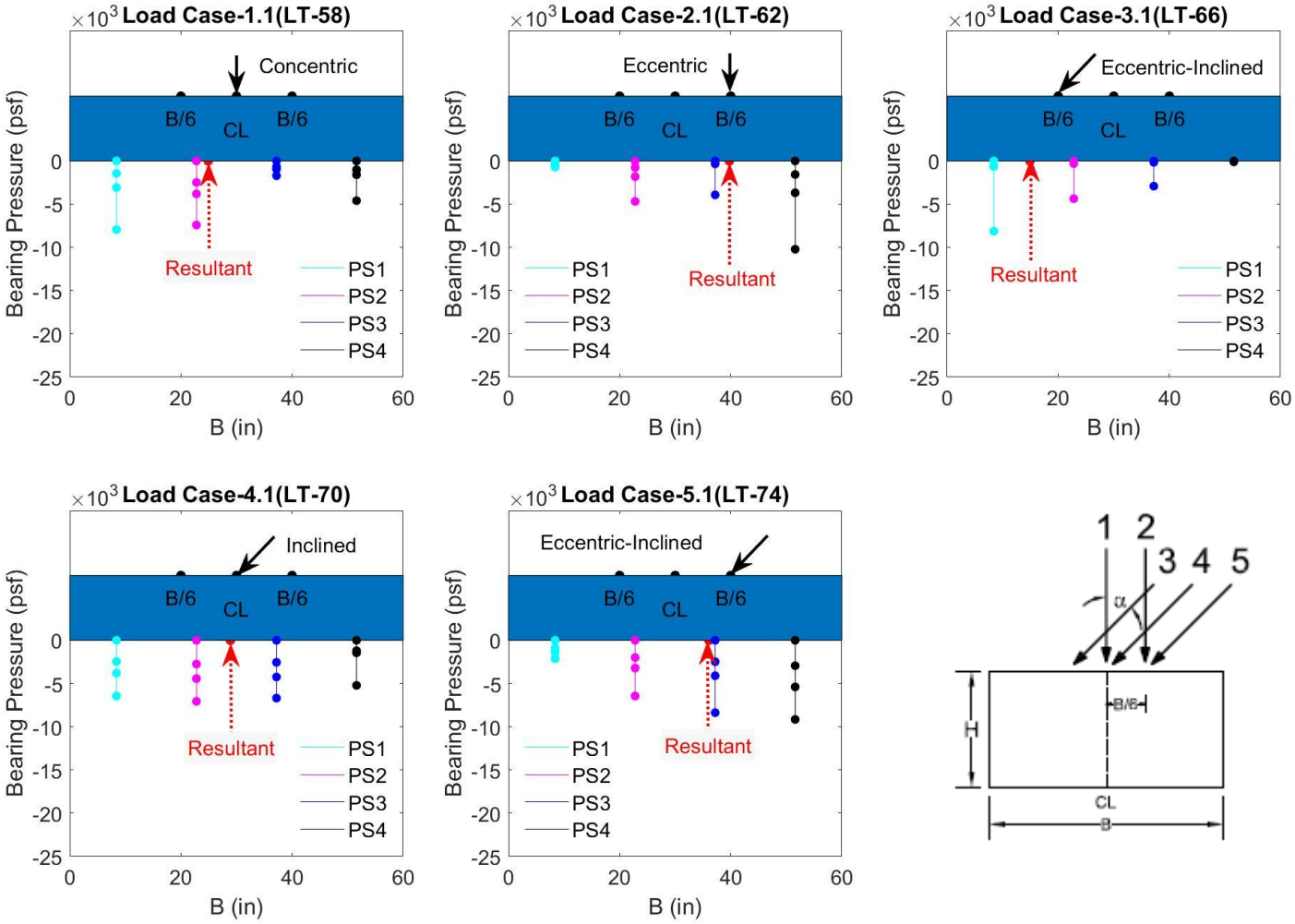

Figure 5.17 Bearing pressure distribution for Load Cases 1–5 with lateral-to-axial ratio = 0.1 and D_f = 0

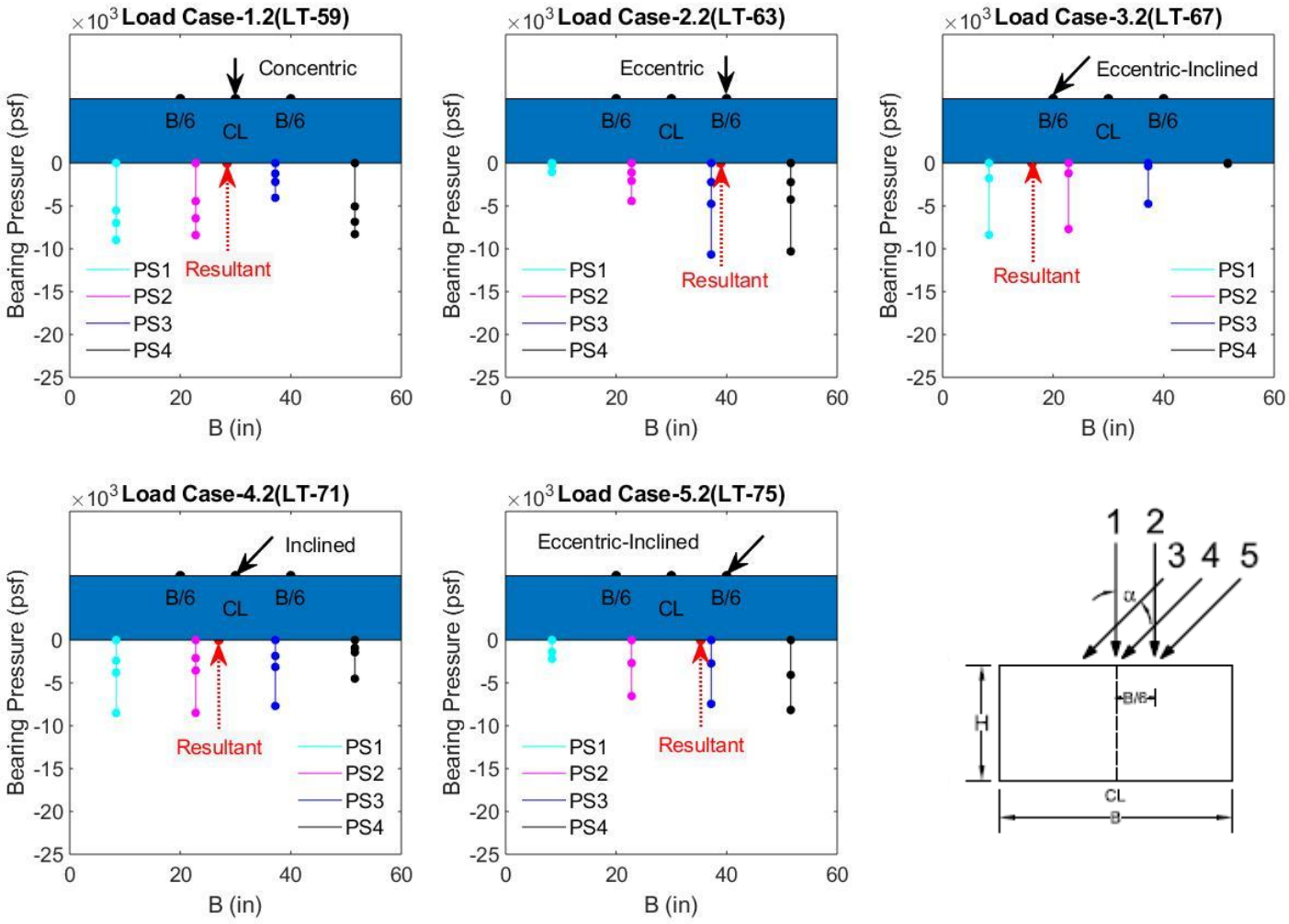

Figure 5.18 Bearing pressure distribution for Load Cases 1–5 with lateral-to-axial ratio = 0.1 and D_f = 0

5.2.2 Lateral-to-Axial Ratio of 0.10 with Depth of Embedment Equal to 0.5B

In this series of tests, the rectangular footing was loaded for Load Cases 1–5 with depth of embedment equal to 0.5B. The AASHTO A3 soil used in the test had an average dry unit weight, $\gamma_{dry,}$ in the range of 101.41 lb/ft^3 to 101.54 lb/ft^3 and average relative density, D_r in the range of 63.17% to 64.85% for the top soil layers where the failure surface was observed. The average peak friction angle from the direct shear test was estimated to be in the range of 32.45° to 32.67°. The model footing was tested at N = 40 G which results in a prototype footing width and length of 5 feet by 50 feet with the L/B ratio of 10. All eccentric loads were applied at a distance of B/6 (0.25 inches) from the center of the footing and inclined loads were applied at a lateral-to-axial ratio of 0.10 (5.7°). The net bearing capacity for each test are presented in Figures 5.19. All eccentric and eccentric-inclined loading conditions used the effective width B' to determine the bearing pressure. Listed in Table 5.14 are the internal friction angles, unit weight, relative density, and net measured bearing capacities with percent differences to demonstrate repeatability for each test.

Table 5.14 Summary of measured test parameters and results for L/B = 10 with lateral-to-axial ratio = 0.1 and D_f = 0.5B (MD)

Load Test	Load Case	ϕ (deg)	γ_{dry} (lb/ft^3)	D_r (%)	Δ/B	q_{net} Measured (psf)	Percent Difference (%)
LT-60	1	32.56	101.52	63.79	0.2171	17,104	1.63
LT-61	1	32.49	101.45	63.40	0.2042	16,827	
LT-64	2	32.58	101.54	63.88	0.2432	15,252	1.29
LT-65	2	32.67	101.63	64.37	0.2554	15,450	
LT-68	3	32.64	101.61	64.23	0.1624	8,880	5.45
LT-69	3	32.45	101.41	63.17	0.1981	9,377	
LT-72	4	32.51	101.47	63.52	0.1204	12,503	5.58
LT-73	4	32.61	101.57	64.03	0.142	13,221	
LT-76	5	32.57	101.54	63.85	0.2525	16,390	7.99
LT-77	5	32.55	101.51	63.74	0.2016	15,130	

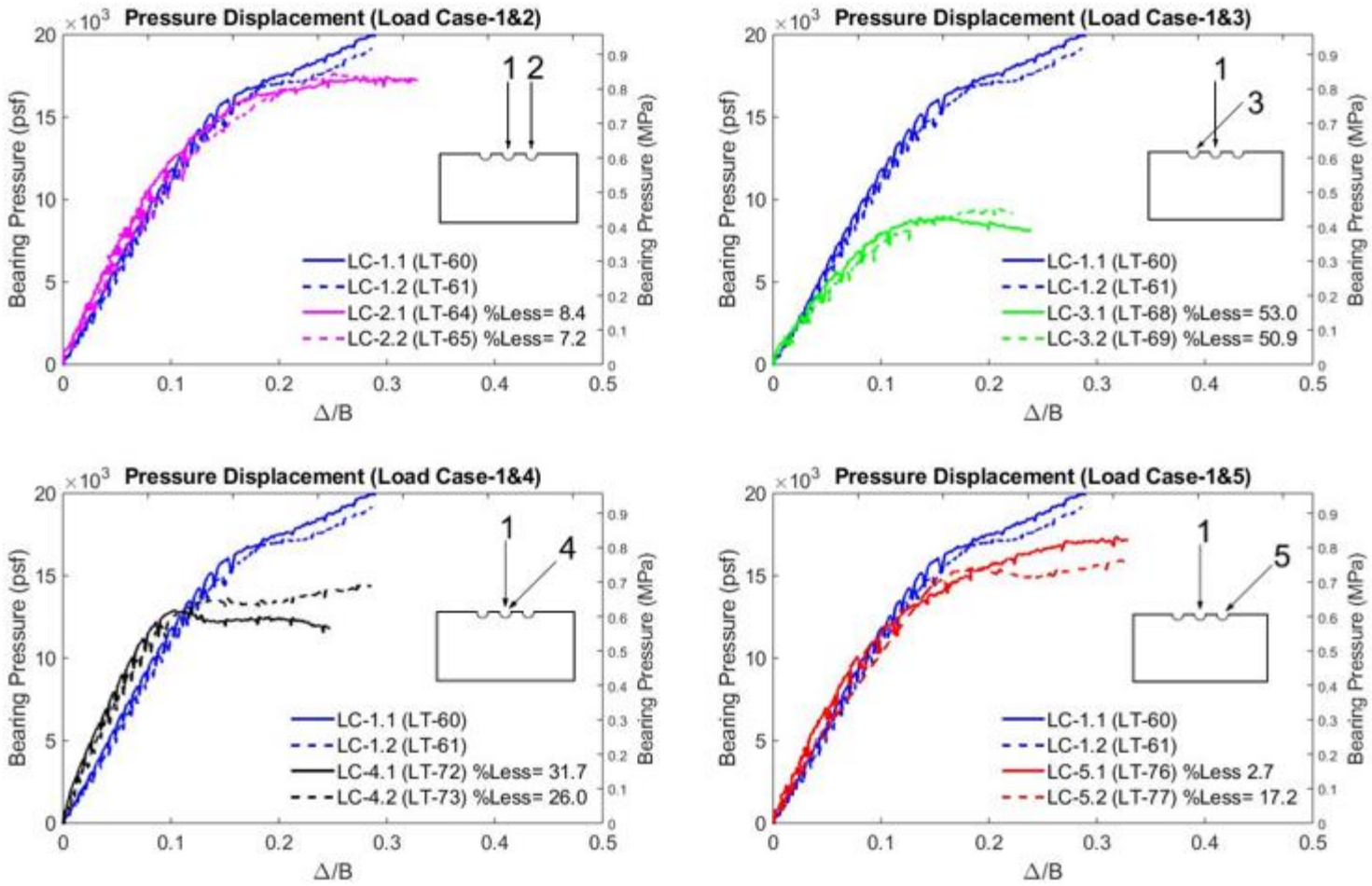

Figure 5.19 Net bearing pressure vs. displacement for Load Cases 1–5 with lateral-to-axial ratio = 0.1 and D_f = 0.5B

Table 5.15 presents the post-test plan view and failure surface views of the soil stratigraphy, which indicate general shear failure did occur. The failure surface ruptured the ground surface in all cases.

Table 5.15 Post-test failure surface for lateral-to-axial ratio equal to 0.10 at embedment depth equal to 0.5B

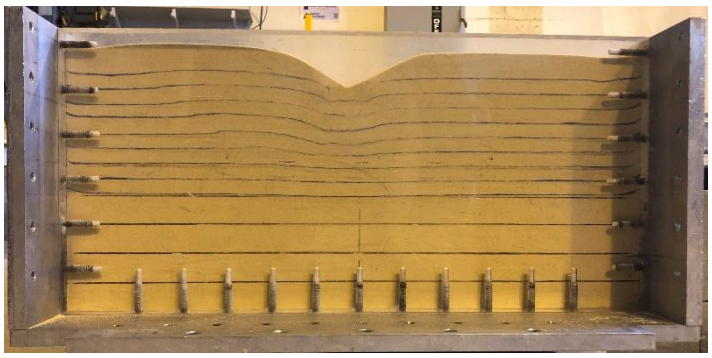 Load Case-1 (LT-60)	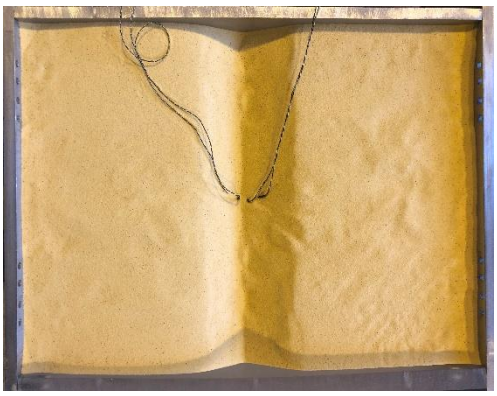
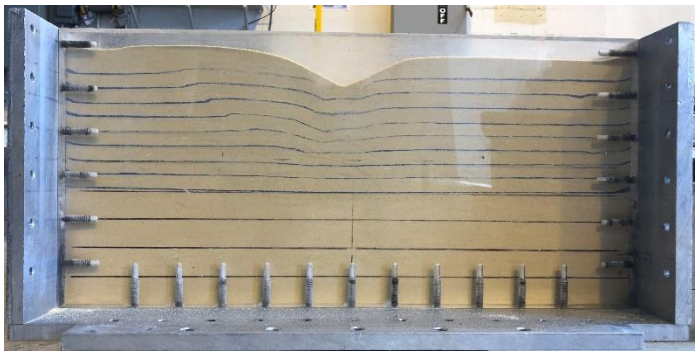 Load Case-1 (LT-61) $D_f = 0$	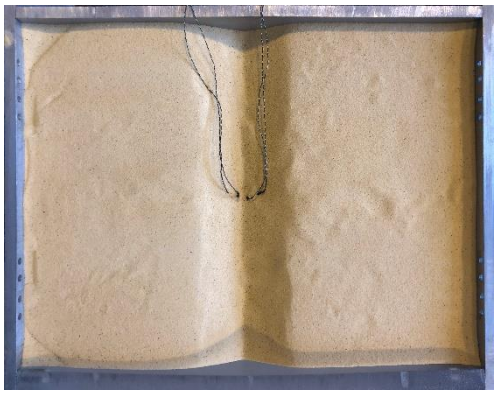
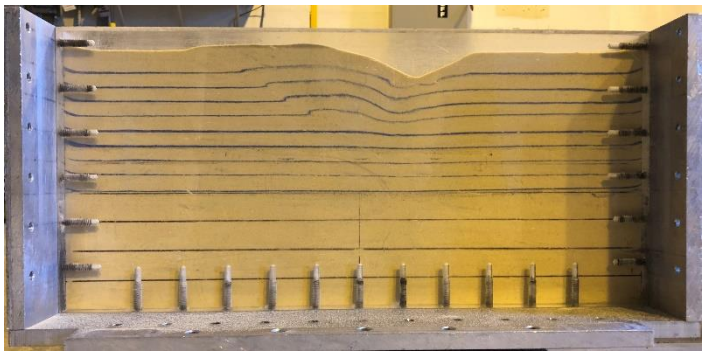 Load Case-2 (LT-64)	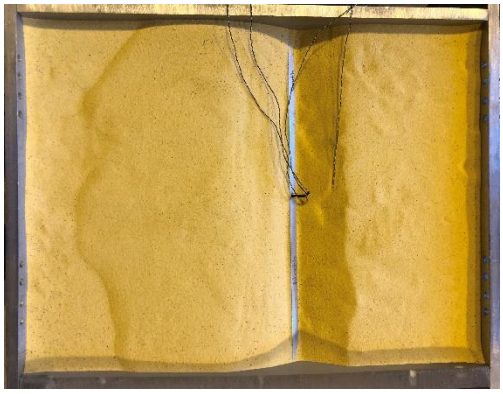

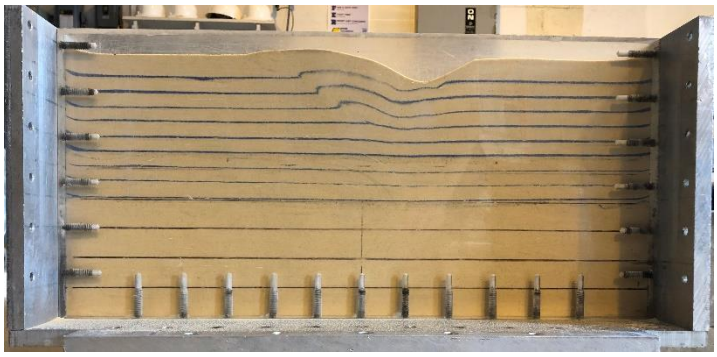 Load Case-2 (LT-65)	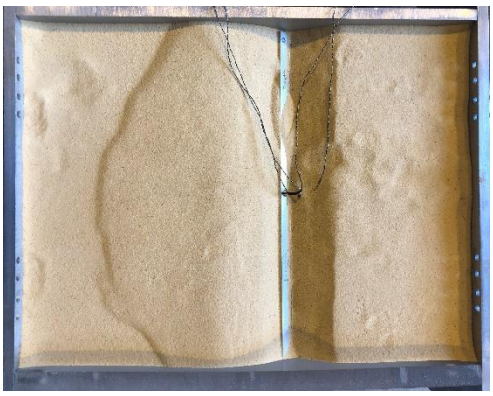
 Load Case-3 (LT-68)	
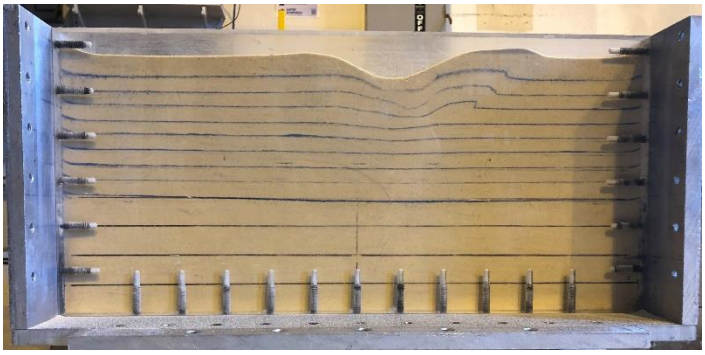 Load Case-3 (LT-69)	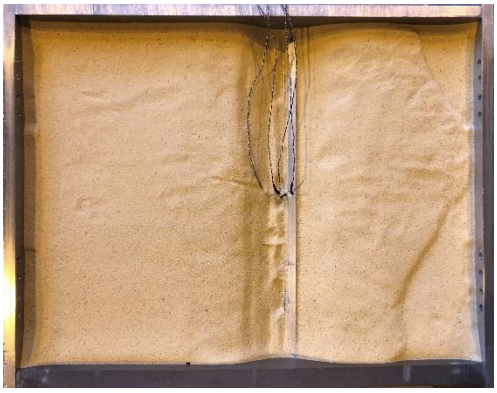
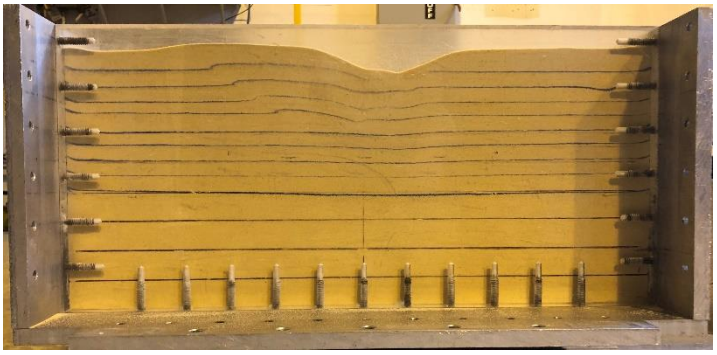 Load Case-4 (LT-72)	

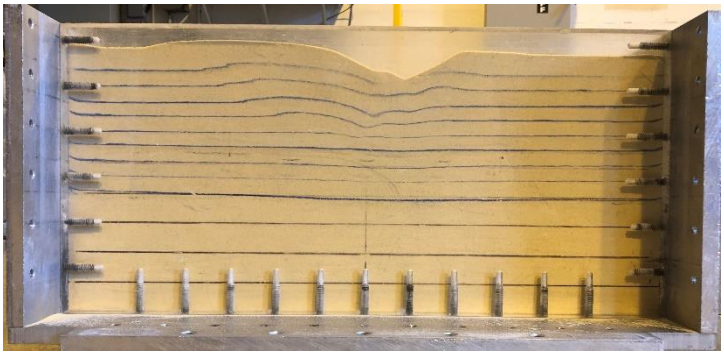 Load Case-4 (LT-73)	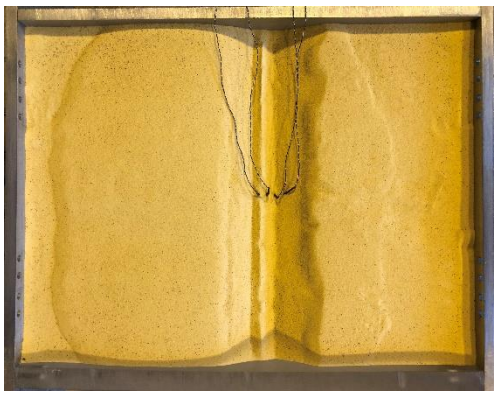
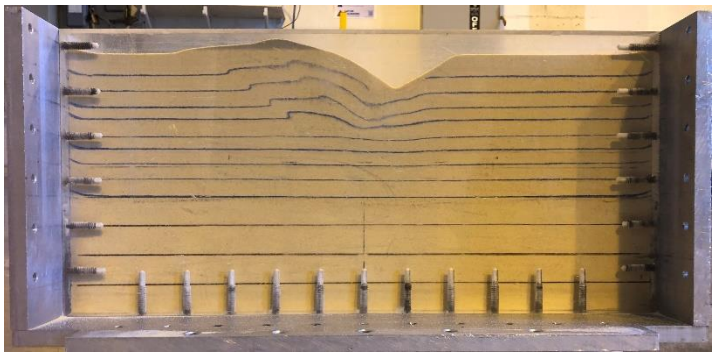 Load Case-5 (LT-76)	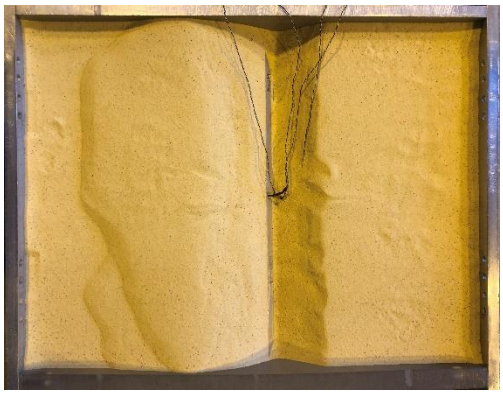
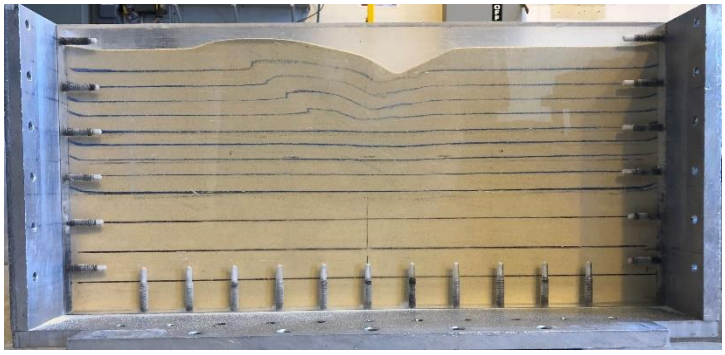 Load Case-5 (LT-77)	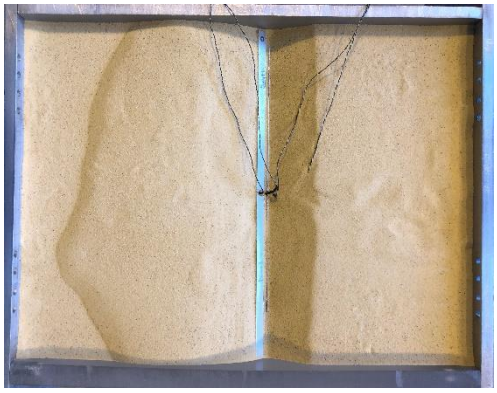

Summary of the post-test images of rupture surfaces:

- The observed rupture surface for Load Case-1 shows the maximum depth and length of the failure surface. Load Case-1 (LT-60 and LT-61) had a failure surface depth of 4.92 inches each and lengths of 9.29 and 9.14 inches. The failure surface ruptured the top layer of soil on the left side of the footing as the test underwent concentric loading at the center of the

footing.

- Load Case-2 (LT-64 and LT-65) had failure surface depth of 3.39 and 2.87 inches with lengths of 9.51 and 8.33 inches. Load Case-2 applies an eccentric load at a distance of B/6 from the center of the footing.
- Load Case-3 (LT-68 and LT-69) had failure surface depth of 2.81 and 2.80 inches with lengths of 7.98 and 7.73 inches. Both LT-68 and LT-69 observed a failure surface on the right side of the footing as the footing underwent inclined-eccentric loading (+) to the direction of the eccentricity.
- Load Case-4 (LT-72 and LT-73) had failure surface depth of 3.31 and 3.30 inches with lengths of 9.21 and 9.30 inches as the footing underwent inclined loading at the center of the footing.
- Load Case-5 (LT-76 and LT-77) had failure surface depth of 3.30 and 3.29 inches with lengths of 8.33 and 9.02 inches. Both LT-74 and LT-75 observed a failure surface on the left side of the footing as the footing underwent inclined-eccentric loading (–) to the direction of the eccentricity.

The bearing pressure distribution observed by the miniature pressure transducers is presented for each load test in Figures 5.20 and 5.21. The loading position and orientation is displayed in each plot to illustrate how the pressure distribution is developed. The pressure sensors were position beneath the footing in sequential order (PS-1 through PS-4) from left to right at a spacing of 0.36 inches in model scale as previously stated.

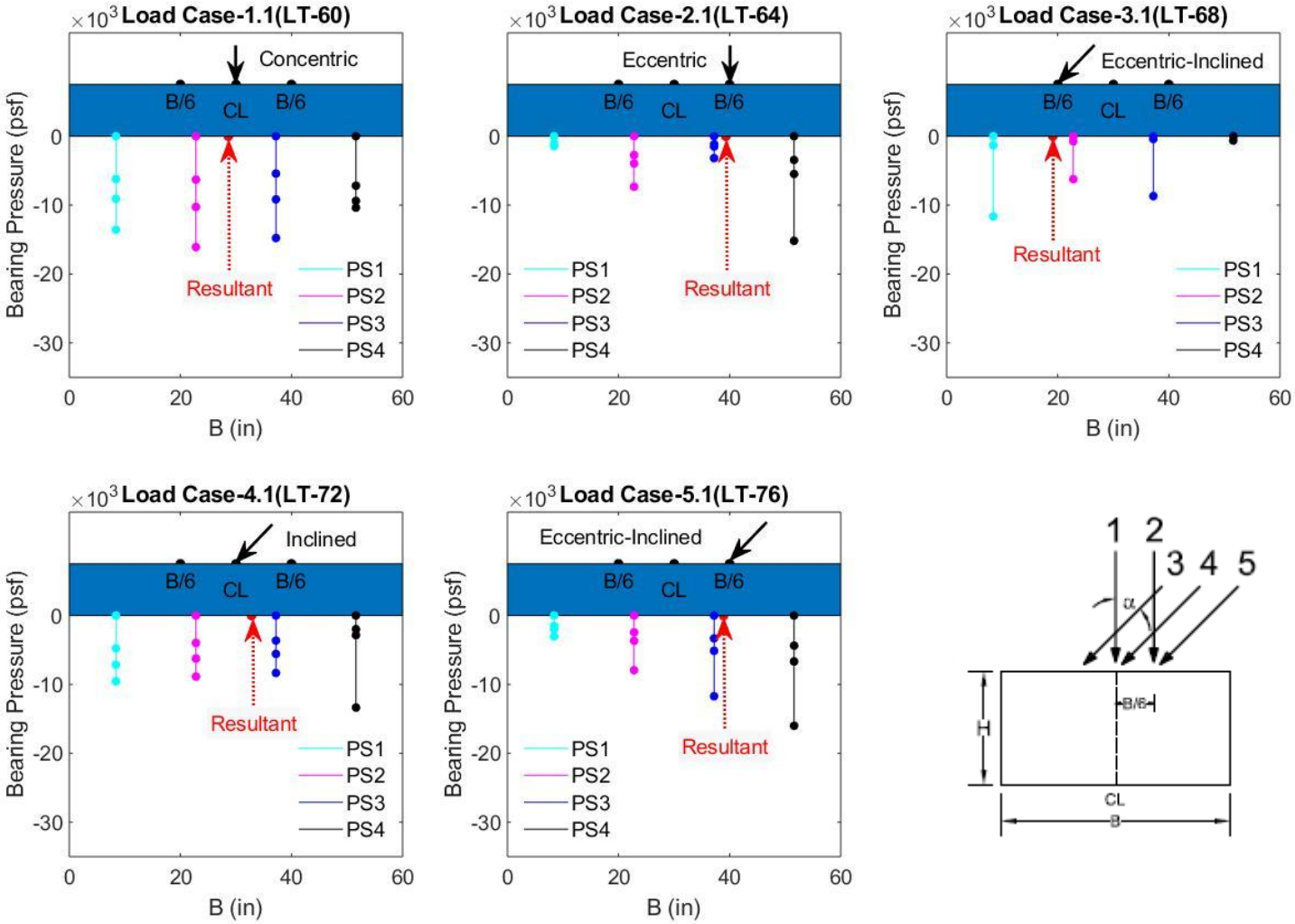

Figure 5.20 Bearing pressure distribution for Load Cases 1–5 with lateral-to-axial ratio = 0.1 and D_f = 0.5B

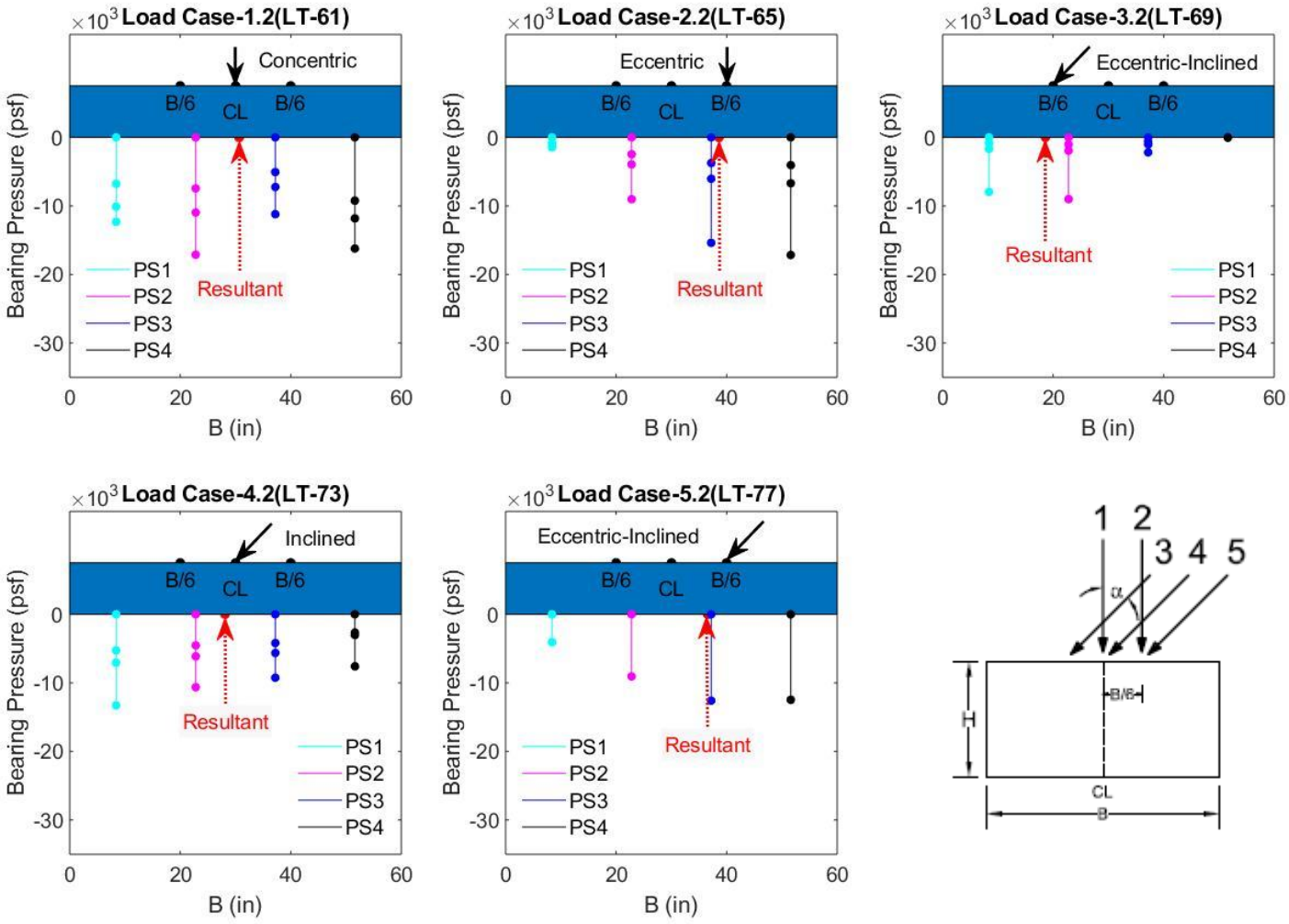

Figure 5.21 Bearing pressure distribution for Load Cases 1–5 with lateral-to-axial ratio = 0.1 and D_f = 0.5B

Load Case-1 (LT-60 and LT-61) demonstrates a non-uniform pressure distribution with an increasing radial shape towards the center of the footing. This pressure profile is consistent with previous numerical modeling research presented by Loukidis et al. (2008) for sand as shown in Figure 5.6. Load Case-2 (LT-64 and LT-65), Load Case-3 (LT-68 and LT-69), Load Case-4 (LT-72 and LT-73), and Load Case-5 (LT-76 and LT-77) demonstrates a trapezoidal shape with increasing pressure on the side of eccentricity, inclination or eccentric-inclined loading. The trapezoidal shift in pressure towards the side of eccentric or inclined loading is also present in Loukidis et al. (2008) analysis.

5.2.3 Lateral-to-Axial Ratio of 0.25 with Depth of Embedment Equal to Zero

In this series of tests, the rectangular footing was loaded for Load Cases 1–5 with depth of embedment equal to zero. The AASHTO A3 soil used in the tests had an average dry unit weight, $\gamma_{dry,}$ in the range of 101.43 lb/ft^3 to 101.59 lb/ft^3 and average relative density, D_r in the range of 63.32% to 64.16% for the top soil layers where the failure surface was observed. The average peak friction angle from the direct shear test was estimated to be in the range of 32.48° to 32.63°. The model footing was tested at N = 40 G which results in a prototype footing width and length of 5 feet by 50 feet with the L/B ratio of 10. All eccentric loads were applied at a distance of B/6 (0.25 inches) from the center of the footing and inclined loads were applied at a lateral-to-axial ratio of 0.25 (14.0°). The combined eccentric-inclined load test applied the same geometric loading conditions as the individual parts. The net bearing capacity for each test is presented in Figures 5.22. All eccentric and eccentric-inclined loading conditions used the effective width B' to determine the bearing pressure. Listed in Table 5.16 are the internal friction angles, unit weight, relative density, and net measured bearing capacities with percent differences to demonstrate repeatability for each test.

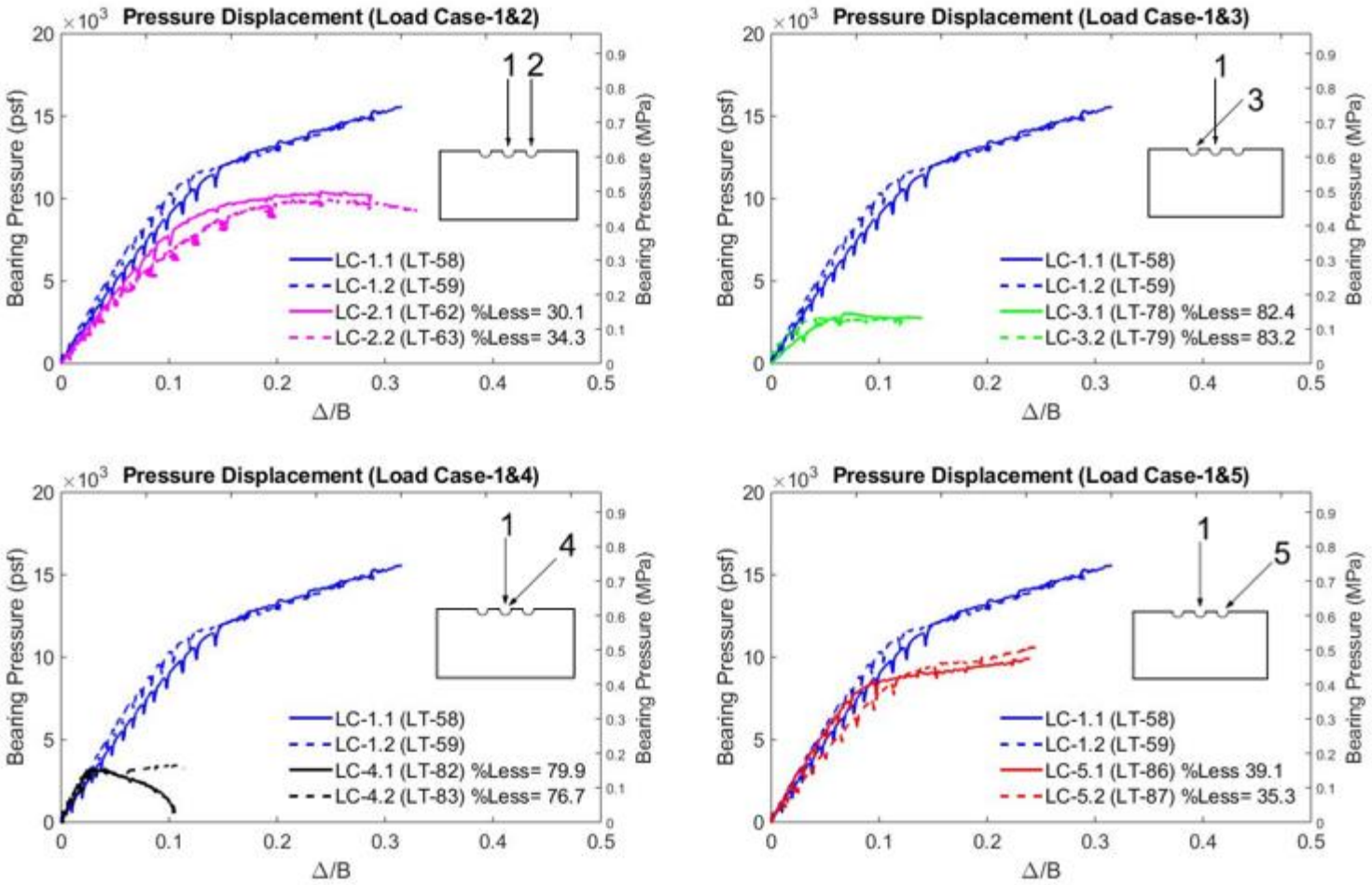

Figure 5.22 Net bearing pressure vs. displacement for Load Cases 1–5 with lateral-to-axial ratio = 0.25 and $D_f = 0$

Table 5.16 Summary of measured test parameters and results for L/B = 10 with lateral-to-axial ratio = 0.25 and D_f = 0 (MD)

Load Test	Load Case	ϕ (deg)	γ_{dry} (lb/ft^3)	D_r (%)	Δ/B	q_{net} Measured (psf)	Percent Difference (%)
LT-58	1	32.54	101.50	63.65	0.2315	13,303	7.41
LT-59	1	32.61	101.58	64.08	0.2105	12,352	
LT-62	2	32.56	101.53	63.8	0.2003	10,103	4.05
LT-63	2	32.63	101.59	64.16	0.2313	9,702	
LT-78	3	32.51	101.47	63.53	0.0828	2,829	9.75
LT-79	3	32.55	101.51	63.74	0.1011	2,566	
LT-82	4	32.48	101.43	63.32	0.0451	3,239	1.41
LT-83	4	32.54	101.51	63.69	0.0875	3,285	
LT-86	5	32.55	101.51	63.74	0.1548	9,143	1.43
LT-87	5	32.54	101.5	63.66	0.1576	9,275	

Table 5.17 presents the post-test plan view and failure surface views of the soil stratigraphy, which indicate general shear failure did occur. The failure surface ruptured the ground surface in all cases. Load Case-1 (LT-58 and LT-59) and Load Case-2 (LT-62 and LT-63) were previously presented in Section 5.3.1 and are shown again for comparison with Load Cases 3-5 at L/A ratio equal to 0.25.

Table 5.17 Post-test failure surface for lateral-to-axial ratio equal to 0.25 at embedment depth equal to zero

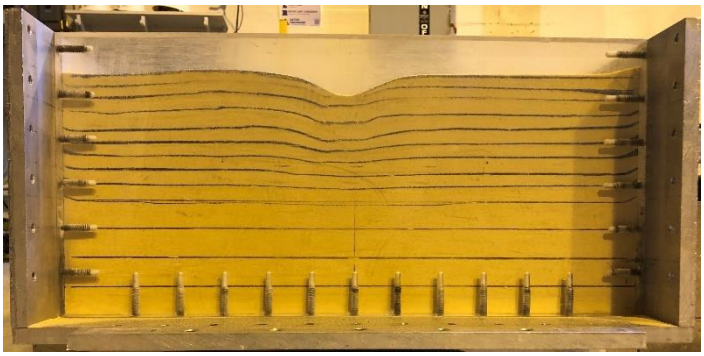

Load Case-1 (LT-58)

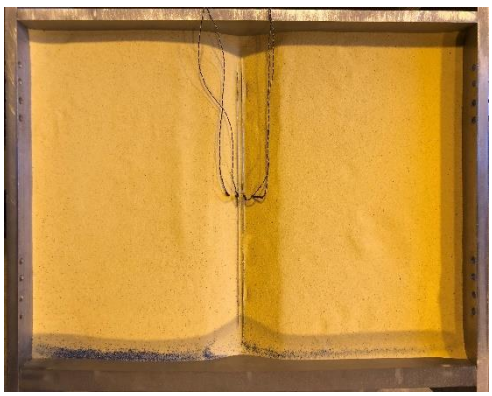

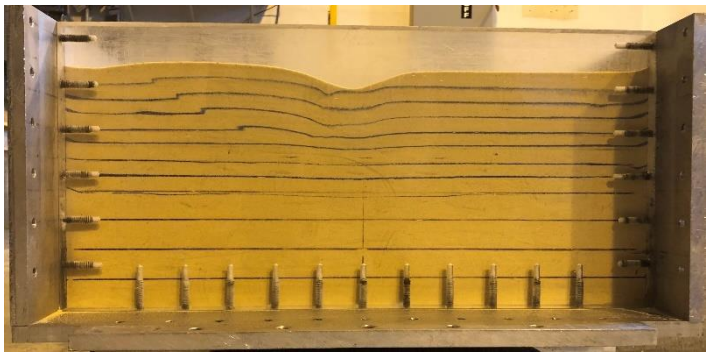 Load Case-1 (LT-59) $D_f = 0$	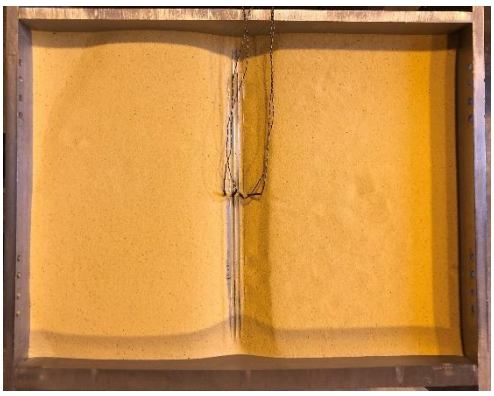
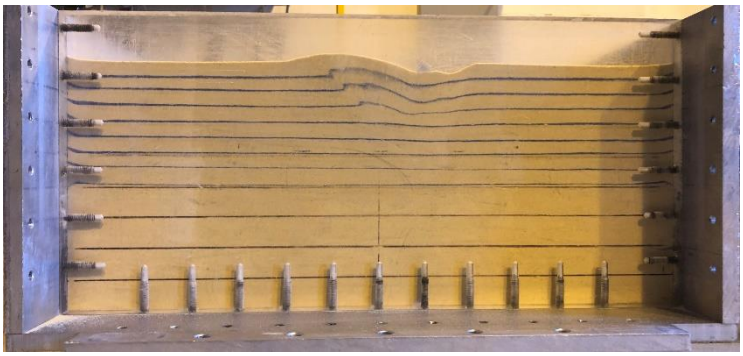 Load Case-2 (LT-62)	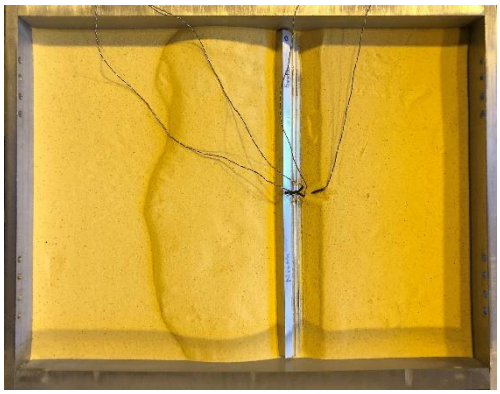
 Load Case-2 (LT-63)	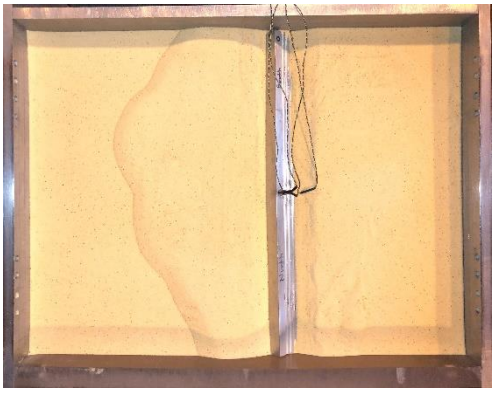
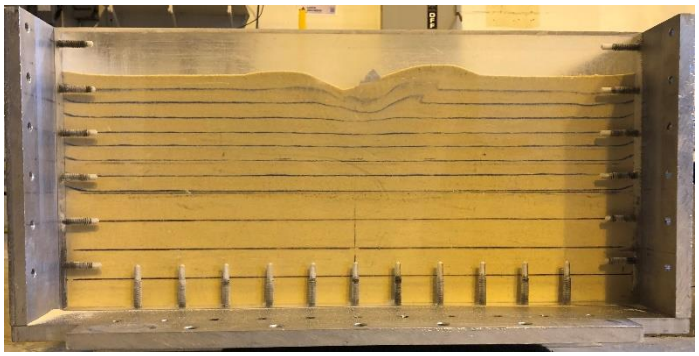 Load Case-3 (LT-78)	

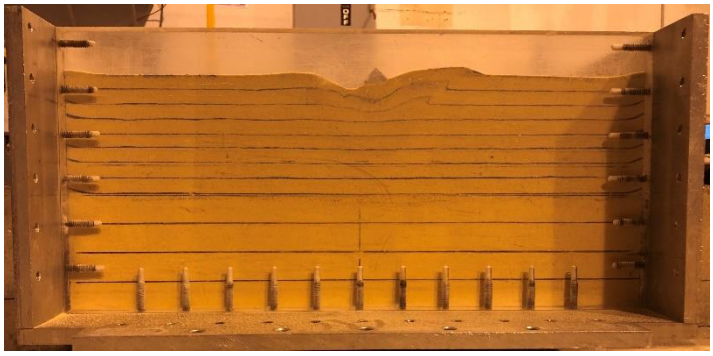

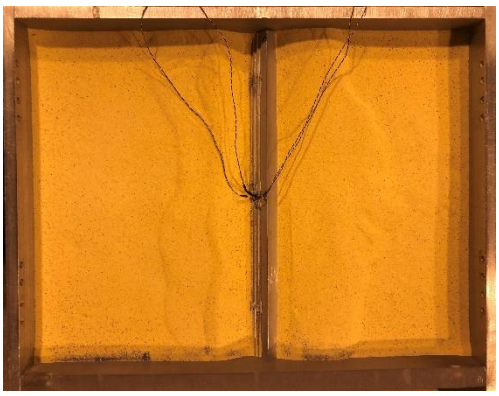

Load Case-3 (LT-79)

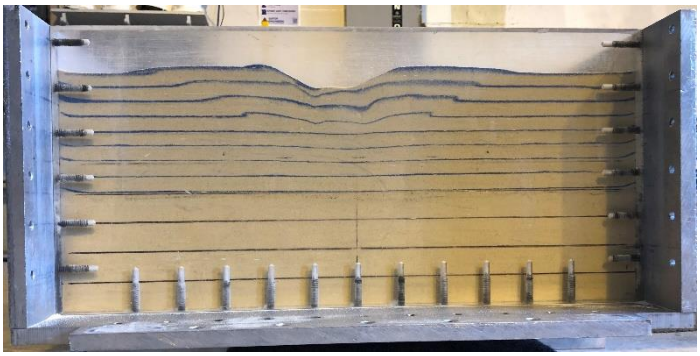

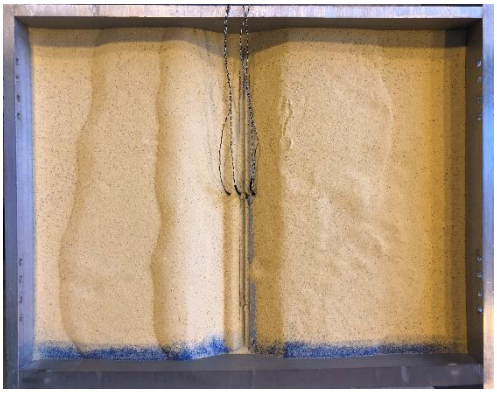

Load Case-4 (LT-82)

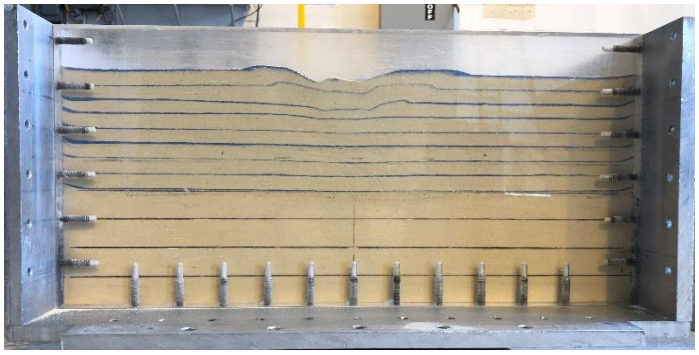

Load Case-4 (LT-83)

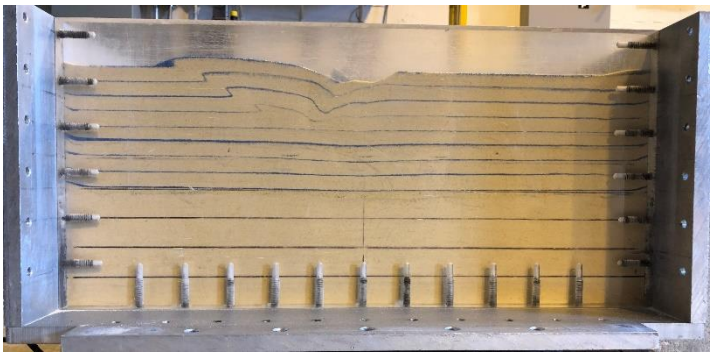

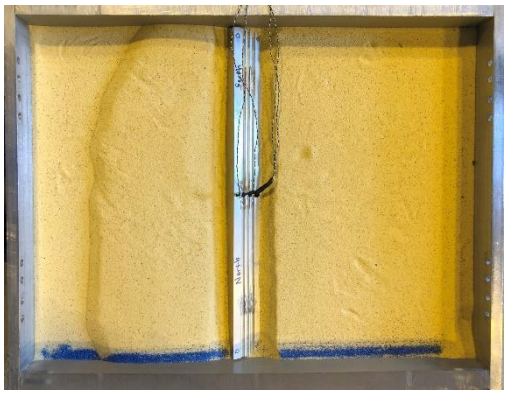

Load Case-5 (LT-86)

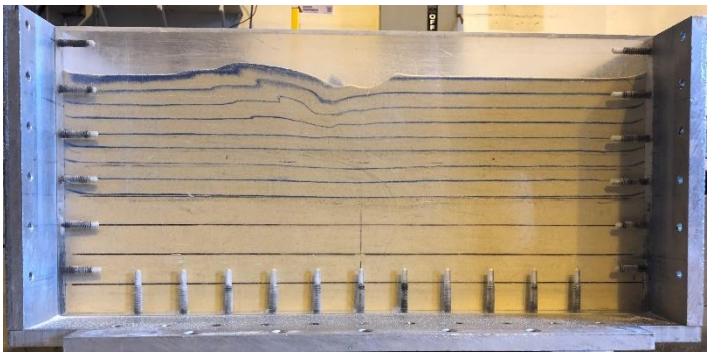

Load Case-5 (LT-87)

Summary of the post-test images of rupture surfaces:

- The observed rupture surface for Load Case-1 (LT-58 and LT-59) shows the maximum depth and length of the failure surface. Load Case-1 (LT-58 and LT-59) had a failure surface depth of 3.79 and 4.16 inches and lengths of 8.88 and 8.75 inches. The failure surface ruptured the top layer of soil on the left side of the footing as the test underwent concentric loading at the center of the footing.
- Load Case-2 (LT-62 and LT-63) had failure surface depth of 2.57 and 2.53 inches with lengths of 6.43 and 6.72 inches. Load Case-2 applies an eccentric load at a distance of B/6 from the center of the footing.
- Load Case-3 (LT-78 and LT-79) had failure surface depth of 2.01 and 1.87 inches with lengths of 5.16 and 5.40 inches. Both LT-78 and LT-79 observed a failure surface on the right side of the footing as the footing underwent inclined-eccentric loading (+) to the direction of the eccentricity.
- Load Case-4 (LT-82 and LT-83) had failure surface depth of 2.51 and 2.52 inches with lengths of 7.69 and 5.89 inches as the footing underwent inclined loading at the center of the footing.
- Load Case-5 (LT-86 and LT-87) had failure surface depth of 3.08 and 3.09 inches with

lengths of 6.74 and 7.30 inches. Both LT-86 and LT-87 observed a failure surface on the left side of the footing as the footing underwent inclined-eccentric loading (–) to the direction of the eccentricity.

The bearing pressure distribution observed by the miniature pressure transducers is presented for each load test in Figures 5.23 and 5.24. The loading position and orientation is displayed in each plot to illustrate how the pressure distribution is developed. The pressure sensors were positioned beneath the footing in sequential order (PS-1 through PS-4) from left to right at a spacing of 0.36 inches in model scale as previously stated.

Load Case-1 (LT-58 and LT-59) demonstrates a non-uniform pressure distribution with an increasing radial shape towards the center of the footing.

Load Case-2 (LT-62 and LT-63), Load Case-3 (LT-78 and LT-79), Load Case-4 (LT-82 and LT-83), and Load Case-5 (LT-86 and LT-87) demonstrates a trapezoidal shape with increasing pressure on the side of eccentricity, inclination or eccentric-inclined loading. The trapezoidal shift in pressure towards the side of eccentric or inclined loading is also present in Loukidis et al. (2008) analysis.

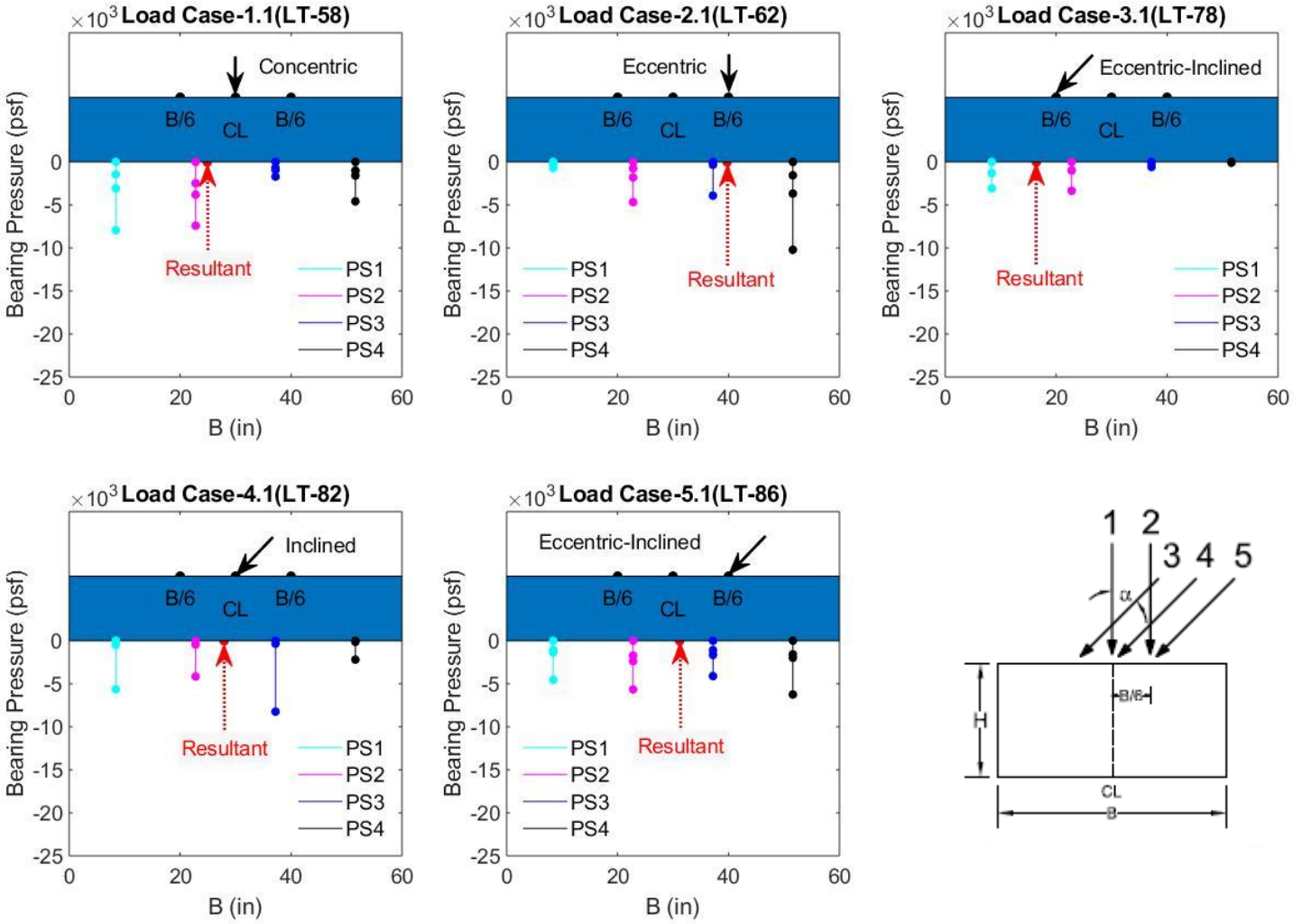

Figure 5.23 Bearing pressure distribution for Load Cases 1–5 with lateral-to-axial ratio = 0.25 and D_f = 0

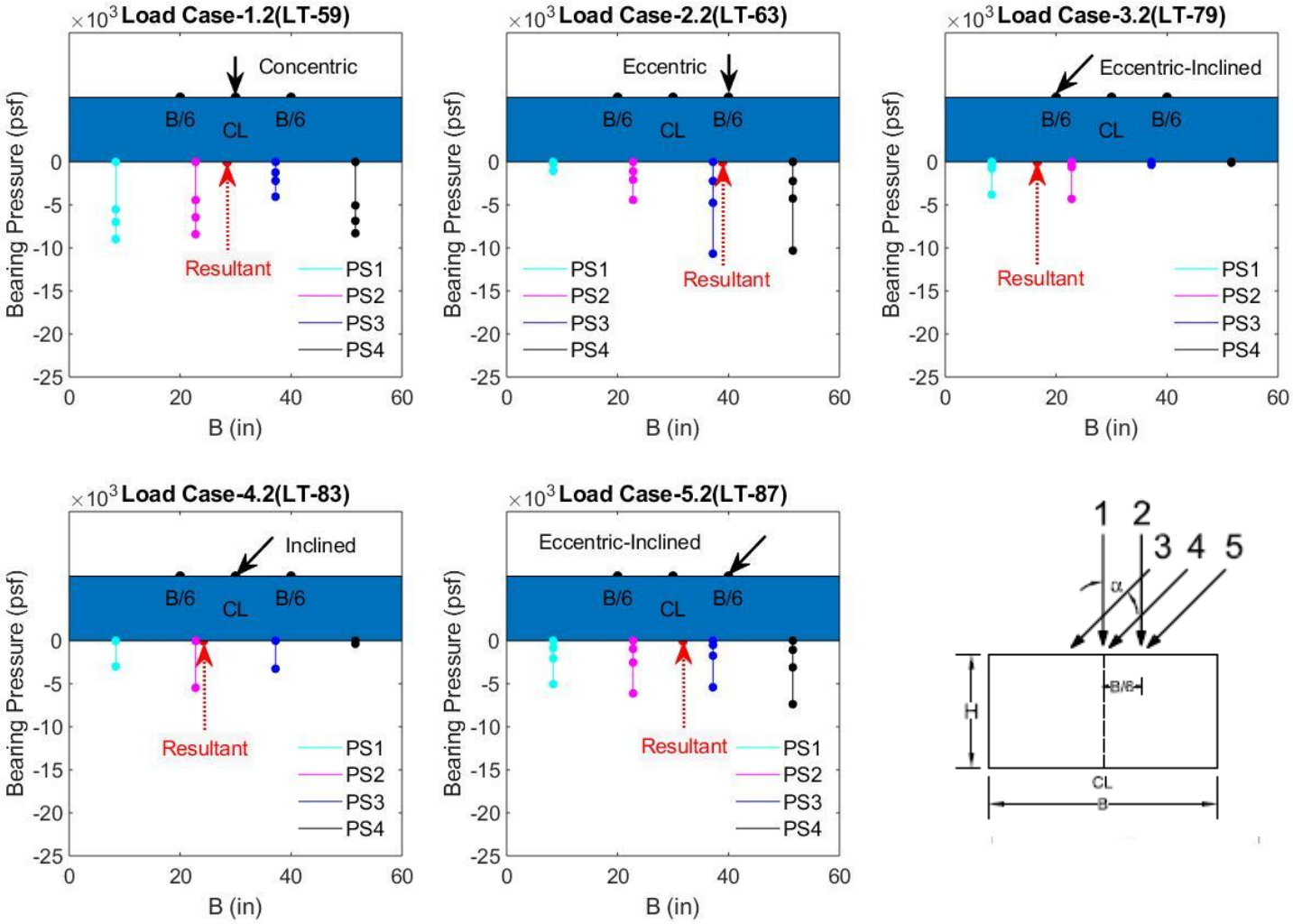

Figure 5.24 Bearing pressure distribution for Load Cases 1–5 with lateral-to-axial ratio = 0.25 and $D_f = 0$

5.2.4 Lateral-to-Axial Ratio of 0.25 with Depth of Embedment Equal to 0.5B

In this series of tests, the rectangular footing was loaded for Load Cases 1–5 with depth of embedment equal to 0.5B. The AASHTO A3 soil used in the tests had an average dry unit weight, $\gamma_{dry,}$ in the range of 101.44 lb/ft^3 to 101.63 lb/ft^3 and average relative density, D_r in the range of 63.34% to 64.37% for the top soil layers where the failure surface was observed. The average peak friction angle from the direct shear test was estimated to be in the range of 32.48° to 32.67°. The model footing was tested at N = 40 G which results in a prototype footing width and length of 5 feet by 50 feet with the L/B ratio of 10. All eccentric loads were applied at a distance of B/6 (0.25 inches) from the center of the footing and inclined loads were applied at a lateral-to-axial ratio of 0.25 (14.0°). The combined eccentric-inclined load test applied the same geometric loading conditions as the individual parts. The net bearing capacity for each test is presented in Figures 5.25. All eccentric and eccentric-inclined loading conditions used the effective width B' to determine the bearing pressure. Listed in Table 5.18 are the internal friction angles, unit weight, relative density, and net measured bearing capacities with percent differences to demonstrate repeatability for each test.

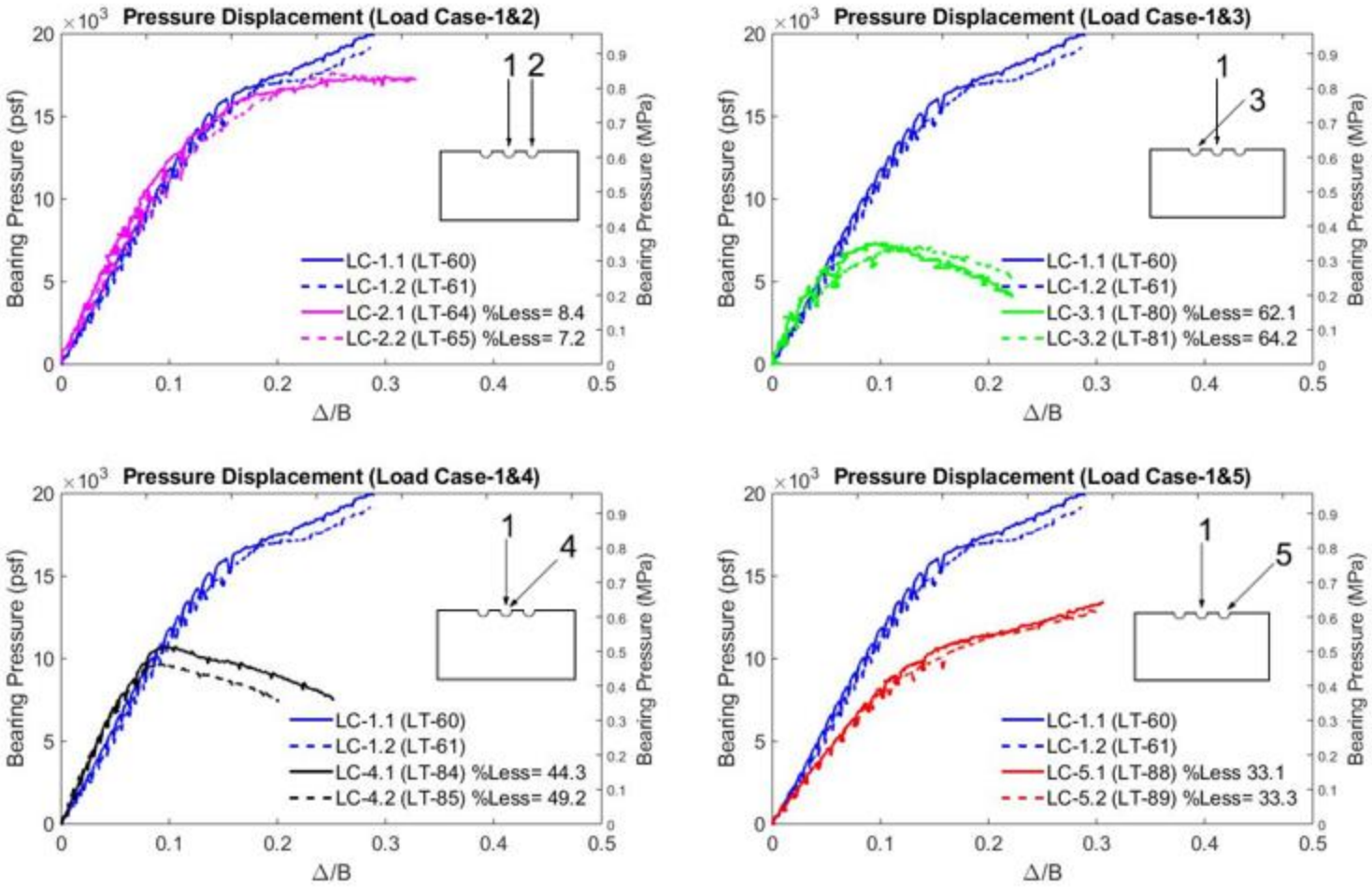

Figure 5.25 Net bearing pressure vs. displacement for Load Cases 1–5 with lateral-to-axial ratio = 0.25 and D_f = 0.5B

Table 5.18 Summary of measured test parameters and results for L/B = 10 with lateral-to-axial ratio = 0.25 and D_f = 0.5B (MD)

Load Test	Load Case	ϕ (deg)	γ_{dry} (lb/ft^3)	D_r (%)	Δ/B	q_{net} Measured (psf)	Percent Difference (%)
LT-60	1	32.56	101.52	63.79	0.2171	17,104	1.63
LT-61	1	32.49	101.45	63.40	0.2042	16,827	
LT-64	2	32.58	101.54	63.88	0.2432	15,252	1.29
LT-65	2	32.67	101.63	64.37	0.2554	15,450	
LT-80	3	32.64	101.61	64.24	0.106	7,006	1.19
LT-81	3	32.52	101.49	63.59	0.1351	6,923	
LT-84	4	32.63	101.60	64.19	0.1112	10,828	11.35
LT-85	4	32.61	101.58	64.06	0.1106	9,665	
LT-88	5	32.48	101.44	63.34	0.2427	12,403	0.26
LT-89	5	32.59	101.55	63.92	0.2703	12,436	

Table 5.19 presents the post-test plan views and failure surface views of the soil stratigraphy, which indicate general shear failure did occur. The failure surface ruptured the ground surface in all cases. Load Case-1 (LT-60 and LT-61) and Load Case-2 (LT-64 and LT-65) were previously presented in Section 5.3.2 and are shown again for comparison with Load Cases 3-5 at L/A ratio equal to 0.25.

Table 5.19 Post-test failure surface for lateral-to-axial ratio equal to 0.25 at embedment depth equal to 0.5B

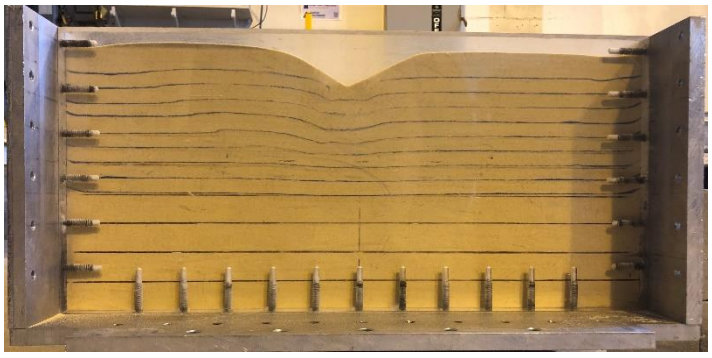

Load Case-1 (LT-60)

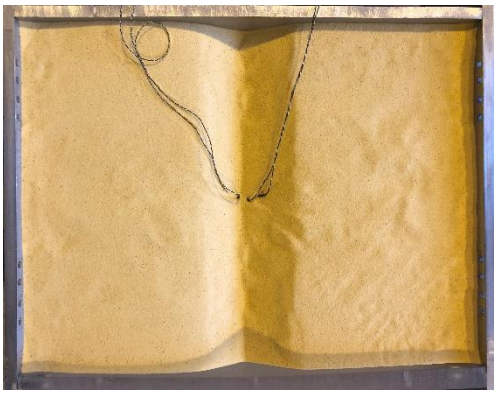

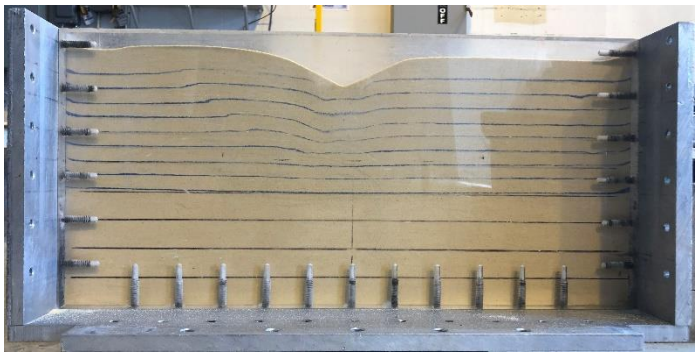 Load Case-1 (LT-61) $D_f = 0$	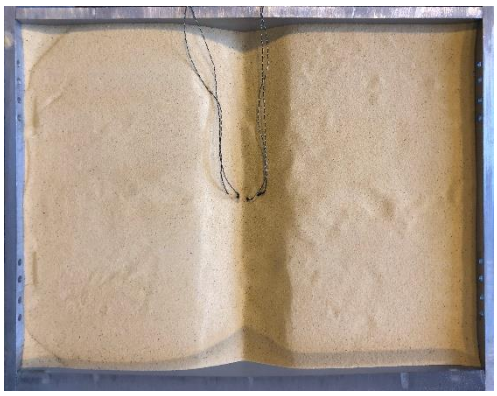
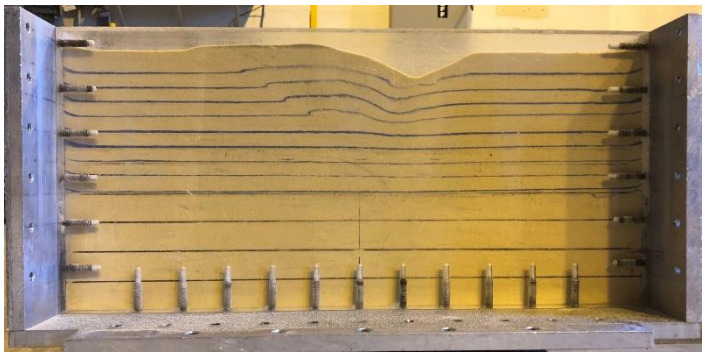 Load Case-2 (LT-64)	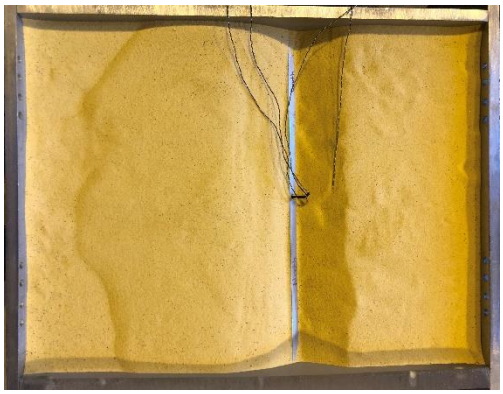
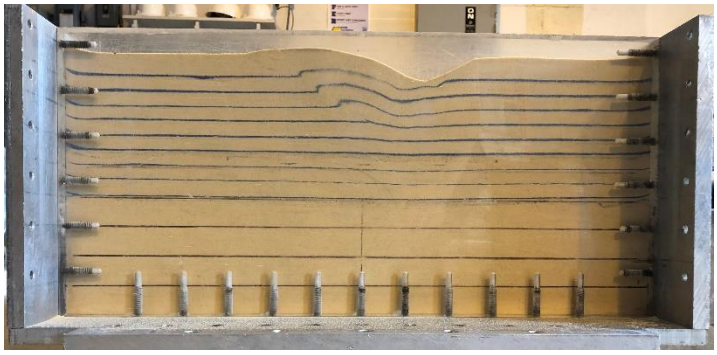 Load Case-2 (LT-65)	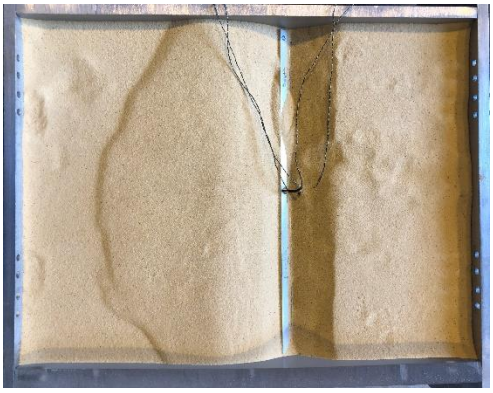
 Load Case-3 (LT-80)	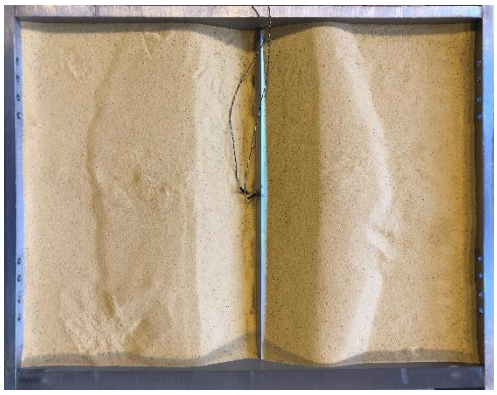

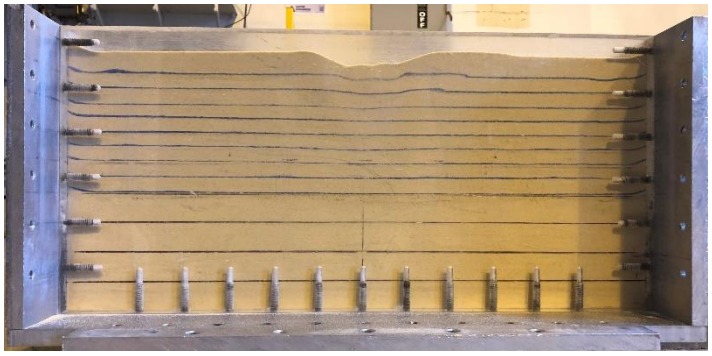 Load Case-3 (LT-81)	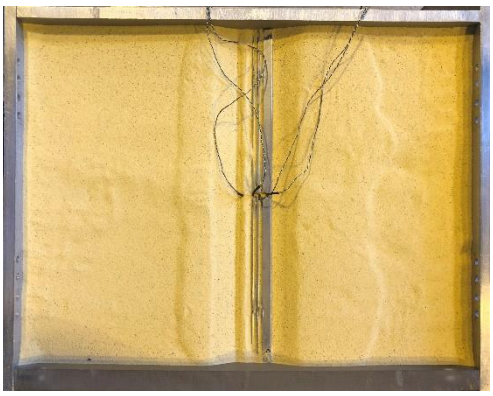
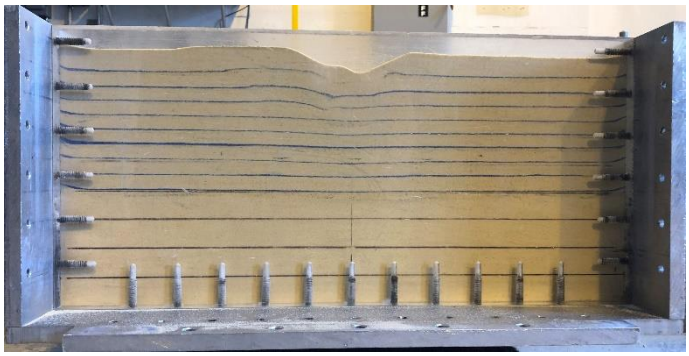 Load Case-4 (LT-84)	
 Load Case-4 (LT-85)	
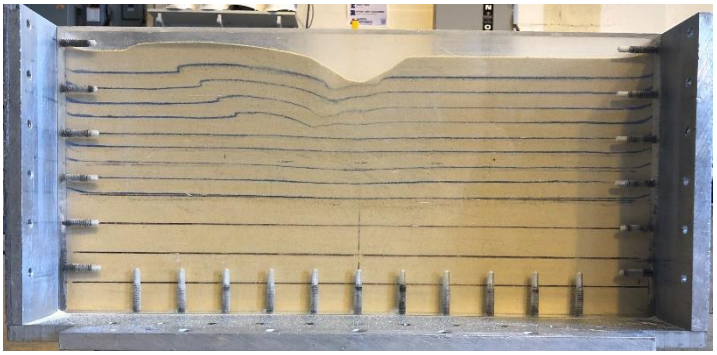 Load Case-5 (LT-88)	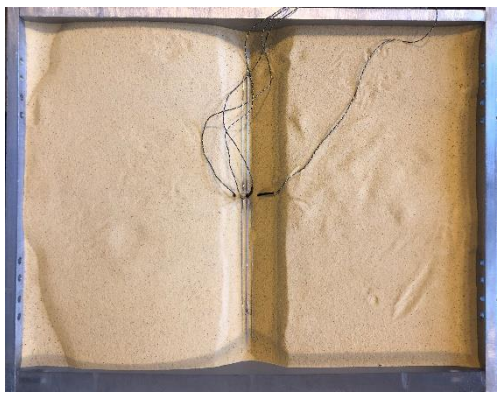

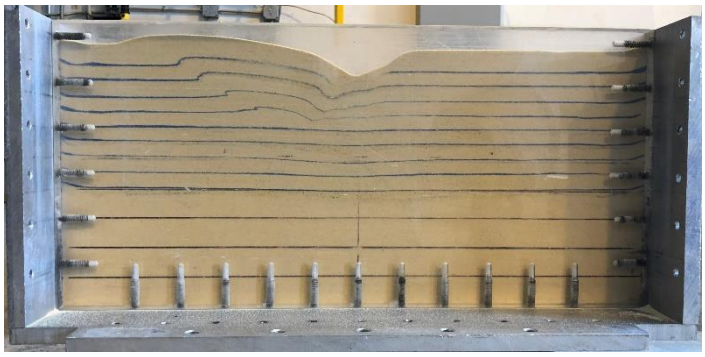

Load Case-5 (LT-89)

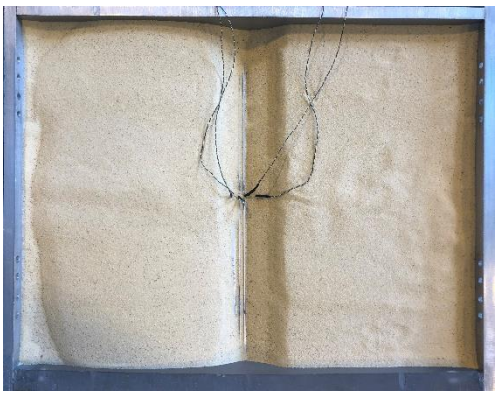

Summary of the post-test images of rupture surfaces:

- The observed rupture surface for Load Case-1 shows the maximum depth and length of the failure surface. Load Case-1 (LT-60 and LT-61) had a failure surface depth of 4.92 inches each and lengths of 9.29 and 9.14 inches. The failure surface ruptured the top layer of soil on the left side of the footing as the test underwent concentric loading at the center of the footing.
- Load Case-2 (LT-64 and LT-65) had failure surface depth of 3.39 and 2.87 inches with lengths of 9.51 and 8.33 inches. Load Case-2 applies an eccentric load at a distance of B/6 from the center of the footing.
- Load Case-3 (LT-80 and LT-81) had failure surface depth of 2.61 and 2.24 inches with lengths of 6.06 and 5.64 inches. Both LT-80 and LT-81 observed a failure surface on the right side of the footing as the footing underwent inclined-eccentric loading (+) to the direction of the eccentricity.
- Load Case-4 (LT-84 and LT-85) had failure surface depth of 2.76 and 2.79 inches with lengths of 7.75 and 7.96 inches as the footing underwent inclined loading at the center of the footing.

- Load Case-5 (LT-88 and LT-89) had failure surface depth of 3.21 and 3.20 inches with lengths of 9.28 and 8.88 inches. Both LT-88 and LT-89 observed a failure surface on the left side of the footing as the footing underwent inclined-eccentric loading (–) to the direction of the eccentricity.

The bearing pressure distribution observed by the miniature pressure transducers is presented for each load test in Figures 5.26 and 5.27. The loading position and orientation is displayed in each plot to illustrate how the pressure distribution is developed. The pressure sensors were position beneath the footing in sequential order (PS-1 through PS-4) from left to right at a spacing of 0.36 inches in model scale as previously stated.

Load Case-1 (LT-60 and LT-61) demonstrates a non-uniform pressure distribution with an increasing radial shape towards the center of the footing. This pressure profile is consistent with previous numerical modeling research presented by Loukidis et al. (2008) for sand as shown in Figure 5.10.

Load Case-2 (LT-64 and LT-65), Load Case-3 (LT-80 and LT-81), Load Case-4 (LT-84 and LT-85), and Load Case-5 (LT-88 and LT-89) demonstrates a trapezoidal shape with increasing pressure on the side of eccentricity, inclination or eccentric-inclined loading. The trapezoidal shift in pressure towards the side of eccentric or inclined loading is also present in Loukidis et al. (2008) analysis.

A summary of the measured test results are presented in Table 5.20 which provides the load case, relative density, D_r, friction angle, ϕ, embedment depth, D_f, L/A ratio, inclination angle, eccentricity, measured bearing capacity, q_u, load and corresponding failure surface direction, failure surface depth, and failure surface length.

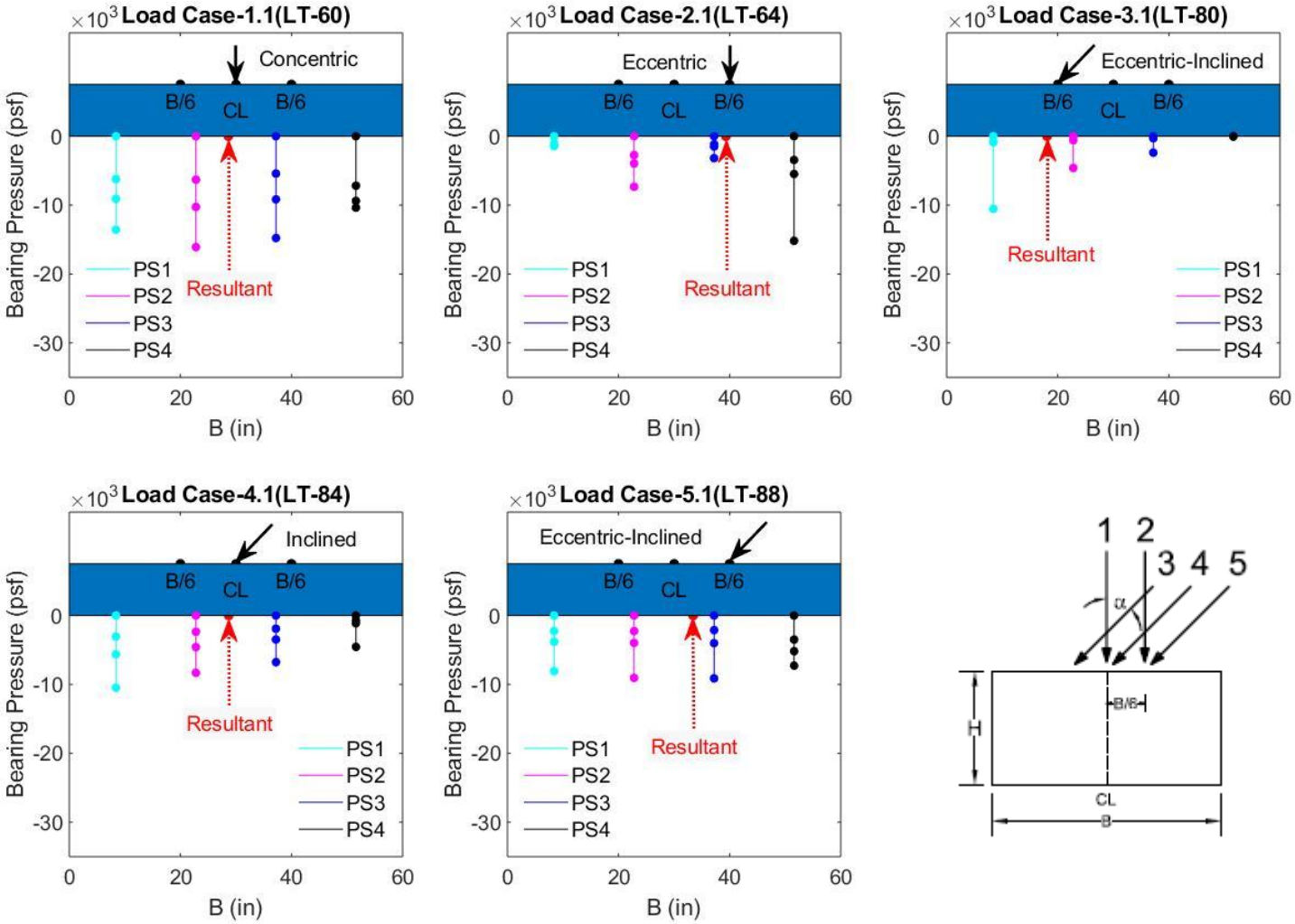

Figure 5.26 Bearing pressure distribution for Load Cases 1–5 with lateral-to-axial ratio = 0.25 and D_f = 0.5B

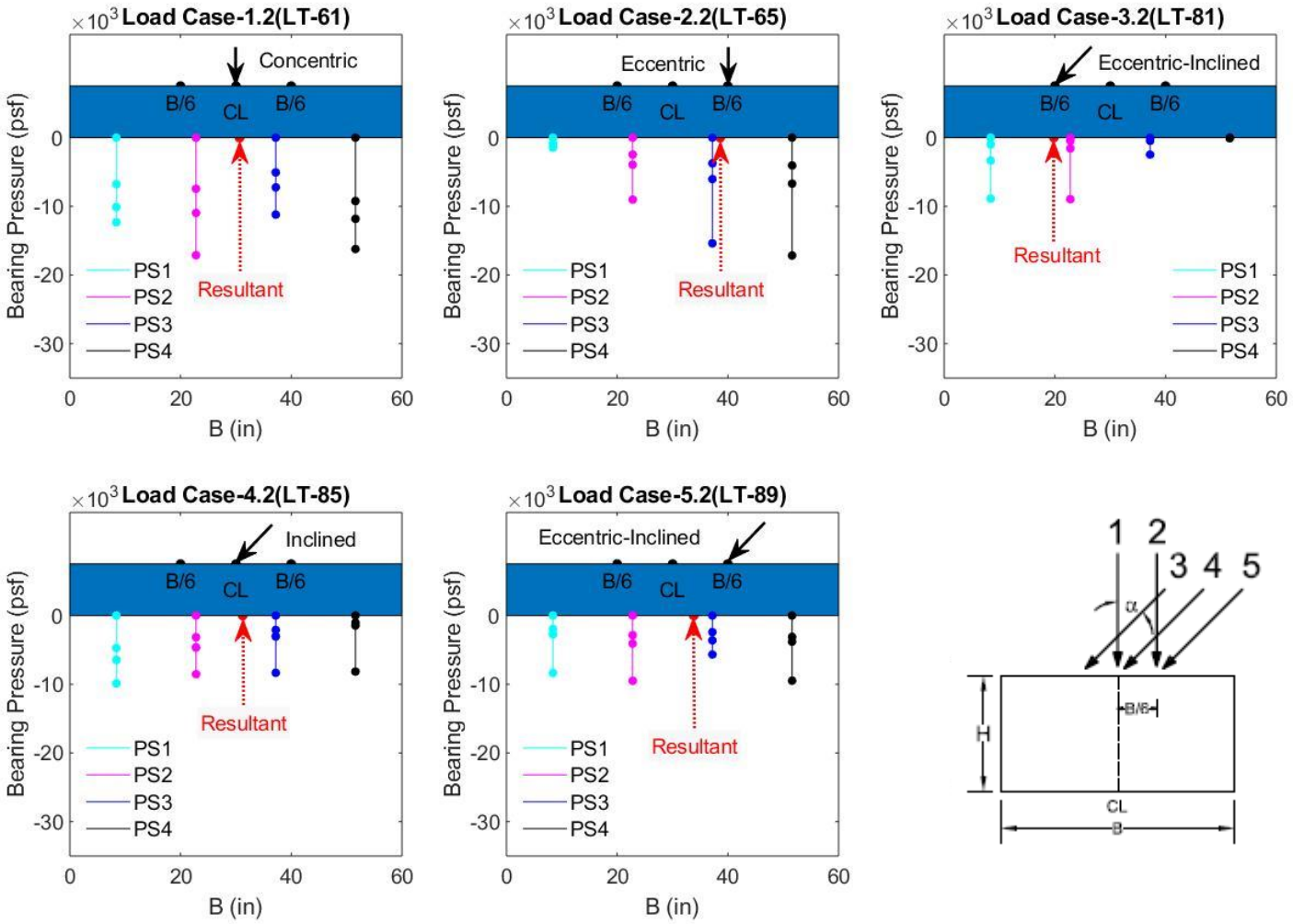

Figure 5.27 Bearing pressure distribution for Load Cases 1–5 with lateral-to-axial ratio = 0.25 and D_f = 0.5B

Table 5.20 List of load tests on medium dense soil (L/B = 10)

Load Test	Load Case	D_r (%)	ϕ (deg)	D_f (ft)	L/A Ratio	Inclination Angle (deg)	e	q_{ult} Measured (psf)	Load & Failure Surface Direction	Failure Surface Depth (in)	Failure Surface Length (in)
LT-58	1	63.65	32.54	0.00	0.00	0.0	0	13,303	↓←	3.79	8.88
LT-59	1	64.08	32.61	0.00	0.00	0.0	0	12,352	↓←	4.16	8.75
LT-60	1	63.79	32.56	2.45	0.00	0.0	0	17,104	↓←	4.92	9.29
LT-61	1	63.40	32.49	2.45	0.00	0.0	0	16,827	↓←	4.92	9.14
LT-62	2	63.80	32.56	0.00	0.00	0.0	0.25	10,103	↓←	2.57	6.43
LT-63	2	64.16	32.63	0.00	0.00	0.0	0.25	9,702	↓←	2.53	6.72
LT-64	2	63.88	32.58	2.45	0.00	0.0	0.25	15,252	↓←	3.39	9.51
LT-65	2	64.37	32.67	2.45	0.00	0.0	0.25	15,450	↓←	2.87	8.33
LT-66	3	64.56	32.70	0.00	0.10	5.7 (+)	0.25	7,502	↙→	2.07	7.44
LT-67	3	64.26	32.65	0.00	0.10	5.7 (+)	0.25	7,634	↙→	2.09	7.60
LT-68	3	64.23	32.64	2.45	0.10	5.7 (+)	0.25	8,880	↙→	2.81	7.98
LT-69	3	63.17	32.45	2.45	0.10	5.7 (+)	0.25	9,377	↙→	2.80	7.73
LT-70	4	64.25	32.65	0.00	0.10	5.7	0	8,564	↙←	2.55	8.21
LT-71	4	63.27	32.47	0.00	0.10	5.7	0	9,252	↙←	3.03	9.69
LT-72	4	63.52	32.51	2.45	0.10	5.7	0	12,503	↙←	3.31	9.21
LT-73	4	64.03	32.61	2.45	0.10	5.7	0	13,221	↙←	3.30	9.30

Table 5.20 (continued)

LT-74	5	64.39	32.67	0.00	0.10	5.7 (–)	0.25	10,918	↙←	2.54	7.51
LT-75	5	64.08	32.61	0.00	0.10	5.7 (–)	0.25	10,061	↙←	2.52	7.17
LT-76	5	63.85	32.57	2.45	0.10	5.7 (–)	0.25	16,390	↙←	3.30	8.33
LT-77	5	63.74	32.55	2.45	0.10	5.7 (–)	0.25	15,130	↙←	3.29	9.02
LT-78	3	63.53	32.51	0.00	0.25	14.6 (+)	0.25	2,829	↙→	2.01	5.16
LT-79	3	63.74	32.55	0.00	0.25	14.6 (+)	0.25	2,566	↙→	1.87	5.40
LT-80	3	64.24	32.64	2.45	0.25	14.6 (+)	0.25	7,006	↙→	2.61	6.06
LT-81	3	63.59	32.52	2.45	0.25	14.6 (+)	0.25	6,923	↙→	2.24	5.64
LT-82	4	63.32	32.48	0.00	0.25	14.6	0	3,239	↙←	2.51	7.69
LT-83	4	63.39	32.54	0.00	0.25	14.6	0	3,285	↙←	2.52	5.89
LT-84	4	64.19	32.63	2.45	0.25	14.6	0	10,828	↙←	2.76	7.75
LT-85	4	64.06	32.61	2.45	0.25	14.6	0	9,665	↙←	2.79	7.96
LT-86	5	63.74	32.55	0.00	0.25	14.6 (–)	0.25	9,143	↙←	3.08	6.74
LT-87	5	63.66	32.54	0.00	0.25	14.6 (–)	0.25	9,275	↙←	3.09	7.30
LT-88	5	63.34	32.48	2.45	0.25	14.6 (–)	0.25	12,403	↙←	3.21	9.28
LT-89	5	63.92	32.59	2.45	0.25	14.6 (–)	0.25	12,436	↙←	3.20	8.88

(-) indicates the load is inclined against the direction of eccentricity. (+) indicates the load is inclined in the direction of eccentricity.

5.3 Conclusions on Rectangular Footing (L/B = 10) Tests

Centrifuge tests of L/B = 10 footings on very dense and medium dense sand were conducted to investigate the influence of inclined and inclined-eccentric loading on the bearing capacity when the depth of embedment is zero and 0.5B. For the tests on very dense sand, the following observations of the bearing capacity are made.

- Load Case-3 (eccentric-inclined loading with + load combination (partially compensating)) is the most critical of all the cases. When $D_f = 0$, the bearing capacity was 53.4% and 81.6% less than the concentrically loaded footing (Load Case-1) for the lateral-to-axial load ratios of 0.10 and 0.25, respectively. When $D_f = 0.5B$, the bearing capacity was 54.9% and 68.9% less than the concentrically loaded footing with $D_f = 0.5B$ (Load Case-1) for the lateral-to-axial load ratios of 0.10 and 0.25, respectively.
- Load Case-4 (inclined loading): When $D_f = 0$ the bearing capacity was 25.6% and 64.7% less than the concentrically loaded footing (Load Case-1) for the lateral-to-axial load ratios of 0.10 and 0.25, respectively. When $D_f = 0.5B$, the bearing capacity was 21.5% and 55.6% less than the concentrically loaded footing with $D_f = 0.5B$ (Load Case-1) for the lateral-to-axial load ratios of 0.10 and 0.25, respectively.
- Load Case-5 (eccentric-inclined loading with – load combination (reinforcing) generally showed less decrease in bearing capacity than Load Cases 3 and 4. When $D_f = 0$, the bearing capacity was 21.7% and 36.4% less than the concentrically loaded footing (Load Case-1) for the lateral-to-axial load ratios of 0.10 and 0.25, respectively. When $D_f = 0.5B$, the bearing capacity was 20.1% and 27.6% less than the concentrically loaded footing with $D_f = 0.5B$ (Load Case-1) for the lateral-to-axial load ratios of 0.10 and 0.25, respectively.

- Embedment of 0.5B had marked effect on the bearing capacity of all load cases. Bearing capacity increased by 23.7% for Load Case-2 (eccentric load). Between tests of Load Case-3 (most critical), there was a 41.1% and 90% increase for the lateral-to-axial load ratios of 0.10 and 0.25, respectively. For Load Case-4, there was a 49.3% and 61.3% increase for the lateral-to-axial load ratios of 0.10 and 0.25, respectively. For Load Case-5, there was a 46.2% and 56.4% increase for the lateral-to-axial load ratios of 0.10 and 0.25, respectively.

For the tests on medium dense sand, the following observations of the bearing capacity are made.

- Load Case-3 (eccentric-inclined loading with + load combination (partially compensating)) is the most critical of all the cases. When $D_f = 0$, the bearing capacity was 41.5% and 79% less than the concentrically loaded footing (Load Case-1) for the lateral-to-axial load ratios of 0.10 and 0.25, respectively. When $D_f = 0.5B$, the bearing capacity was 46.2% and 58.9% less than the concentrically loaded footing with $D_f = 0.5B$ (Load Case-1) for the lateral-to-axial load ratios of 0.10 and 0.25, respectively.
- Load Case-4 (inclined loading): When $D_f = 0$ the bearing capacity was 30.6% and 72.2% less than the concentrically loaded footing (Load Case-1) for the lateral-to-axial load ratios of 0.10 and 0.25, respectively. When $D_f = 0.5B$, the bearing capacity was 24.2% and 39.6% less than the concentrically loaded footing with $D_f = 0.5B$ (Load Case-1) for the lateral-to-axial load ratios of 0.10 and 0.25, respectively.
- Load Case-5 (eccentric-inclined loading with – load combination (reinforcing) generally showed less decrease in bearing capacity than Load Cases 3 and 4. When $D_f = 0$, the bearing capacity was 18.2% and 28.2% less than the concentrically loaded footing (Load Case-1) for the lateral-to-axial load ratios of 0.10 and 0.25, respectively. When $D_f = 0.5B$, the bearing

capacity was 7.1% and 26.8% less than the concentrically loaded footing with D_f = 0.5B (Load Case-1) for the lateral-to-axial load ratios of 0.10 and 0.25, respectively.

- Embedment of 0.5B had marked effect on the bearing capacity of all load cases. Bearing capacity increased by 43.1% for Load Case-2 (eccentric load). Between tests of Load Case-3 (most critical), there was a 18.6% and 88% increase for the lateral-to-axial load ratios of 0.10 and 0.25, respectively. For Load Case-4, there was a 36.3% and 100% increase for the lateral-to-axial load ratios of 0.10 and 0.25, respectively. For Load Case-5, there was a 40.1% and 29.6% increase for the lateral-to-axial load ratios of 0.10 and 0.25, respectively.

6.0 SQUARE FOOTING (L/B = 1) TESTS

6.1 Model Load Tests — Concentric Loading on Square Footing (L/B = 1) for Very Dense Condition

Each load case was tested at $D_f = 0$ and $D_f = 0.5B$ for lateral to axial load ratios of 0.10 and 0.25, and on medium dense and very dense sand. All eccentric loads were applied B/6 from the centerline of the footing. Replicates of each case were performed to check for experimental repeatability. A total of 32 tests were performed in this series. Table 6.1 lists the identifiers for each test with the date, soil condition, load case and footing configuration.

Table 6.1 List of load test for square footings on very dense soil

Name	Date	Load Case	Relative Density (D_r)	Embedment Depth (D_f)	Eccentricity	Inclination L/A ratio	Series #
LT-125	9/10/19	1	Very Dense	0	0	0	1
LT-126	9/12/19	1	Very Dense	0	0	0	2
LT-127	9/12/19	1	Very Dense	0	0	0	3
LT-128	9/12/19	1	Very Dense	0.5B	0	0	1
LT-129	9/14/19	1	Very Dense	0.5B	0	0	2
LT-130	9/15/19	2	Very Dense	0	B/6	0	1
LT-131	9/15/19	2	Very Dense	0	B/6	0	2
LT-132	9/15/19	2	Very Dense	0.5B	B/6	0	1
LT-133	9/16/19	2	Very Dense	0.5B	B/6	0	2
LT-134	9/16/19	3	Very Dense	0	B/6	0.10	1
LT-135	9/16/19	3	Very Dense	0	B/6	0.10	2
LT-136	9/17/19	3	Very Dense	0.5B	B/6	0.10	1
LT-137	9/17/19	3	Very Dense	0.5B	B/6	0.10	2
LT-138	9/17/19	4	Very Dense	0	0	0.10	1
LT-139	9/18/19	4	Very Dense	0	0	0.10	2
LT-140	9/18/19	4	Very Dense	0.5B	0	0.10	1
LT-141	9/19/19	4	Very Dense	0.5B	0	0.10	2
LT-142	9/19/19	5	Very Dense	0	B/6	0.10	1
LT-143	9/19/19	5	Very Dense	0	B/6	0.10	2
LT-144	9/19/19	5	Very Dense	0.5B	B/6	0.10	1
LT-145	9/20/19	5	Very Dense	0.5B	B/6	0.10	2
LT-146	9/21/19	3	Very Dense	0	B/6	0.25	1
LT-147	9/21/19	3	Very Dense	0	B/6	0.25	2
LT-148	9/21/19	3	Very Dense	0.5B	B/6	0.25	1
LT-149	9/21/19	3	Very Dense	0.5B	B/6	0.25	2

Table 6.1 (continued)

LT-150	9/22/19	4	Very Dense	0	0	0.25	1
LT-151	9/22/19	4	Very Dense	0	0	0.25	2
LT-152	9/22/19	4	Very Dense	0.5B	0	0.25	1
LT-153	9/22/19	4	Very Dense	0.5B	0	0.25	2
LT-154	9/23/19	5	Very Dense	0	B/6	0.25	1
LT-155	9/23/19	5	Very Dense	0	B/6	0.25	2
LT-156	9/23/19	5	Very Dense	0	B/6	0.25	3
LT-157	9/23/19	5	Very Dense	0.5B	B/6	0.25	1
LT-158	9/24/19	5	Very Dense	0.5B	B/6	0.25	2

6.1.1 Lateral-to-Axial Ratio of 0.10 with Depth of Embedment Equal to Zero

In this series of tests, the square footing was loaded for Load Cases 1–5 with depth of embedment equal to zero. The A3 sand used in the tests had an average dry unit weight, $\gamma_{dry,}$ in the range of 107.64 lb/ft^3 to 108.19 lb/ft^3 and average relative density, D_r in the range of 94.16% to 96.75% for the top soil layers where the failure surface was observed. The average peak friction angle from the direct shear test was estimated to be in the range of 38.10° to 38.58°. The model footing was tested at N = 40 G, which represents a prototype footing length of 5 feet by 5 feet in width with the L/B ratio of 1. All eccentric loads were applied B/6 (0.25 inches) from the center of the footing and inclined loads were applied at a lateral-to-axial ratio of 0.10 (5.7°). For the combined eccentric-inclined load tests, the same geometric loading conditions were applied as the tests of eccentric (Load Case-2) and inclined loads (Load Case-4).

The bearing pressure displacement curves for each test are shown in Figure 6.1. The bearing capacity of each test is taken as the peak pressure or the pressure at the intercept of the two linear parts of the curve. All eccentric and eccentric-inclined loading conditions used the effective width B' to determine the bearing pressure. Listed in Table 6.2 are the internal friction angles, unit weight, relative density, normalized displacements, and net measured bearing capacities with percent differences to demonstrate repeatability for each test.

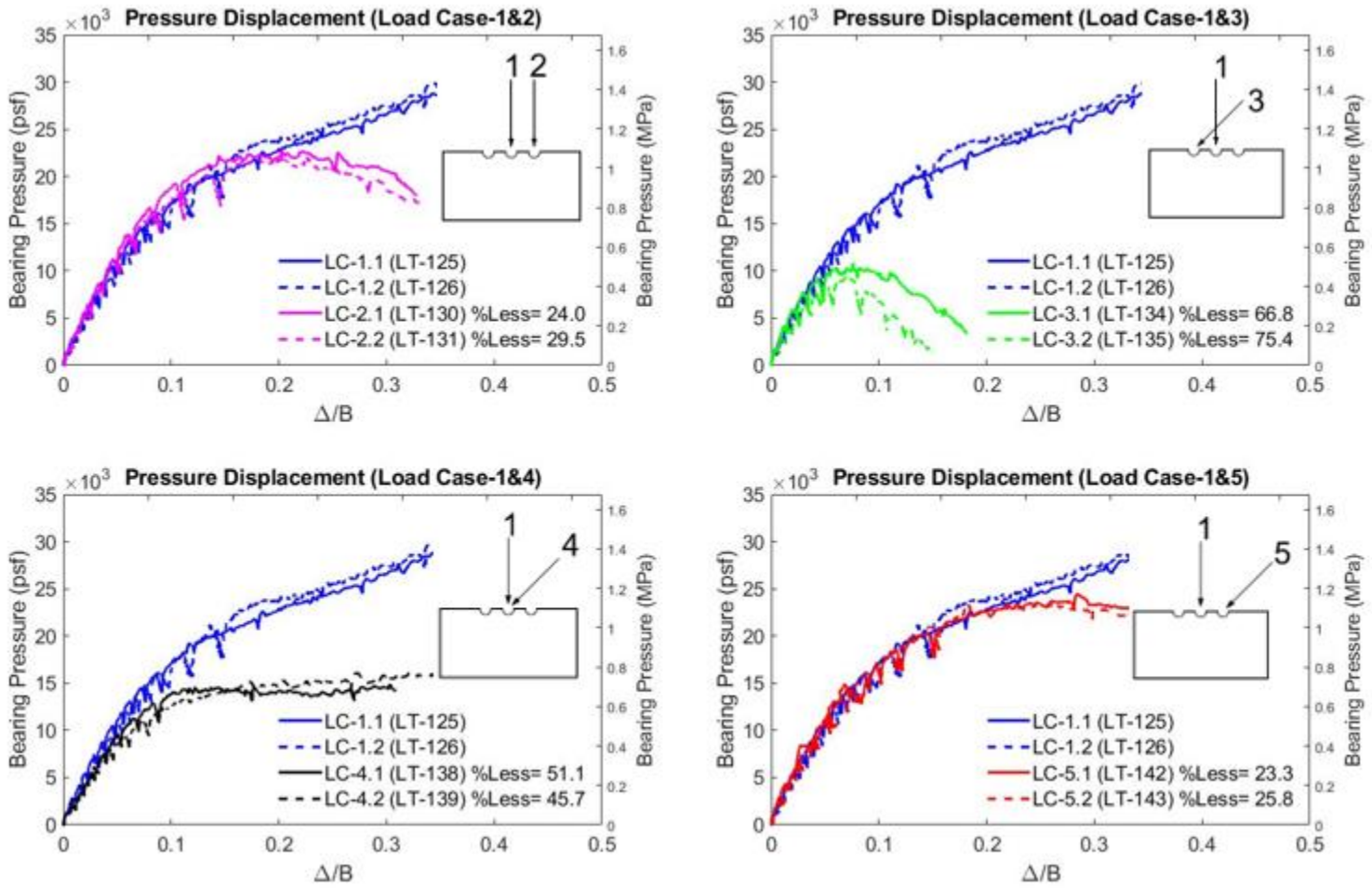

Figure 6.1 Net bearing pressure vs. displacement for Load Cases 1–5 with lateral-to-axial ratio = 0.1 and D_f = 0 (VD)

Table 6.2 Summary of measured test parameters and results for L/B = 1 with lateral-to-axial ratio = 0.1 and D_f = 0 (VD)

Load Test	Load Case	ϕ (deg)	γ_{dry} (lb/ft^3)	D_r (%)	Δ/B	q_{net} Measured (psf)	Percent Difference (%)
LT-125	1	38.10	107.64	94.16	0.075	24,140	2.90
LT-126	1	38.44	108.03	95.98	0.106	24,850	
LT-130	2	38.19	107.74	94.63	0.185	22,210	3.53
LT-131	2	38.58	108.19	96.75	0.185	21,440	
LT-134	3	38.45	108.05	96.08	0.061	10,955	8.02
LT-135	3	38.50	108.10	96.31	0.070	10,110	
LT-138	4	38.52	108.12	96.42	0.117	14,610	1.45
LT-139	4	38.50	108.11	96.35	0.129	14,400	
LT-142	5	38.52	108.12	96.41	0.234	22,140	0.63
LT-143	5	38.48	108.09	96.24	0.236	22,000	

Table 6.3 is the observed shear failure surface on the soil for all load cases of the L/B = 1 footing on the soil surface (D_f = 0) with inclination ratio = 0.10. The lateral extent of the failure surfaces are clearly developed for all load cases except Load Case-1. While the general bearing capacity was achieved in Load Case-1 (concentric load), the full development of a failure surface would require greater vertical displacement of the footing in order to push up a greater volume of soil than in the other cases. The observations alone don't indicate enough about the relative magnitudes of the bearing capacities between the load cases but may be useful in the analysis for appropriate factors to be used for predicting behavior under various loads.

The bearing pressure distribution observed by the miniature pressure transducers is presented for each load test in Figures 6.2 and 6.3. The loading position and orientation is displayed in each plot to illustrate how the pressure distribution is developed. The pressure sensors were positioned beneath the footing in sequential order (PS-1 through PS-4) from left to right at a spacing of 0.36 inches in model scale.

Table 6.3 Observed failure surfaces of square footings on the surface of very dense soil

 Load Case-1	 Load Case-2
 Load Case-3	 Load Case-4

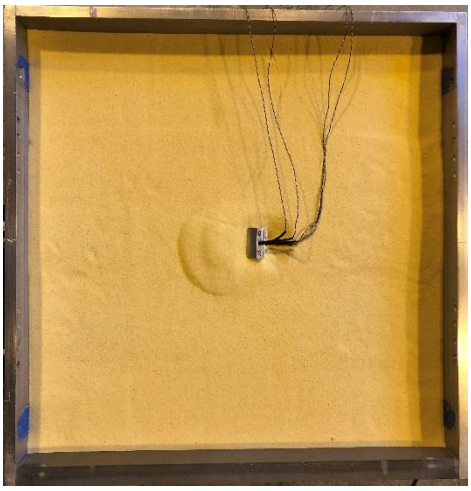 Load Case-5	 Load Case-5

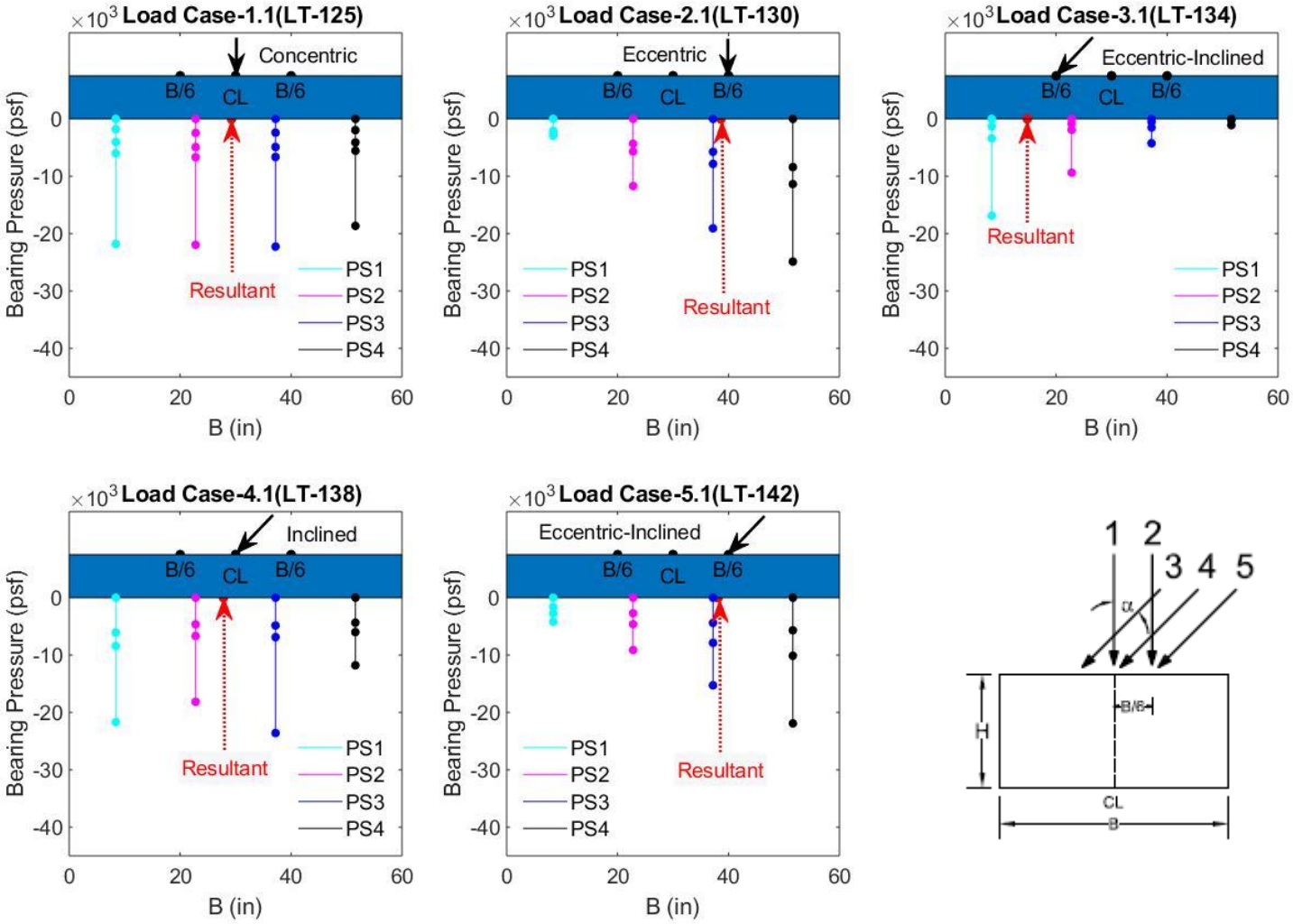

Figure 6.2 Bearing pressure distribution for Load Cases 1–5 with lateral-to-axial ratio = 0.1 and D_f = 0

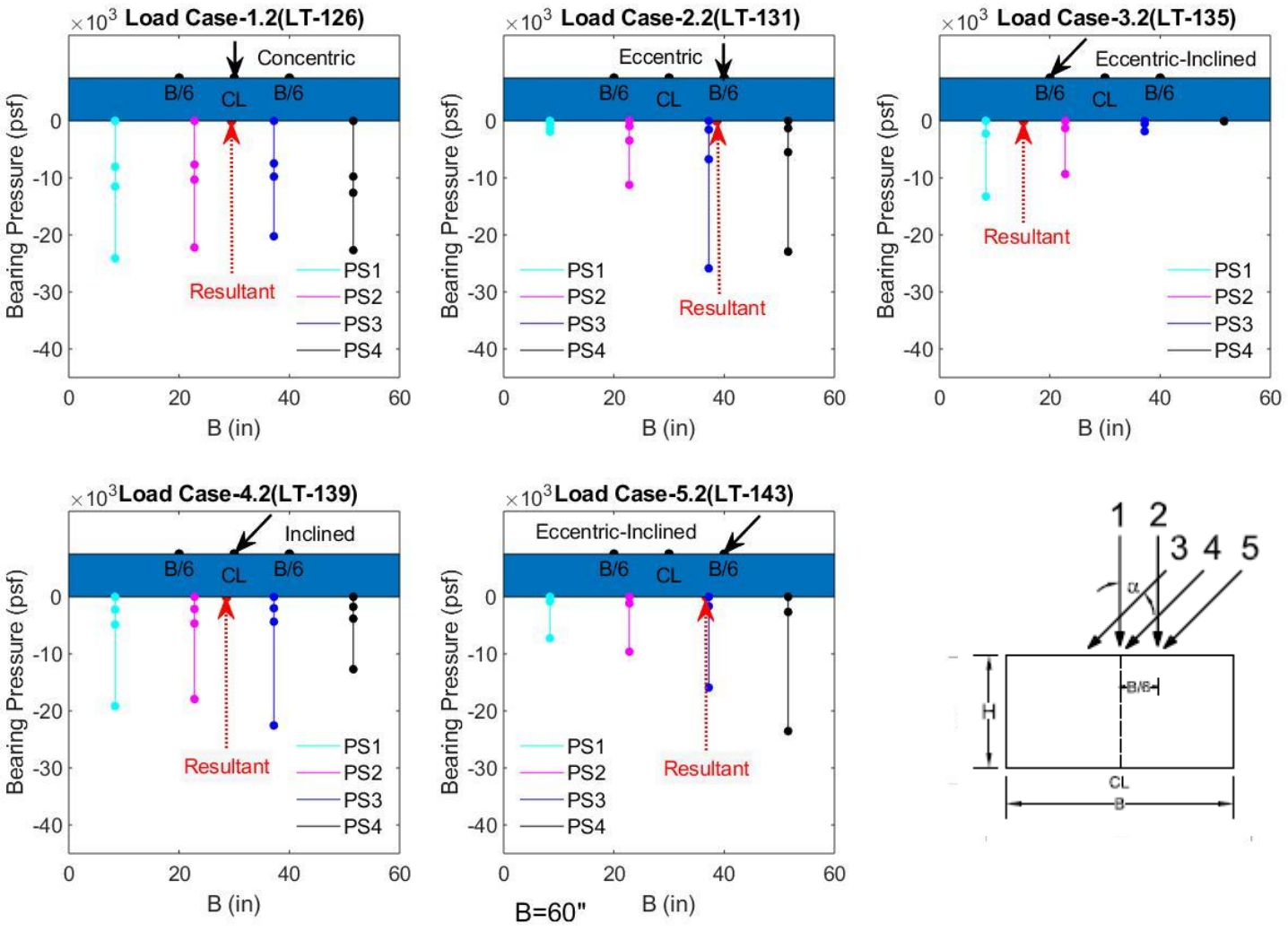

Figure 6.3 Bearing pressure distribution for Load Cases 1–5 with lateral-to-axial ratio = 0.1 and D_f = 0

Load Case-1 (LT-125 and LT-126) generally shows more of a uniform pressure distribution compared with the L/B = 10 tests. The pressure displacement results and the lack of an observed failure surface at the sand surface indicates that general shear failure was not obtained for the footing penetrations. The curves suggest local or punching shear failure which may explain the higher edge pressures when the shear is not mobilized in a square footing compared to a rectangular footing. Load Case-2 (LT-130 and LT-131), Load Case-3 (LT-134 and LT-135), Load Case-4 (LT-138 and LT-139), and Load Case-5 (LT-142 and LT-143) demonstrates a trapezoidal shape with increasing pressure on the side of eccentricity, inclination or eccentric-inclined loading, which was also observed in numerical models by Loukidis et al. (2008) (Figure 6.4).

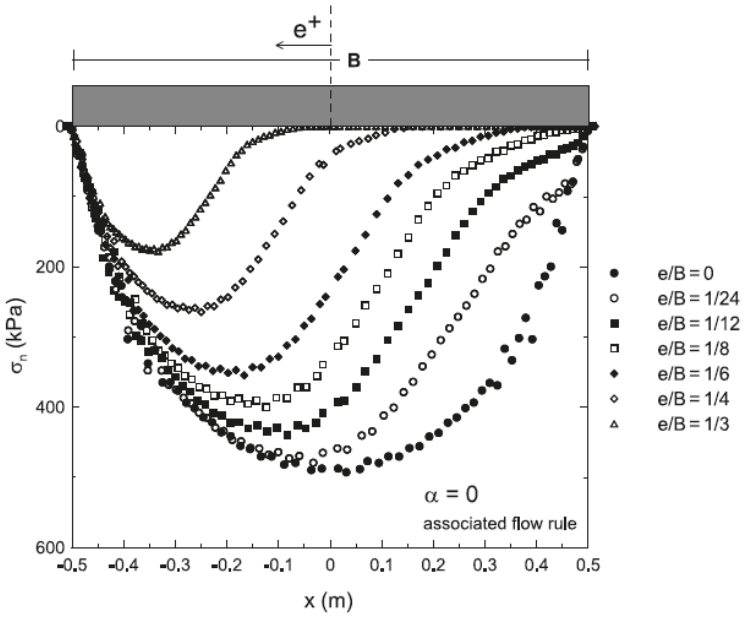

Figure 6.4 Pressure distributions from numerical models of eccentrically loaded footing on granular soil (Loukidis et al., 2008)

6.1.2 Lateral-to-Axial Ratio of 0.10 with Depth of Embedment Equal to 0.5B

In this series of tests, the square footing was loaded for Load Cases 1–5 with depth of embedment equal to 0.5B. The AASHTO A3 soil used in the tests had an average dry unit weight, $\gamma_{dry,}$ in the range of 107.90 lb/ft^3 to 108.22 lb/ft^3 and average relative density, D_r in the range of 95.37% to 96.87% for the top soil layers where the failure surface was observed. The average peak friction angle from the direct shear test was estimated to be in the range of 38.33° to 38.60°. The model footing was tested at N = 40 G, which equates to a prototype footing length of 5 feet by 5 feet in width with the L/B ratio of 1 and embedment depth equal to 0.5B. All eccentric loads were applied B/6 (0.25 inches) from the center of the footing and inclined loads were applied at a lateral-to-axial ratio of 0.10 (5.7°). The combined eccentric-inclined load test applied the same geometric loading conditions as the individual parts.

The net bearing capacity for each test are presented in Figure 6.5. All eccentric and eccentric-inclined loading conditions used the effective width B' to determine the bearing pressure. Listed in Table 6.4 are the internal friction angles, unit weight, relative density, and net measured bearing capacities with percent differences to demonstrate repeatability for each test.

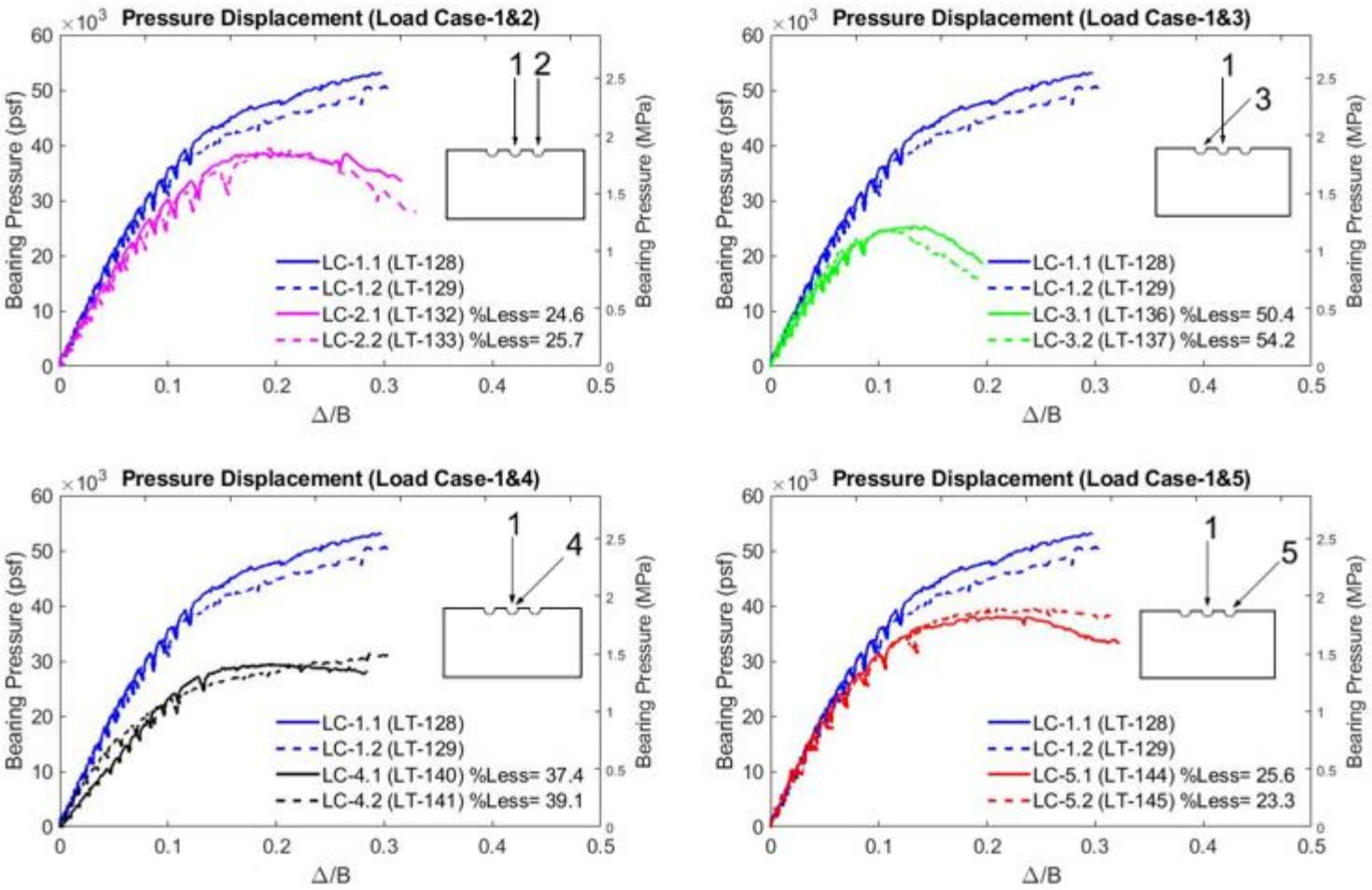

Figure 6.5 Net bearing pressure vs. displacement for Load Cases 1–5 with lateral-to-axial ratio = 0.1 and D_f = 0.5B (VD)

Table 6.4 Summary of measured test parameters and results for L/B = 1 with lateral-to-axial ratio = 0.1 and D_f = 0B (VD)

Load Test	Load Case	ϕ (deg)	γ_{dry} (lb/ft^3)	D_r (%)	Δ/B	q_{net} Measured (psf)	Percent Difference (%)
LT-128	1	38.43	108.03	95.97	0.207	47,712	3.80
LT-129	1	38.33	107.90	95.37	0.205	45,933	
LT-132	2	38.49	108.09	96.26	0.189	38,922	0.90
LT-133	2	38.43	108.02	95.95	0.194	38,572	
LT-136	3	38.51	108.11	96.37	0.128	24,242	0.29
LT-137	3	38.49	108.10	96.30	0.121	24,312	
LT-140	4	38.60	108.22	96.87	0.185	30,084	2.65
LT-141	4	38.51	108.12	96.39	0.191	29,297	
LT-144	5	38.51	108.11	96.36	0.149	38,857	13.48
LT-145	5	38.55	108.17	96.63	0.191	44,472	

The bearing pressure distribution measured for each load test is shown in Figures 6.6 and 6.7. The loading position and orientation is displayed in each plot to illustrate how the pressure distribution is developed. Load Case-1 (LT-128 and LT-129) generally shows more of a uniform pressure distribution compared with the L/B = 10 tests. The pressure displacement results and the lack of an observed failure surface at the sand surface indicates that general shear failure was not obtained for the footing penetrations. The curves suggest local or punching shear failure which may explain the higher edge pressures when the shear is not mobilized in a square footing compared to a rectangular footing. Load Case-2 (LT-132 and LT-133), Load Case-3 (LT-136 and LT-137), Load Case-4 (LT-140 and LT-141), and Load Case-5 (LT-144 and LT-145) demonstrates a trapezoidal shape with increasing pressure on the side of eccentricity, inclination or eccentric-inclined loading, which was also observed in numerical models by Loukidis et al. (2008) (Figure 6.4).

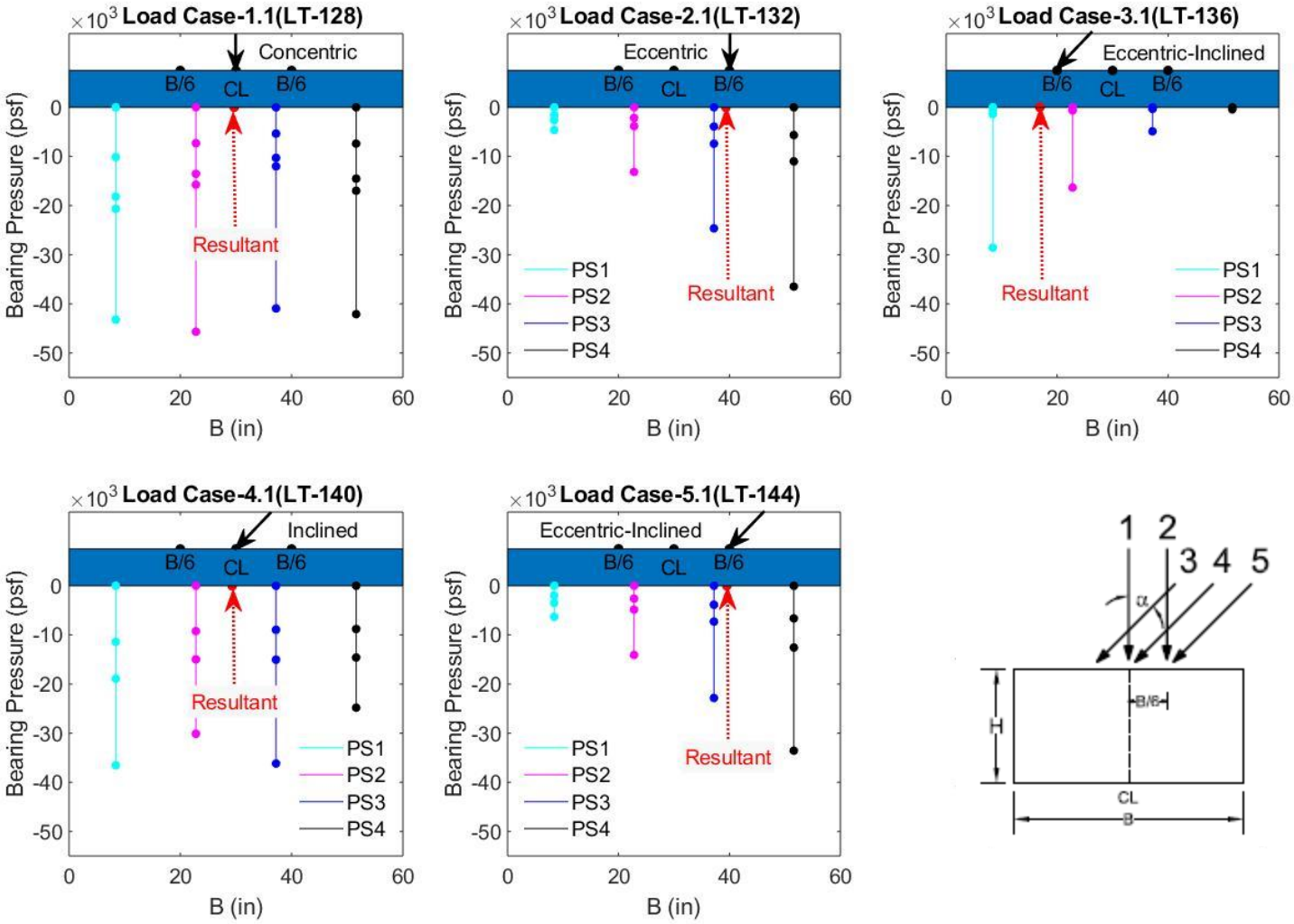

Figure 6.6 Bearing pressure distribution for Load Cases 1–5 with lateral-to-axial ratio = 0.1 and D_f = 0.5B

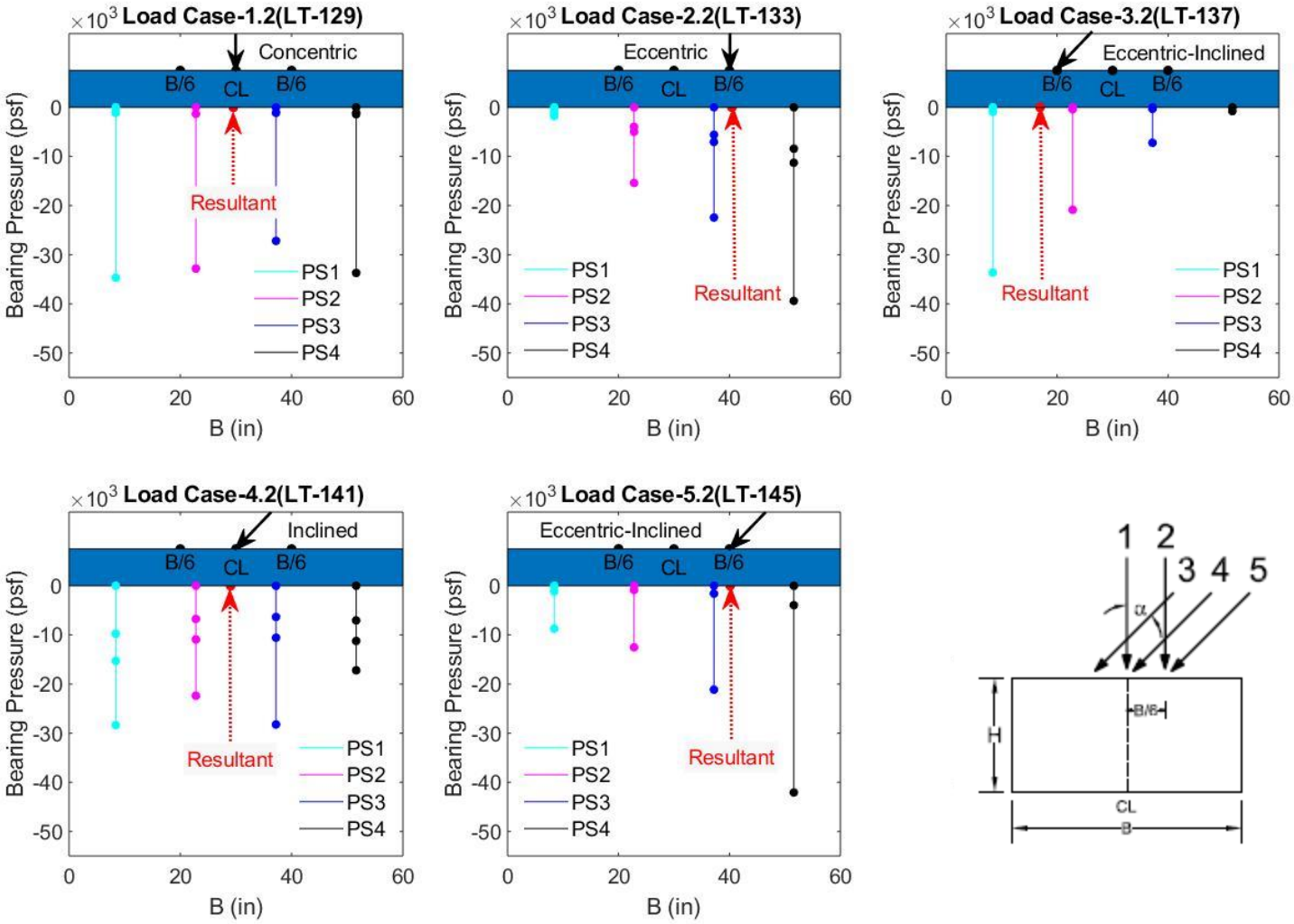

Figure 6.7 Bearing pressure distribution for Load Cases 1–5 with lateral-to-axial ratio = 0.1 and D_f = 0.5B

6.1.3 Lateral-to-Axial Ratio of 0.25 with Depth of Embedment Equal to Zero

In this series of tests, the square footing was loaded for Load Cases 1–5 with depth of embedment equal to zero. The A3 sand used in the tests had an average dry unit weight, $\gamma_{dry,}$ in the range of 107.64 lb/ft^3 to 108.19 lb/ft^3 and average relative density, D_r in the range of 94.16% to 96.75% for the top soil layers where the failure surface was observed. The average peak friction angle from the direct shear test was estimated to be in the range of 38.10° to 38.58°. The model footing was tested at N = 40 G, which represents a prototype footing length of 5 feet by 5 feet in width with the L/B ratio of 1 and embedment depth equal to zero. All eccentric loads were applied B/6 (0.25 inches) from the center of the footing and inclined loads were applied at a lateral-to-axial ratio of 0.25 (14.0°).

The net bearing capacity for each test is shown in presented in Figures 6.8. All eccentric and eccentric-inclined loading conditions used the effective width B' to determine the bearing pressure. Listed in Table 6.5 are the internal friction angles, unit weight, relative density, and net measured bearing capacities with percent differences to demonstrate repeatability for each test.

Table 6.5 Summary of measured test parameters and results for L/B = 1 with lateral-to-axial ratio = 0.25 and D_f = 0 (VD)

Load Test	Load Case	ϕ (deg)	γ_{dry} (lb/ft^3)	D_r (%)	Δ/B	q_{net} Measured (psf)	Percent Difference (%)
LT-125	1	38.10	107.64	94.16	0.075	24,140	2.90
LT-126	1	38.44	108.03	95.98	0.106	24,850	
LT-130	2	38.19	107.74	94.63	0.185	22,210	3.53
LT-131	2	38.58	108.19	96.75	0.185	21,440	
LT-146	3	38.51	108.12	96.40	0.093	8,575	7.33
LT-147	3	38.52	108.13	96.44	0.091	9,227	
LT-150	4	38.45	108.05	96.06	0.067	10,127	8.99
LT-151	4	38.44	108.04	96.02	0.084	11,080	
LT-154	5	38.51	108.12	96.40	0.181	17,918	0.21
LT-155	5	38.50	108.11	96.35	0.186	17,881	

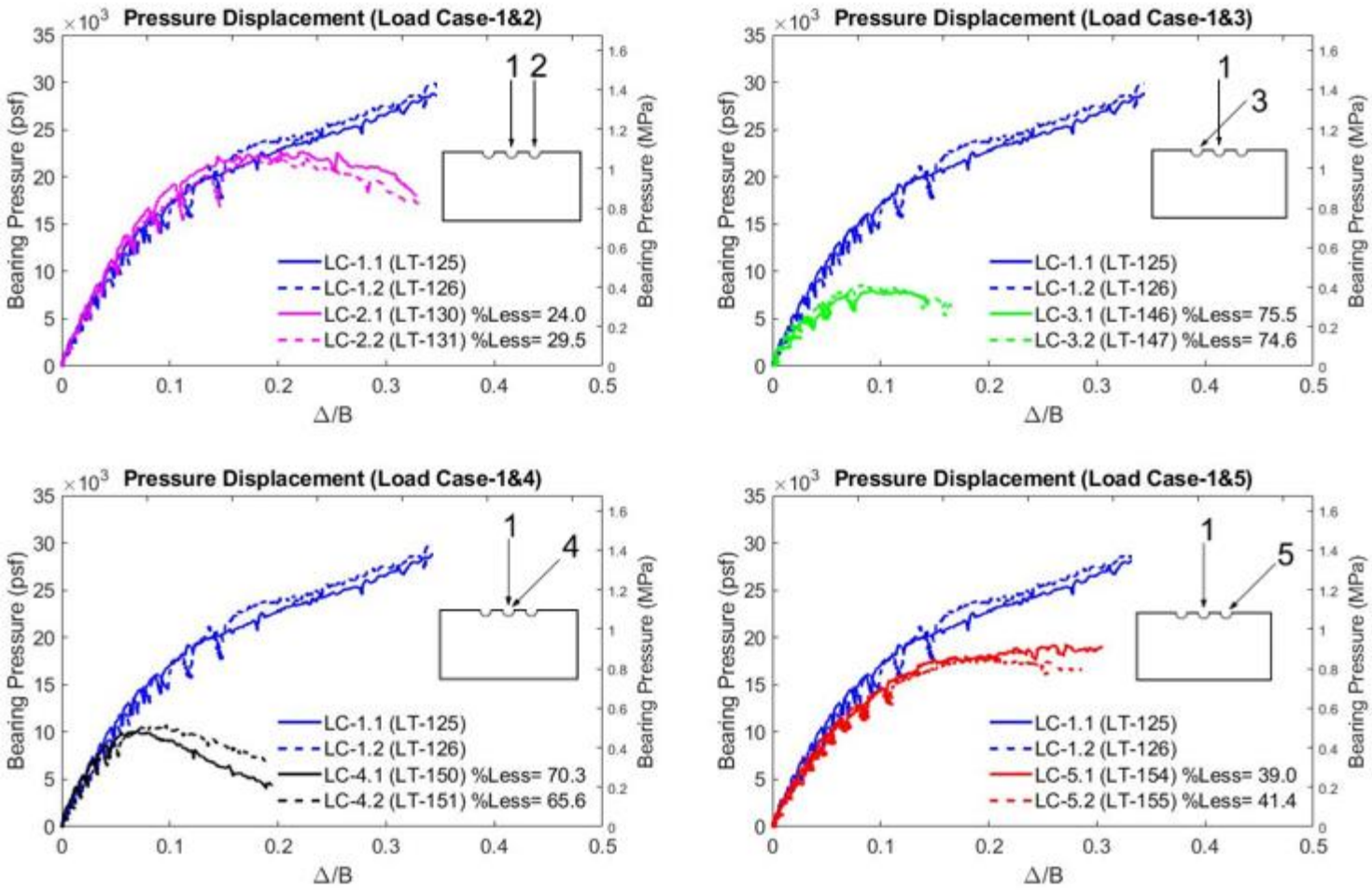

Figure 6.8 Net bearing pressure vs. displacement for Load Cases 1–5 with lateral-to-axial ratio = 0.25 and D_f = 0 (VD)

The bearing pressure distribution measured for each load test is shown in Figures 6.9 and 6.10. The loading position and orientation is displayed in each plot to illustrate how the pressure distribution is developed. Load Case-1 (LT-125 and LT-126) generally shows more of a uniform pressure distribution compared with the L/B = 10 tests. The pressure displacement results and the lack of an observed failure surface at the sand surface indicates that general shear failure was not obtained for the footing penetrations. The curves suggest local or punching shear failure which may explain the higher edge pressures when the shear is not mobilized in a square footing compared to a rectangular footing. Load Case-2 (LT-130 and LT-131), Load Case-3 (LT-146 and LT-147), Load Case-4 (LT-150 and LT-151), and Load Case-5 (LT-154 and LT-155) demonstrates a trapezoidal shape with increasing pressure on the side of eccentricity, inclination or eccentric-inclined loading, which was also observed in numerical models by Loukidis et al. (2008) (Figure 6.4).

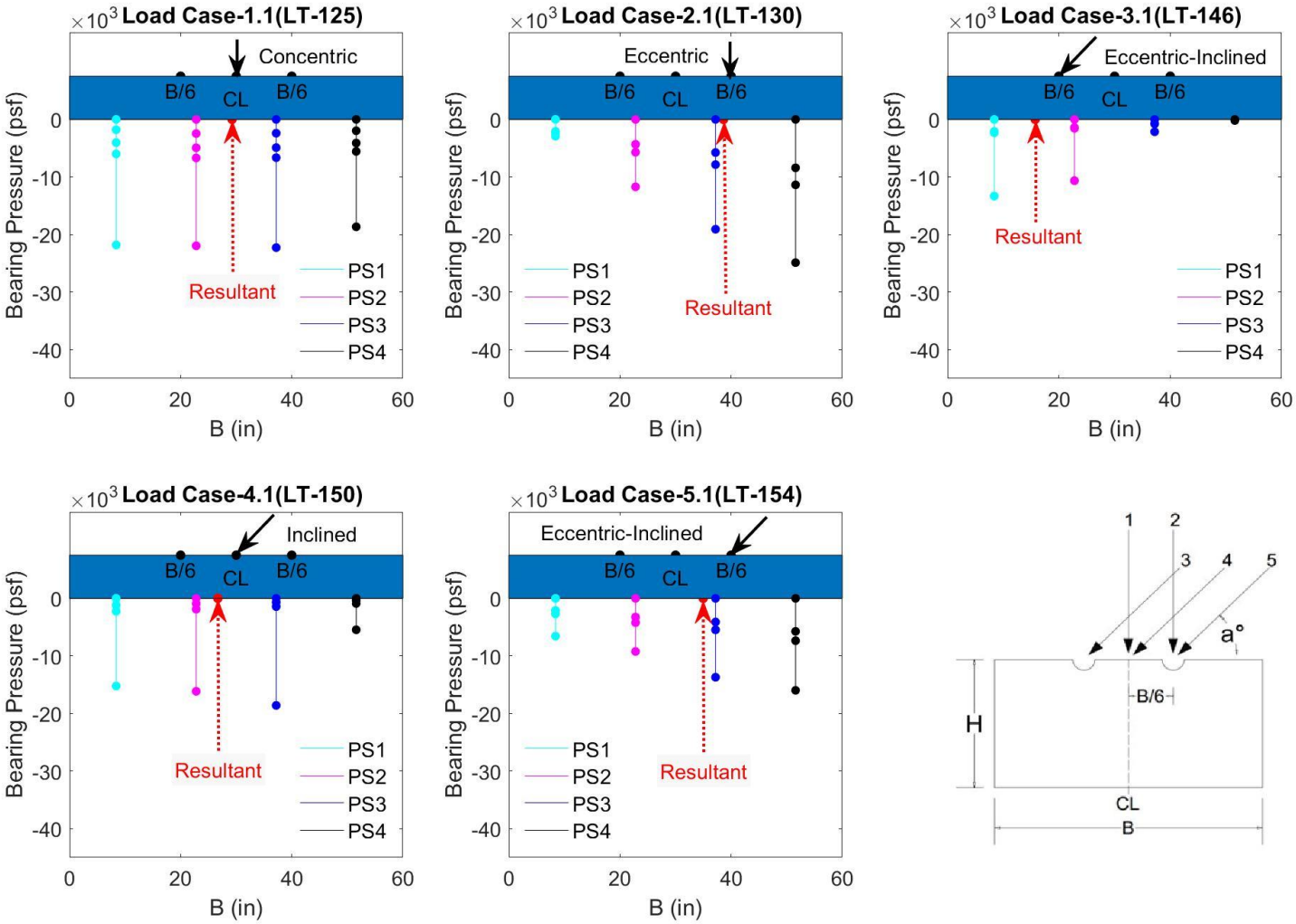

Figure 6.9 Bearing pressure distribution for Load Cases 1–5 with lateral-to-axial ratio = 0.25 and D_f = 0

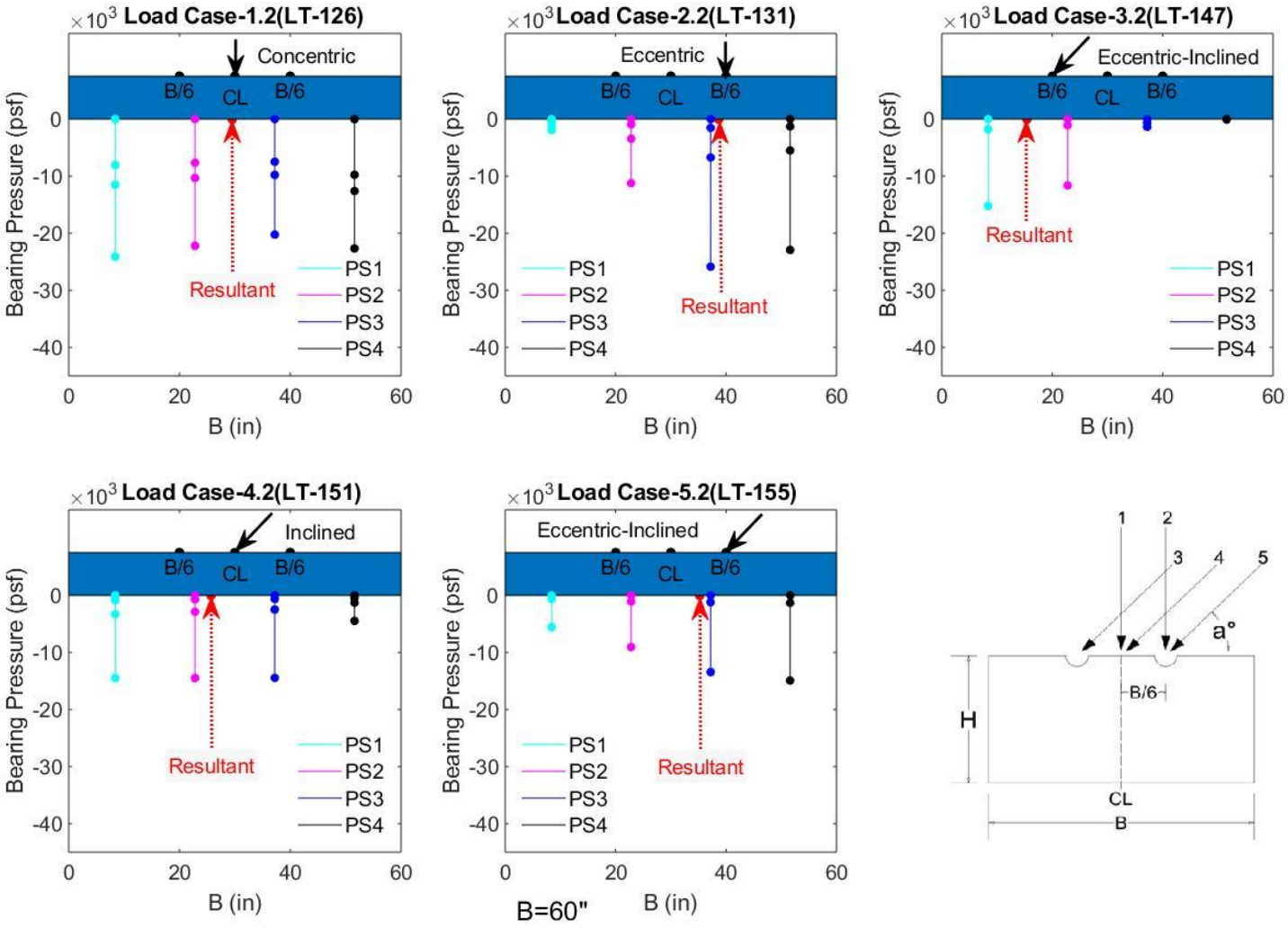

Figure 6.10 Bearing pressure distribution for Load Cases 1–5 with lateral-to-axial ratio = 0.25 and $D_f = 0$

6.1.4 Lateral-to-Axial Ratio of 0.25 with Depth of Embedment Equal to 0.5B

In this series of tests, the square footing was loaded for Load Cases 1–5 with depth of embedment equal to 0.5B. The AASHTO A3 soil used in the tests had an average dry unit weight, $\gamma_{dry,}$ in the range of 107.90 lb/ft^3 to 108.17 lb/ft^3 and average relative density, D_r in the range of 95.37% to 96.64% for the top soil layers where the failure surface was observed. The average peak friction angle from the direct shear test was estimated to be in the range of 38.33° to 38.56°. The model footing was tested at N = 40 G, which represents a prototype footing length of 5 feet by 5 feet in width (L/B = 1) and embedment depth equal to 0.5B. All eccentric loads were applied B/6 (0.25 inches) from the center of the footing and inclined loads were applied at a lateral-to-axial ratio of 0.25 (14.0°).

The net bearing capacity for each test are presented in Figures 6.11. All eccentric and eccentric-inclined loading conditions used the effective width B' to determine the bearing pressure. Listed in Table 6.6 are the internal friction angles, unit weight, relative density, and net measured bearing capacities with percent differences to demonstrate repeatability for each test.

Table 6.6 Summary of measured test parameters and results for L/B = 1 with lateral-to-axial ratio = 0.25 and D_f = 0.5B (VD)

Load Test	Load Case	ϕ (deg)	γ_{dry} (lb/ft^3)	D_r (%)	Δ/B	q_{net} Measured (psf)	Percent Difference (%)
LT-128	1	38.43	108.03	95.97	0.207	47,712	3.80
LT-129	1	38.33	107.90	95.37	0.205	45,933	
LT-132	2	38.49	108.09	96.26	0.189	38,922	0.90
LT-133	2	38.43	108.02	95.95	0.194	38,572	
LT-148	3	38.50	108.11	96.35	0.096	17,193	2.30
LT-149	3	38.51	108.12	96.39	0.109	17,593	
LT-152	4	38.52	108.12	96.42	0.096	20,120	7.17
LT-153	4	38.44	108.03	95.98	0.095	18,729	
LT-157	5	38.56	108.17	96.64	0.264	37,767	4.01
LT-158	5	38.40	107.99	95.79	0.256	36,284	

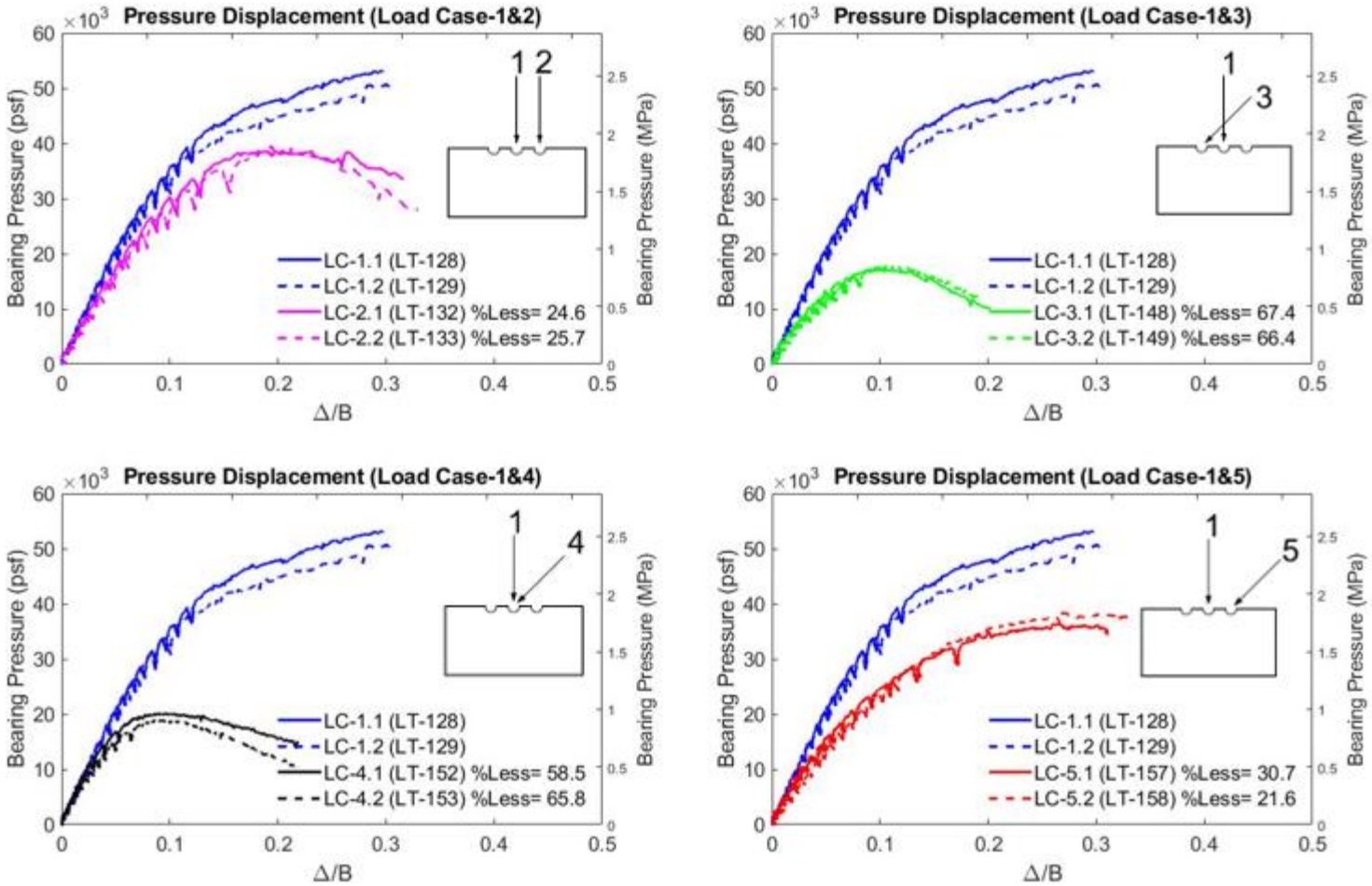

Figure 6.11 Net bearing pressure vs. displacement for Load Cases 1–5 with lateral-to-axial ratio = 0.25 and D_f = 0.5B (VD)

The bearing pressure distribution measured for each load test is shown in Figures 6.12 and 6.13. The loading position and orientation is displayed in each plot to illustrate how the pressure distribution is developed. Load Case-1 (LT-128 and LT-129) generally shows more of a uniform pressure distribution compared with the L/B = 10 tests. The pressure displacement results and the lack of an observed failure surface at the sand surface indicates that general shear failure was not obtained for the footing penetrations. The curves suggest local or punching shear failure which may explain the higher edge pressures when the shear is not mobilized in a square footing compared to a rectangular footing. Load Case-2 (LT-132 and LT-133), Load Case-3 (LT-148 and LT-149), Load Case-4 (LT-152 and LT-153), and Load Case-5 (LT-157 and LT-158) demonstrates a trapezoidal shape with increasing pressure on the side of eccentricity, inclination or eccentric-inclined loading, which was also observed in numerical models by Loukidis et al. (2008) (Figure 6.4).

.

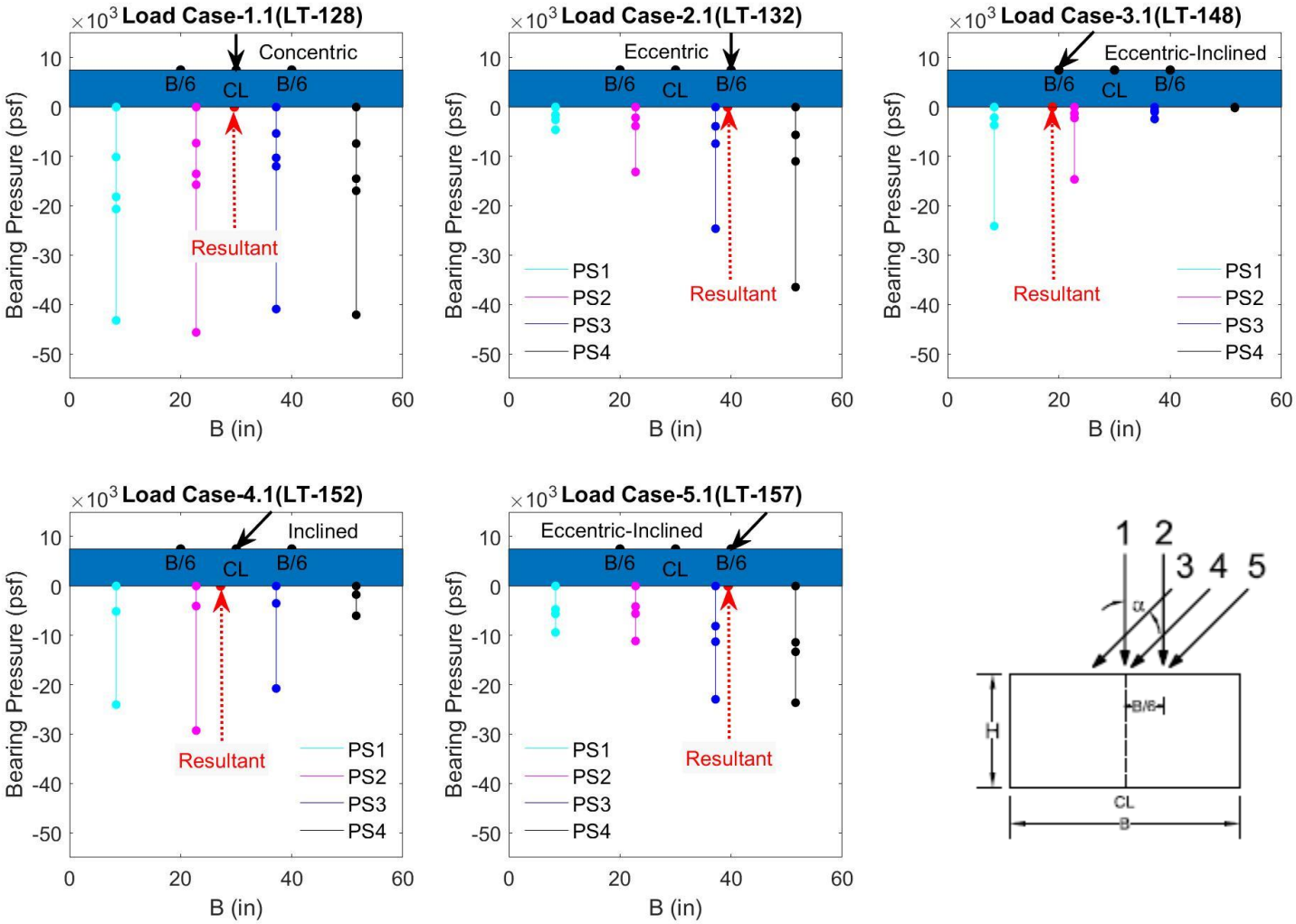

Figure 6.12 Bearing pressure distribution for Load Cases 1–5 with lateral-to-axial ratio = 0.25 and D_f = 0.5B

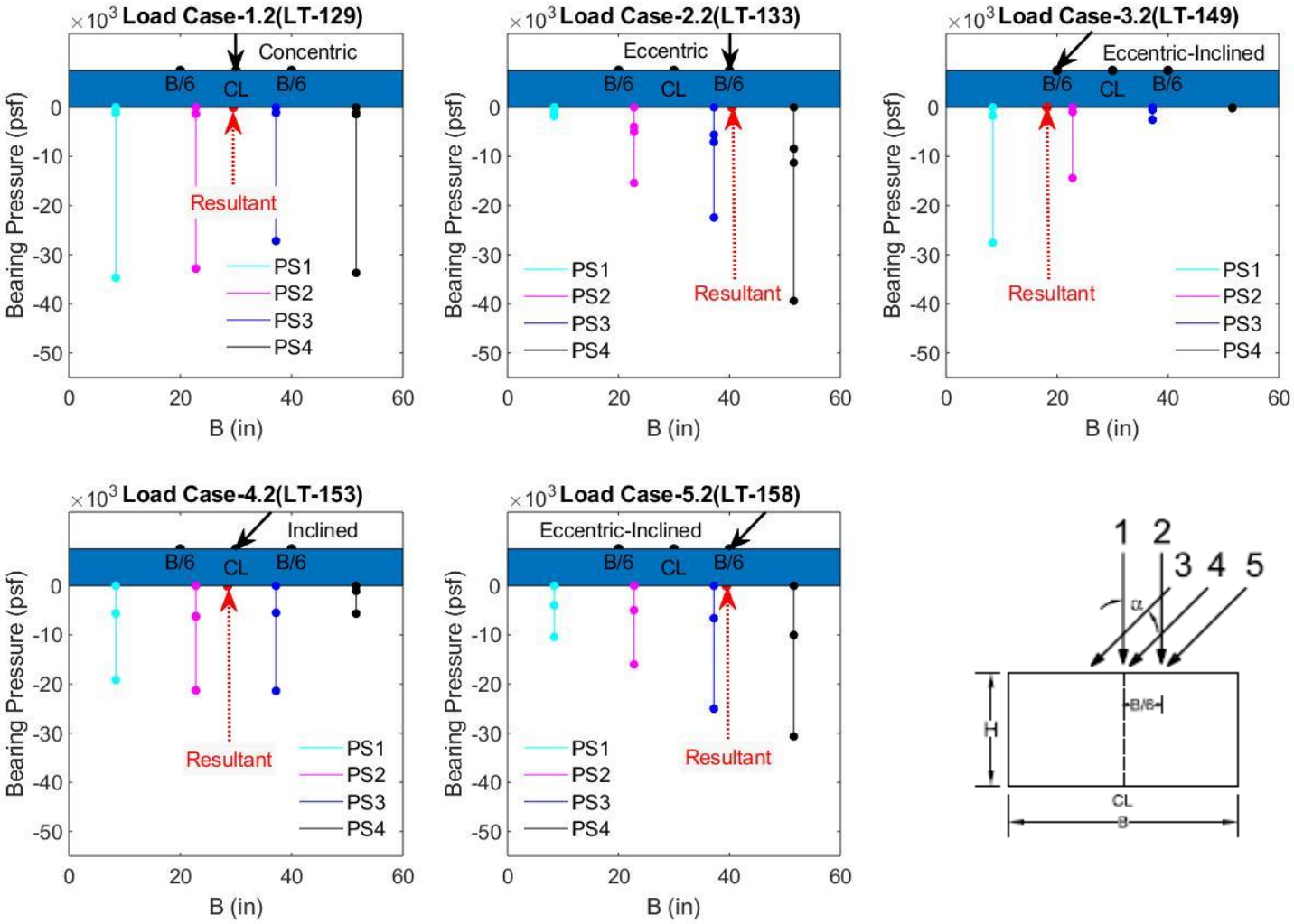

Figure 6.13 Bearing pressure distribution for Load Cases 1–5 with lateral-to-axial ratio = 0.25 and D_f = 0.5B

6.1.5 Lateral-to-Axial Ratio of 0.10 & 0.25 with Depth of Embedment Equal to B

In this series of tests, the square footing was loaded for Load Case-3 with L/A = 0.10 & 0.25 and Load Case-4 with L/A = 0.25 with depth of embedment equal to B. These load cases were determined to be the most critical scenarios for bearing capacity reductions. The AASHTO A3 soil used in the tests had an average dry unit weight, $\gamma_{dry,}$ in the range of 107.74 lb/ft^3 to 107.85 lb/ft^3 and average relative density, D_r in the range of 94.63% to 95.16% for the top soil layers where the failure surface was observed. The average peak friction angle from the direct shear test was estimated to be in the range of 38.19° to 38.29°. The model footing was tested at N = 40 G, which represents a prototype footing length of 5 feet by 5 feet in width (L/B = 1) and embedment depth equal to the footing width, B. All eccentric loads were applied B/6 (0.25 inches) from the center of the footing and inclined loads were applied at a lateral-to-axial ratio of 0.25 (14.0°).

The net bearing capacity for each test are presented in Figure 6.14. All eccentric and eccentric-inclined loading conditions used the effective width B' to determine the bearing pressure. Listed in Table 6.7 are the internal friction angles, unit weight, relative density, and net measured bearing capacities with percent differences to demonstrate repeatability for each test.

Table 6.7 Summary of measured test parameters and results for L/B = 1 with lateral-to-axial ratio = 0.1 and 0.25 with D_f = B (VD)

Load Test	Load Case	ϕ (deg)	γ_{dry} (lb/ft^3)	D_r (%)	Δ/B	q_{net} Measured (psf)	Percent Difference (%)
LT-180	3	38.21	107.76	94.72	0.170	35,750	1.94
LT-181	3	38.19	107.74	94.63	0.176	35,060	
LT-182	3	38.27	107.83	95.07	0.199	39,400	1.53
LT-183	3	38.29	107.85	95.16	0.222	38,800	
LT-184	4	38.25	107.81	94.95	0.194	42,490	1.32
LT-185	4	38.28	107.84	95.11	0.228	41,930	

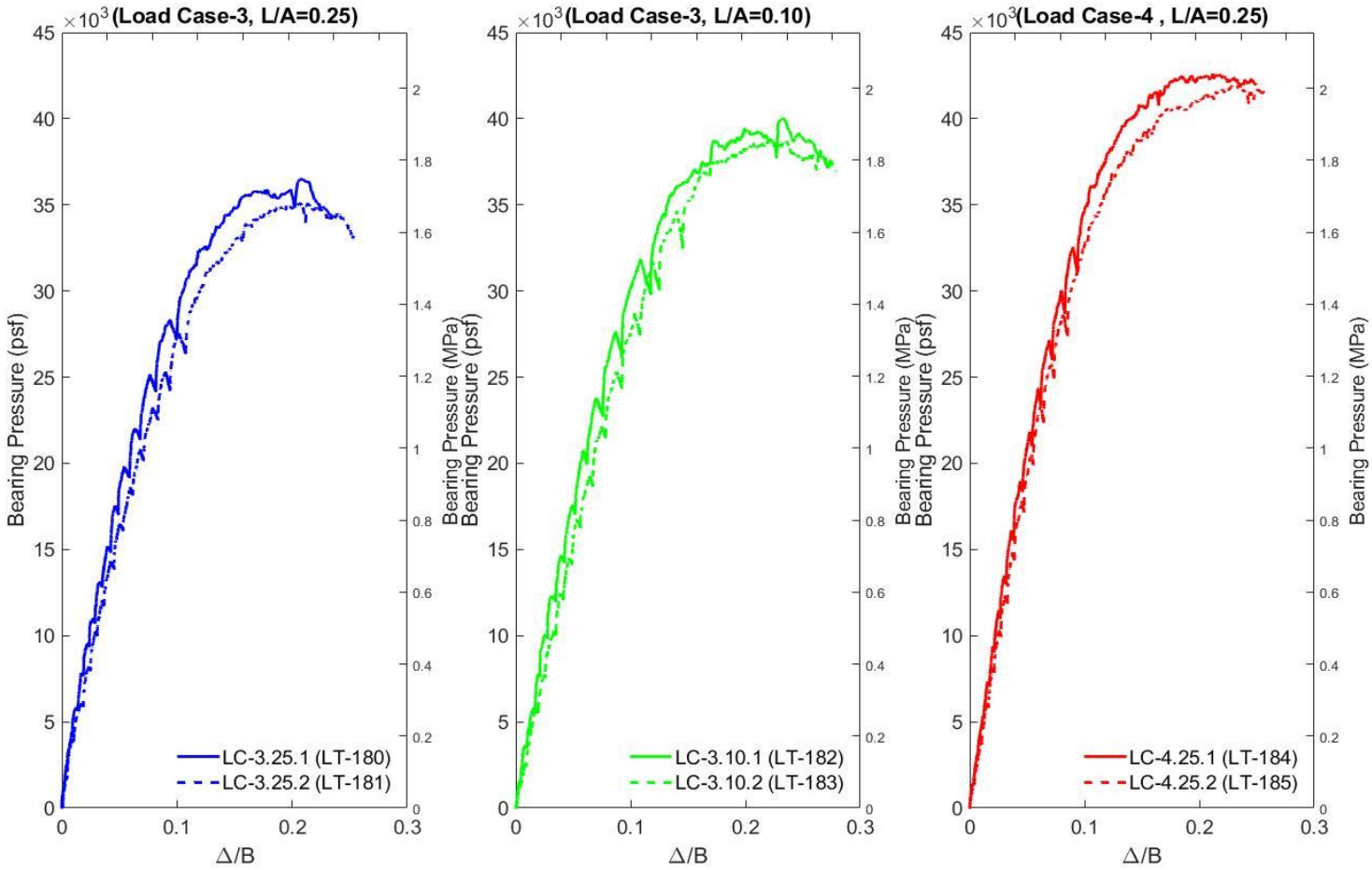

Figure 6.14 Net bearing pressure vs. displacement for Load Cases 3.10, 3.25, and 4.25 with D_f = B (VD)

The bearing pressure distribution measured for each load test is shown in Figure 6.15. The loading position and orientation is displayed in each plot to illustrate how the pressure distribution is developed. Load Case-3 with L/A = 0.25 (LT-180 and LT-181) demonstrates a trapezoidal shape with increasing pressure on the side of eccentric-inclined loading. Load Case-3 with L/A = 0.10 and Load Case-4 with L/A = 0.25 have similar pressure distribution shapes with the highest pressure located at PS-2. Load Case-3 with L/A = 0.25 reports the lowest bearing pressures as expected followed by Load Case-3 with L/A = 0.10, then Load Case-4 with L/A = 0.25.

6.2 Model Load Tests on Square Footing (L/B = 1) for Medium Dense Condition

Each load case was tested at two separate embedment depths (D_f = 0 and D_f = 0.5B) for lateral-to-axial ratios of 0.10 and 0.25 for two relative density conditions (medium dense and very dense). All eccentric loads were applied B/6 from centerline of the footing. Replicates of each case were performed to check for experimental repeatability. Table 6.8 lists the identifiers for each test with the date, soil condition, load case and footing configuration.

Table 6.8 List of load test for square footings on medium dense soil

Name	Date	Load Case	Density (D_r)	Embedment Depth (D_f)	Eccentricity	Inclination L/A ratio	Series #
LT-91	8/28/19	1	Medium Dense	0	0	0	1
LT-92	8/29/19	1	Medium Dense	0	0	0	2
LT-93	8/29/19	1	Medium Dense	0	0	0	3
LT-94	8/29/19	1	Medium Dense	0.5B	0	0	1
LT-95	8/30/19	1	Medium Dense	0.5B	0	0	2
LT-96	8/30/19	2	Medium Dense	0	B/6	0	1
LT-97	9/01/19	2	Medium Dense	0	B/6	0	2
LT-98	9/01/19	2	Medium Dense	0.5B	B/6	0	1
LT-99	9/02/19	2	Medium Dense	0.5B	B/6	0	2
LT-100	9/02/19	3	Medium Dense	0	B/6	0.10	1
LT-101	9/02/19	3	Medium Dense	0	B/6	0.10	2
LT-102	9/02/19	3	Medium Dense	0.5B	B/6	0.10	1
LT-103	9/03/19	3	Medium Dense	0.5B	B/6	0.10	2
LT-104	9/03/19	4	Medium Dense	0	0	0.10	1
LT-105	9/03/19	4	Medium Dense	0	0	0.10	2
LT-106	9/03/19	4	Medium Dense	0	0	0.10	3
LT-107	9/03/19	4	Medium Dense	0.5B	0	0.10	1
LT-108	9/04/19	4	Medium Dense	0.5B	0	0.10	2
LT-109	9/04/19	5	Medium Dense	0	B/6	0.10	1
LT-110	9/04/19	5	Medium Dense	0	B/6	0.10	2
LT-111	9/05/19	5	Medium Dense	0.5B	B/6	0.10	1
LT-112	9/05/19	5	Medium Dense	0.5B	B/6	0.10	2
LT-113	9/06/19	3	Medium Dense	0	B/6	0.25	1
LT-114	9/06/19	3	Medium Dense	0	B/6	0.25	2
LT-115	9/06/19	3	Medium Dense	0.5B	B/6	0.25	1
LT-116	9/06/19	3	Medium Dense	0.5B	B/6	0.25	2
LT-117	9/07/19	4	Medium Dense	0	0	0.25	1
LT-118	9/07/19	4	Medium Dense	0	0	0.25	2

Table 6.8 (continued)

LT-119	9/07/19	4	Medium Dense	0.5B	0	0.25	1
LT-120	9/07/19	4	Medium Dense	0.5B	0	0.25	2
LT-121	9/08/19	5	Medium Dense	0	B/6	0.25	1
LT-122	9/09/19	5	Medium Dense	0	B/6	0.25	2
LT-123	9/09/19	5	Medium Dense	0.5B	B/6	0.25	1
LT-124	9/10/19	5	Medium Dense	0.5B	B/6	0.25	2

6.2.1 Lateral-to-Axial Ratios of 0.10 with Depth of Embedment Equal to Zero

In this series of tests, the square footing was loaded for Load Cases 1–5 with depth of embedment equal to zero. The AASHTO A3 soil used in the tests had an average dry unit weight, $\gamma_{dry,}$ in the range of 101.39 lb/ft^3 to 101.57 lb/ft^3 and average relative density, D_r in the range of 63.09% to 64.02% for the top soil layers where the failure surface was observed. The average peak friction angle from the direct shear test was estimated to be in the range of 32.43° to 32.60°. The model footing was tested at N = 40 G, which equates to a prototype footing length of 5 feet by 5 feet in width with the L/B ratio of 1. All eccentric loads were applied B/6 (0.25 inches) from the center of the footing and inclined loads were applied at a lateral-to-axial ratio of 0.10 (5.7°). The combined eccentric-inclined load test applied the same geometric loading conditions as the individual parts.

The net bearing capacity for each test is presented in Figure 6.15. All eccentric and eccentric-inclined loading conditions used the effective width B' to determine the bearing pressure.

Listed in Table 6.9 are the internal friction angles, unit weight, relative density, and net measured bearing capacities with percent differences to demonstrate repeatability for each test.

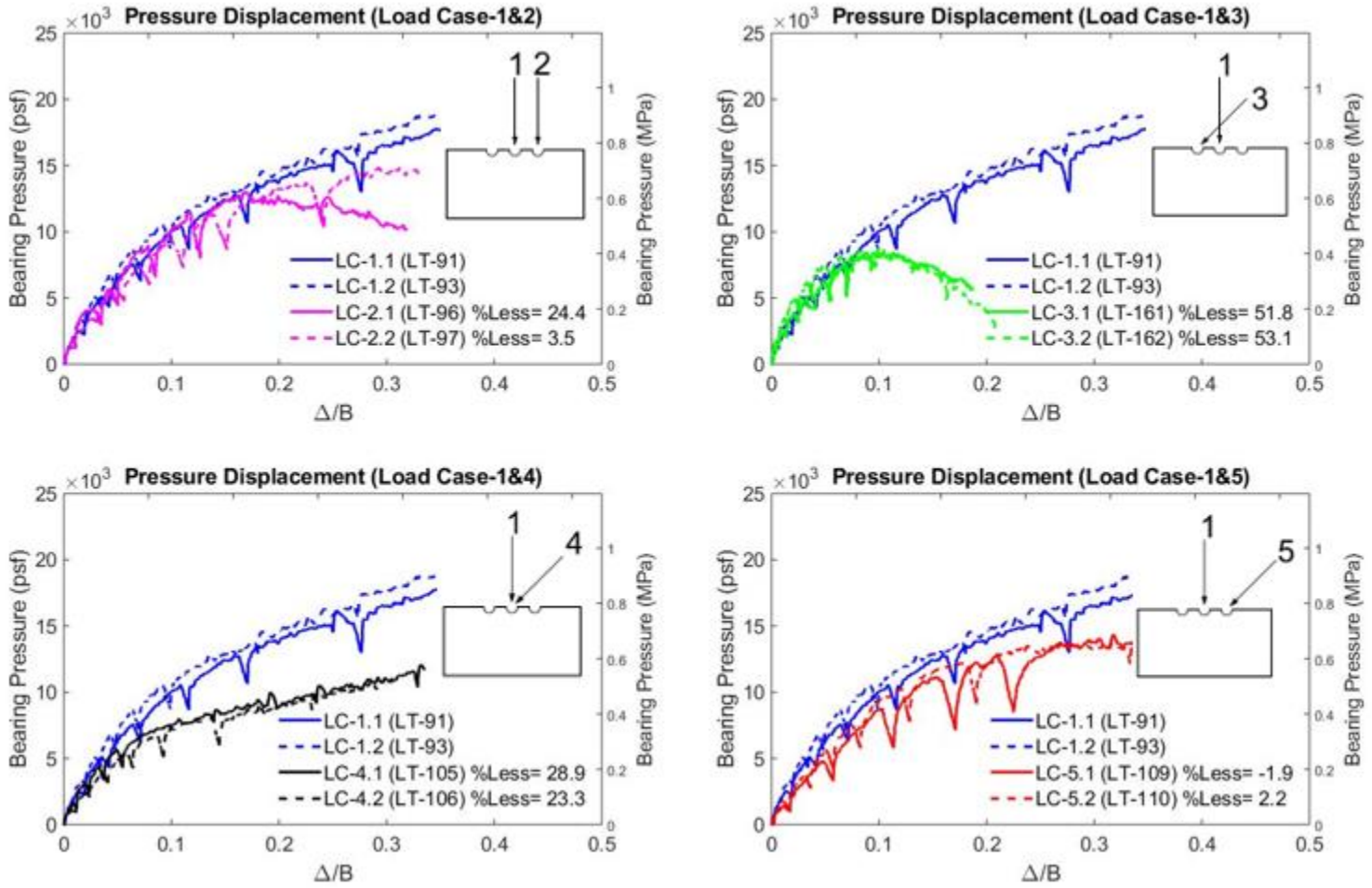

Figure 6.15 Net bearing pressure vs. displacement for Load Cases 1–5 with lateral-to-axial ratio = 0.1 and D_f = 0 (MD)

Table 6.9 Summary of measured test parameters and results for L/B = 1 with lateral-to-axial ratio = 0.1 and D_f = 0 (MD)

Load Test	Load Case	ϕ (deg)	γ_{dry} (lb/ft^3)	D_r (%)	Δ/B	q_{net} Measured (psf)	Percent Difference (%)
LT-91	1	32.48	101.44	63.33	0.138	12,875	0.97
LT-93	1	32.55	101.50	63.67	0.111	13,000	
LT-96	2	32.43	101.39	63.09	0.164	11,600	3.83
LT-97	2	32.58	101.54	63.90	0.223	11,164	
LT-161	3	32.53	101.48	63.56	0.084	8,618	2.88
LT-162	3	32.51	101.47	63.52	0.098	8,870	
LT-105	4	32.50	101.46	63.46	0.070	7,732	6.06
LT-106	4	32.55	101.51	63.71	0.076	7,277	
LT-109	5	32.65	101.61	64.25	0.141	10,570	0.09
LT-110	5	32.6	101.57	64.02	0.140	10,580	

The bearing pressure distribution observed by the miniature pressure transducers is presented for each load test in Figures 6.16 and 6.17. The loading position and orientation is displayed in each plot to illustrate how the pressure distribution is developed. The pressure sensors were position beneath the footing in sequential order (PS-1 through PS-4) from left to right at a spacing of 0.36 inches in model scale as previously stated.

Load Case-1 (LT-91 and LT-93) generally shows more of a uniform pressure distribution compared with the L/B = 10 tests. The pressure displacement results and the lack of an observed failure surface at the sand surface indicates that general shear failure was not obtained for the footing penetrations. The curves suggest local or punching shear failure which may explain the higher edge pressures when the shear is not mobilized in a square footing compared to a rectangular footing. Load Case-2 (LT-96 and LT-97), Load Case-3 (LT-161 and LT-162), Load Case-4 (LT-105 and LT-106), and Load Case-5 (LT-109 and LT-110) demonstrates a trapezoidal shape with increasing pressure on the side of eccentricity, inclination or eccentric-inclined loading, which was also observed in numerical models by Loukidis et al. (2008) (Figure 6.4).

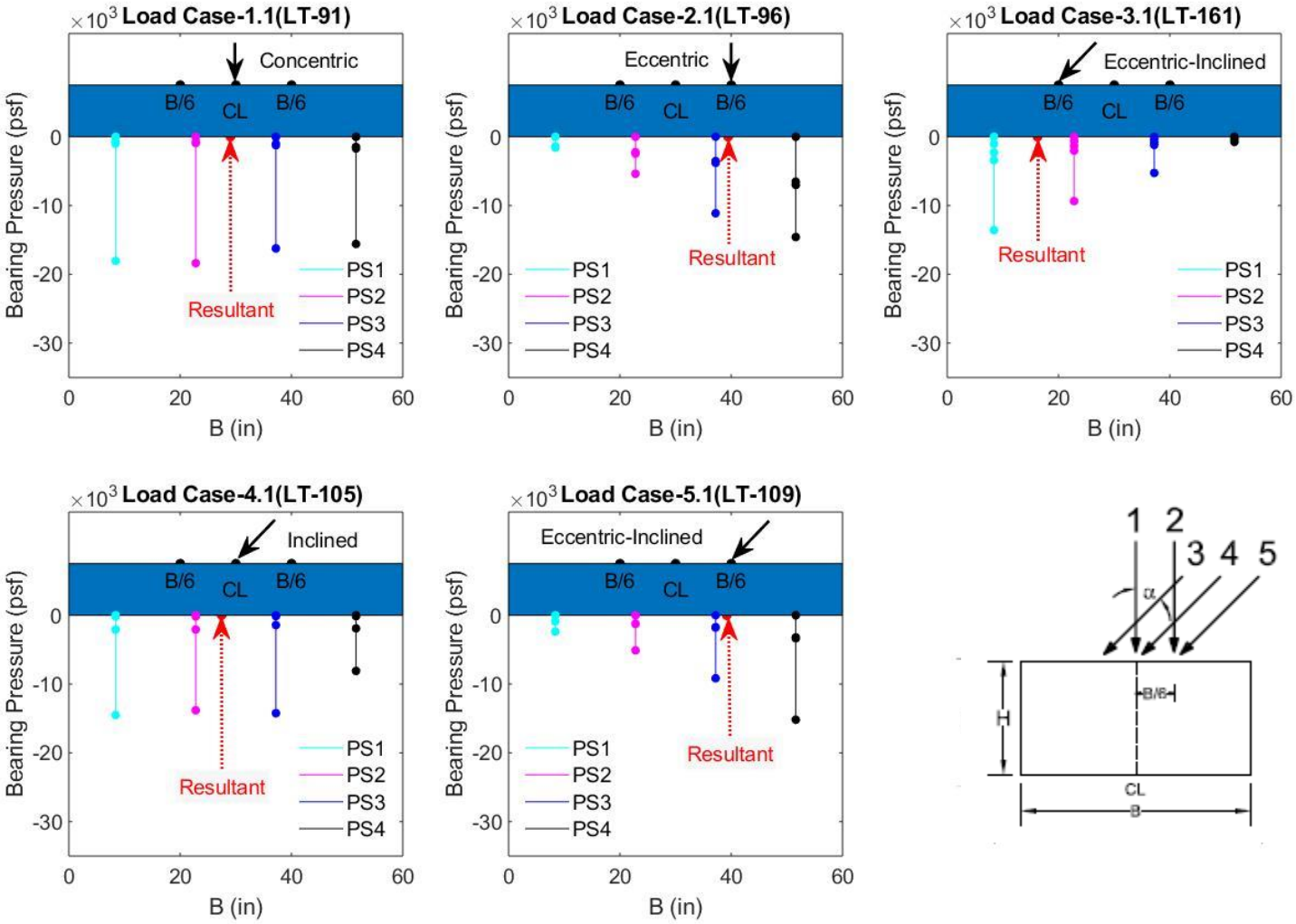

Figure 6.16 Bearing pressure distribution for Load Cases 1–5 with lateral-to-axial ratio = 0.1 and D_f = 0

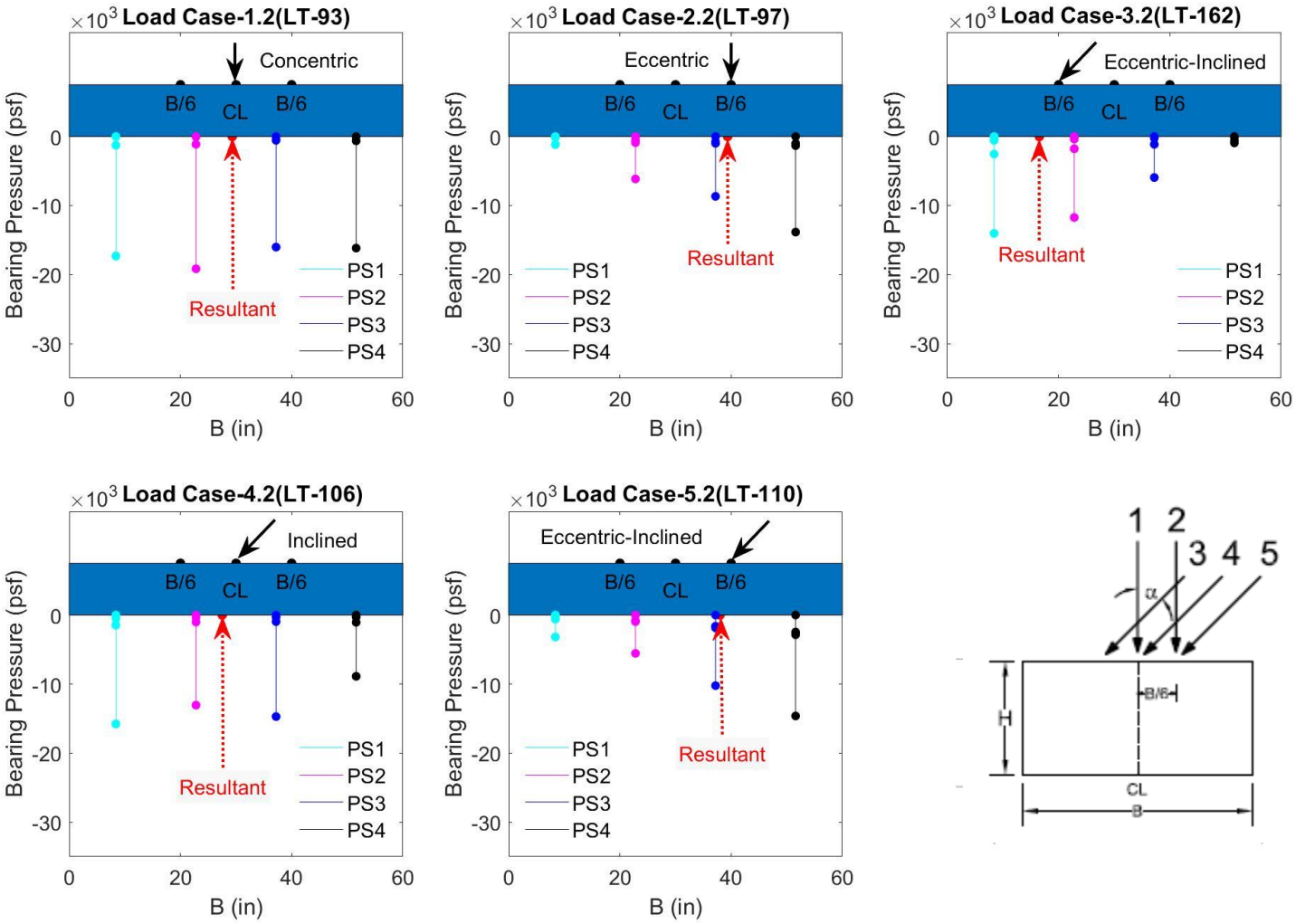

Figure 6.17 Bearing pressure distribution for Load Cases 1–5 with lateral-to-axial ratio = 0.1 and D_f = 0

Load Case-4 (LT-105 and LT-106) demonstrate a non-uniform pressure distribution with an increasing radial shape towards the center of the footing similar to Load Case-1.
Similar to the results presented in the pressure displacement plots, Load Case-1 reports the highest bearing pressure and Load Case-3 reports the lowest bearing pressures. Comparing Load Case-3 and Load Case-5, the latter shows an increase in bearing pressure over Load Case-3.

6.2.2 Lateral-to-Axial Ratios of 0.10 with Depth of Embedment Equal to 0.5B

In this series of tests, the square footing was loaded for Load Cases 1–5 with depth of embedment equal to 0.5B. The AASHTO A3 soil used in the tests had an average dry unit weight, $\gamma_{dry,}$ in the range of 101.45 lb/ft^3 to 101.58 lb/ft^3 and average relative density, D_r in the range of 63.38% to 64.11% for the top soil layers where the failure surface was observed. The average peak friction angle from the direct shear test was estimated to be in the range of 32.49° to 32.62°. The model footing was tested at N = 40 G, which equates to a prototype footing length of 5 feet by 5 feet in width with the L/B ratio of 1 and embedment depth equal to 0.5B. All eccentric loads were applied at a distance of B/6 (0.25 inches) from the center of the footing and inclined loads were applied at a lateral-to-axial ratio of 0.10 (5.7°). The combined eccentric-inclined load test applied the same geometric loading conditions as the individual parts. The net bearing capacity for each test are presented in Figure 6.18. All eccentric and eccentric-inclined loading conditions used the effective width B' to determine the bearing pressure.

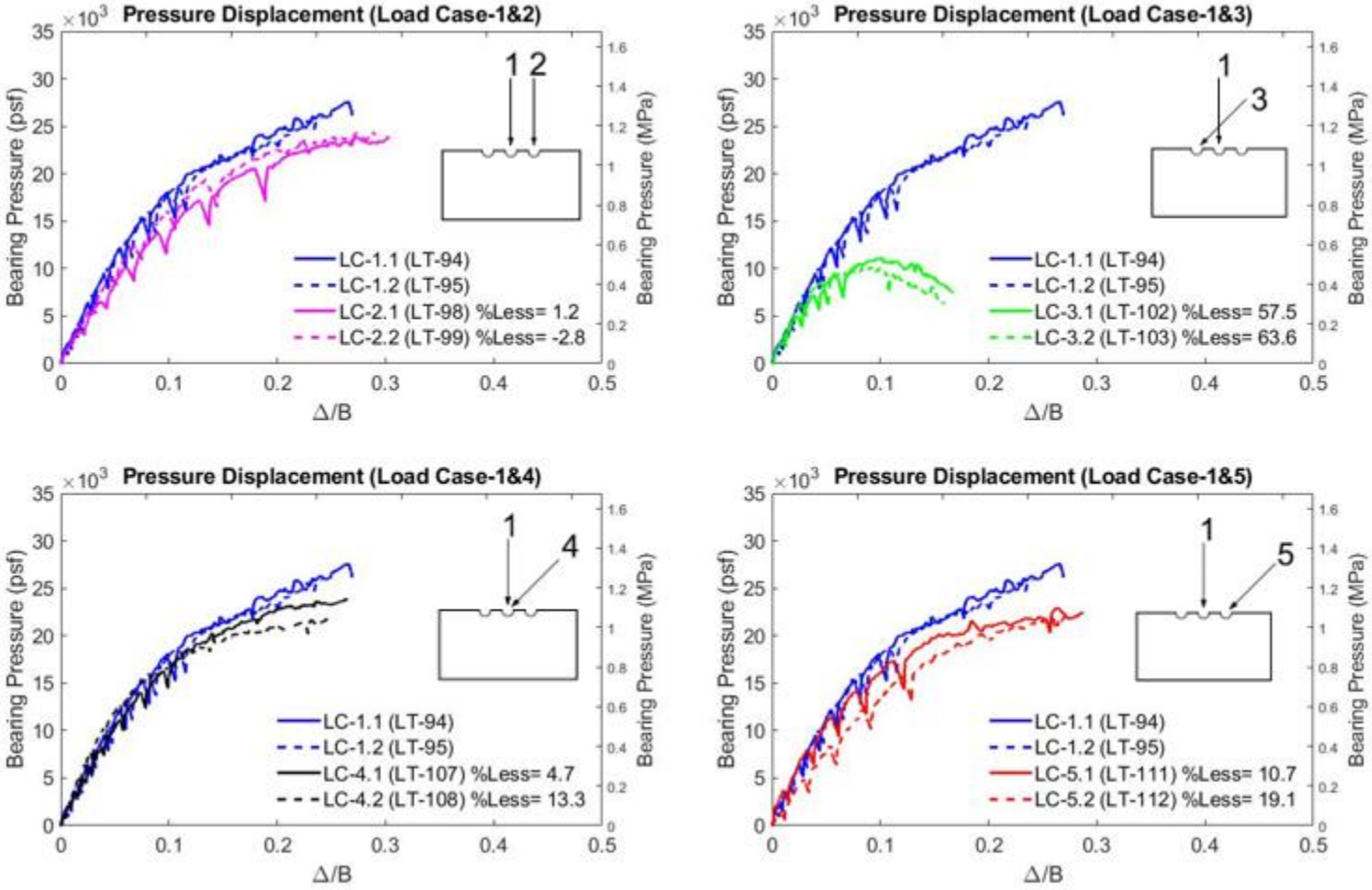

Figure 6.18 Net bearing pressure vs. displacement for Load Cases 1–5 with lateral-to-axial ratio = 0.1 and D_f = 0.5B (MD)

Listed in Table 6.10 are the internal friction angles, unit weight, relative density, and net measured bearing capacities with percent differences to demonstrate repeatability for each test.

Table 6.10 Summary of measured test parameters and results for L/B = 1 with lateral-to-axial ratio = 0.1 and D_f = 0.5B (MD)

Load Test	Load Case	ϕ (deg)	γ_{dry} (lb/ft^3)	D_r (%)	Δ/B	q_{net} Measured (psf)	Percent Difference (%)
LT-94	1	32.60	101.56	64.00	0.090	19,670	2.57
LT-95	1	32.60	101.52	63.77	0.083	19,170	
LT-98	2	32.49	101.45	63.38	0.139	18,421	4.16
LT-99	2	32.52	101.48	63.56	0.117	17,671	
LT-102	3	32.57	101.53	63.81	0.099	10,861	6.07
LT-103	3	32.62	101.58	64.11	0.092	10,221	
LT-107	4	32.62	101.58	64.09	0.083	16,871	3.31
LT-108	4	32.61	101.57	64.03	0.069	16,321	
LT-111	5	32.61	101.56	64	0.093	18,221	1.10
LT-112	5	32.51	101.47	63.52	0.118	18,021	

The bearing pressure distribution observed by the miniature pressure transducers is presented for each load test in Figures 6.19 and 6.20. The loading position and orientation is displayed in each plot to illustrate how the pressure distribution is developed. The pressure sensors were position beneath the footing in sequential order (PS-1 through PS-4) from left to right at a spacing of 0.36 inches in model scale as previously stated.

Load Case-1 (LT-94 and LT-95) generally shows more of a uniform pressure distribution compared with the L/B = 10 tests. The pressure displacement results and the lack of an observed failure surface at the sand surface indicates that general shear failure was not obtained for the footing penetrations. The curves suggest local or punching shear failure which may explain the higher edge pressures when the shear is not mobilized in a square footing compared to a rectangular footing.

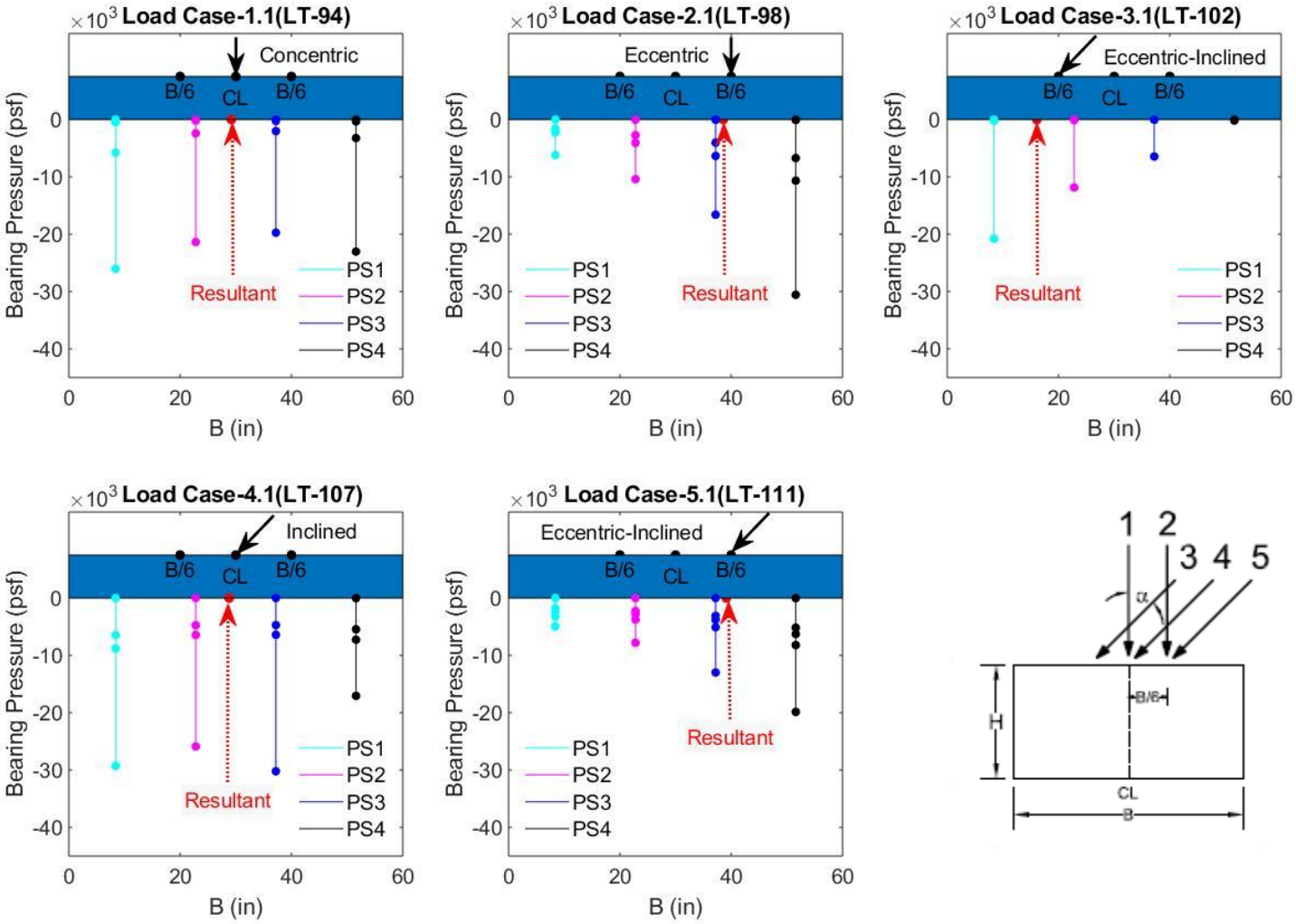

Figure 6.19 Bearing pressure distribution for Load Cases 1–5 with lateral-to-axial ratio = 0.1 and D_f = 0.5B

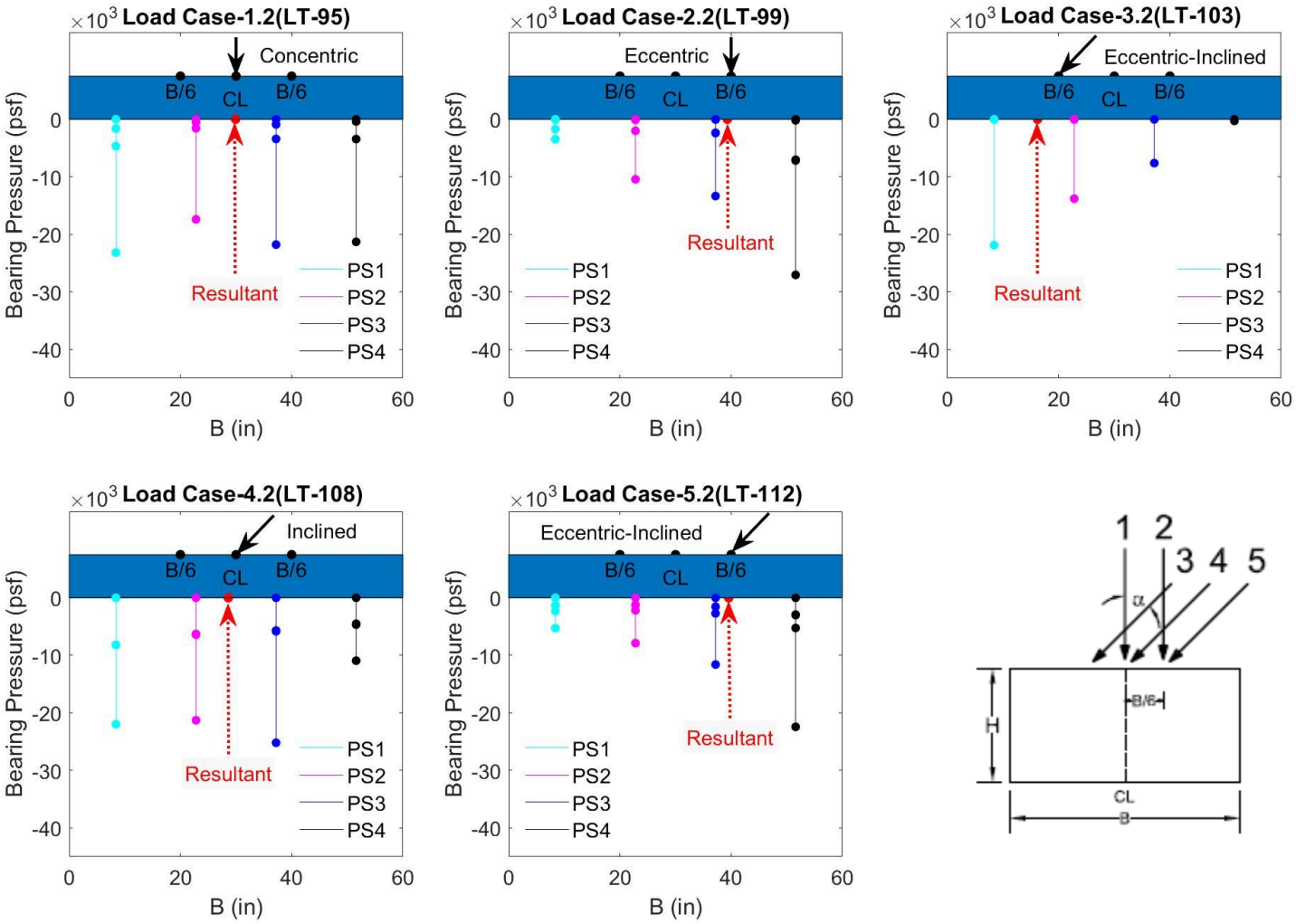

Figure 6.20 Bearing pressure distribution for Load Cases 1–5 with lateral-to-axial ratio = 0.1 and D_f = 0.5B

Load Case-2 (LT-98 and LT-99), Load Case-3 (LT-102 and LT-103), and Load Case-5 (LT-111 and LT-112) demonstrate a trapezoidal shape while Load Case-4 (LT-107 and LT-108) is a non-uniform distribution, although each shows the effect of increasing pressure on the side of eccentricity, inclination or eccentric-inclined loading, which was also observed in numerical models by Loukidis et al. (2008) (Figure 6.4).

6.2.3 Lateral-to-Axial Ratios of 0.25 with Depth of Embedment Equal to Zero

In this series of tests, the square footing was loaded for Load Cases 1–5 with depth of embedment equal to zero. The AASHTO A3 soil used in the tests had an average dry unit weight, $\gamma_{dry,}$ in the range of 101.39 lb/ft^3 to 101.63 lb/ft^3 and average relative density, D_r in the range of 63.09% to 64.36% for the top soil layers where the failure surface was observed. The average peak friction angle from the direct shear test was estimated to be in the range of 32.43° to 32.67°. The model footing was tested at N = 40 G, which equates to a prototype footing length of 5 feet by 5 feet in width with the L/B ratio of 1 and embedment depth equal to zero. All eccentric loads were applied B/6 (0.25 inches) from the center of the footing and inclined loads were applied at a lateral-to-axial ratio of 0.25 (14.0°). The combined eccentric-inclined load tests applied the same geometric loading conditions as the individual parts. The net bearing capacity for each test are presented in Figure 6.21.

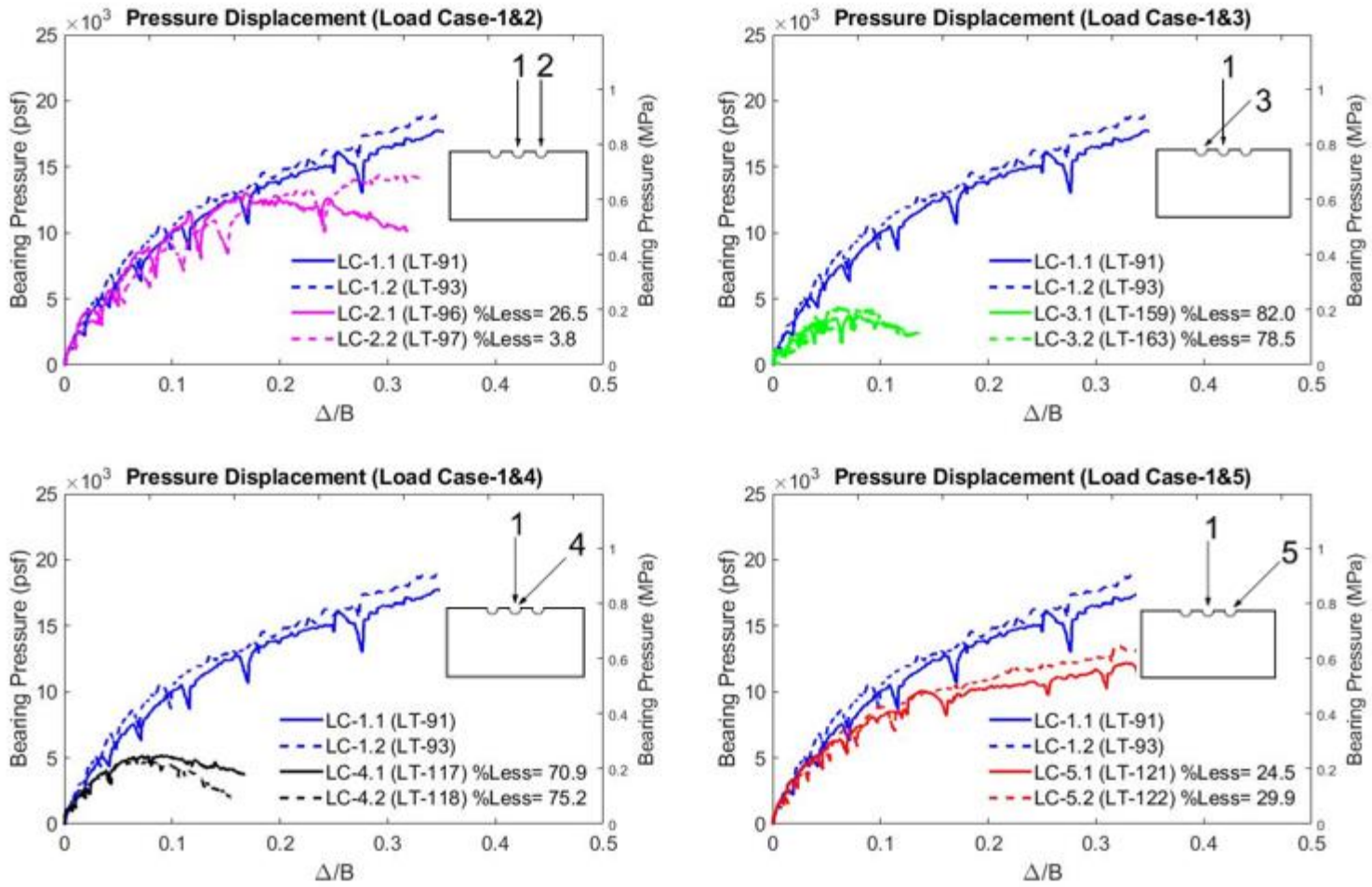

Figure 6.21 Net bearing pressure vs. displacement for Load Case-1 to Load Case-5 with lateral-to-axial ratio = 0.25 and D_f = 0 (MD)

All eccentric and eccentric-inclined loading conditions used the effective width B' to determine the bearing pressure. Listed in Table 6.11 are the internal friction angles, unit weight, relative density, and net measured bearing capacities with percent differences to demonstrate repeatability for each test.

Table 6.11 Summary of measured test parameters and results for L/B = 1 with lateral-to-axial ratio = 0.25 and D_f = 0 (MD)

Load Test	Load Case	ϕ (deg)	γ_{dry} (lb/ft^3)	D_r (%)	Δ/B	q_{net} Measured (psf)	Percent Difference (%)
LT-91	1	32.48	101.44	63.33	0.138	12,875	0.97
LT-93	1	32.55	101.50	63.67	0.1112	13,000	
LT-96	2	32.43	101.39	63.09	0.164	11,600	3.83
LT-97	2	32.58	101.54	63.90	0.22	11,164	
LT-159	3	32.56	101.52	63.79	0.07	3,825	15.77
LT-163	3	32.57	101.53	63.84	0.061	4,480	
LT-117	4	32.67	101.63	64.36	0.093	5,165	9.00
LT-118	4	32.62	101.58	64.1	0.068	4,720	
LT-121	5	32.53	101.49	63.61	0.143	10,054	2.50
LT-122	5	32.51	101.49	63.63	0.163	10,309	

The bearing pressure distribution observed by the miniature pressure transducers is presented for each load test in Figures 6.22 and 6.23. The loading position and orientation is displayed in each plot to illustrate how the pressure distribution is developed. The pressure sensors were positioned beneath the footing in sequential order (PS-1 through PS-4) from left to right at a spacing of 0.36 inches in model scale as previously stated.

Load Case-1 (LT-91 and LT-93) generally shows more of a uniform pressure distribution compared with the L/B = 10 tests. The pressure displacement results and the lack of an observed failure surface at the sand surface indicates that general shear failure was not obtained for the footing penetrations. The curves suggest local or punching shear failure which may explain the higher edge pressures when the shear is not mobilized in a square footing compared to a

rectangular footing. Load Case-2 (LT-96 and LT-97), Load Case-3 (LT-159 and LT-163), Load Case-4 (LT-117 and LT-118), and Load Case-5 (LT-121 and LT-122) demonstrate a trapezoidal shape with increasing pressure on the side of eccentricity, inclination or eccentric-inclined loading, which was also observed in numerical models by Loukidis et al. (2008) (Figure 6.4).

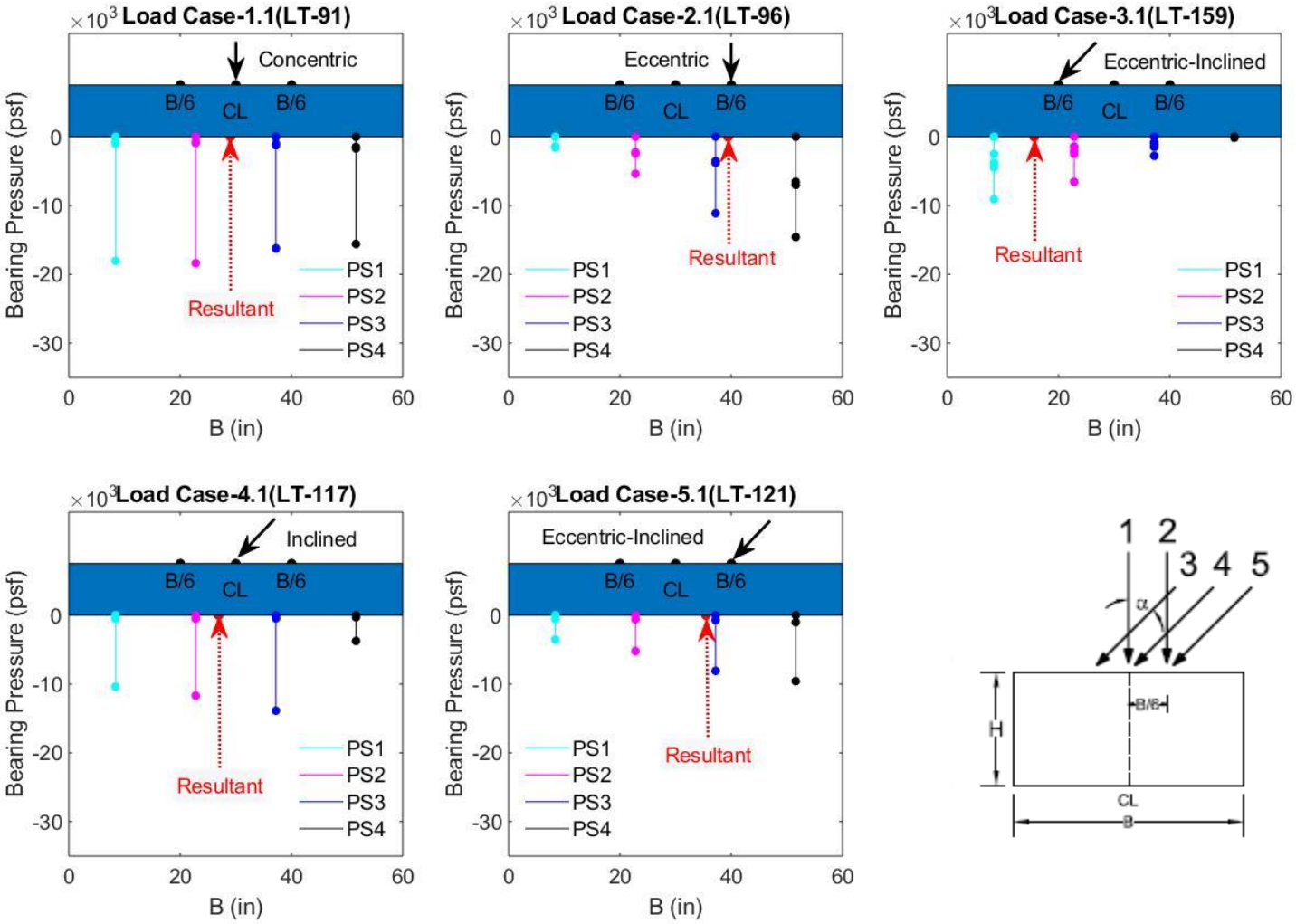

Figure 6.22 Bearing pressure distribution for Load Cases 1–5 with lateral-to-axial ratio = 0.25 and D_f = 0

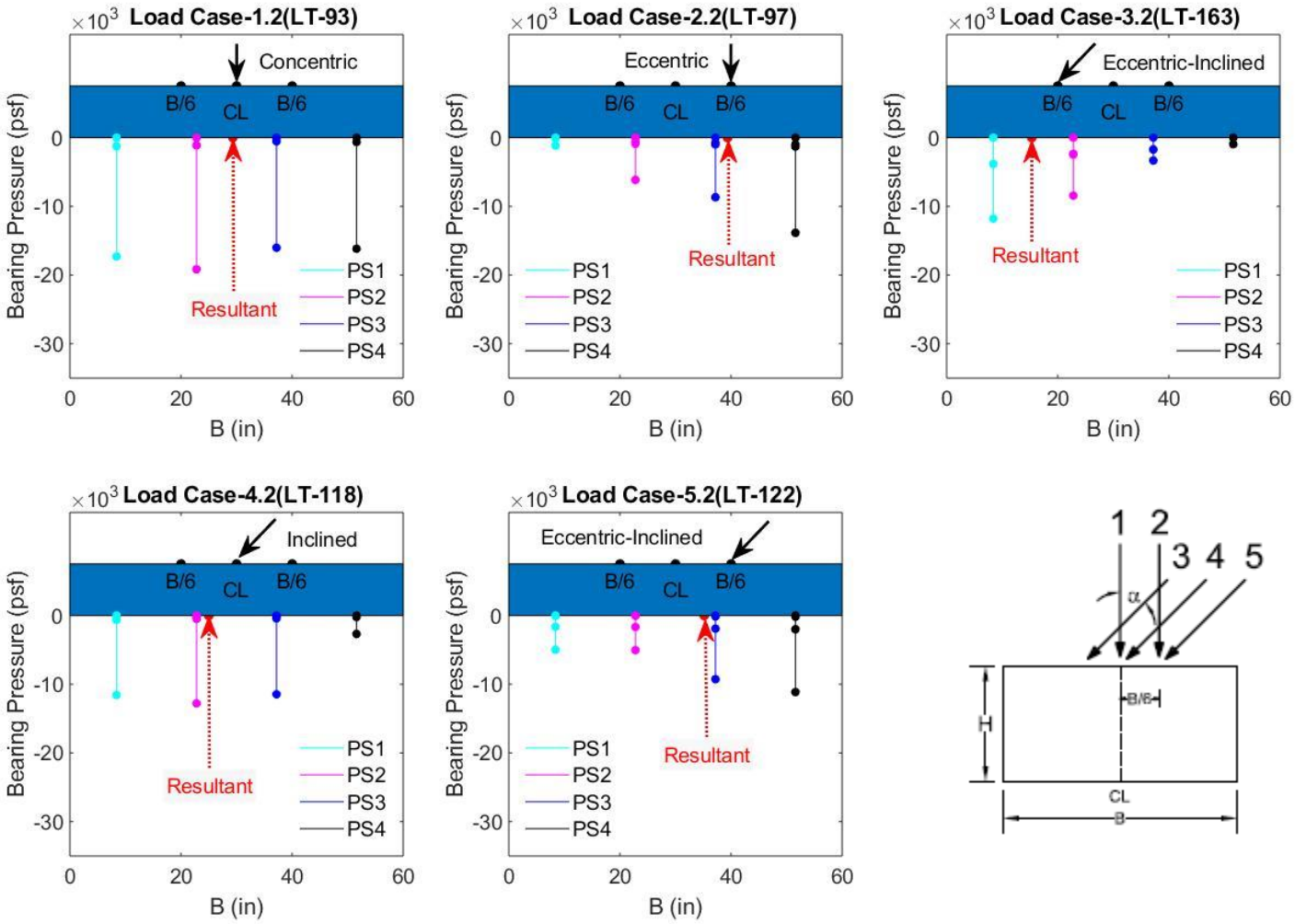

Figure 6.23 Bearing pressure distribution for Load Cases 1–5 with lateral-to-axial ratio = 0.25 and $D_f = 0$

6.2.4 Lateral-to-Axial Ratios of 0.25 with Dept of Embedment Equal to 0.5B

In this series of tests, the square footing was loaded for Load Cases 1–5 with depth of embedment equal to 0.5B. The AASHTO A3 soil used in the tests had an average dry unit weight, $\gamma_{dry,}$ in the range of 101.45 lb/ft^3 to 101.56 lb/ft^3 and average relative density, D_r in the range of 63.38% to 64.00% for the top soil layers where the failure surface was observed. The average peak friction angle from the direct shear test was estimated to be in the range of 32.49° to 32.60°. The model footing was tested at N = 40 G, which equates to a prototype footing length of 5 feet by 5 feet in width with the L/B ratio of 1 and embedment depth equal to zero. All eccentric loads were applied at a distance of B/6 (0.25 inches) from the center of the footing and inclined loads were applied at a lateral-to-axial ratio of 0.25 (14.0°). The combined eccentric-inclined load test applied the same geometric loading conditions as the individual parts. The net bearing capacity for each test is presented in Figure 6.24. All eccentric and eccentric-inclined loading conditions used the effective width B' to determine the bearing pressure. Listed in Table 6.12 are the internal friction angles, unit weight, relative density, and net measured bearing capacities with percent differences to demonstrate repeatability for each test.

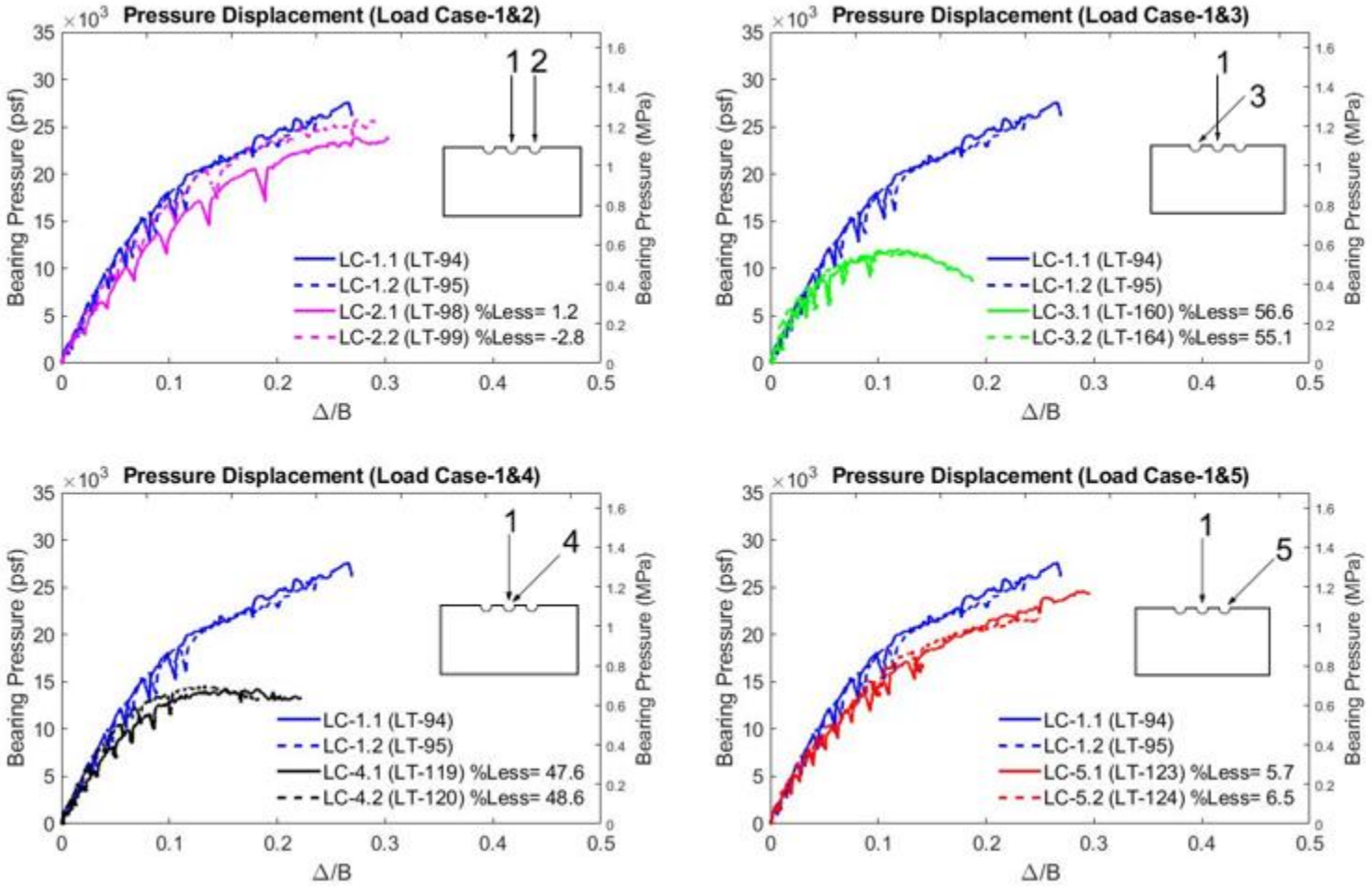

Figure 6.24 Net bearing pressure vs. displacement for Load Case-1 to Load Case-5 with lateral-to-axial ratio = 0.25 and D_f = 0.5B (MD)

Table 6.12 Summary of measured test parameters and results for L/B = 1 with lateral-to-axial ratio = 0.25 and D_f = 0.5B (MD)

Load Test	Load Case	ϕ (deg)	γ_{dry} (lb/ft^3)	D_r (%)	Δ/B	q_{net} Measured (psf)	Percent Difference (%)
LT-94	1	32.60	101.56	64.00	0.09	19,670	2.57
LT-95	1	32.60	101.52	63.77	0.08	19,170	
LT-98	2	32.49	101.45	63.38	0.139	18,421	4.16
LT-99	2	32.52	101.48	63.56	0.117	17,671	
LT-115	3	32.50	101.46	63.43	0.104	11,081	5.18
LT-116	3	32.52	101.45	63.43	0.119	10,521	
LT-119	4	32.54	101.50	63.69	0.129	13,782	1.58
LT-120	4	32.52	101.49	63.59	0.134	14,002	
LT-123	5	32.55	101.51	63.72	0.163	17,822	0.55
LT-124	5	32.58	101.54	63.87	0.158	17,921	

The bearing pressure distribution observed by the miniature pressure transducers is presented for each load test in Figures 6.25 and 6.26. The loading position and orientation are displayed in each plot to illustrate how the pressure distribution is developed. The pressure sensors were positioned beneath the footing in sequential order (PS-1 through PS-4) from left to right at a spacing of 0.36 inches in model scale as previously stated.

Load Case-1 (LT-94 and LT-95) generally shows more of a uniform pressure distribution compared with the L/B = 10 tests and for some test's higher pressures at the outside edges (LT-95 shows non-uniform distribution thought to be due to possible arching in the sand). The pressure displacement results and the lack of an observed failure surface at the sand surface suggests that general shear failure was not obtained for the footing penetrations. The curves suggest local or punching shear failure which may explain the higher edge pressures when the shear is not mobilized in a square footing compared to a rectangular footing. Load Case-2 (LT-98 and LT-99), Load Case-3 (LT-115 and LT-116), Load Case-4 (LT-119 and LT-120), and Load Case-5 (LT-123 and LT-124) demonstrate a trapezoidal shape with increasing pressure on

the side of eccentricity, inclination or eccentric-inclined loading, which was also observed in numerical models by Loukidis et al. (2008) (Figure 6.4).

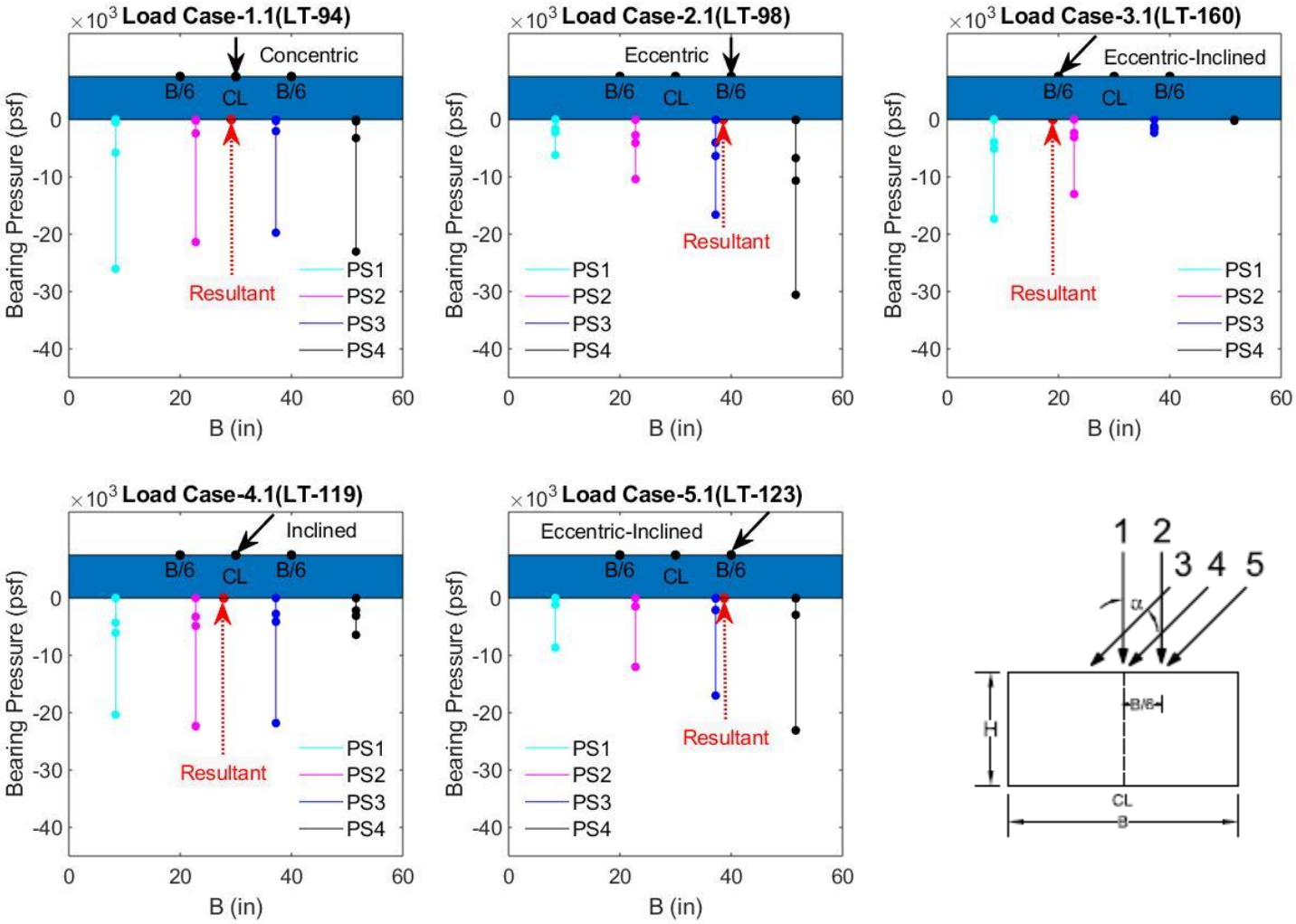

Figure 6.25 Bearing pressure distribution for Load Cases 1–5 with lateral-to-axial ratio = 0.25 and D_f = 0.5B

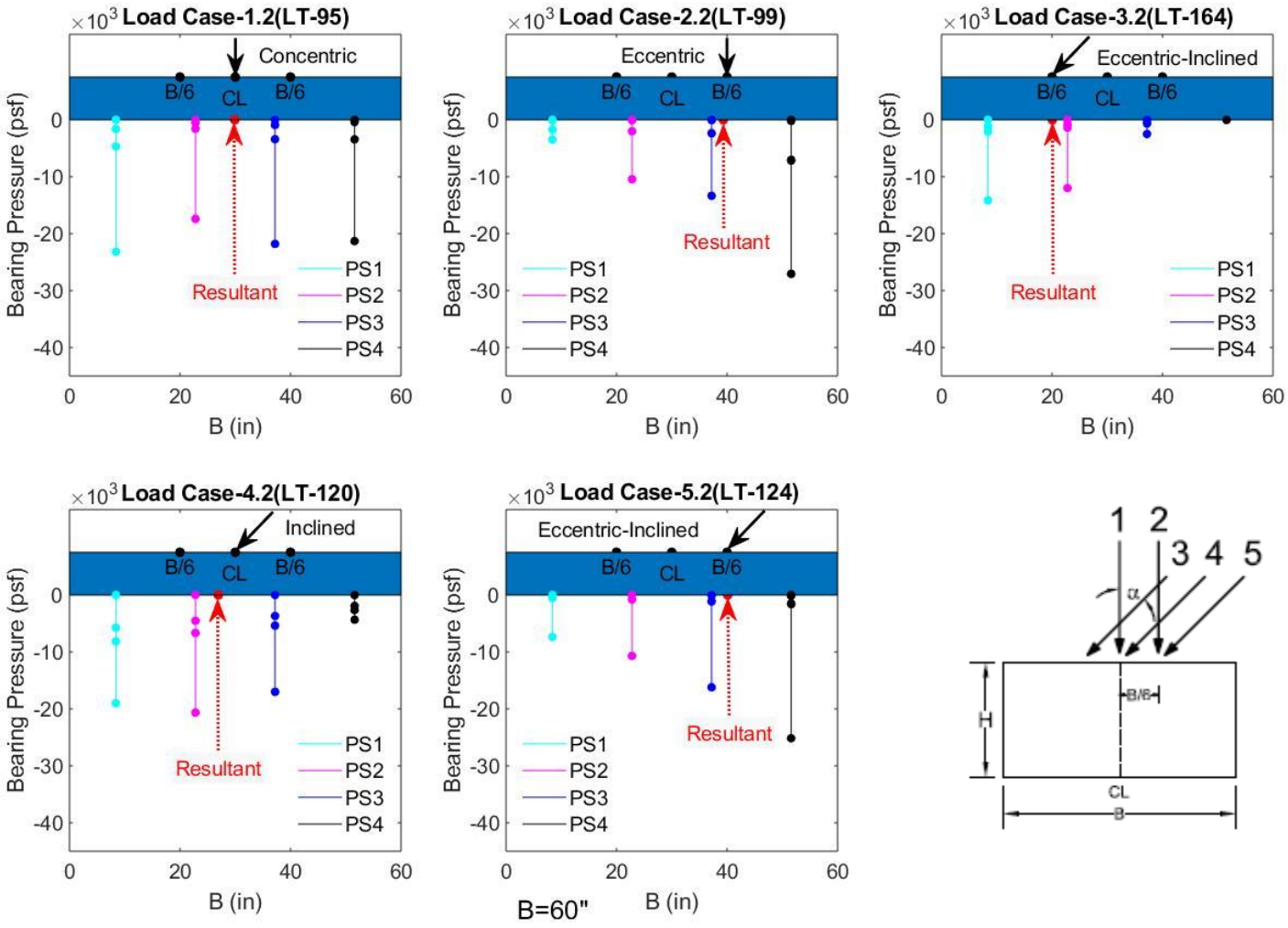

Figure 6.26 Bearing pressure distribution for Load Cases 1–5 with lateral-to-axial ratio = 0.25 and D_f = 0.5B

6.3 Conclusions on Square Footing (L/B = 1) Tests

Centrifuge tests of L/B = 1 footings on very dense and medium dense sand were conducted to investigate the influence of inclined and inclined-eccentric loading on the bearing capacity when the depth of embedment is zero and 0.5B. For the tests on very dense sand, the following observations of the bearing capacity were made.

- Load Case-3 (eccentric-inclined loading with + load combination (partially compensating)) is the most critical of all the cases. When $D_f = 0$, the bearing capacity was 55.3% and 63.7% less than the concentrically loaded footing (Load Case-1) for the lateral-to-axial load ratios of 0.10 and 0.25, respectively. When $D_f = 0.5B$, the bearing capacity was 48.2% and 62.9% less than the concentrically loaded footing with $D_f = 0.5B$ (Load Case-1) for the lateral-to-axial load ratios of 0.10 and 0.25, respectively.
- Load Case-4 (inclined loading): When $D_f = 0$ the bearing capacity was 40.8% and 56.7% less than the concentrically loaded footing (Load Case-1) for the lateral-to-axial load ratios of 0.10 and 0.25, respectively. When $D_f = 0.5B$, the bearing capacity was 36.6% and 56.5% less than the concentrically loaded footing with $D_f = 0.5B$ (Load Case-1) for the lateral-to-axial load ratios of 0.10 and 0.25, respectively.
- Load Case-5 (eccentric-inclined loading with – load combination (reinforcing)) generally showed less decrease in bearing capacity than Load Cases 3 and 4. When $D_f = 0$, the bearing capacity was 9.9% and 26.9% less than the concentrically loaded footing (Load Case-1) for the lateral-to-axial load ratios of 0.10 and 0.25, respectively. When $D_f = 0.5B$, the bearing capacity was 15.3% and 20.9% less than the concentrically loaded footing with $D_f = 0.5B$ (Load Case-1) for the lateral-to-axial load ratios of 0.10 and 0.25, respectively.

- Embedment of 0.5B had a marked effect on the bearing capacity of all load cases. Bearing capacity increased by 55.7% for Load Case-2 (eccentric load). Between tests of Load Case-3 (most critical), there was a 78.8% and 64.3% increase for the lateral-to-axial load ratios of 0.10 and 0.25, respectively. For Load Case-4, there was a 64.3% and 58.5% increase for the lateral-to-axial load ratios of 0.10 and 0.25, respectively. For Load Case-5, there was a 56.9% and 69.3% increase for the lateral-to-axial load ratios of 0.10 and 0.25, respectively.
- Two additional Load Case-3 (lateral-to-axial load ratios of 0.10 and 0.25) and one additional Load Case-4 (lateral-to-axial load ratio of 0.25) at an embedment of 1B were performed to further test the influence of this embedment. Between tests of Load Case-3 at embedment of 0.5B and 1B, there was a 37.8% and 59.7% increase for the lateral-to-axial load ratios of 0.10 and 0.25, respectively. Between tests of load case at embedment of 0.5B and 1B, there was a 65.7% increase for the lateral-to-axial load ratio 0.25 (most critical for Load Case-4).

For the tests on medium dense sand, the following observations of the bearing capacity were made.

- Load Case-3 (eccentric-inclined loading with + load combination (partially compensating)) is the most critical of all the cases. When $D_f = 0$, the bearing capacity was 33.4% and 67.9% less than the concentrically loaded footing (Load Case-1) for the lateral-to-axial load ratios of 0.10 and 0.25, respectively. When $D_f = 0.5B$, the bearing capacity was 45.7% and 44.4% less than the concentrically loaded footing with $D_f = 0.5B$ (Load Case-1) for the lateral-to-axial load ratios of 0.10 and 0.25, respectively.
- Load Case-4 (inclined loading): When $D_f = 0$ the bearing capacity was 42% and 61.8% less than the concentrically loaded footing (Load Case-1) for the lateral-to-axial load ratios of 0.10 and 0.25, respectively. When $D_f = 0.5B$, the bearing capacity was 14.5% and 28.5% less

than the concentrically loaded footing with $D_f = 0.5B$ (Load Case-1) for the lateral-to-axial load ratios of 0.10 and 0.25, respectively.

- Load Case-5 (eccentric-inclined loading with – load combination (reinforcing)) generally showed less decrease in bearing capacity than Load Cases 3 and 4. When $D_f = 0$, the bearing capacity was 18.3% and 21.3% less than the concentrically loaded footing (Load Case-1) for the lateral-to-axial load ratios of 0.10 and 0.25, respectively. When $D_f = 0.5B$, the bearing capacity was 6.7% and 8% less than the concentrically loaded footing with $D_f = 0.5B$ (Load Case-1) for the lateral-to-axial load ratios of 0.10 and 0.25, respectively.
- Embedment of 0.5B also had a marked effect on the bearing capacity of all load cases in medium dense sand. Bearing capacity increased by 45% for Load Case-2 (eccentric load). Between tests of Load Case-3 (most critical), there was a 18.2% and 88.6% increase for the lateral-to-axial load ratios of 0.10 and 0.25, respectively. For Load Case-4, there was a 75.2% and 94.8% increase for the lateral-to-axial load ratios of 0.10 and 0.25, respectively. For Load Case-5, there was a 52.3% and 54.6% increase for the lateral-to-axial load ratios of 0.10 and 0.25, respectively.

7.0 ANALYSIS OF TEST RESULTS AND COMPARISON TO EXISTING METHODS FOR BEARING CAPACITY

7.1 Analysis of Strip Footing Test Results

It was necessary to identify the appropriate N_γ and depth factors (d_q and d_γ) to be used in analysis of subsequent bearing capacity tests (L/B = 10 and 1) with eccentric and eccentric-inclined loads. Eq. 7.1 is the bearing capacity equation for an embedded footing with a concentric load. Factors to account for the footing shape (s_q and s_γ) and embedment (depth factors d_q and d_γ) influence on the embedment component and the soil self-weight component were included. The shape of L/B = 20 footings have negligible influence of bearing capacity, as evidenced by shape factors ≈ 1 (Section 7.4). Therefore, L/B = 20 footings embedded 0, 0.5B and B, were tested to identify these factors. Note, in the equations for bearing capacity and the influence factors, B = B′ and L = L′ for eccentrically loaded footings.

Eq. 7.1 is the traditional bearing capacity equation for the case of an embedded footing in cohesionless soil. In the case of a strip footing located at the surface, the bearing capacity equation reduces to the form presented in Eq. 7.2.

$$q_u = D_f \gamma N_q s_q d_q + 0.5 \gamma B N_\gamma s_\gamma d_\gamma \quad \text{Eq. 7.1}$$

$$q_u = 0.5 \gamma B N_\gamma s_\gamma d_\gamma \quad \text{Eq. 7.2}$$

Equations 7.3 and 7.4 are the AASHTO (2016) recommended bearing capacity factors for overburden, N_q (Reissner, 1924) and soil self-weight, N_γ (Vesić, 1973), respectively.

$$N_q = e^{\pi \tan \phi_f} tan^2 \left(45^\circ + \frac{\phi_f}{2}\right) \quad \text{Eq. 7.3}$$

$$N_\gamma = 2\left(N_q + 1\right) tan\left(\phi_f\right) \quad \text{Eq. 7.4}$$

Other methods for N_γ identified in the literature review, and presented in Task 1, based on centrifuge tests of strip footings (L/B = 5) on dense sand by Zhu et al. (2001) (shown in Equation 7.5) and another based on empirical relationships by Hansen's (1970) (shown in Equation 7.6)

was also used for analysis of bearing capacity results from the centrifuge tests.

$$N_\gamma = 2(N_q + 1)tan(1.07\phi_f) \quad \text{Eq. 7.5}$$

$$N_\gamma = 1.5(N_q - 1)tan(\phi_f) \quad \text{Eq. 7.6}$$

7.1.1 Depth of Embedment Factors Considered in Analysis

Factors to account for depth of embedment greater than zero for the overburden contribution, d_q, and self-weight contribution, d_γ, by Hansen (1970) and Vesić (1973) are shown in Equation 7.7 and 7.8, respectively.

$$d_q = 1 + 2\tan\phi_f \cdot (1 - \sin\phi_f)^2 \left(\frac{d_f}{B}\right) \text{ for } \frac{d_f}{B} \leq 1 \quad \text{Eq. 7.7}$$

$$d_\gamma = 1 \quad \text{Eq. 7.8}$$

Meyerhof (1963) proposed Eq. 7.9 and Eq. 7.10 for d_q and d_γ, respectively.

$$d_q = 1 + 0.1\sqrt{K_p}\left(\frac{d_f}{B}\right) \text{ for } \phi_f > 10^\circ \quad \text{Eq. 7.9}$$

$$d_\gamma = d_q \quad \text{Eq. 7.10}$$

where

$$K_p = \tan^2\left(45^\circ + \frac{\phi_f}{2}\right) \quad \text{Eq. 7.11}$$

The influence of depth of embedment in the tests is investigated through normalized bearing capacity values plotted against the footing embedment at peak load, where settlement at the peak load was added to the initial depth of embedment (Eq. 7.12). The normalized values were plotted against predicted values using the methods for d_q (Hansen (1970) and Vesić (1973) – Eqs. 7.7 and 7.8; and Meyerhof (1963) – Eqs. 7.9 and 7.10) and for the N_γ methods considered in the D_f = 0, 0.5B, and B cases (Vesić, 1973; Zhu et al., 2001; Hansen, 1970) in Figures 7.1 – 7.3.

$$\frac{q_u}{\gamma B} = \left(\frac{D_f + \delta}{B}\right) N_{qm} + (1/2)N_{\gamma m} \quad \text{Eq. 7.12}$$

Based on the limited number of tests of medium dense soil (ϕ = 30°-31°) the Meyerhof method for d_q is more representative than the Hansen method over the range of depth of embedment. Vacuuming in the preparation of the soil in earlier models which were prepared in a very dense state, resulted in tests on with less ϕ as indicated by Figure 7.2. Very dense soil resulted in ϕ = 34° - 36°, which is well reflected in Figure 7.3, where the normalized measured were well represented by the Meyerhof method for d_q and Vesić (1973) N_γ for smaller D_f and Hansen (1970) N_γ for larger D_f. In all cases, the Meyerhof method for d_q is the most representative of the test performed and were used in subsequent analysis.

The experimental values for N_q and N_γ were directly obtained from Figures 7.1-7.3, as the slope and twice the intercept for medium dense conditions and very dense condition using depth correction factors, d_q, by Meyerhof (1951) and Vesić (1975) and Hansen (1970). The values for N_q and N_γ achieved from the plots are presented in Table 7.1 with predicted Vesić-N_γ. Generally, for the MD and VD cases, N_q and N_γ solved through normalization (Eq. 7.12) agree with the predicted values, except for N_γ for the VD cases. This may be due to the capacity occurring at post-peak angle of internal friction, a reduced value closer to the residual angle of internal friction. Aiban and Znidarčić (1995) showed similar behavior in analysis of depth factors for bearing capacity of a footing on dense sand. The difference in the N_γ may be due to the error in predicting the angle of internal friction or the variability of the model soil. There is a change in N_γ of 55.05 to 80.05 for a change in angle of internal friction of 2.5°.

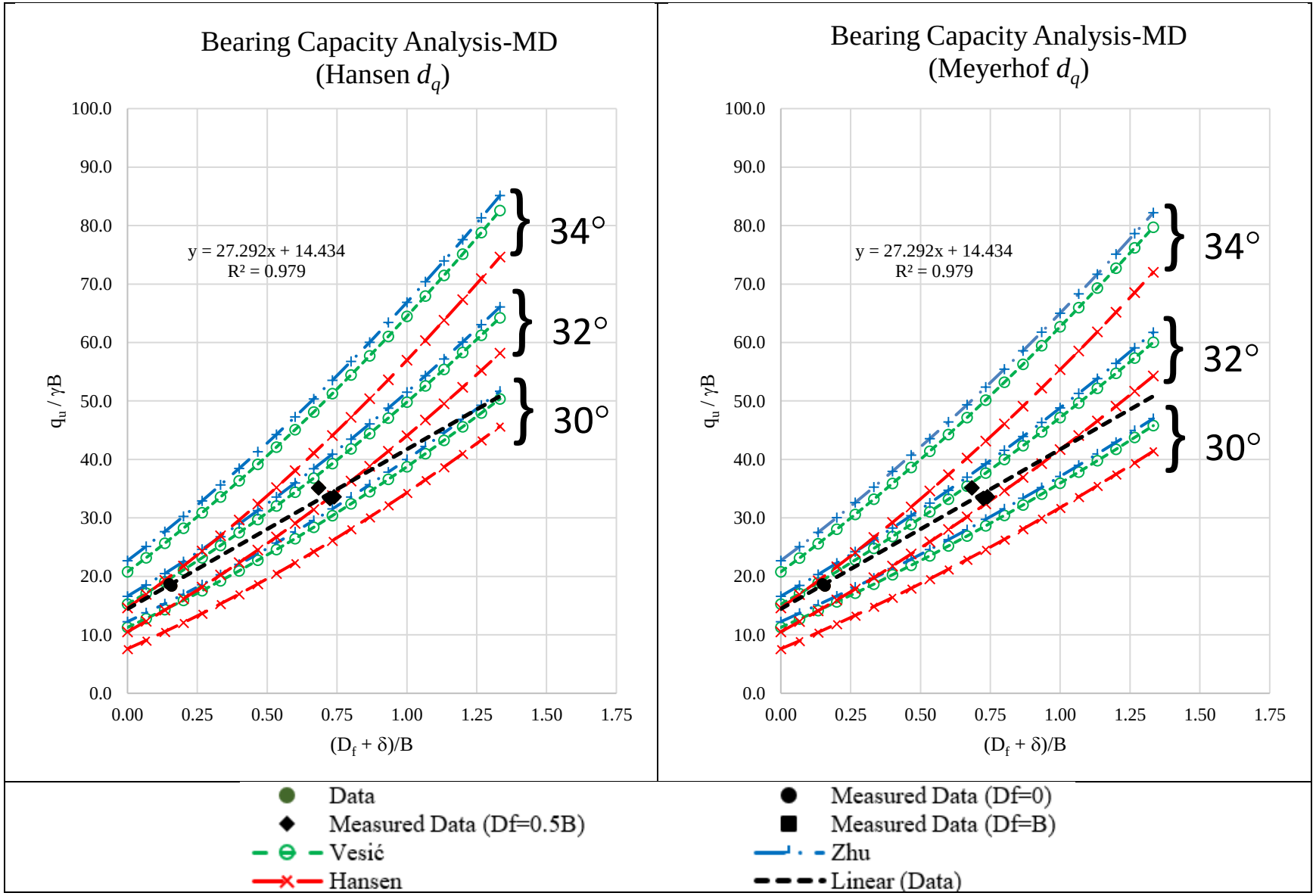

Figure 7.1 Experimental values for N_q and N_γ by slope and intercept method of medium dense cases

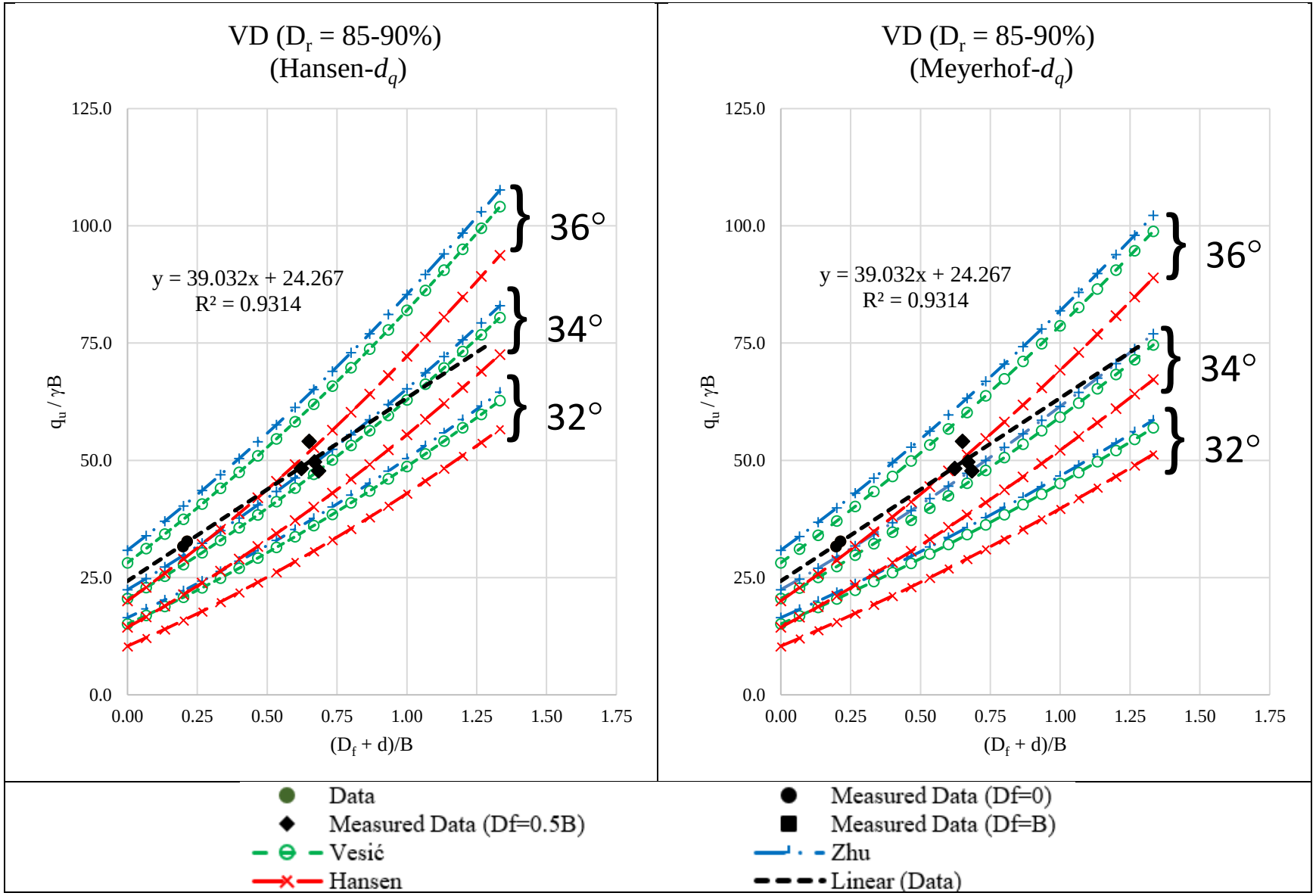

Figure 7.2 Experimental values for N_q and N_γ by slope and intercept method for very dense cases D_r = 85–90%

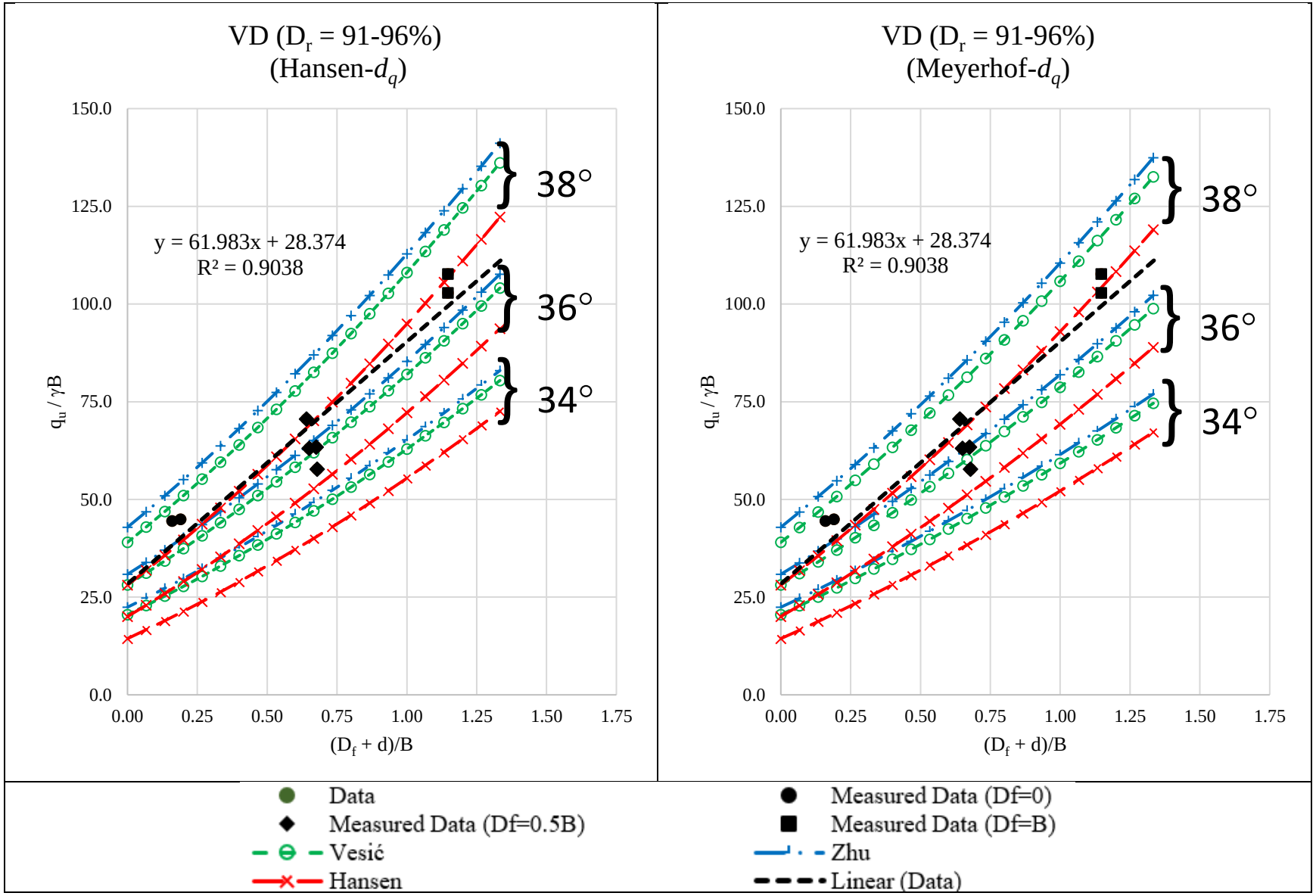

Figure 7.3 Experimental values for N_q and N_γ by slope and intercept method for very dense cases D_r = 91–96%

Table 7.1 Experimental values for N_q and N_γ by slope and intercept method

Relative Density	N_q (slope)	N_γ (2 * intercept)	Reissner -N_q	Vesić-N_γ
MD	27.29	28.87	24.88	33.10
VD*	39.03	48.53	34.44	50.12
VD**	61.98	56.75	49.59	72.43

* D_r = 85-90%, ** D_r = 91-96%

7.1.2 Shape Factors Considered in Analysis

Equations 7.13 and 7.14 are shape factors for overburden and soil self-weight originally by DeBeer (1970), and modified by Vesić (1973), recommended by AASHTO (2016) for rectangular footings.

Rectangular:

$$s_q = 1 + \left(\frac{B}{L}\tan\phi_f\right) \quad \text{Eq. 7.13}$$

$$s_\gamma = 1 - 0.4\left(\frac{B}{L}\right) \quad \text{Eq. 7.14}$$

Paikowsky et al. (2010) presented other equations for shape factor. Equations 7.15 and 7.16 are shape factors for overburden and soil self-weight recommended in EuroCode 7 (2005) and DIN 4017 (2006) for rectangular footings.

Rectangular:

$$s_q = 1 + \frac{B}{L}\sin\phi_f \quad \text{Eq. 7.15}$$

$$s_\gamma = 1 - 0.3\frac{B}{L} \quad \text{Eq. 7.16}$$

Equations 7.17 and 7.18 are shape factors for overburden and soil self-weight originally by Meyerhof (1963) for rectangular footings.

Rectangular:

$$s_q = 1 + 0.1K_p\left(\frac{B}{L}\right) \text{ for } \phi_f > 10^\circ \quad \text{Eq. 7.17}$$

$$s_\gamma = 1 + 0.1K_p\left(\frac{B}{L}\right) \quad \text{Eq. 7.18}$$

where

$$K_p = \tan^2\left(45^\circ + \frac{\phi_f}{2}\right) \quad \text{Eq. 7.19}$$

Equations 7.20 and 7.21 are shape factors for overburden and soil self-weight originally by Perau (1995, 1997) for rectangular footings.

Rectangular:

$$s_q = 1 + 1.6\tan\phi_f \cdot \left(\frac{\frac{B}{L}}{1+\left(\frac{B}{L}\right)^2}\right) \quad \text{Eq. 7.20}$$

$$s_\gamma = \frac{1}{1+\frac{B}{L}} \quad \text{Eq. 7.21}$$

Equation 7.22 and 7.23 are the shape factors for overburden and soil self-weight originally by Zhu and Michalowski (2005) for rectangular footings.

Rectangular:

$$s_q = 1 + 1.9tan^2(\phi_f)\sqrt{\frac{B}{L}} \quad \text{Eq. 7.22}$$

$$s_\gamma = 1 + \left(1.3sin^2(\phi_f) - 0.5\right)\left(\frac{L}{B}\right)^{1.5} \cdot e^{\left(-\frac{L}{B}\right)} \text{ for } \phi_f > 30^\circ \quad \text{Eq. 7.22}$$

Presented in Table 7.2 are the values calculated in our analysis for the various shape factors. As you can see there in minimal difference in the values presented from each method. Analysis of the shape factors that best fit the experimental data is in the subsequent section.

Table 7.2 Shape factors for overburden and soil self-weight

Reference	s_q	s_γ
DeBeer (1970) as modified by Vesić (1973)	1.04	0.98
Paikowsky et. al (2010)	1.03	0.99
Meyerhof (1963)	1.02	1.02
Perau (1995, 1997)	1.06	0.95
Zhu and Michalowski (2005)	1.17-1.24	1.00

7.1.3 Bearing Capacity Factor Analysis

Upon completion of the analysis on bearing capacity factors for depth and shape factors,

an investigation of the most representative N_γ from Vesić (1973), Zhu et. al. (2001), and Hansen (1970) was done. Shown in Figure 7.4 are the progression plots for the Vesić N_γ, Zhu et. al. N_γ, and Hansen N_γ methods for comparison. The Reissner (1924) method for N_q (Equation 7.3) was used in the analysis. The Vesić N_γ appears to be the most representative of the three design methods for the cases where $D_f = 0$ and $D_f = 0.5B$, followed closely by the Zhu et. al. method. The Hansen method appears to be representative for the cases where $D_f = 0.5B$ and B as seen in Figure 7.4.

Figure 7.5 shows the measured (back-calculated N_γ using Equation 4.50) plotted against the predicted N_γ based on Vesić (1973), which was the most representative method and is the method currently recommended by AASHTO (2016) for all the test cases. The Reissner (1924) method for N_q (Equation 7.3) was used in the analysis. Based on the limited test cases of medium dense and very dense soil and for $0 \leq D_f \leq B$, the $R^2 = 0.982$ for N_γ based on Vesić (1973) when the methods for depth of embedment and shape factors recommended here are used.

$$q_u = D_f \gamma N_q s_q d_q + 0.5 \gamma B N_\gamma s_\gamma d_\gamma \quad \text{Eq. 7.23}$$

$$q_n = q_u - q \quad \text{Eq. 7.24}$$

$$s_q = 1 + \left(\frac{B}{L} \tan \phi_f\right) \quad \text{Eq. 7.25}$$

$$s_\gamma = 1 - 0.4 \left(\frac{B}{L}\right) \quad \text{Eq. 7.26}$$

$$d_q = 1 + 2 \tan \phi_f \cdot \left(1 - \sin \phi_f\right)^2 \left(\frac{d_f}{B}\right) \text{ for } \frac{d_f}{B} \leq 1 \quad \text{Eq. 7.27}$$

$$d_\gamma = 1 \quad \text{Eq. 7.28}$$

$$N_\gamma = \frac{q_n - D_f \gamma N_q s_q d_q}{0.5 \gamma B s_\gamma d_\gamma} \quad \text{Eq. 7.29}$$

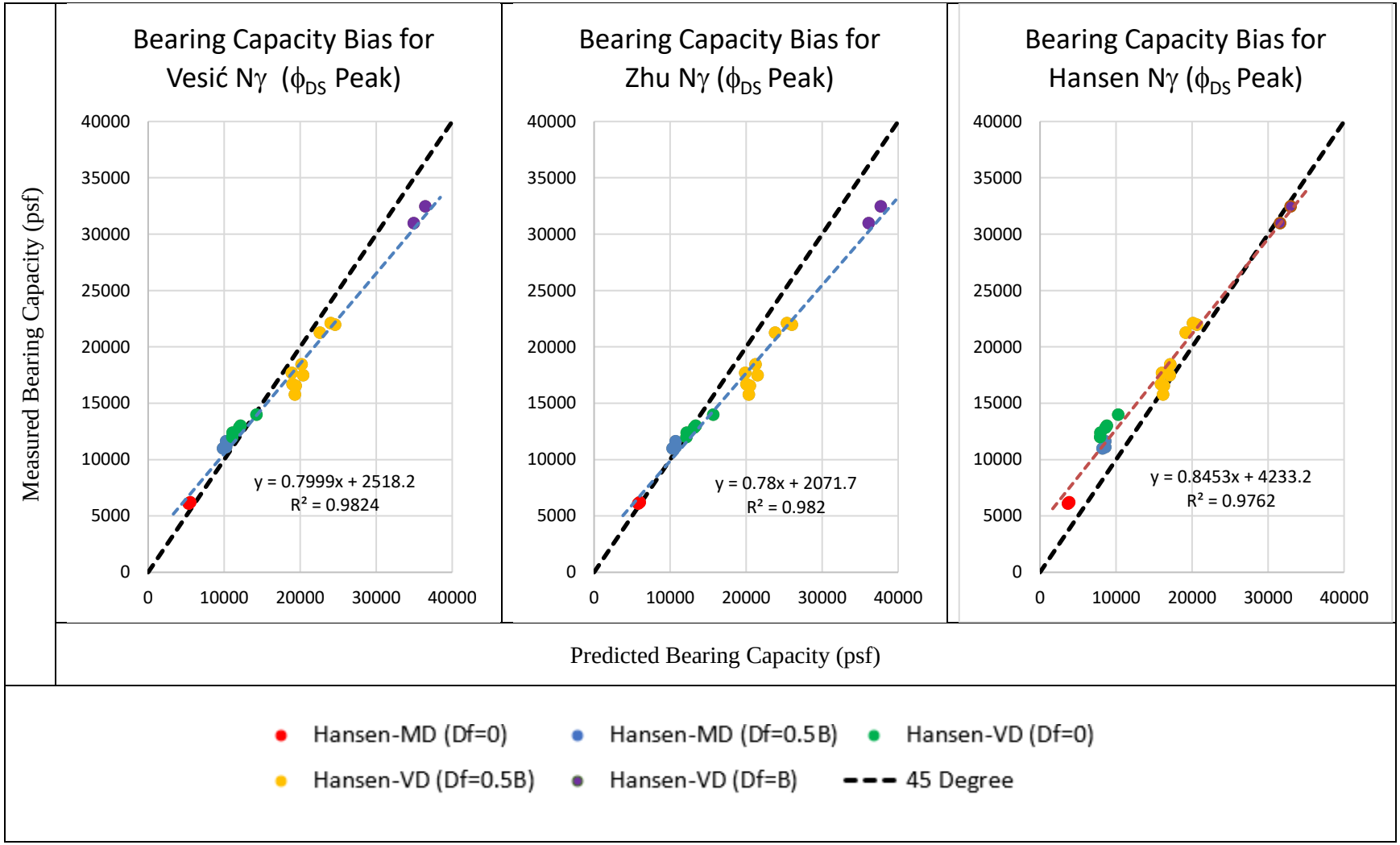

Figure 7.4 Measure vs. predicted bearing capacity plot for Vesić-N_γ (AASHTO), Zhu-N_γ, and Hansen-N_γ design methods

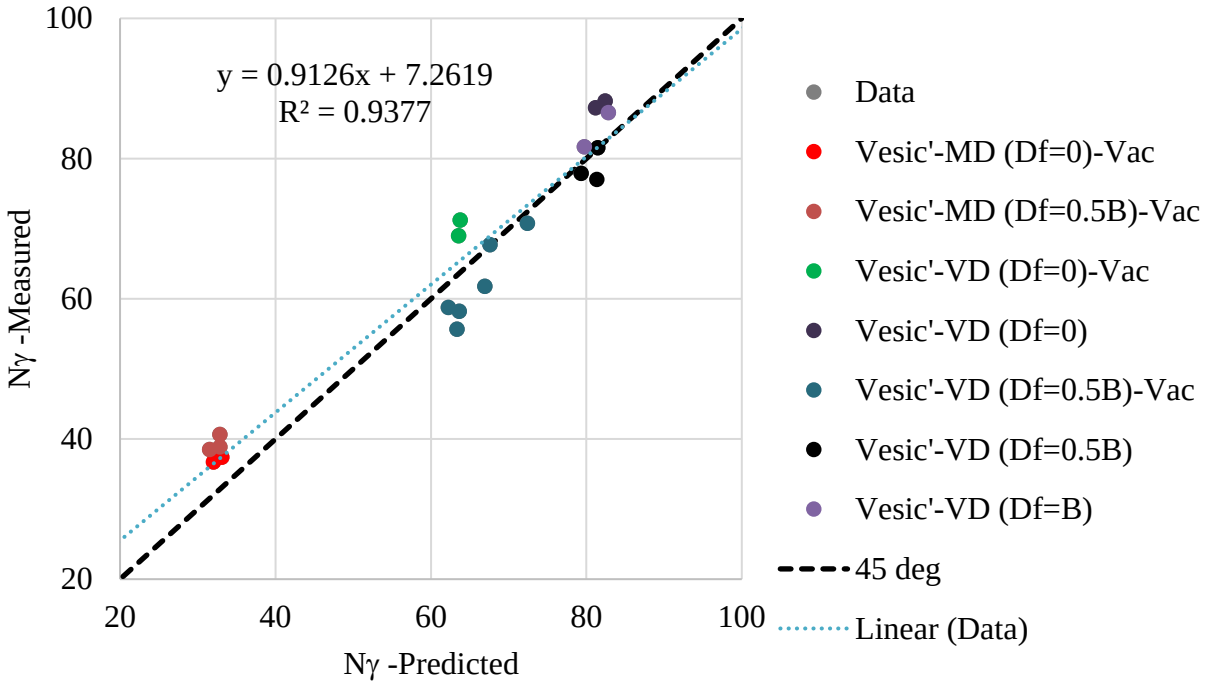

Figure 7.5 Bearing capacity factor-N_γ (Bias) plot for $D_f = 0$ and $D_f > 0$

7.1.4 Direct Shear and Triaxial Shear Peak Friction Angle Analysis

As discussed earlier, the peak friction angle obtained from the direct shear test was used in the comprehensive analysis. Based on Figure 7.6, the direct shear test provided more consistent and conservative values in comparison to the values obtained in the triaxial shear test. Shown in Figure 7.6 are the measured bearing capacity factor-N_γ for the medium dense and very dense conditions plot with the phi values obtained from the direct shear and triaxial shear relationships. In the medium dense and very dense conditions, the phi values obtained from the direct shear testing were more representative for the bearing resistances (i.e. plane strain).

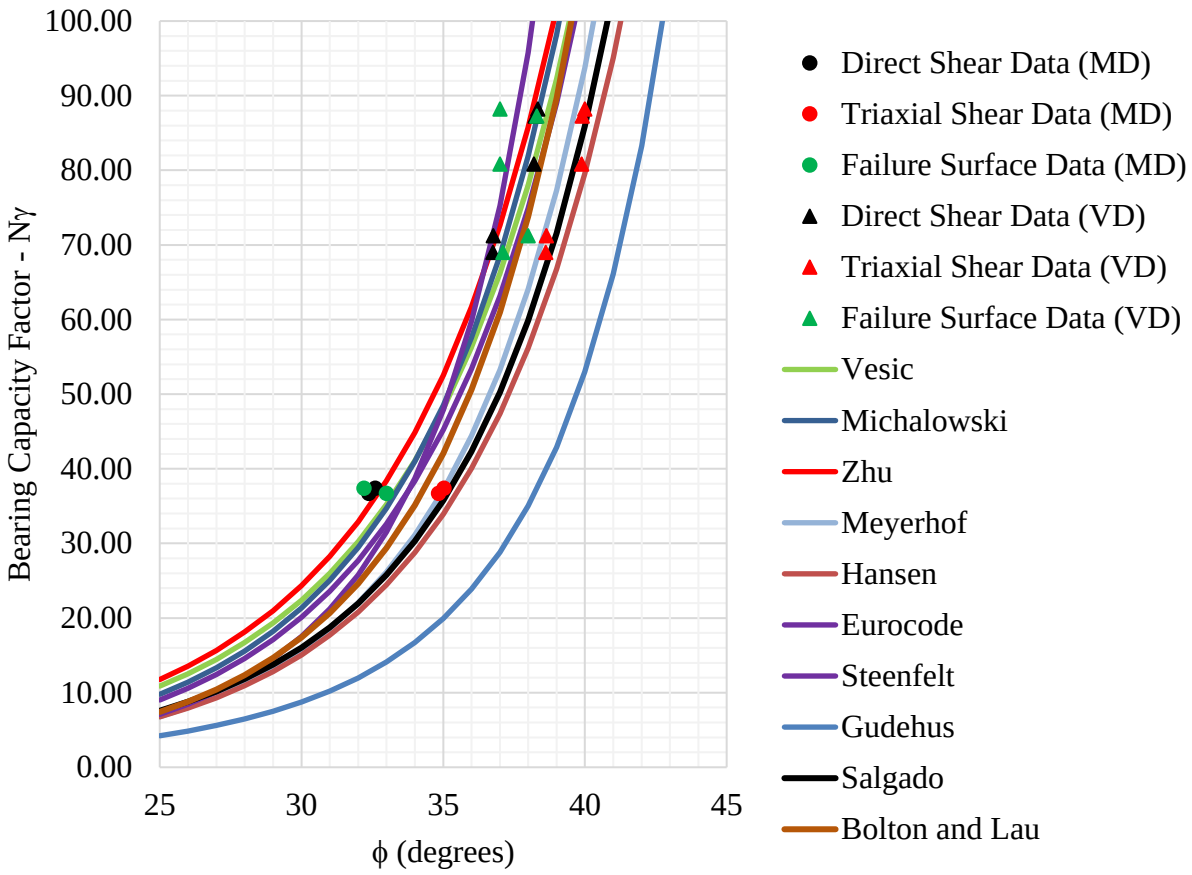

Figure 7.6 Direct shear and triaxial shear data plot

Progression plots for the experimental phi determined from the failure surface plots (measured) versus the direct shear and triaxial shear relationships (predicted) are presented in Figures 7.7 -7.8. The direct shear and triaxial relationship shown appear to be representative to the measured phi values determined from the failure surface plots.

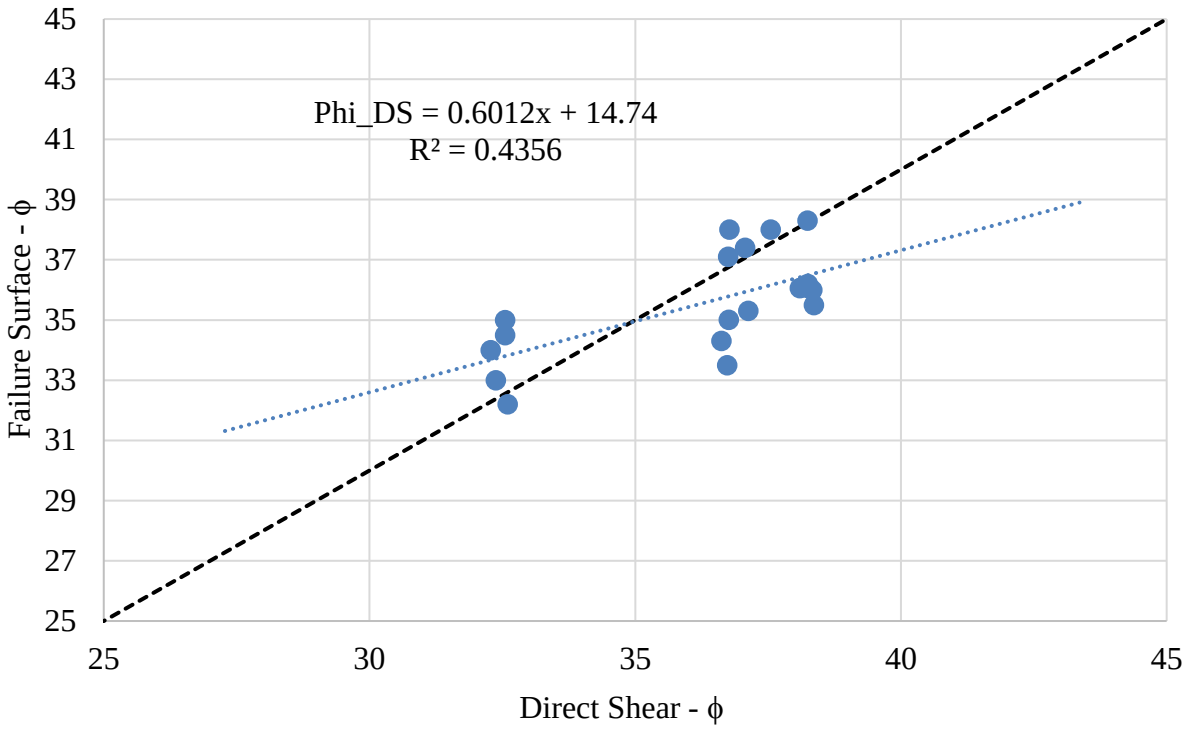

Figure 7.7 Direct shear bias plot

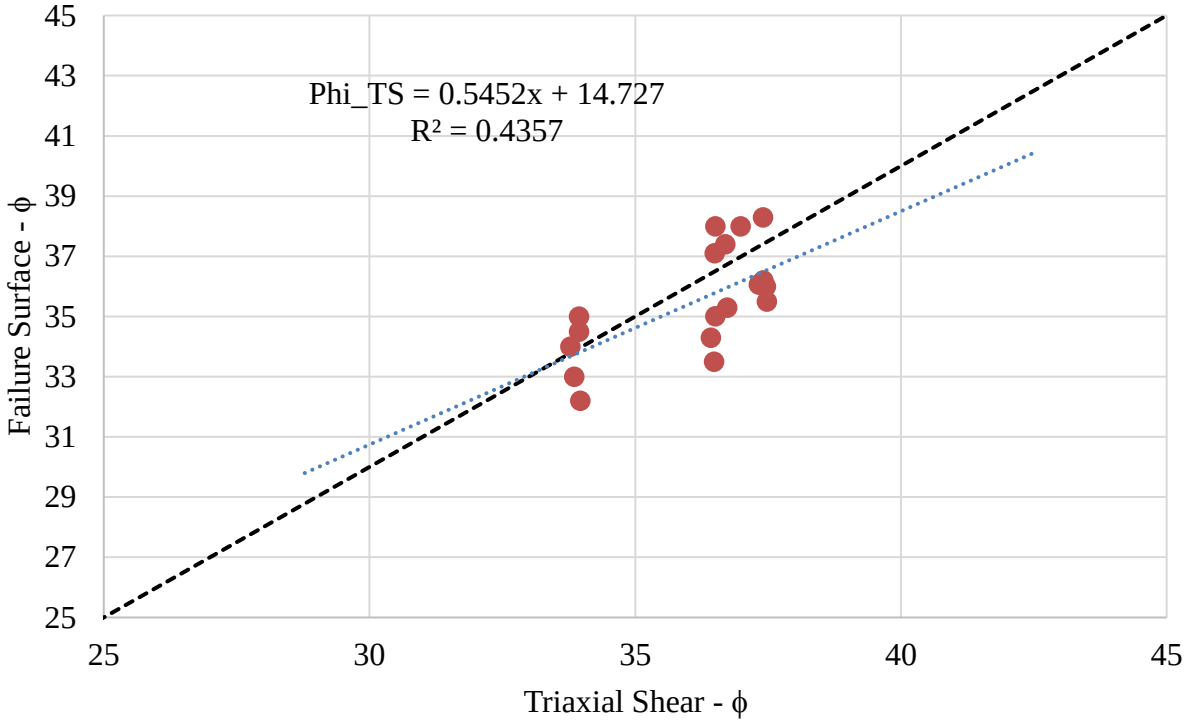

Figure 7.8 Triaxial shear bias plot

The results of the direct shear and triaxial shear plot also provided a guide in the selection process for determining which design methods to use in the analysis. As shown in Figure 7.6 Vesić and Zhu et al. methods were good predictors for both the medium dense condition and very dense condition when using peak friction angles obtained from the direst shear test.

A second analysis was performed to confirm the findings from Figure 7.6. The observed failure surface for each load test were compared to the theoretical failure surface as presented in Figure 7.9 and described by Eq.7.30 and Eq.7.31, Prandtl (1920). Equation 7.30 describes the linear portions of the geometry presented in Figure 7.9 and Eq. 7.31 describes the log spiral fan portion,

$$\alpha = 45^{\circ} - \frac{\phi}{2} \qquad \text{Eq. 7.30}$$

$$r = R_o e^{\theta \tan \phi} \qquad \text{Eq. 7.31}$$

where

θ is the angle of rotation

ϕ is the internal friction angle

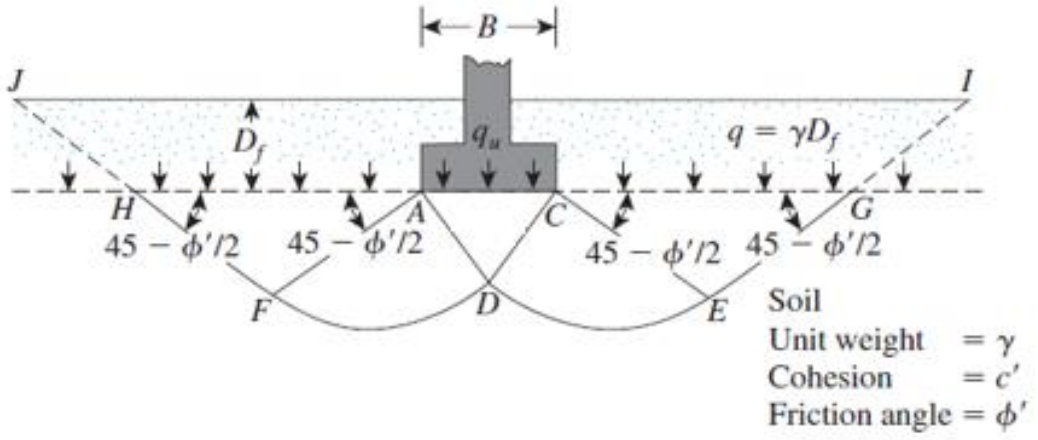

Figure 7.9 Theoretical failure surface Das (2016).

The theoretical failure surface replotted using the peak friction angle obtained from the direct shear and triaxial shear tests and compared to the observed failure surface for all load test with depth of embedment equal to zero. Shown in Figure 7.10 is theoretical failure surface using the peak friction angle obtained from the direct shear test. The theoretical failure surface is a near match to the point of the max failure surface observed from the plan view.

Shown in Figure 7.11 is the theoretical failure surface using the peak friction angle obtained from the triaxial shear test on LT-17. The theoretical failure surface extends beyond the point of max failure surface observed from the plan view. In the majority of the load tests this was the consistent theme.

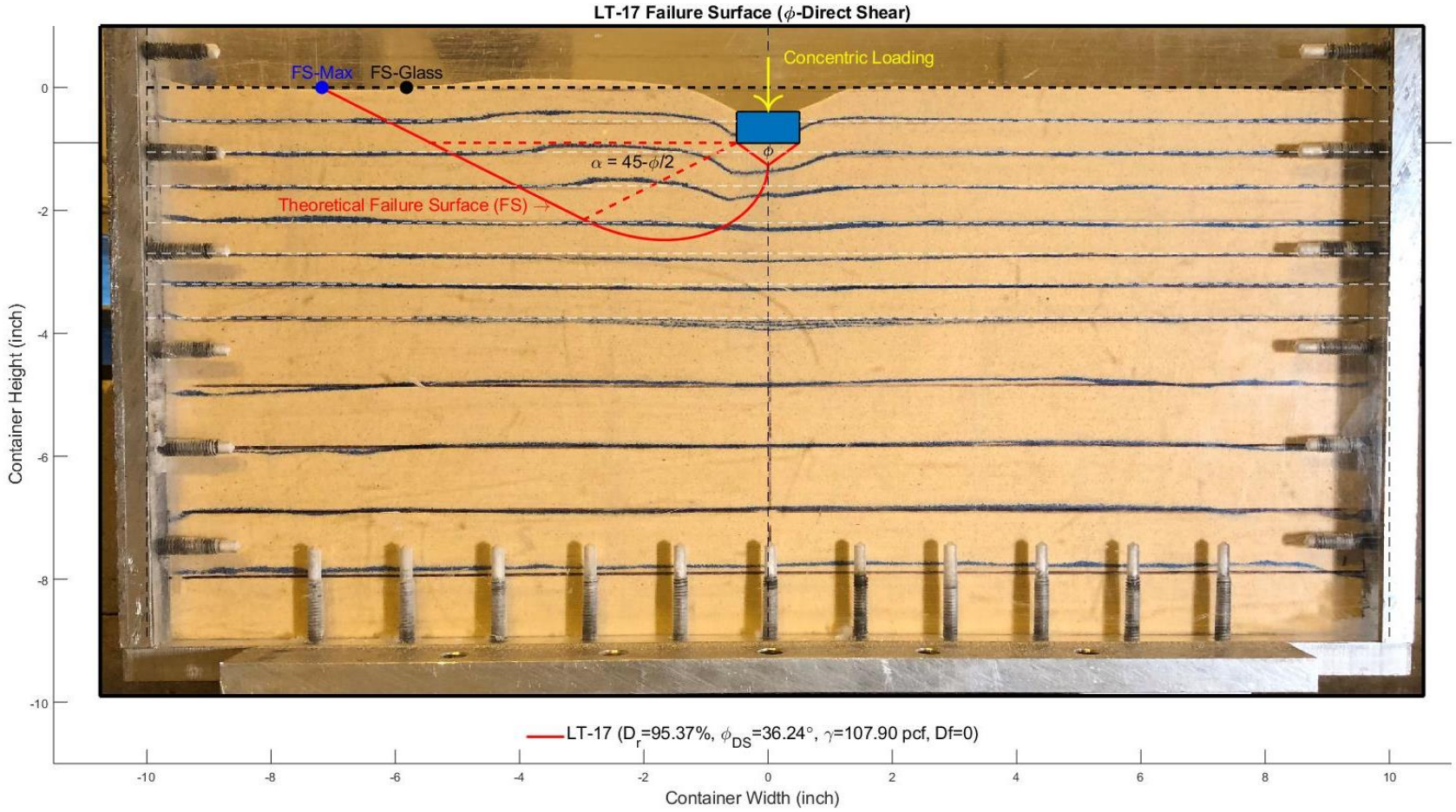

Figure 7.10 Theoretical failure surface using direct shear peak friction angle

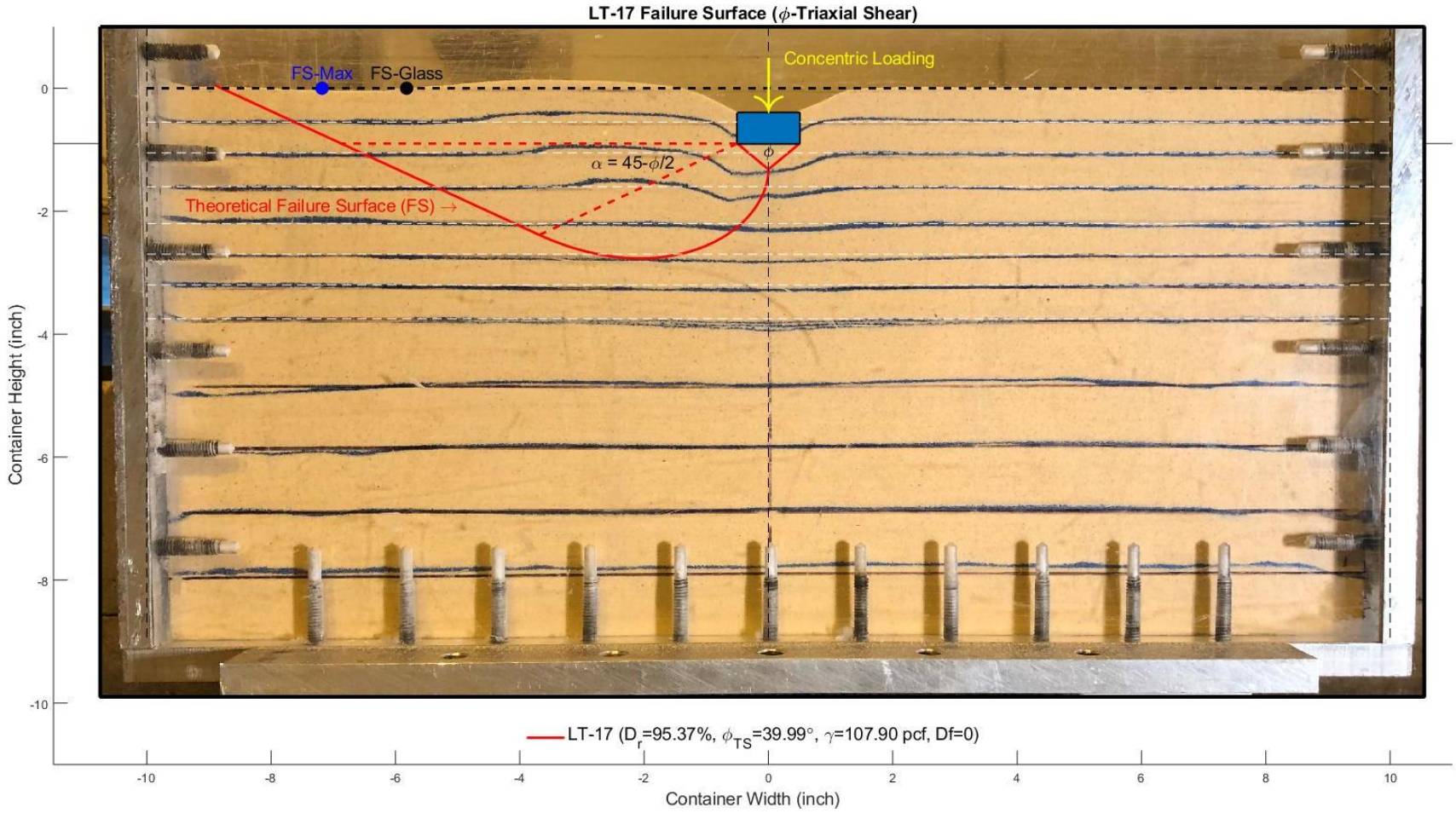

Figure 7.11 Theoretical failure surface using triaxial shear peak friction angle

7.2 Analysis of Rectangular and Square Footing

7.2.1 Measured Shape Factor Analysis

AASHTO (2016) recommends factors to correct for the effect of footing shape other than strip footings. Equations 7.32 – 7.35 are shape factors for overburden and soil self-weight originally by DeBeer (1970), and modified by Vesić (1973), recommended by ASHTO (2016) for rectangular and square footings.

Rectangular:

$$s_q = 1 + \left(\frac{B}{L}\tan\phi_f\right) \quad \text{Eq. 7.32}$$

$$s_\gamma = 1 - 0.4\left(\frac{B}{L}\right) \quad \text{Eq. 7.33}$$

Square:

$$s_q = 1 + \tan\phi_f \quad \text{Eq. 7.34}$$

$$s_\gamma = 0.6 \quad \text{Eq. 7.35}$$

Paikowsky et al. (2010) presented other equations for shape factor. Equations 7.36 – 7.39 are shape factors for overburden and soil self-weight recommended in EuroCode 7 (2005) and DIN 4017 (2006) for rectangular and square footings.

Rectangular:

$$s_q = 1 + \frac{B}{L}\sin\phi_f \quad \text{Eq. 7.36}$$

$$s_\gamma = 1 - 0.3\frac{B}{L} \quad \text{Eq. 7.37}$$

Square:

$$s_q = 1 + \sin\phi_f \quad \text{Eq. 7.38}$$

$$s_\gamma = 0.7 \quad \text{Eq. 7.39}$$

Equations 7.40 and 7.41 are shape factors for overburden and soil self-weight originally by Meyerhof (1963) for rectangular footings.

$$s_q = 1 + 0.1K_p\left(\frac{B}{L}\right) \text{ for } \phi_f > 10^{\circ} \quad \text{Eq. 7.40}$$

$$s_\gamma = 1 + 0.1K_p\left(\frac{B}{L}\right) \quad \text{Eq. 7.41}$$

Equations 7.42 and 7.43 are shape factors for overburden and soil self-weight originally by Zhu and Michalowski (2005) for rectangular and square footings.

Rectangular:

$$s_q = 1 + 1.9tan^2\phi_f\sqrt{\frac{B}{L}} \quad \text{Eq. 7.42}$$

$$s_\gamma = 1 + \left(1.3sin^2\left(\phi_f\right) - 0.5\right)\left(\frac{L}{B}\right)^{1.5} \cdot e^{\left(-\frac{L}{B}\right)} \text{ for } \phi_f > 30^{\circ} \quad \text{Eq. 7.43}$$

To validate the shape factors, s_γ and s_q, load tests performed for footings with L/B=1,5,10, and 20 at the surface and with L/B=1, 10 and 20 embedded were used to identify the effect of shape in each case. The experimentally determined s_γ and s_q factors for the different L/B and very dense sand are shown in Figures 7.12 and 7.13, respectively. The factors are the bearing capacity for each L/B case normalized by L/B = 20 bearing capacity for a footing with B = 5 ft, which was calculated using the experimentally determined N_q and N_γ. In the case for s_γ a trendline was fit to the data using a value of one for the case of L/B=20 for comparison. The method presented by Meyerhof (1963) appears to be most representative of the L/B tested, while the Debeer (1970) method modified by Vesić (1973) is conservative, especially at L/B < 5. In the case of s_q the experimental data is in good agreement with Meyerhof (1963) for L/B > 10 and Debeer (1970) modified by Vesić (1973) for 3 < L/B < 10. Meyerhof (1963) method is generally conservative for L/B < 10 while Debeer (1970) modified by Vesić (1973) are greater than the experimentally determined factors for L/B < 3. Currently, AASHTO recommends Debeer (1970) modified by Vesić (1973) shape factors in bearing capacity design.

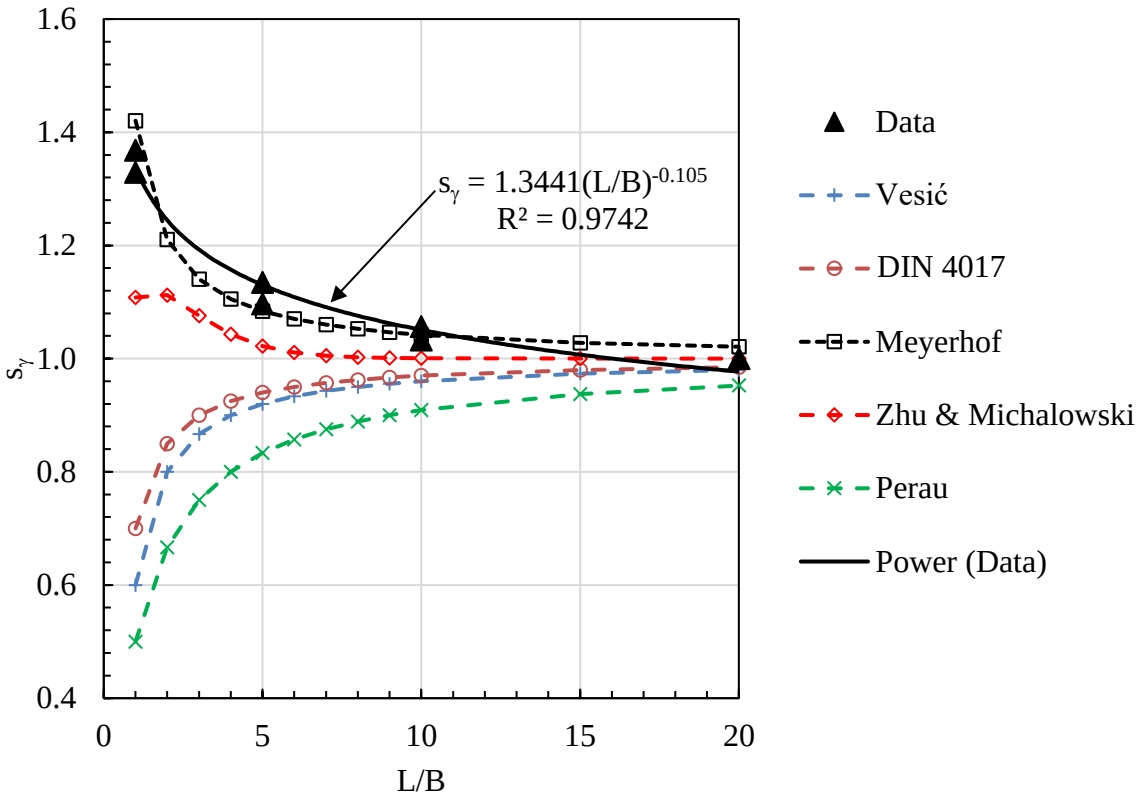

Figure 7.12 Soil self-weight shape factors for L/B = 1-20 footings on very dense sand

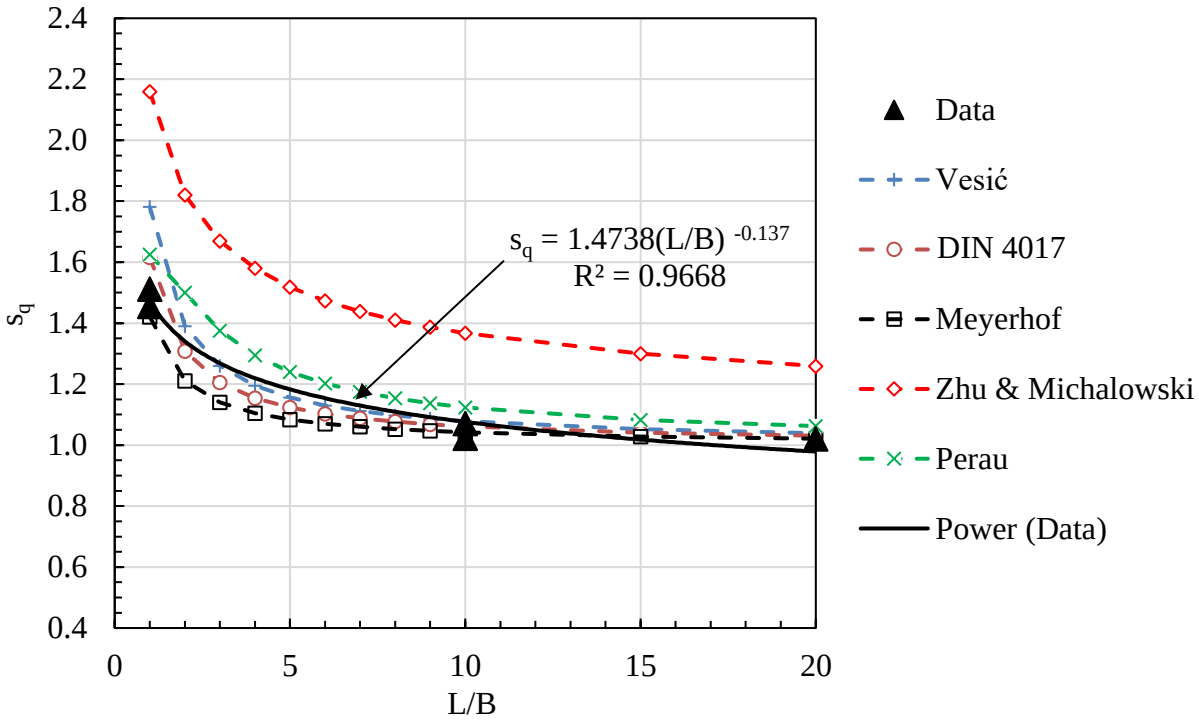

Figure 7.13 Soil overburden shape factors for L/B = 1-20 footings on very dense sand

7.2.2 Measured Eccentricity Analysis

Where eccentric loads are acting on the foundation (in either direction), then the effective dimensions (L' and/or B') should be used in Equation 7.1 (AASHTO, 2016).

$$L' = L - 2 \cdot \mathrm{e}_L \quad \text{Eq. 7.44}$$

$$B' = B - 2 \cdot \mathrm{e}_B \quad \text{Eq. 7.45}$$

$$\mathrm{e}_L = \frac{M_L}{V} \quad \text{Eq. 7.46}$$

$$\mathrm{e}_B = \frac{M_B}{V} \quad \text{Eq. 7.47}$$

where e_L and e_B are the load eccentricities in the L and B directions, respectively, M_L and M_B are the moments due to eccentric loads in the L and B directions, respectively, and V is the total vertical load.

For vertical eccentric loads along the foundation width, B, the decrease in bearing capacity can be estimated with any of the following methods (Equations 7.48 – 7.55) based on small-scale model tests on cohesionless soil with $D_f = 0$ (Paikowsky et al., 2010).

Meyerhof's (1953) empirical factor:

$$\frac{q_u}{q_{u,centric}} = \left(1 - 2\frac{e}{B}\right)^2 \quad \text{Eq. 7.48}$$

Giraudet's (1965) empirical factor:

$$\frac{q_u}{q_{u,centric}} = e^{\left(-12\left(\frac{e}{B}\right)^2\right)} \quad \text{Eq. 7.49}$$

Ticof's (1977) empirical factor:

$$\frac{q_u}{q_{u,centric}} = \left(1 - 1.9\frac{e}{B}\right)^2 \quad \text{Eq. 7.50}$$

Bowles (1996) empirical factor:

$$\frac{q_u}{q_{u,centric}} = 1 - \sqrt{\frac{e}{B}} \quad \text{for } 0 < \frac{e}{B} < 0.3 \qquad \text{Eq. 7.51}$$

Paolucci and Pecker's (1997) empirical factor:

$$\frac{q_u}{q_{u,centric}} = \left(1 - \frac{e}{0.5B}\right)^{1.8} \text{ for } \frac{e}{B} < 0.3 \qquad \text{Eq. 7.52}$$

Ingra and Baecher's (1983) empirical factor:

$$\frac{q_u}{q_{u,centric}} = 1 - 3.5\left(\frac{e}{B}\right) + 3.03\left(\frac{e}{B}\right)^2 \qquad \text{Eq. 7.53}$$

Gottardi and Butterfield's (1993) empirical factor:

$$\frac{q_u}{q_{u,centric}} = 1 - \frac{e}{0.36B} \qquad \text{Eq. 7.54}$$

Perau's (1995, 1997) empirical factor:

$$\frac{q_u}{q_{u,centric}} = 1 - 2.5\frac{e}{B} \qquad \text{Eq. 7.55}$$

The prototypical footing width in this analysis is 60 inches wide. Considering the maximum allowed eccentricity of B/6 this equates to an eccentricity of 10 inches from the centerline of the footing. The pressure transducers located beneath the footing allow for investigation of the measured eccentricity.

7.2.2.1 Rectangular Footing

Figures 7.14 -7.15 are all the Load Case-2 tests which illustrate the distribution of the measured bearing pressures and the resultant force. The location of the resultant force for each test was calculated by summing the moments about the point of loading on the top of the footing. Shown in Table 7.3 are the summary of the measured eccentricities for all the L/B = 10 tests.

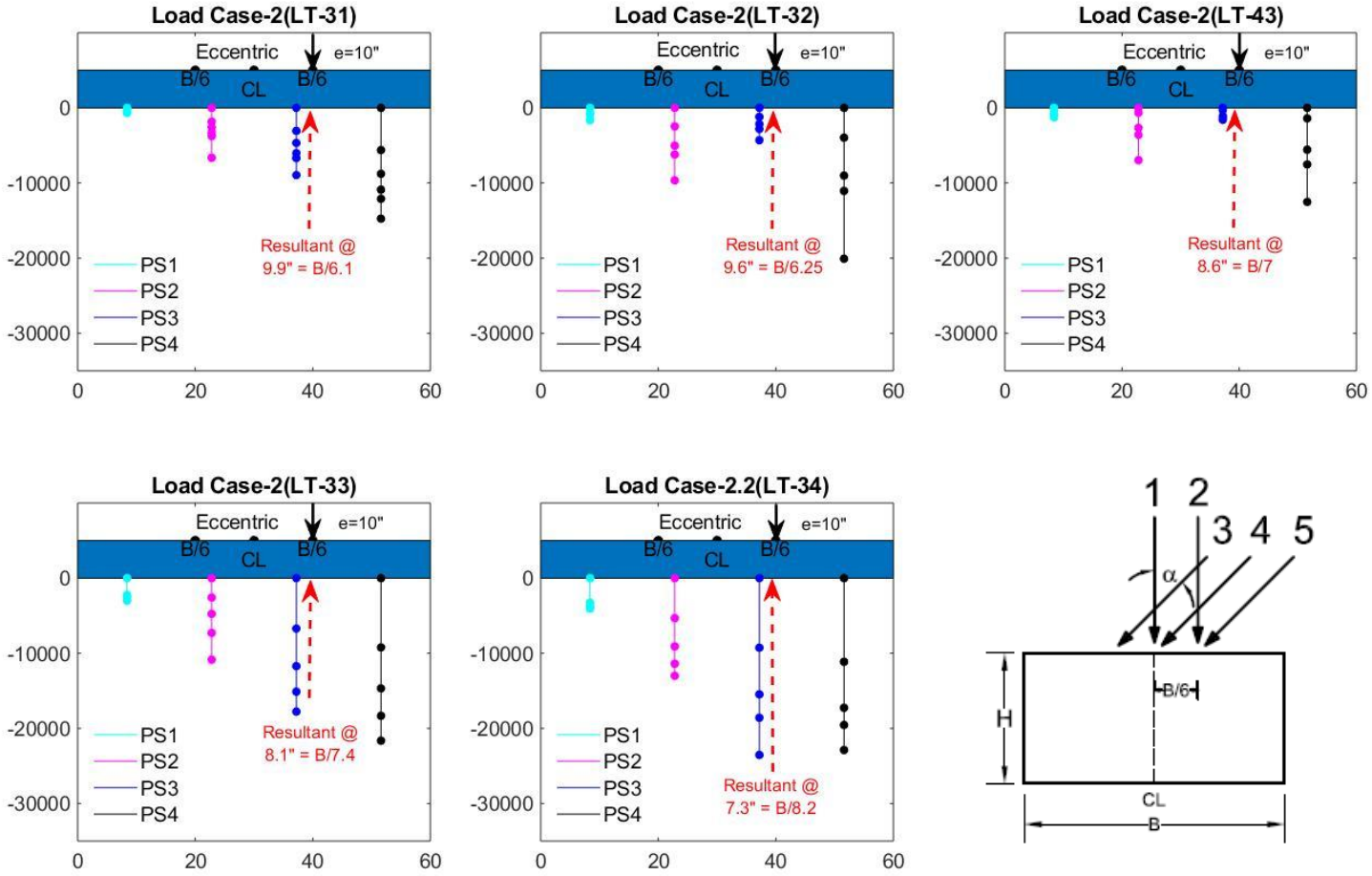

Figure 7.14 Pressure distribution for very dense eccentric load case

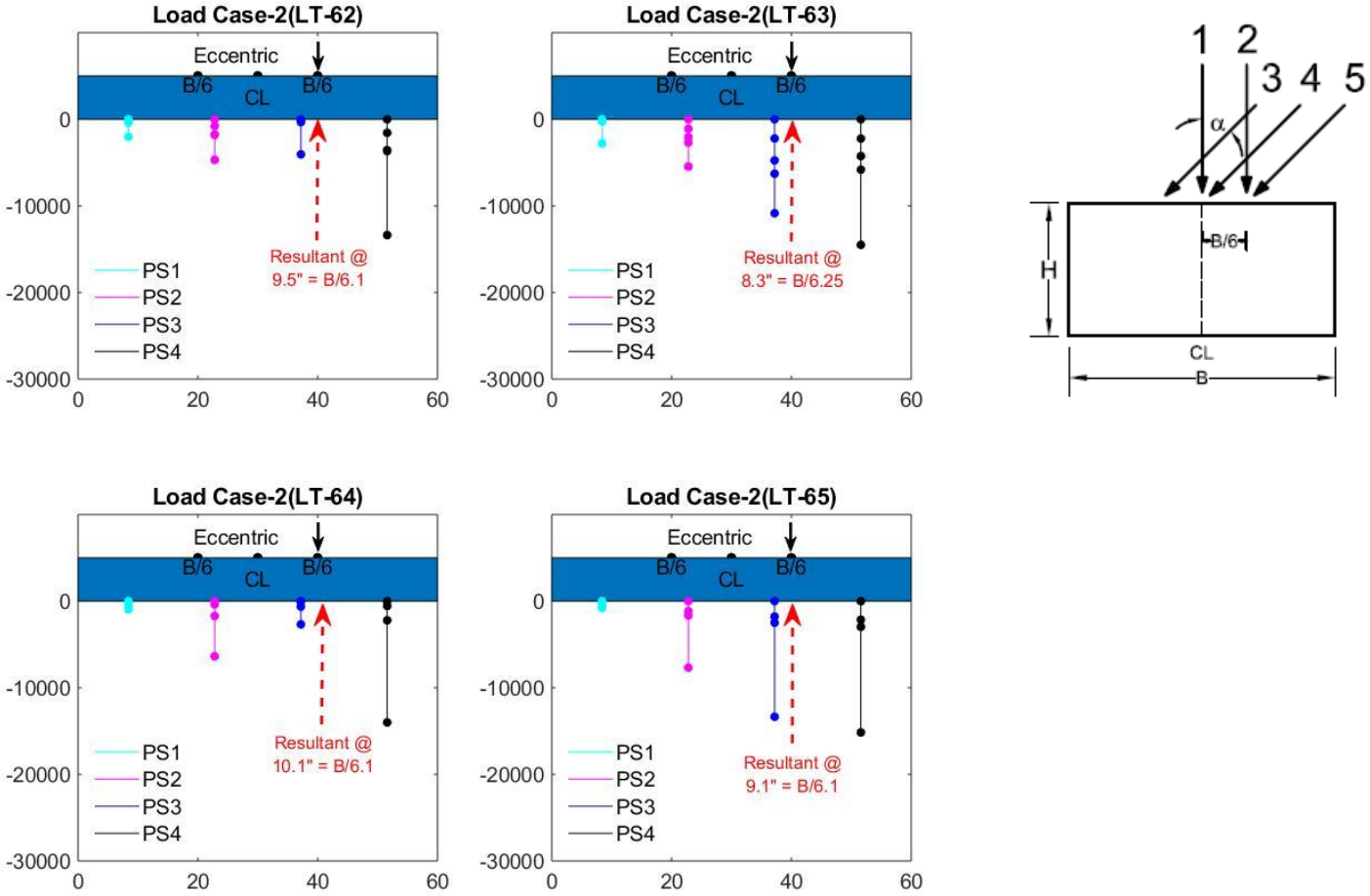

Figure 7.15 Pressure distribution for medium dense eccentric load case

Table 7.3 Summary of eccentricity analysis for L/B = 10 tests

Load Test	Density	Embedment Depth	Measured Eccentricity (in)	Design Eccentricity (in)	Measured Eccentricity	Design Eccentricity	Footing Rotation (degree)
LT-31	VD	0	9.9	10	B/6.1	B/6	6.65
LT-32	VD	0	9.6	10	B/6.25	B/6	7.06
LT-43	VD	0	8.6	10	B/7	B/6	6.54
LT-33	VD	0.5B	8.1	10	B/7.4	B/6	9.13
LT-34	VD	0.5B	7.3	10	B/8.2	B/6	8.46
LT-62	MD	0	9.5	10	B/6.3	B/6	7.89
LT-63	MD	0	8.3	10	B/7.2	B/6	8.02
LT-64	MD	0.5B	10.1	10	B/5.9	B/6	9.99
LT-65	MD	0.5B	9.1	10	B/6.5	B/6	10.51

Figure 7.16 is the bias (measured/predicted) in the eccentricity methods previously presented based on measured results from the tests in Table 7.3. The results shown in Figure 7.16 suggest the AASHTO recommended design method for eccentric load conditions (Eqs. 7.1 and 7.45) is representative for both the very dense and medium dense conditions. The method tends to slightly underpredict the bearing capacity for the medium dense sand and slightly overpredict for the very dense sand with depth of embedment equal to 0.5B. All empirical factor methods (Eqs. 7.48 – 7.55) underpredict the bearing capacity of the eccentrically loaded footings.

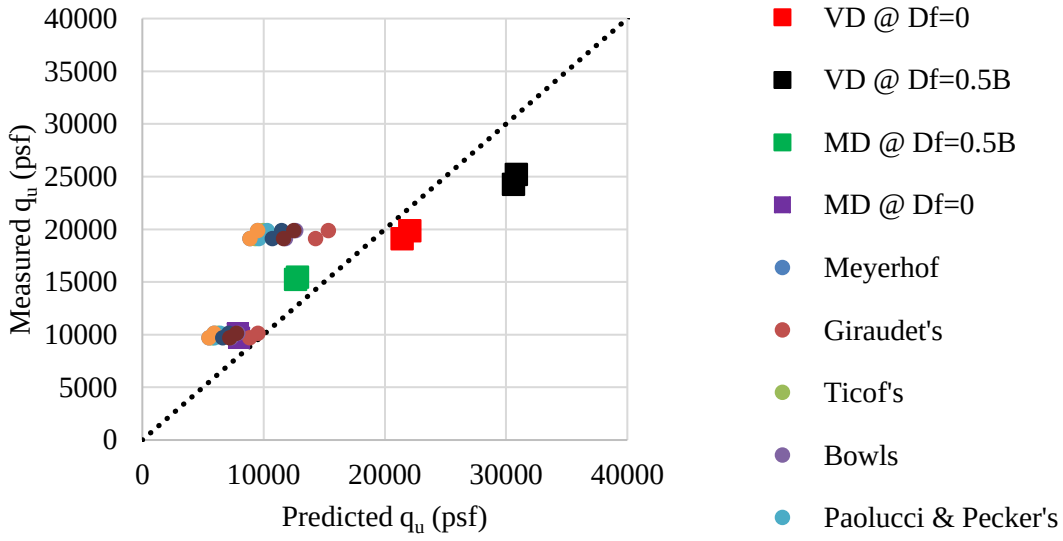

Figure 7.16 Measured vs. predicted eccentricity bias plot for L/B = 10 tests

7.2.2.2 Square Footing

Figures 7.17 -7.18 are all the Load Case-2 tests which illustrate the distribution of the measured bearing pressures and the resultant force. The location of the resultant force for each test was calculated by summing the moments about the point of loading on the top of the footing. Shown in Table 7.4 are the summary of results for the eccentricity analysis.

Table 7.4 Summary of eccentricity analysis L/B = 1 tests

Load Test	Density	Embedment Depth	Measured Eccentricity (in)	Design Eccentricity (in)	Measured Eccentricity	Design Eccentricity
LT-130	VD	0	8.9	10	B/6.7	B/6
LT-131	VD	0	9.1	10	B/6.6	B/6
LT-132	VD	0.5B	9.3	10	B/6.5	B/6
LT-133	VD	0.5B	10.6	10	B/5.7	B/6
LT-96	MD	0	9.8	10	B/6.1	B/6
LT-97	MD	0	9.2	10	B/6.5	B/6
LT-98	MD	0.5B	7.8	10	B/7.7	B/6
LT-99	MD	0.5B	9.3	10	B/6.5	B/6

Figure 7.19 is the bias (measured/predicted) in the eccentricity methods based on the measured results from the tests in Table 7.4. The results shown Figure 7.19 suggest the AASHTO recommended design method for eccentric load conditions (Eqs. 7.1 and 7.45) is generally representative for both the very dense and medium dense conditions. The design method tends to underpredict more so in the square footing for the medium and very dense soil conditions with D_f = 0 & 0.5B. All empirical factor methods (Eqs. 7.48 – 7.55) underpredict the bearing capacity of the eccentrically loaded footings.

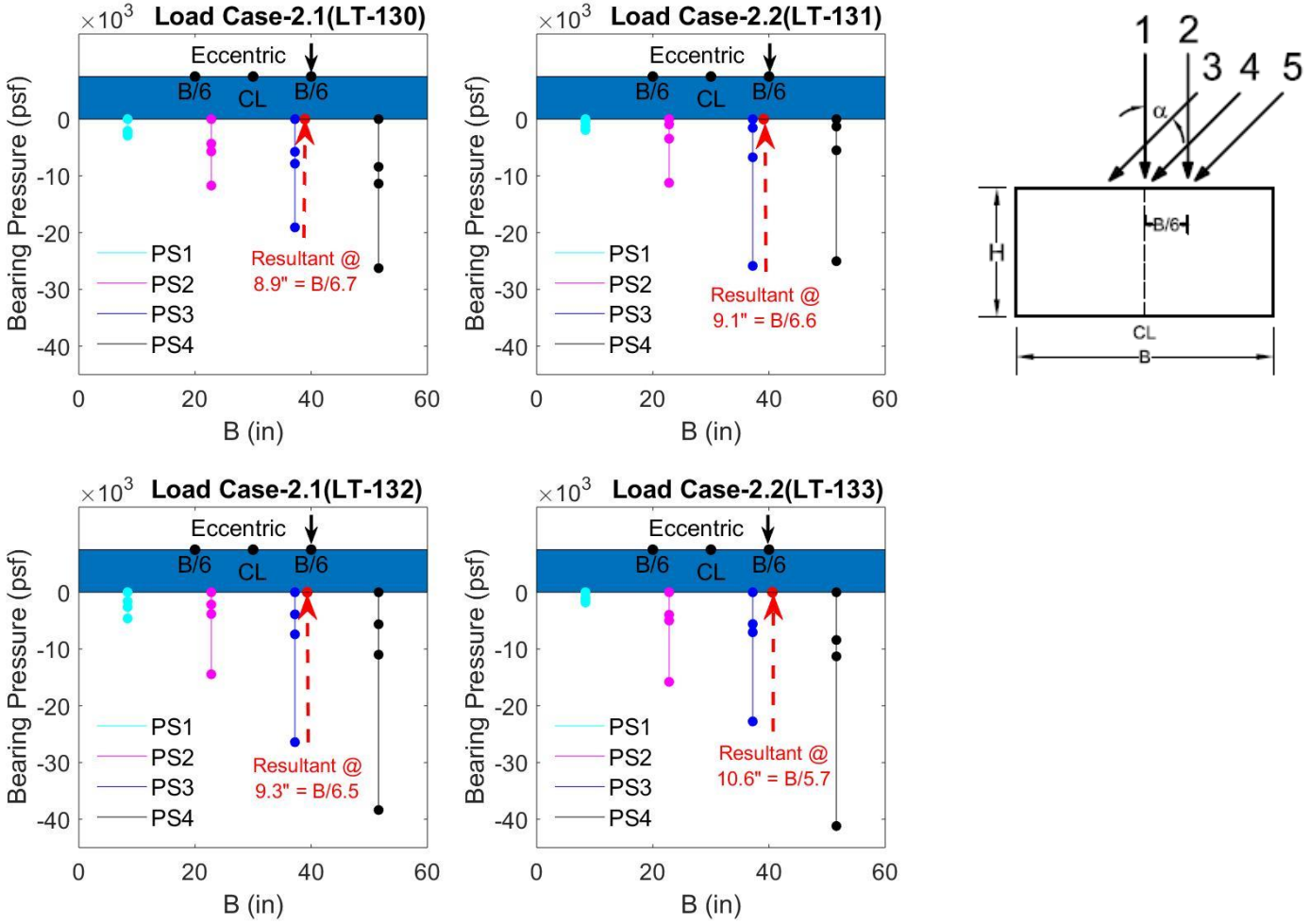

Figure 7.17 Pressure distribution for very dense eccentric load case

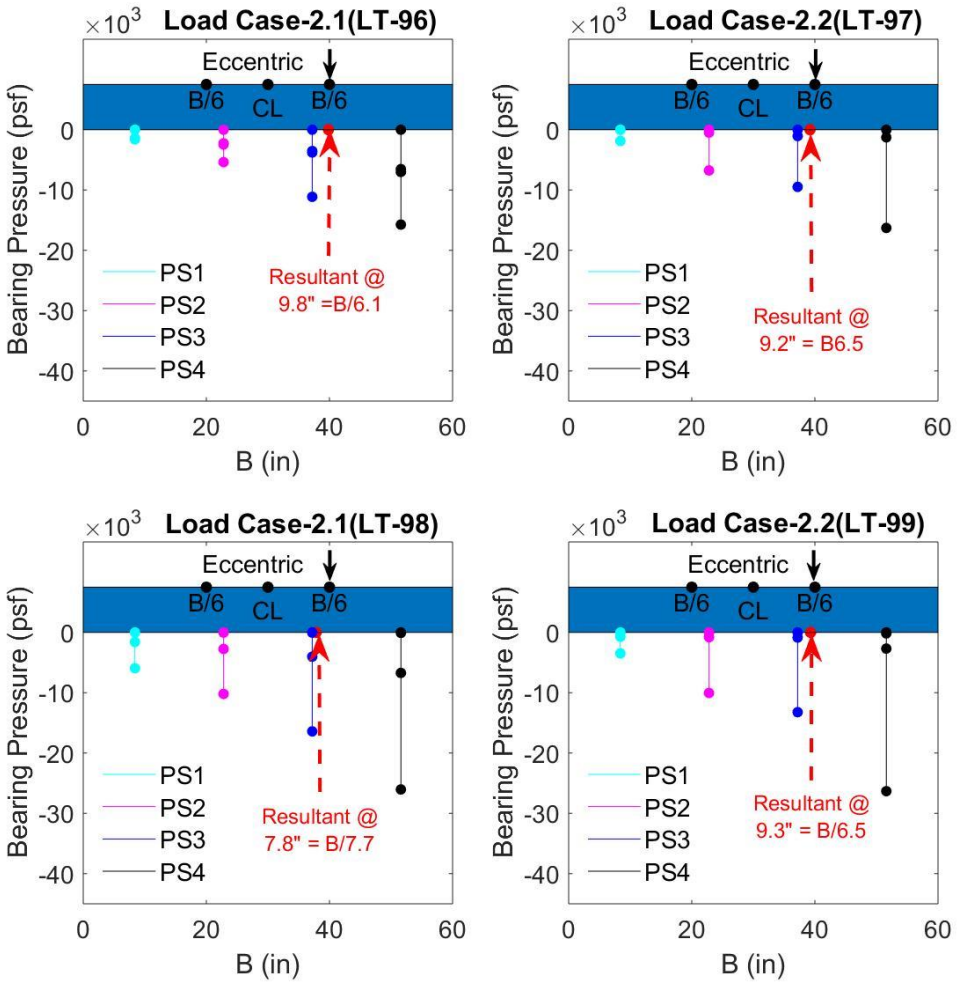

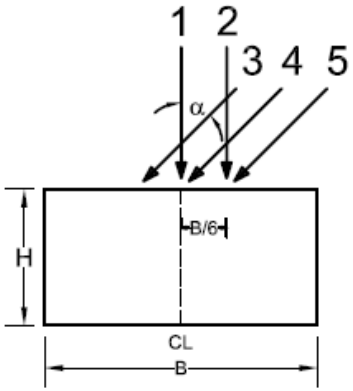

Figure 7.18 Pressure distribution for medium dense eccentric load case

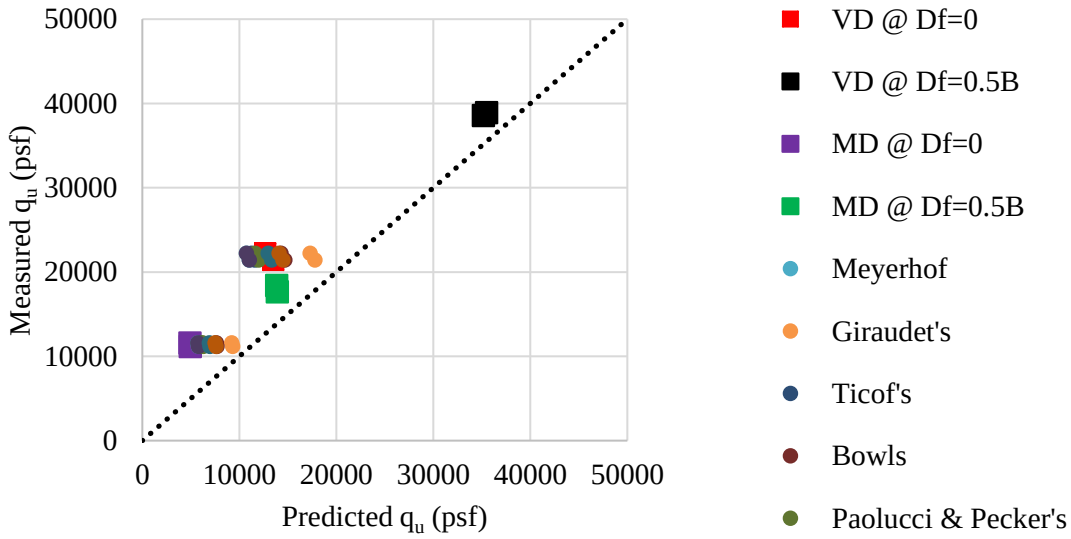

Figure 7.19 Measured vs. predicted eccentricity bias plot for L/B = 1 tests

7.2.3 Measured Inclination Analysis

Centric, inclined loads acting on a shallow footing (resultant, R in Figure 7.20) has the effect of a shallower and shorter failure surface compared cases of centric, vertical loads. AASHTO (2016) recommends accounting for load inclination effects with factors on the resistance due to overburden and soil self-weight using Equations 7.65 and 7.66, respectively. Paikowsky et al. (2010) presents methods for the load inclination factor which are shown in Equations 7.65 – 7.78.

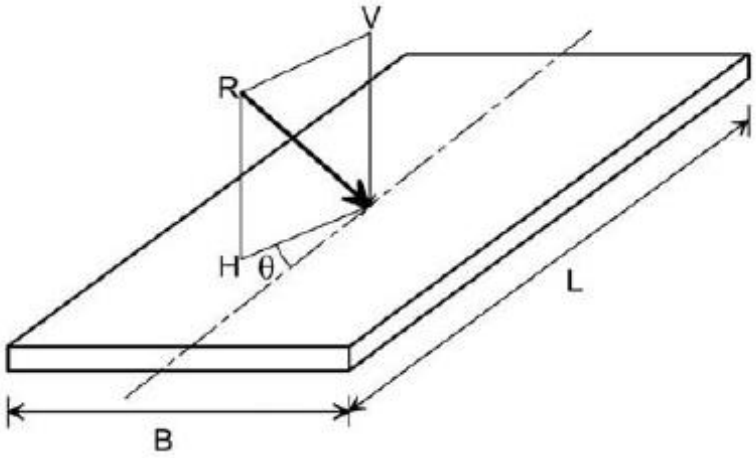

Figure 7.20 Inclined loading convention (Figure C10.6.3.1.2a-1 AASHTO, 2016)

Vesić (1973) load inclination factors:

$$i_q = \left(1 - \frac{H}{(V + cBL\cot\phi_f)}\right)^m \quad \text{Eq. 7.56}$$

$$i_\gamma = \left(1 - \frac{H}{(V + cBL\cot\phi_f)}\right)^{m+1} \quad \text{Eq. 7.57}$$

$$m = [(2+L/B)/(1+L/B)]\cos^2\theta + [(2+B/L)/(1+B/L)]\sin^2\theta \quad \text{Eq. 7.58}$$

where B is the footing width, L is the footing length, H is the unfactored horizontal load, V is the unfactored vertical load, and θ is the projected direction of the resultant load, R, as shown in Figure 7.20.

Meyerhof (1953) load inclination factors:

$$i_q = \left(1 - \frac{\alpha}{90^\circ}\right)^2 \quad \text{Eq. 7.59}$$

$$i_\gamma = \left(1 - \frac{\alpha}{\phi_f}\right)^2 \quad \text{Eq. 7.60}$$

where α is the angle of the inclined load to the vertical.

Meyerhof and Koumoto (1987) modified the earlier equations for more specific cases. Equation 7.70 is the load inclination factor for a foundation with rough base on sand. Equation 7.71 is the load inclination factor for a foundation with embedment ratio (D_f/B) equal to 1 in soil with angle of internal friction greater than 30°. Hansen (1970) recommended Equations 7.72 and 7.73, where the exponent, η, equals 5. Bowles (1997) recommended $2 \leq \eta \leq 5$.

$$i_\gamma = \cos\alpha \left(1 - \frac{\sin\alpha}{\sin\phi_f}\right) \quad \text{Eq. 7.61}$$

$$i_\gamma = \cos\alpha \,(1 - \sin\alpha) \quad \text{Eq. 7.62}$$

Hansen (1970) recommended Equations 7.58 and 7.59, where the exponent, η, equals 5.

$$i_q = \left(1 - \frac{0.5H}{(V + cBL\cot\phi_f)}\right)^\eta \quad \text{Eq. 7.63}$$

$$i_\gamma = \left(1 - \frac{0.7H}{(V + cBL\cot\phi_f)}\right)^\eta \quad \text{Eq. 7.64}$$

Loukidis et al. (2008) recommends Equation 7.74 and Equation 7.75 for combined eccentricity and inclination, where e and α can be negative or positive. The f_{ie} term is applied to the bearing capacity equation in place of B and *i*.

$$i_\gamma = \left(1 - 0.94\frac{tan\alpha}{tan\emptyset}\right)^{(1.5tan\phi + 0.4)^2} \quad \text{Eq. 7.65}$$

$$f_{ie} = \left[1 - \sqrt{3.7\left(\frac{e}{B}\right)^2 + 2.1(tan\alpha)^2 + 1.5\frac{e}{B}tan\alpha}\right]^2 \quad \text{Eq. 7.66}$$

Muhs (1971) recommends Equation 7.76

$$i_\gamma = (1 - tan\alpha)^2 \qquad \text{Eq. 7.67}$$

Reduction factors due to centric, inclined loads acting on foundations on sand without embedment are shown in Equations 7.77 – 7.79.

Ticof's (1977) empirical factor:

$$\frac{q_u}{q_{u,centric}} = \left(1 - 1.36\frac{H}{V}\right)^2 \qquad \text{Eq. 7.68}$$

Ingra and Baecher's (1983) empirical factor:

$$\frac{q_u}{q_{u,centric}} = 1 - 2.41\left(\frac{H}{V}\right) + 1.36\left(\frac{H}{V}\right)^2 \qquad \text{Eq. 7.69}$$

Gottardi and Butterfield's (1993) empirical factor:

$$\frac{q_u}{q_{u,centric}} = 1 - \frac{H}{0.48V} \qquad \text{Eq. 7.70}$$

7.2.3.1 Rectangular Footing

The measured inclination values and self-weight inclination factors, i_γ, methods considered in the analysis are presented in Figure 7.21. These measured inclination values are normalized bearing capacity of Load Case-4 at the surface. Investigating Figure 7.21, Meyerhof (1953) and Hansen (1970) seem to be a good representation for very dense soil conditions with L/A ratios of 0.10. Meyerhof (1953) and Hansen (1970) provide fairly good representation for very dense soil conditions with L/A ratios of 0.25. The measured values for the medium dense soil with L/A = 0.1 agree well with Hansen (1970) while the measured values for 0.25 are slightly less than Meyerhof (1953) and Hansen (1970). Vesić (1973) slightly overpredicts the self-weight inclination factor.

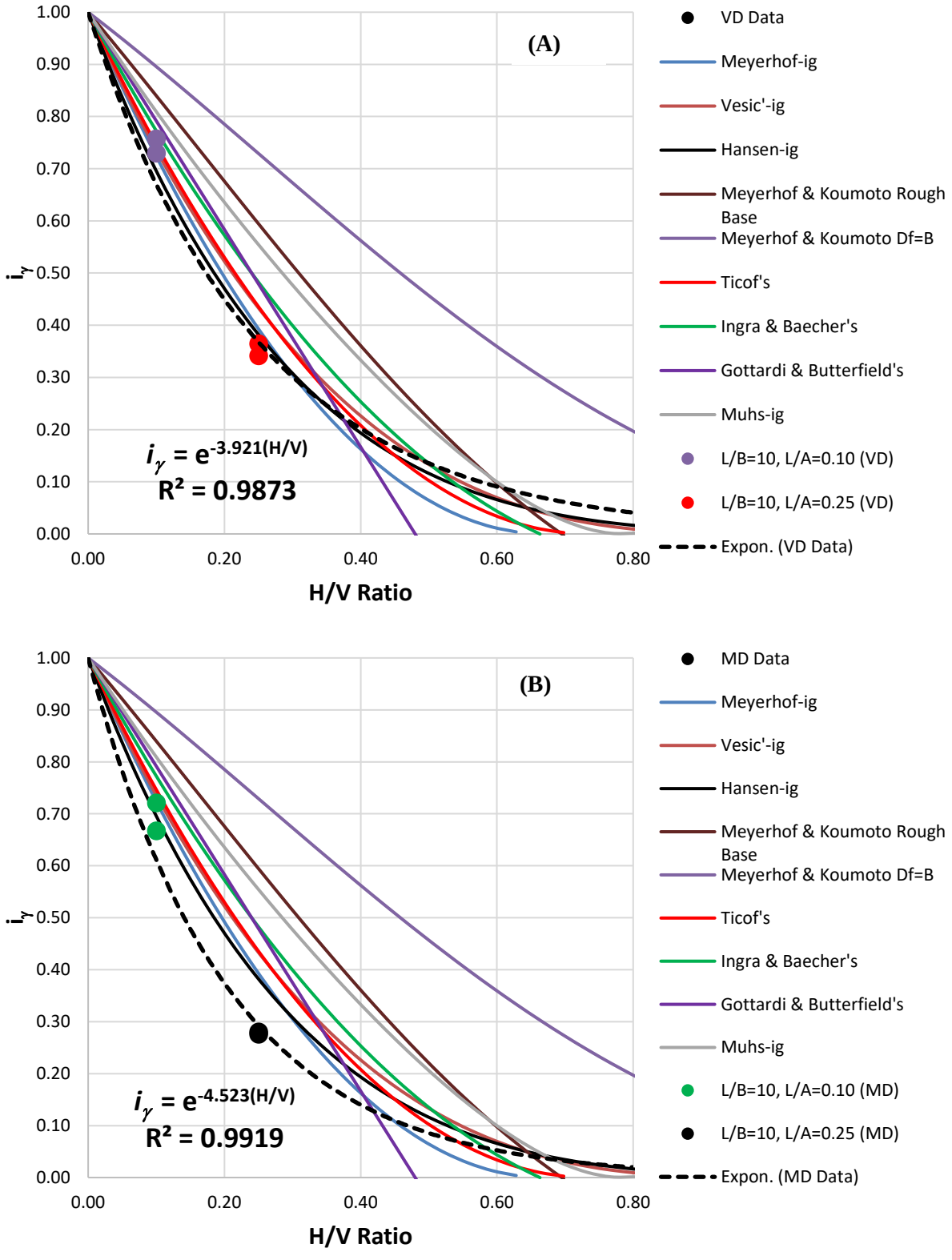

Figure 7.21 Soil self-weight inclination factor plots for L/B = 10 footings on (A) VD sand and (B) MD sand

The measured inclination values and overburden inclination factors, $i_{q,}$ methods considered in the analysis are presented in Figure 7.22. In the case of the medium and very dense conditions, Hansen (1970) is a better representation for the inclination factor with respect to overburden with embedment depth equal to 0.5B with L/A ratios of 0.1 and 0.25. Meyerhof (1953) and Vesić (1973) tend to overpredict i_q more than Hansen (1970) in the very dense soils, but does well in the medium dense soils. In the case of L/A equal to 0.25 the measured values appear to have a wider range than what was observed with the L/A = 0.10.

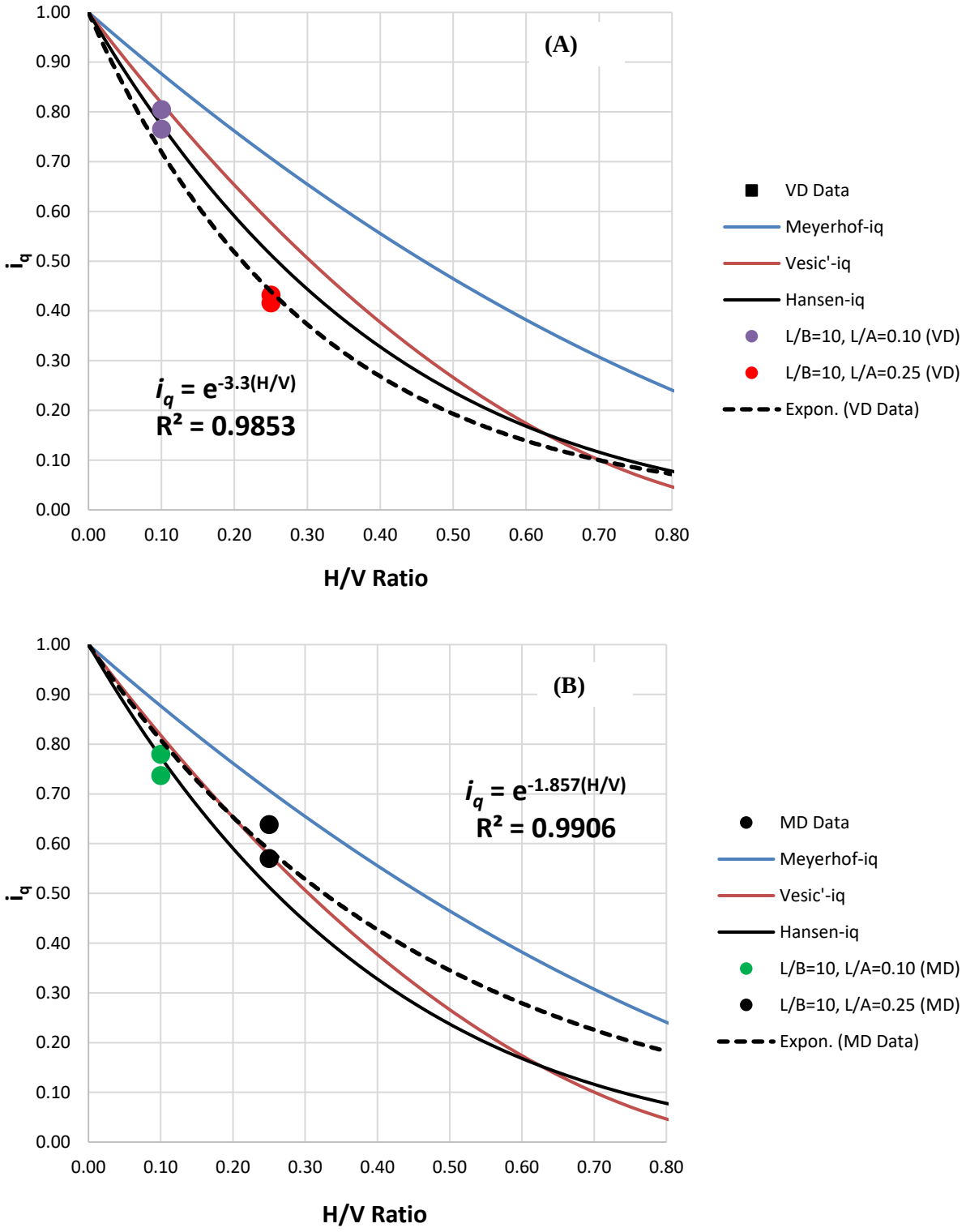

Figure 7.22 Overburden inclination factor plots for L/B = 10 footings on (A) VD sand and (B) MD sand

7.2.3.2 Square Footing

The measured inclination values and self-weight inclination factors, i_γ, methods considered in the analysis are presented in Figure 7.24. The measured inclination values presented are the normalized bearing capacity of Load Case-4 at the surface. Investigating Figure 7.24, Meyerhof (1953) and Hansen (1970) seem to be better representations for medium and very dense soil conditions with L/A ratios of 0.10. Meyerhof (1953) and Hansen (1970) provide fairly good representation for L/A ratios of 0.25. The measured values for L/A = 0.10 appear to be slightly lower than expected. Vesić (1973) tends to overpredict the self-weight inclination factor.

The measured inclination values and overburden inclination factors, $i_{q,}$ methods considered in the analysis are presented in Figure 7.25. In the case of the medium dense soil condition, Meyerhof (1953) and Vesić (1973) were better representation for the inclination factor with respect to overburden with embedment depth equal to 0.5B with L/A ratios of 0.1 and 0.25. In the case of very dense soil condition with L/A equal to 0.10 and 0.25 Hansen (1970) appears to provide a better representation.

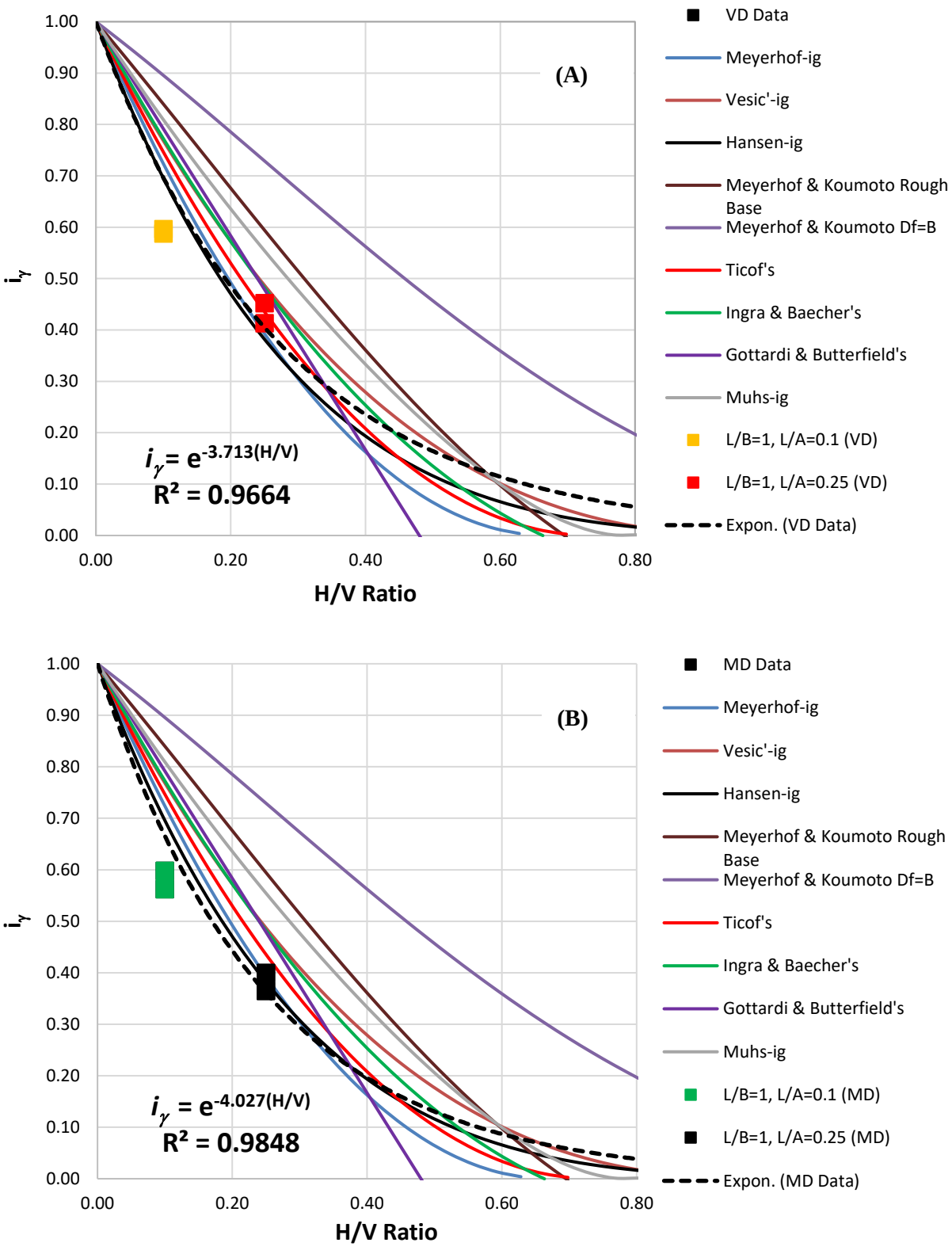

Figure 7.23 Soil self-weight inclination factor plots for L/B = 1 footings on (A) VD sand and (B) MD sand

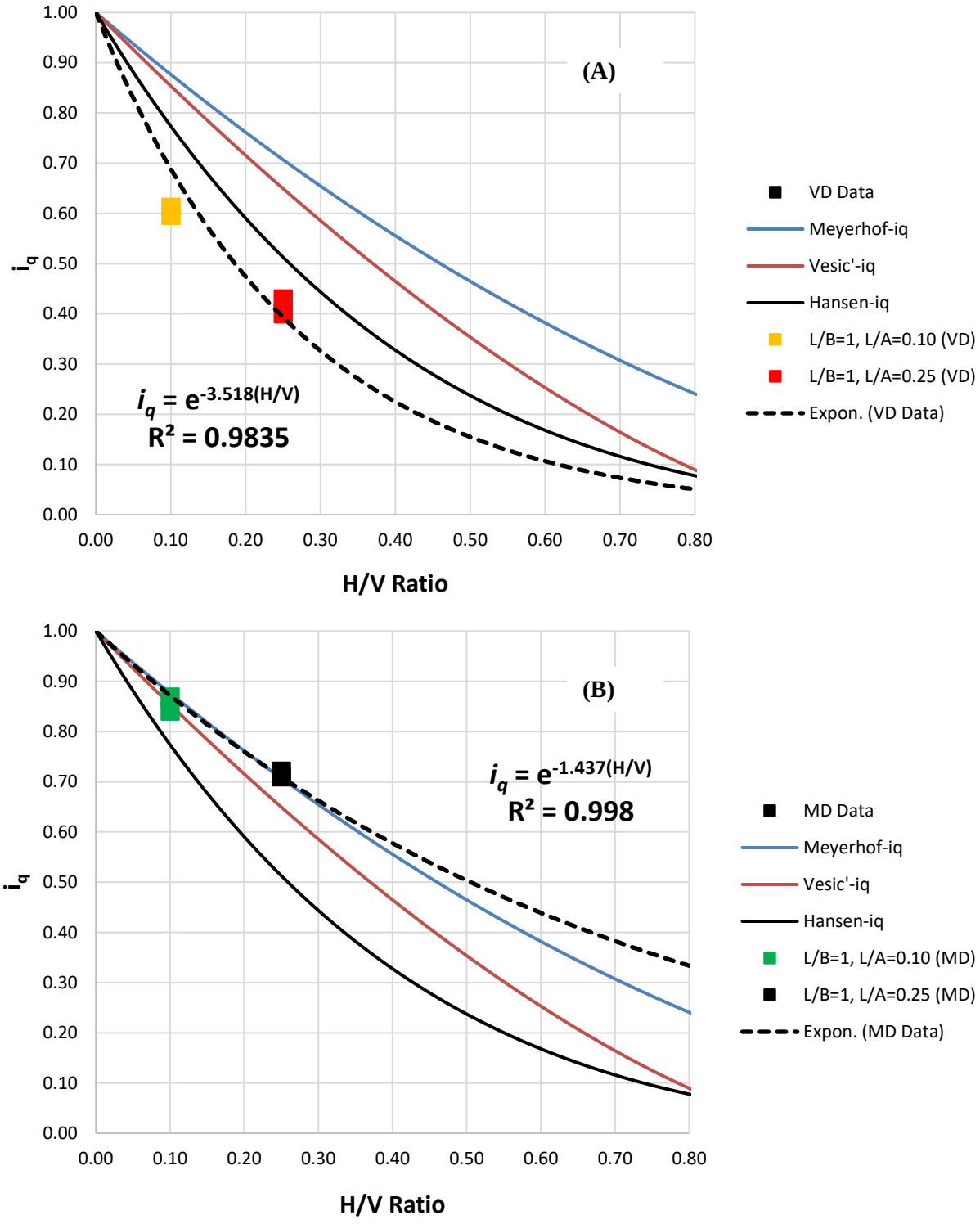

Figure 7.24 Overburden inclination factor factor plots for L/B = 1 footings on (A) VD sand and (B) MD sand

7.3 Measured versus Predicted Bearing Capacity for Rectangular Footing (L/B = 10)

The predicted bearing capacity for this series of testing uses the following design methods as a result of the outcome presented in the L/B = 20 testing, as well as AASHTO (2016) recommendations. The bearing capacity factor for overburden, N_q, presented by (Reissner, 1924). Self-weight bearing capacity factor, N_γ, presented by Vesić (1973), Zhu et. al (2001) and Hansen (1970). Shape factors for overburden and soil self-weight originally by DeBeer (1970), and modified by Vesić (1973), recommended by ASHTO (2016) for rectangular and square footings. Depth factors for overburden and soil self-weight presented by Hansen, (1970) and Vesić (1973). Inclination factors for overburden and soil self-weight by Vesić (1973), Meyerhof (1953), Hansen (1970), and Loukidis et al. (2008). Where eccentric loads are acting on the footing, the effective width, B', recommended by AASHTO (2016).

For Load Case-3, eccentric-inclined, horizontal component positive (+), to the direction of the eccentricity, the analysis used a positive horizontal component or positive angle of inclination for all inclination design methods. For Load Case-5, eccentric-inclined, horizontal component negative (–), to the direction of the eccentricity. The analysis used a negative horizontal component or negative angle of inclination for the design methods that allow for negative values.

7.3.1 Measured versus Predicted for Very Dense Condition

Measured versus predicted bearing capacity plots for various combinations of the design methods with very dense soil conditions are presented in Figure 7.25-7.37. Figures 7.25 and 7.26 present paired design method bias plots for the values of N_γ, s_γ, s_q, and d_q determined to be the best predictors from the individual bearing capacity factor analysis in previous sections. Further study of the s_q factor is performed here where the three methods in Section 7.1.2 were considered

for in all combinations. For the footings on very dense sand, the method by Vesić was determined to be the best performing based on bias (slope of linear trend line fit to data) and the R^2 value. Plots of measured and predicted capacities using the other s_q method (Meyerhof and Zhu) are in the Appendix. The design methods which display the best prediction values are presented in lower right corner of Figure 7.26. Presented in Figure 7.27 are the bias plots for design methods which poses their own depth, shape and inclination factors. The overall predictions for the very dense soil condition are representative. The methods that performed the best overall are listed below.

Very Dense (L/B = 10) Paired Design Methods with Vesić-s_q:

Load Case-1 (D_f = 0): Vesić- N_γ

Load Case-1 (D_f = 0.5B): Hansen- N_γ

Load Case-2 (D_f = 0): Zhu- N_γ

Load Case-2 (D_f = 0.5B): Hansen- N_γ

Load Case-3 (D_f = 0 & L/A = 0.10): Vesić- N_γ with Meyerhof - i_γ and i_q

Load Case-3 (D_f = 0.5B & L/A = 0.10): Hansen- N_γ with Hansen - i_γ and i_q

Load Case-3 (D_f = 0 & L/A = 0.25): Vesić - N_γ with Hansen - i_γ and i_q

Load Case-3 (D_f = 0.5B & L/A = 0.25): Hansen- N_γ with Hansen - i_γ and i_q

Load Case-4 (D_f = 0 & L/A = 0.10): Zhu- N_γ with Meyerhof - i_γ and i_q

Load Case-4 (D_f = 0.5B & L/A = 0.10): Hansen- N_γ with Loukidis f_{ie}

Load Case-4 (D_f = 0 & L/A = 0.25): Hansen- N_γ with Vesić - i_γ and i_q

Load Case-4 (D_f = 0.5B & L/A = 0.25): Hansen- N_γ with Hansen - i_γ and i_q

Load Case-5 (D_f = 0 & L/A = 0.10): Vesić- N_γ with Loukidis f_{ie}

Load Case-5 (D_f = 0.5B & L/A = 0.10): Vesić - N_γ with Vesić - i_γ and i_q

Load Case-5 (D_f = 0 & L/A = 0.25): Vesić - N_γ with Loukidis f_{ie}

Load Case-5 (D_f = 0.5B & L/A = 0.25): Vesić - N_γ with Loukidis f_{ie}

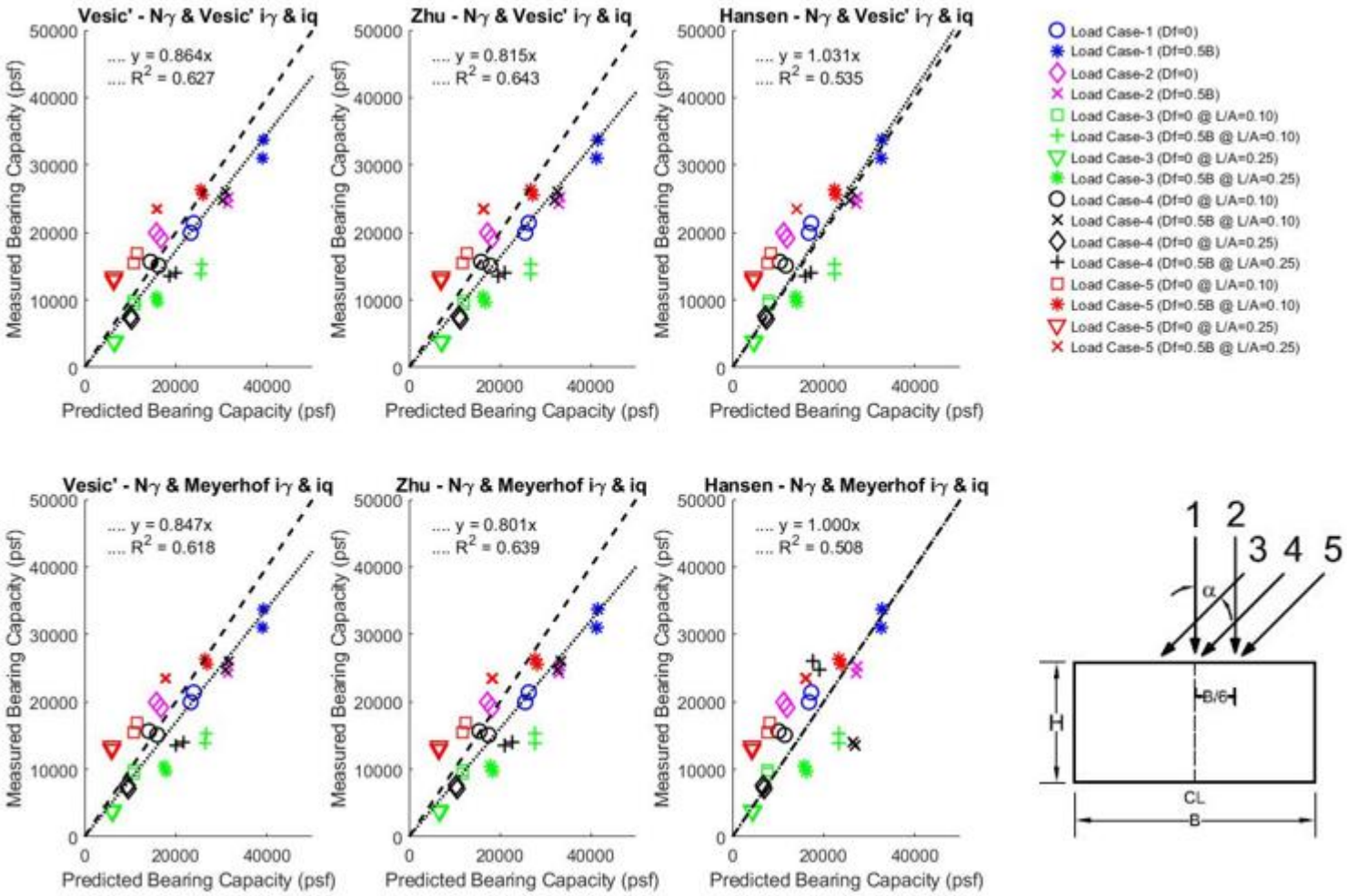

Figure 7.25 Bearing capacity-q_u bias plots for L/B = 10 very dense condition with paired design methods

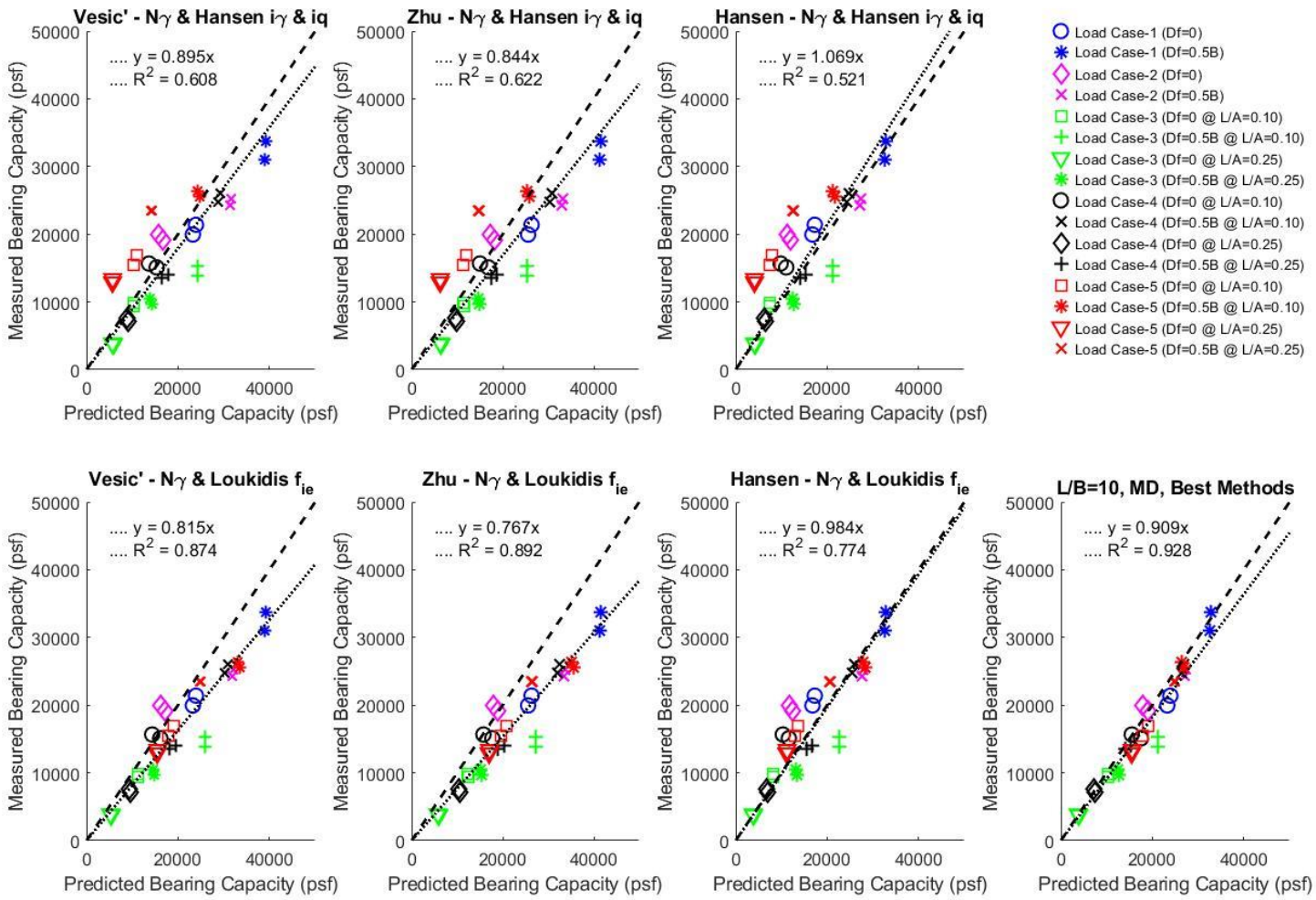

Figure 7.26 Bearing capacity-q_u bias plots for L/B = 10 very dense condition with paired and best design methods

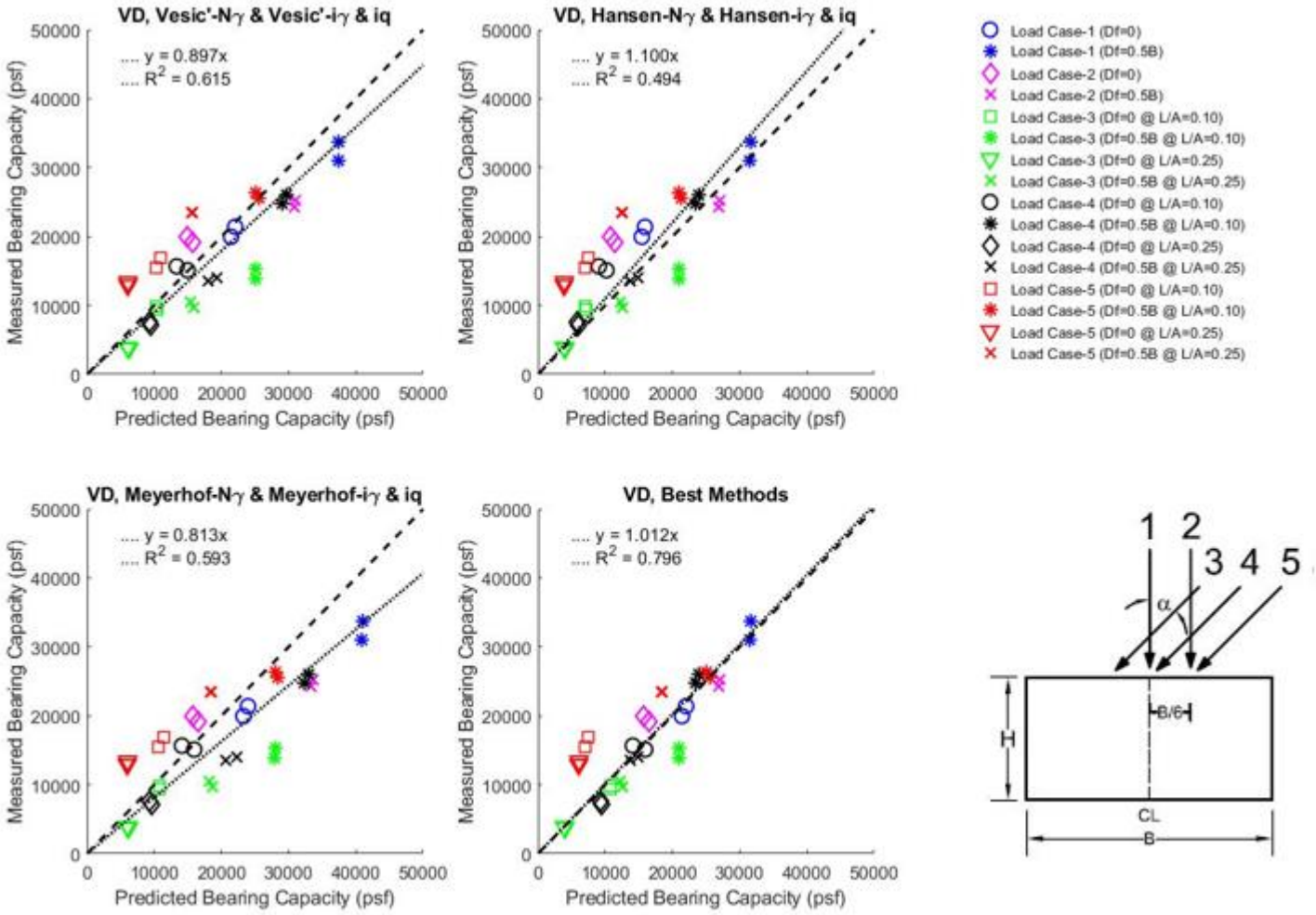

Figure 7.27 Bearing capacity-q_u bias plots for L/B = 10 very dense condition with matched design methods

7.3.2 Measured versus Predicted for Medium Dense Condition

Figures 7.28 and 7.30 present paired design method bias plots for the values of N_γ, s_γ, s_q and d_q determined to be the best predictors for the medium dense condition. Further study of the s_q factor is performed here where the three methods in Section 7.1.2 were considered for in all combinations. For the footings on medium dense sand, the method by Zhu was determined to generally be the best performing based on bias (slope of linear trend line fit to data) and the R^2 value. Plots of measured and predicted capacities using the other s_q method (Vesić and Meyerhof) are in the Appendix. The design methods which display the best prediction values are presented in lower right corner of Figure 7.29. Presented in Figure 7.30 are the bias plots for design methods which poses their own depth, shape and inclination factors. The overall predictions for the very dense soil condition are fairly representative. The methods that performed the best overall are listed below.

Medium Dense (L/B = 10) Paired Design Methods with Zhu-s_q:

Load Case-1 (D_f = 0): Zhu- N_γ

Load Case-1 (D_f = 0.5B): Vesić- N_γ

Load Case-2 (D_f = 0): Zhu- N_γ

Load Case-2 (D_f = 0.5B): Zhu- N_γ

Load Case-3 (D_f = 0 & L/A = 0.10): Zhu- N_γ with Loukidis f_{ie}

Load Case-3 (D_f = 0.5B & L/A = 0.10): Hansen- N_γ with Hansen - i_γ and i_q

Load Case-3 (D_f = 0 & L/A = 0.25): Zhu- N_γ with Vesić - i_γ and i_q

Load Case-3 (D_f = 0.5B & L/A = 0.25): Zhu- N_γ with Loukidis f_{ie}

Load Case-4 (D_f = 0 & L/A = 0.10): Zhu- N_γ with Vesić - i_γ and i_q

Load Case-4 (D_f = 0.5B & L/A = 0.10): Vesić - N_γ with Meyerhof - i_γ and i_q

Load Case-4 (D_f = 0 & L/A = 0.25): Vesić - N_γ with Vesić - i_γ and i_q

Load Case-4 (D_f = 0.5B & L/A = 0.25): Zhu- N_γ with Meyerhof - i_γ and i_q

Load Case-5 (D_f = 0 & L/A = 0.10): Zhu- N_γ with Loukidis f_{ie}

Load Case-5 (D_f = 0.5B & L/A = 0.10): Zhu- N_γ with Loukidis f_{ie}

Load Case-5 (D_f = 0 & L/A = 0.25): Zhu- N_γ with Loukidis f_{ie}

Load Case-5 (D_f = 0.5B & L/A = 0.25): Zhu- N_γ with Loukidis f_{ie}

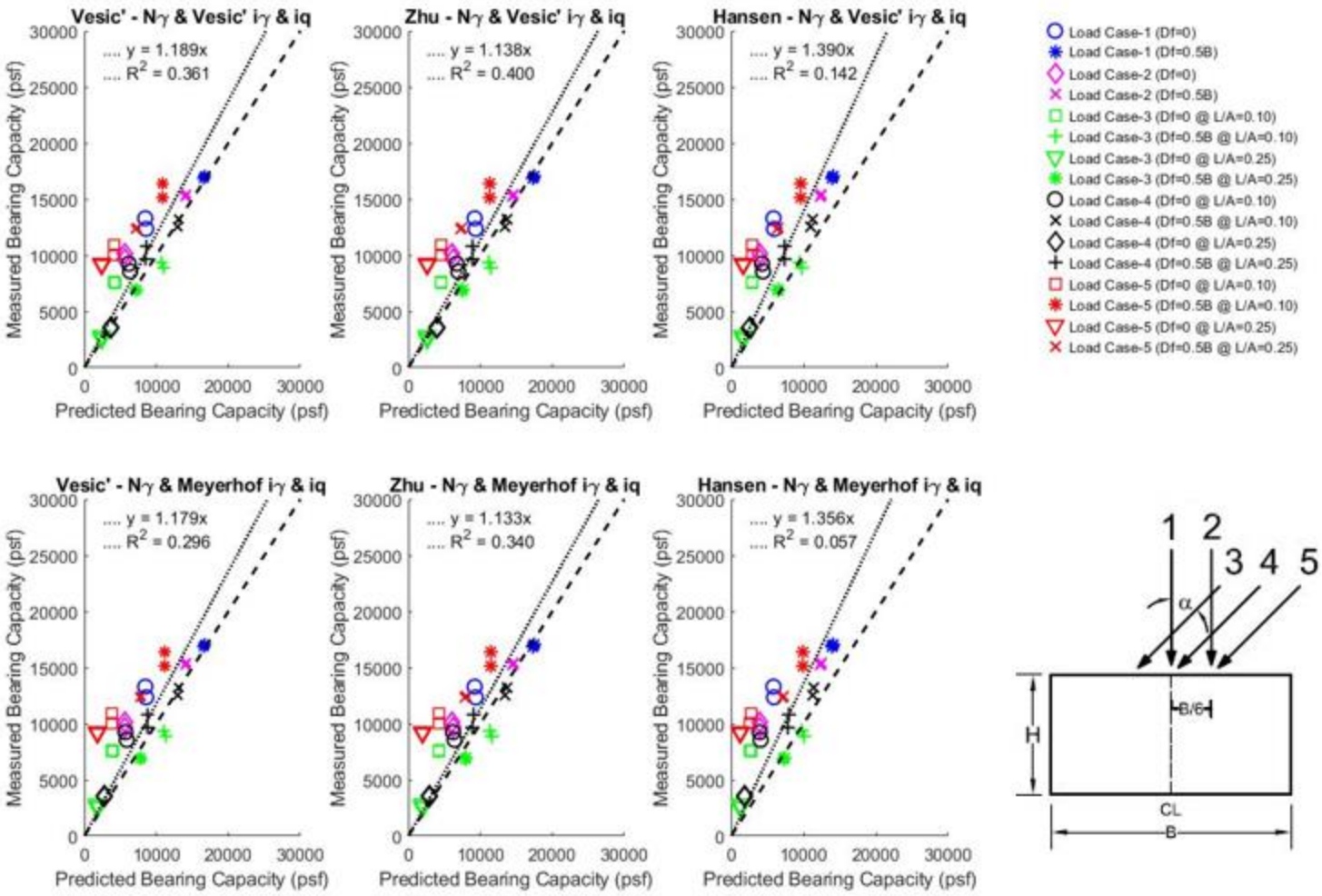

Figure 7.28 Bearing capacity-q_u bias plots for L/B = 10 medium dense condition with paired design methods

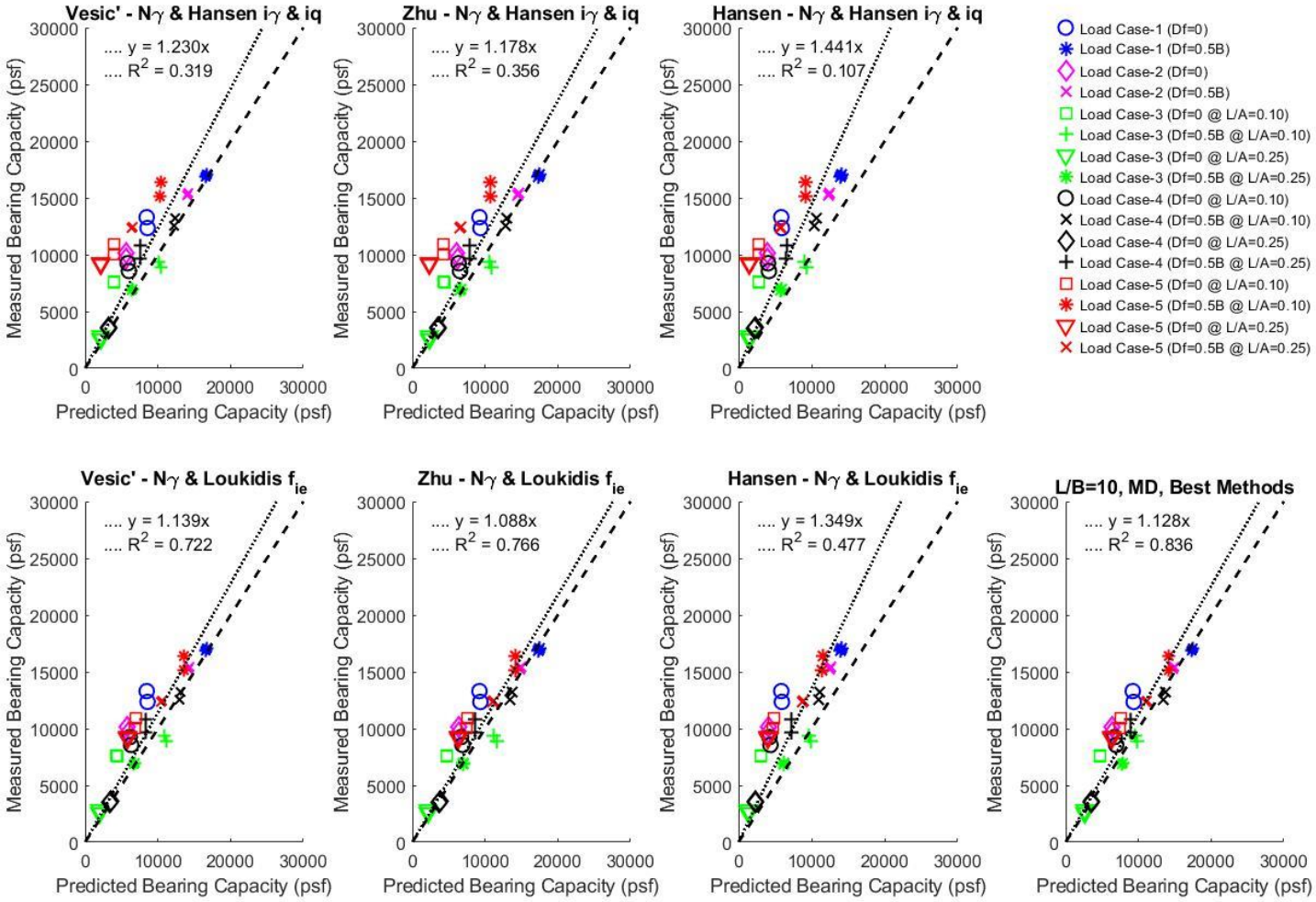

Figure 7.29 Bearing capacity-q_u bias plot for L/B = 10 medium dense condition with paired and best design methods

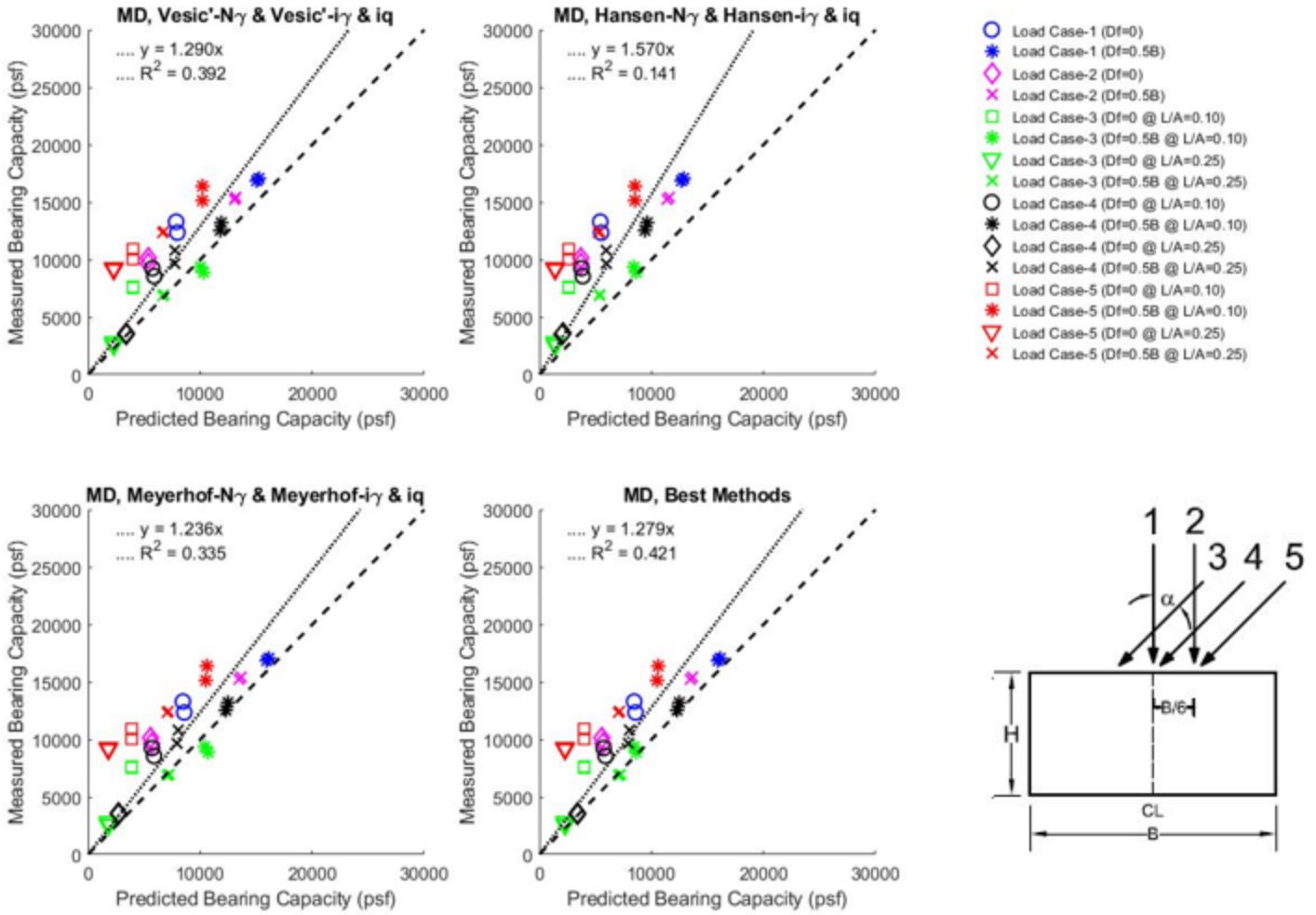

Figure 7.30 Bearing capacity-q_u bias plot for L/B = 10 medium dense condition with matched design methods

7.4 Measured versus Predicted Bearing Capacity for Square Footing (L/B = 1)

7.4.1 Measured versus Predicted for Very Dense Condition

Measured versus predicted bearing capacity plots for various combinations of the design methods with very dense soil conditions are presented in Figure 7.31-7.33.

Figures 7.31 and 7.33 present paired design method bias plots for the values of N_γ, s_γ, s_q and d_q determined to be the best predictors from the individual bearing capacity factor analysis in previous sections. Further study of the s_q factor is performed here where the three methods in Section 7.1.2 were considered for in all combinations. For the footings on very dense sand, the method by Meyerhof was determined to be the best performing based on bias (slope of linear trend line fit to data) and the R^2 value. Plots of measured and predicted capacities using the other s_q method (Vesić and Zhu) are in the Appendix. The design methods which display the best prediction values are presented in lower right corner of Figure 7.31. Presented in Figure 7.32 are the bias plots for design methods which poses their own depth, shape and inclination factors. The overall predictions for the very dense soil condition were fairly representative. The prediction methods that performed the best overall are listed below.

Very Dense (L/B = 1) Paired Design Methods with Meyerhof-s_q:

Load Case-1 (D_f = 0): Hansen- N_γ

Load Case-1 (D_f = 0.5B): Hansen- N_γ

Load Case-2 (D_f = 0): Zhu- N_γ

Load Case-2 (D_f = 0.5B): Vesić- N_γ

Load Case-3 (D_f = 0 & L/A = 0.10): Hansen- N_γ with Vesić - i_γ and i_q

Load Case-3 (D_f = 0.5B & L/A = 0.10): Hansen- N_γ with Hansen - i_γ and i_q

Load Case-3 (D_f = B & L/A = 0.10): Hansen- N_γ with Hansen - i_γ and i_q

Load Case-3 (D_f = 0 & L/A = 0.25): Vesić- N_γ with Vesić - i_γ and i_q

Load Case-3 (D_f = 0.5B & L/A = 0.25): Hansen- N_γ with Loukidis f_{ie}

Load Case-3 (D_f = B & L/A = 0.25): Vesić- N_γ with Vesić - i_γ and i_q

Load Case-4 (D_f = 0 & L/A = 0.10): Hansen- N_γ with Hansen - i_γ and i_q

Load Case-4 (D_f = 0.5B & L/A = 0.10): Hansen- N_γ with Hansen - i_γ and i_q

Load Case-4 (D_f = 0 & L/A = 0.25): Hansen- N_γ with Loukidis f_{ie}

Load Case-4 (D_f = 0.5B & L/A = 0.25): Hansen- N_γ with Hansen - i_γ and i_q

Load Case-4 (D_f = B & L/A = 0.25): Vesić- N_γ with Loukidis f_{ie}

Load Case-5 (D_f = 0 & L/A = 0.10): Vesić - N_γ with Loukidis f_{ie}

Load Case-5 (D_f = 0.5B & L/A = 0.10): Vesić - N_γ with Loukidis f_{ie}

Load Case-5 (D_f = 0 & L/A = 0.25): Vesić - N_γ with Loukidis f_{ie}

Load Case-5 (D_f = 0.5B & L/A = 0.25): Vesić - N_γ with Loukidis f_{ie}

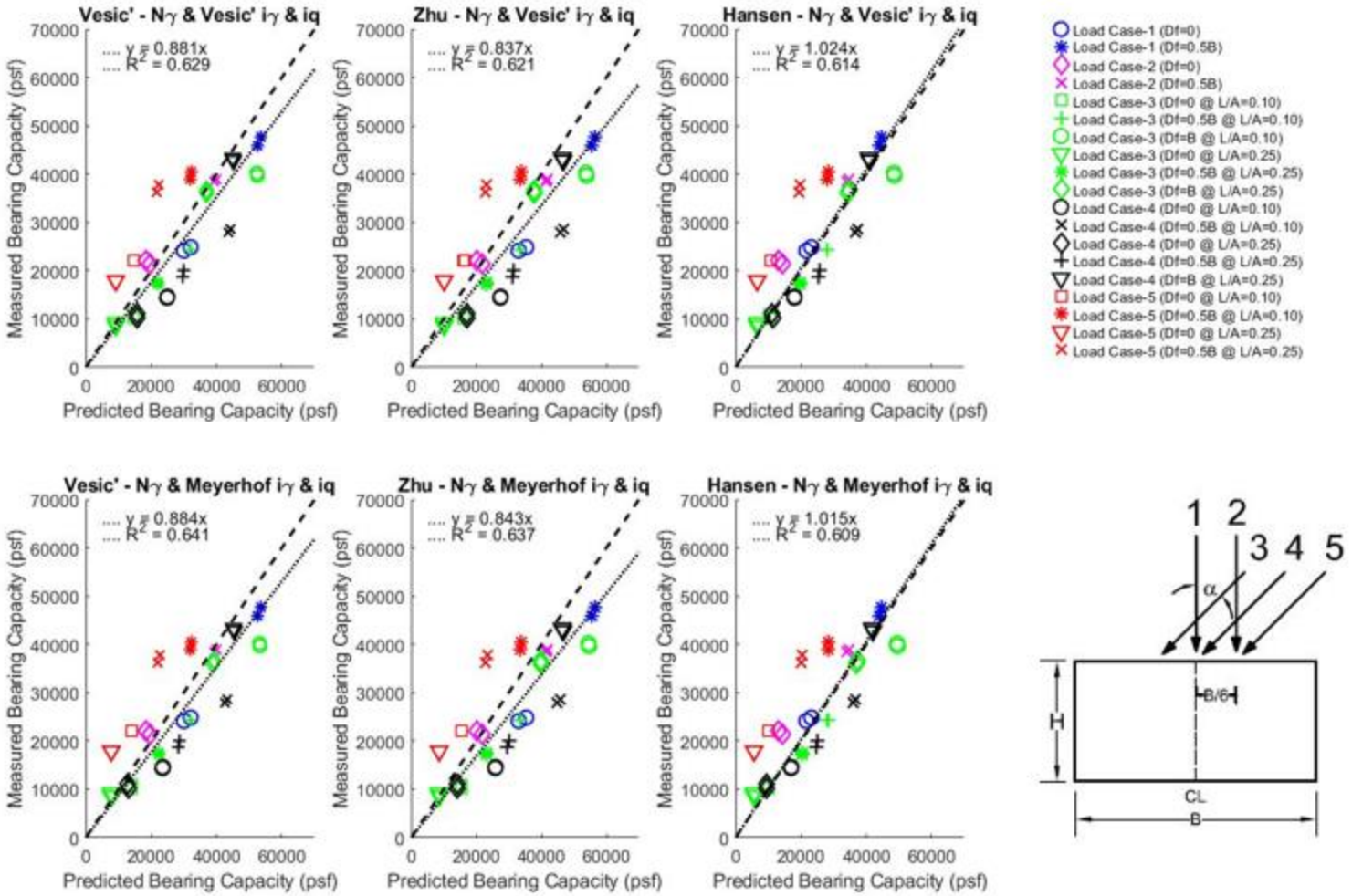

Figure 7.31 Bearing capacity-q_u bias plots for L/B = 1 very dene condition with paired design methods

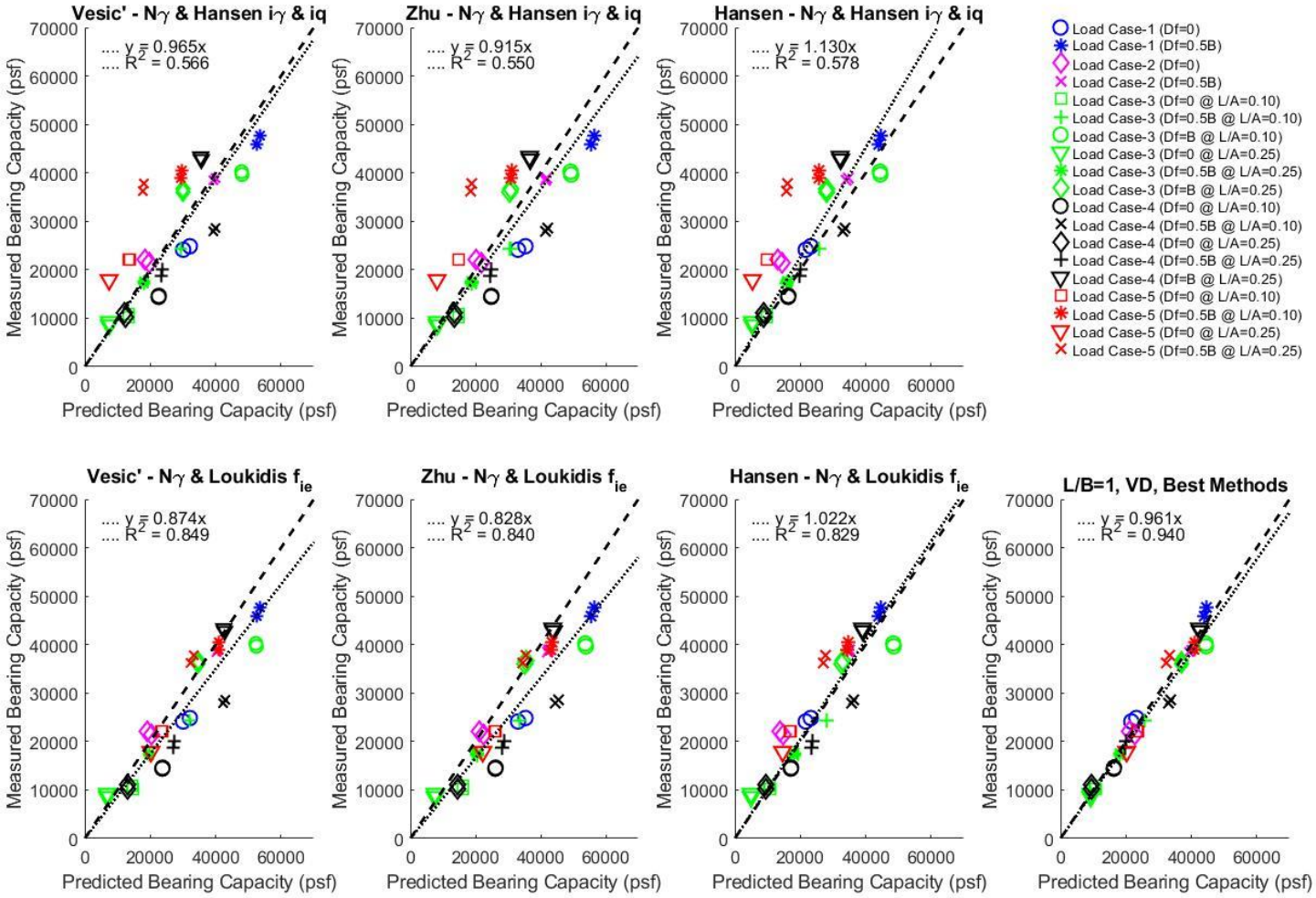

Figure 7.32 Bearing capacity-q_u bias plots for L/B = 1 very dense condition with paired and best design methods

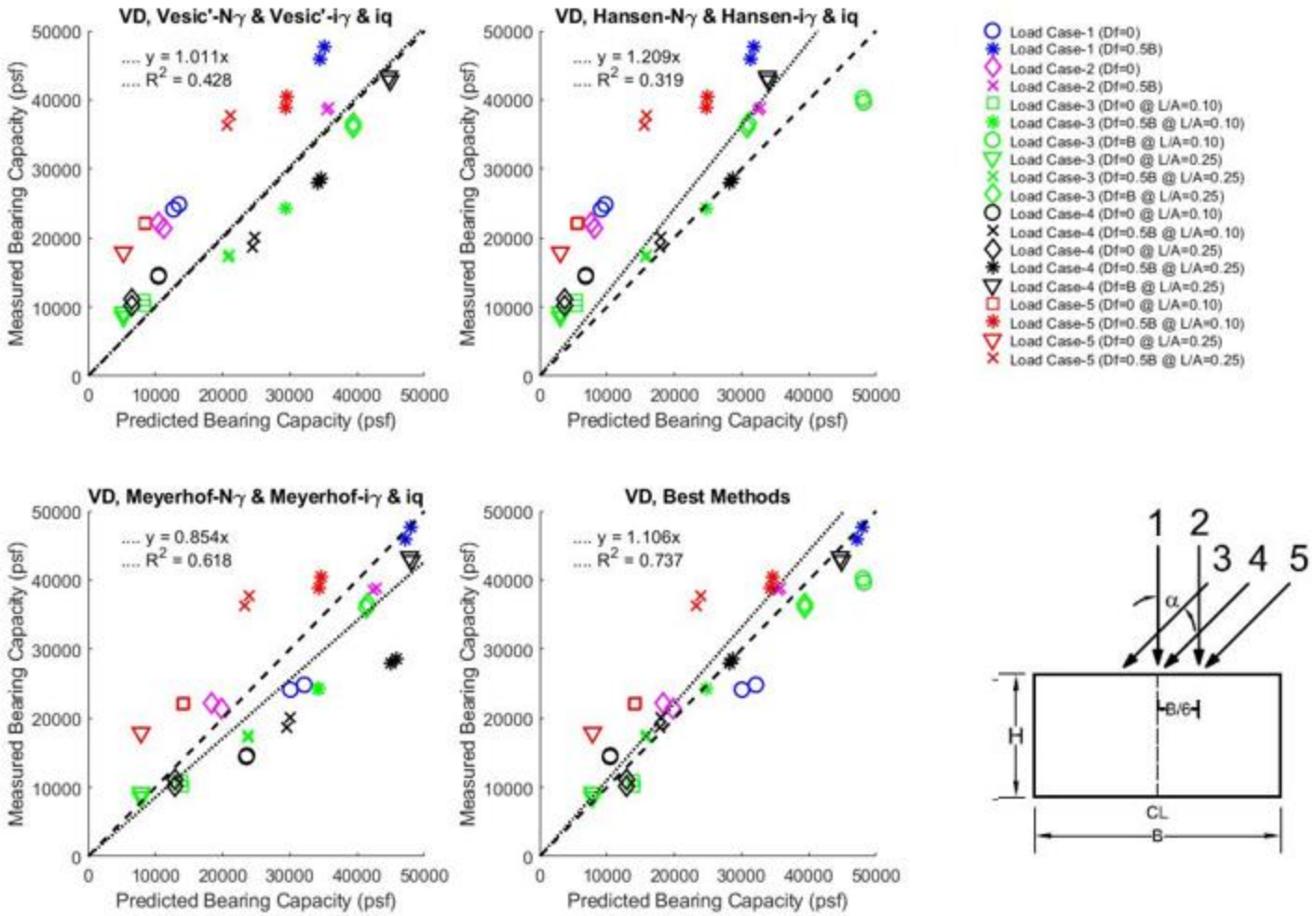

Figure 7.33 Bearing capacity-q_u bias plots for L/B = 1 very dense condition with matched design methods

7.4.2 Measured versus Predicted for Medium Dense Condition

Figures 7.34 and 7.35 present paired design method bias plots for the values of N_γ, s_γ, s_q and d_q determined to be the best predictors for the medium dense condition. Further study of the s_q factor is performed here where the three methods in Section 7.1.2 were considered for in all combinations. For the footings on medium dense sand, the method by Zhu was determined to generally be the best performing based on bias (slope of linear trend line fit to data) and the R^2 value. Plots of measured and predicted capacities using the other s_q method (Vesić and Meyerhof) are in the Appendix. The design methods which display the best prediction values are presented in lower right corner of Figure 7.35. Presented in Figure 7.36 are the bias plots for design methods which poses their own depth, shape and inclination factors. The overall predictions for the very dense soil condition were fairly representative. The prediction methods that performed the best overall are listed below.

Medium Dense (L/B = 1) Paired Design Methods with Zhu-s_q:

Load Case-1 (D_f = 0): Zhu- N_γ

Load Case-1 (D_f = 0.5B): Hansen- N_γ

Load Case-2 (D_f = 0): Zhu- N_γ

Load Case-2 (D_f = 0.5B): Vesić- N_γ

Load Case-3 (D_f = 0 & L/A = 0.10): Zhu- N_γ with Loukidis f_{ie}

Load Case-3 (D_f = 0.5B & L/A = 0.10): Hansen- N_γ with Hansen- i_γ and i_q

Load Case-3 (D_f = 0 & L/A = 0.25): Zhu- N_γ with Vesić - i_γ and i_q

Load Case-3 (D_f = 0.5B & L/A = 0.25): Vesić - N_γ with Loukidis f_{ie}

Load Case-4 (D_f = 0 & L/A = 0.10): Vesić- N_γ with Hansen - i_γ and i_q

Load Case-4 (D_f = 0.5B & L/A = 0.10): Hansen- N_γ with Vesić - i_γ and i_q

Load Case-4 (D_f = 0 & L/A = 0.25): Zhu- N_γ with Loukidis f_{ie}

Load Case-4 (D_f = 0.5B & L/A = 0.25): Zhu- N_γ with Vesić - i_γ and i_q

Load Case-5 (D_f = 0 & L/A = 0.10): Zhu- N_γ with Loukidis f_{ie}

Load Case-5 (D_f = 0.5B & L/A = 0.10): Zhu- N_γ with Loukidis f_{ie}

Load Case-5 (D_f = 0 & L/A = 0.25): Zhu- N_γ with Loukidis f_{ie}

Load Case-5 (D_f = 0.5B & L/A = 0.25): Zhu- N_γ with Loukidis f_{ie}

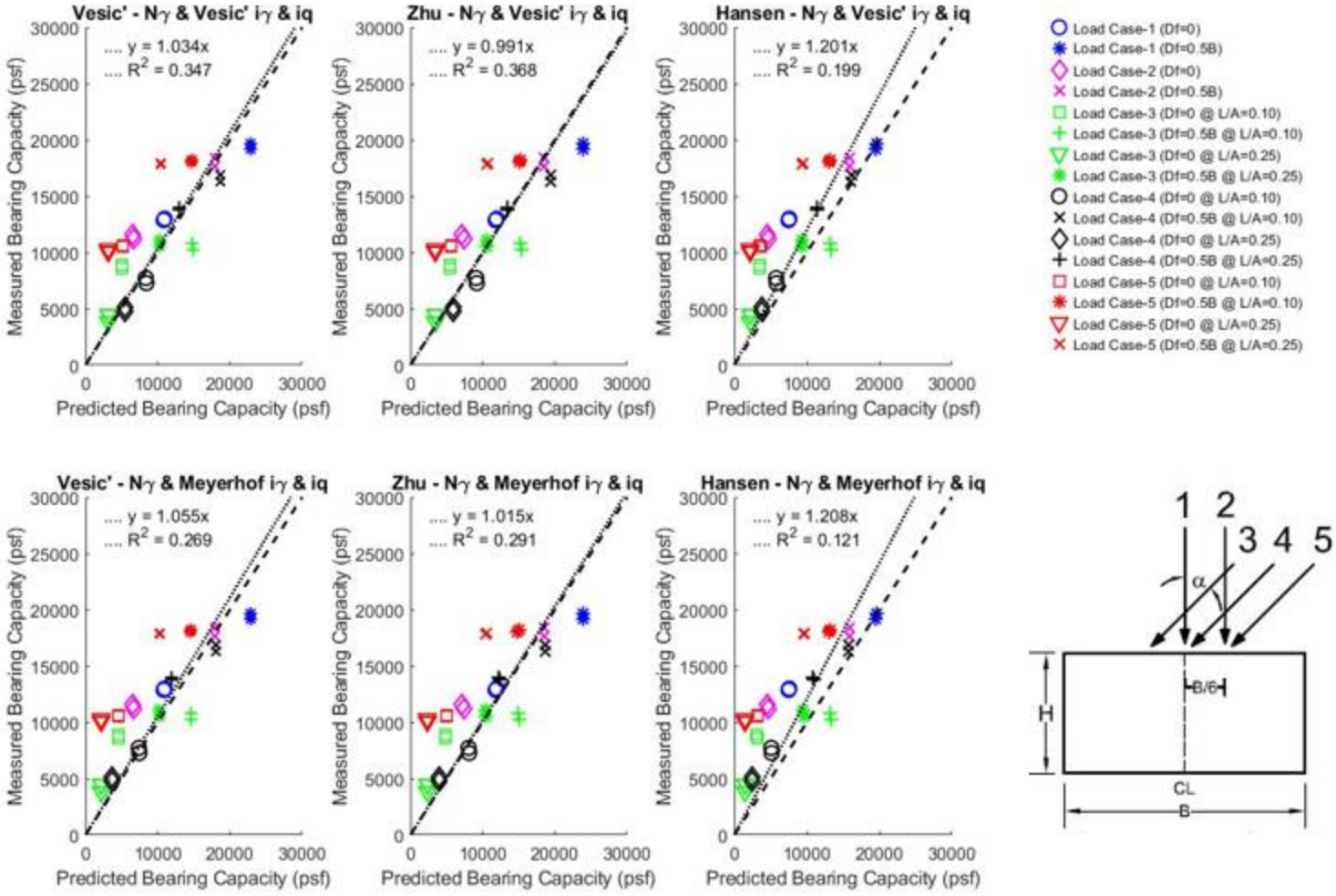

Figure 7.34 Bearing capacity-q_u bias plots for L/B = 1 medium dense condition with paired design methods

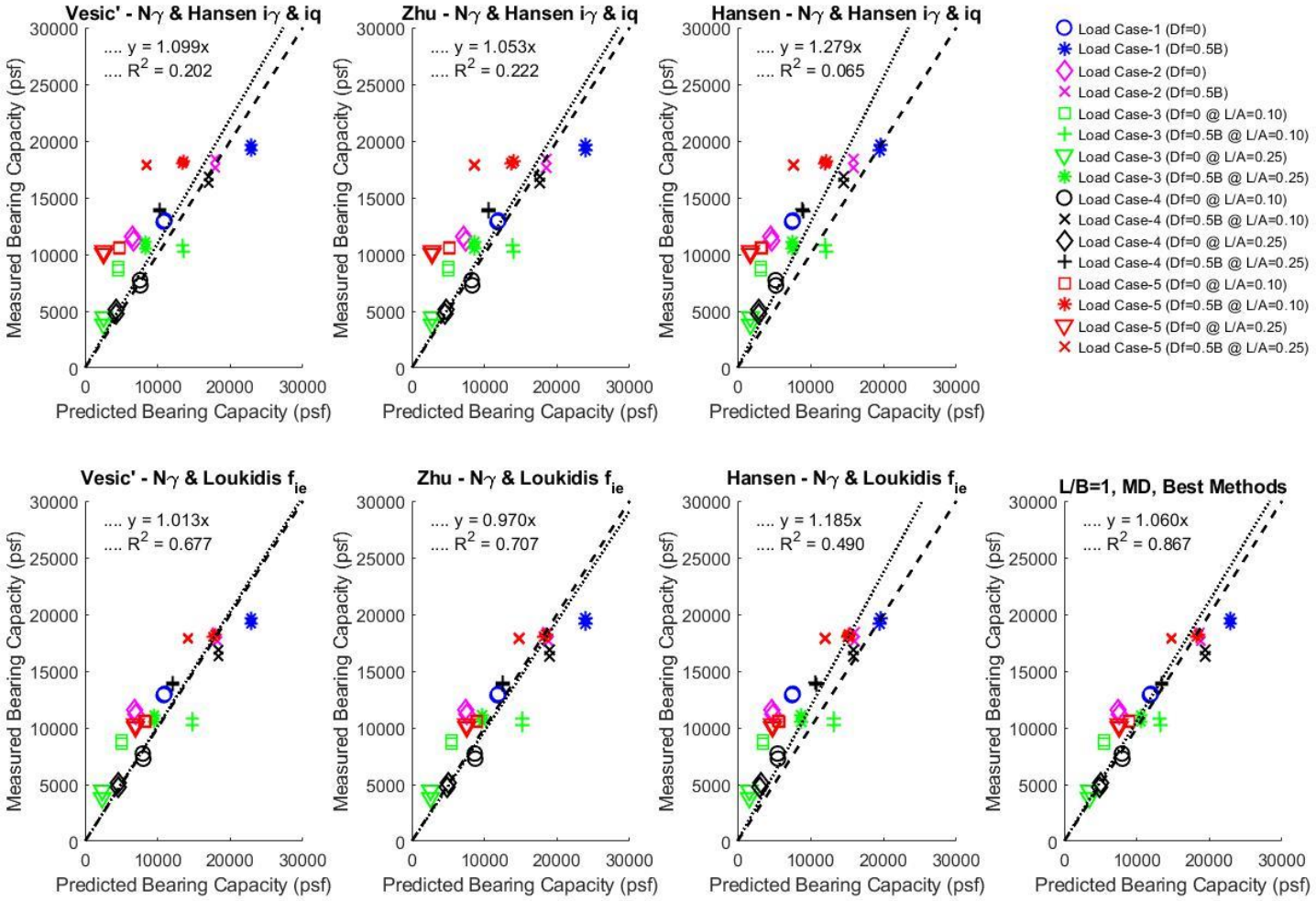

Figure 7.35 Bearing capacity-q_u bias plot for L/B = 1 medium dense condition with paired and best design methods

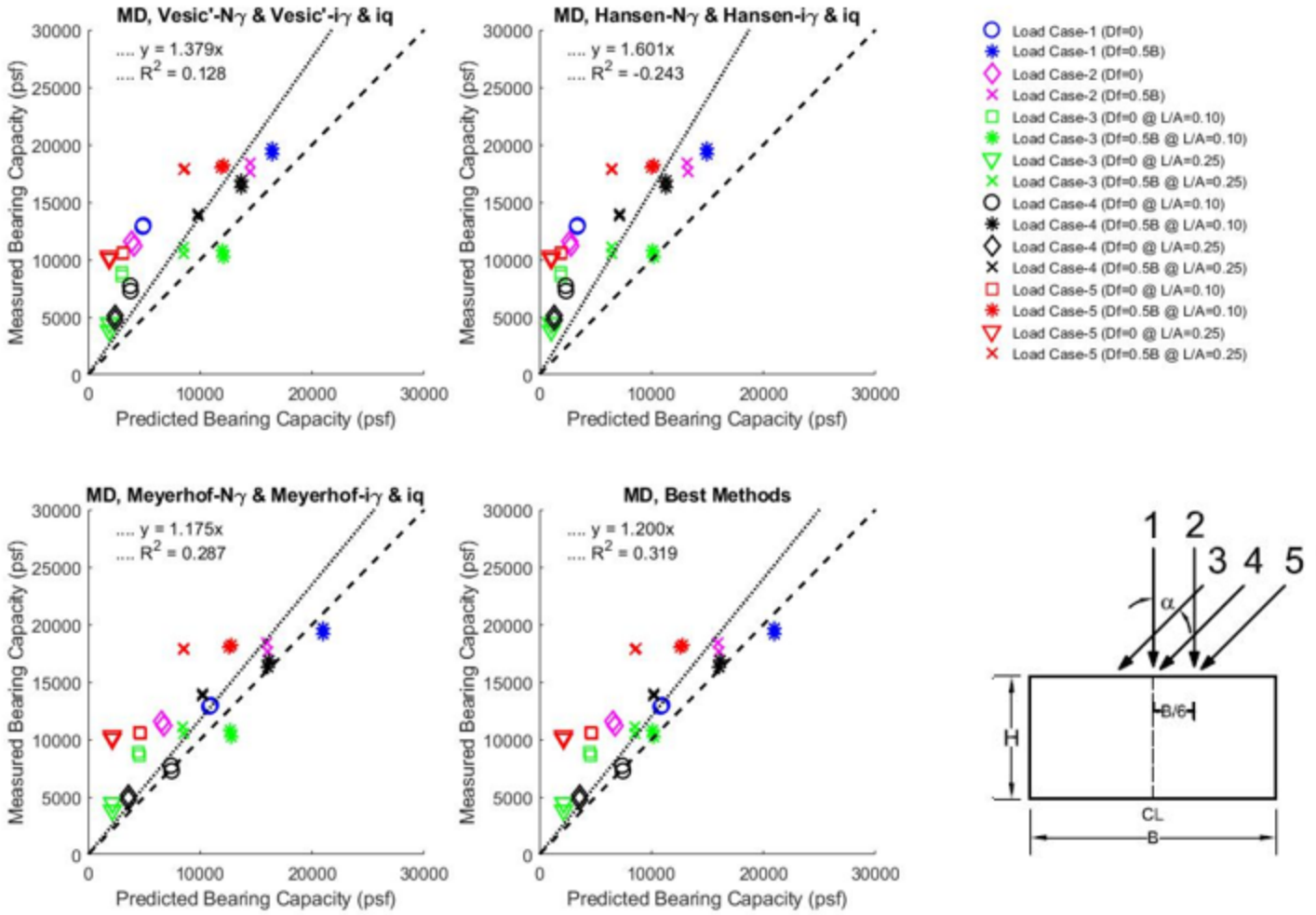

Figure 7.36 Bearing capacity-q_u bias plots for L/B = 1 medium dense condition with matched design methods

8.0 CONCLUSIONS AND RECOMMENDATIONS

A series of centrifuge tests of strip, rectangular, and square footings to model prototype footings on very dense and medium dense sand subjected to concentric and inclined-eccentric loads were conducted. The following are conclusions of: 1) the experiments to evaluate the influence of footing embedment on the bearing capacity of when the footing is subjected to inclined-eccentric loads and the effect on the bearing capacity for the direction of load inclination relative to the direction of eccentricity and 2) comparison of results with existing methods to estimate the bearing capacity and factors for overburden, soil self-weight, depth of embedment, footing shape, load inclination, and eccentricity.

8.1 Conclusions for Rectangular Footing Bearing Capacity Tests

8.1.1 Rectangular Footing Conclusions for Very Dense Condition

- Load Case-3 (eccentric-inclined loading with + load combination (partially compensating)) is the most critical of all the cases. When $D_f = 0$, the bearing capacity was 53.4% and 81.6% less than the concentrically loaded footing (Load Case-1) for the lateral-to-axial load ratios of 0.10 and 0.25, respectively. When $D_f = 0.5B$, the bearing capacity was 54.9% and 68.9% less than the concentrically loaded footing with $D_f = 0.5B$ (Load Case-1) for the lateral-to-axial load ratios of 0.10 and 0.25, respectively.
- Load Case-4 (inclined loading): When $D_f = 0$ the bearing capacity was 25.6% and 64.7% less than the concentrically loaded footing (Load Case-1) for the lateral-to-axial load ratios of 0.10 and 0.25, respectively. When $D_f = 0.5B$, the bearing capacity was 21.5% and 55.6% less than the concentrically loaded footing with $D_f = 0.5B$ (Load Case-1) for the lateral-to-axial load ratios of 0.10 and 0.25, respectively.
- Load Case-5 (eccentric-inclined loading with – load combination (reinforcing)) generally showed less decrease in bearing capacity than Load Cases 3 and 4. When $D_f = 0$, the bearing

capacity was 21.7% and 36.4% less than the concentrically loaded footing (Load Case-1) for the lateral-to-axial load ratios of 0.10 and 0.25, respectively. When D_f = 0.5B, the bearing capacity was 20.1% and 27.6% less than the concentrically loaded footing with D_f = 0.5B (Load Case-1) for the lateral-to-axial load ratios of 0.10 and 0.25, respectively.

- Embedment of 0.5B had marked effect on the bearing capacity of all load cases. Bearing capacity increased by 23.7% for Load Case-2 (eccentric load). Between tests of Load Case-3 (most critical), there was a 41.1% and 90% increase for the lateral-to-axial load ratios of 0.10 and 0.25, respectively. For Load Case-4, there was a 49.3% and 61.3% increase for the lateral-to-axial load ratios of 0.10 and 0.25, respectively. For Load Case-5, there was a 46.2% and 56.4% increase for the lateral-to-axial load ratios of 0.10 and 0.25, respectively.

8.1.2 Rectangular Footing Conclusions for Medium Dense Condition

- Load Case-3 (eccentric-inclined loading with + load combination (partially compensating)) is the most critical of all the cases. When D_f = 0, the bearing capacity was 41.5% and 79% less than the concentrically loaded footing (Load Case-1) for the lateral-to-axial load ratios of 0.10 and 0.25, respectively. When D_f = 0.5B, the bearing capacity was 46.2% and 58.9% less than the concentrically loaded footing with D_f = 0.5B (Load Case-1) for the lateral-to-axial load ratios of 0.10 and 0.25, respectively.
- Load Case-4 (inclined loading): When D_f = 0 the bearing capacity was 30.6% and 72.2% less than the concentrically loaded footing (Load Case-1) for the lateral-to-axial load ratios of 0.10 and 0.25, respectively. When D_f = 0.5B, the bearing capacity was 24.2% and 39.6% less than the concentrically loaded footing with D_f = 0.5B (Load Case-1) for the lateral-to-axial load ratios of 0.10 and 0.25, respectively.
- Load Case-5 (eccentric-inclined loading with – load combination (reinforcing)) generally showed less decrease in bearing capacity than Load Cases 3 and 4. When D_f = 0, the bearing

capacity was 18.2% and 28.2% less than the concentrically loaded footing (Load Case-1) for the lateral-to-axial load ratios of 0.10 and 0.25, respectively. When D_f = 0.5B, the bearing capacity was 7.1% and 26.8% less than the concentrically loaded footing with D_f = 0.5B (Load Case-1) for the lateral-to-axial load ratios of 0.10 and 0.25, respectively.

- Embedment of 0.5B had marked effect on the bearing capacity of all load cases. Bearing capacity increased by 43.1% for load case 2 (eccentric load). Between tests of load case 3 (most critical), there was a 18.6% and 88% increase for the lateral/axial load ratios of 0.10 and 0.25, respectively. For load case 4, there was a 36.3% and 100% increase for the lateral/axial load ratios of 0.10 and 0.25, respectively. For load case 5, there was a 40.1% and 29.6% increase for the lateral/axial load ratios of 0.10 and 0.25, respectively.

8.2 Conclusions for Square Footing Bearing Capacity Tests

8.2.1 Square Footing Conclusions for Very Dense Condition

- Load Case-3 (eccentric-inclined loading with + load combination (partially compensating)) is the most critical of all the cases. When D_f = 0, the bearing capacity was 55.3% and 63.7% less than the concentrically loaded footing (Load Case-1) for the lateral-to-axial load ratios of 0.10 and 0.25, respectively. When D_f = 0.5B, the bearing capacity was 48.2% and 62.9% less than the concentrically loaded footing with D_f = 0.5B (Load Case-1) for the lateral-to-axial load ratios of 0.10 and 0.25, respectively.
- Load Case-4 (inclined loading): When D_f = 0 the bearing capacity was 40.8% and 56.7% less than the concentrically loaded footing (Load Case-1) for the lateral-to-axial load ratios of 0.10 and 0.25, respectively. When D_f = 0.5B, the bearing capacity was 36.6% and 56.5% less than the concentrically loaded footing with D_f = 0.5B (Load Case-1) for the lateral-to-axial load ratios of 0.10 and 0.25, respectively.

- Load Case-5 (eccentric-inclined loading with – load combination (reinforcing)) generally showed less decrease in bearing capacity than Load Cases 3 and 4. When $D_f = 0$, the bearing capacity was 9.9% and 26.9% less than the concentrically loaded footing (Load Case-1) for the lateral-to-axial load ratios of 0.10 and 0.25, respectively. When $D_f = 0.5B$, the bearing capacity was 15.3% and 20.9% less than the concentrically loaded footing with $D_f = 0.5B$ (Load Case-1) for the lateral-to-axial load ratios of 0.10 and 0.25, respectively.
- Embedment of 0.5B had marked effect on the bearing capacity of all load cases. Bearing capacity increased by 55.7% for Load Case-2 (eccentric load). Between tests of Load Case-3 (most critical), there was a 78.8% and 64.3% increase for the lateral-to-axial load ratios of 0.10 and 0.25, respectively. For Load Case-4, there was a 64.3% and 58.5% increase for the lateral-to-axial load ratios of 0.10 and 0.25, respectively. For Load Case-5, there was a 56.9% and 69.3% increase for the lateral-to-axial load ratios of 0.10 and 0.25, respectively.

8.2.2 Square Footing Conclusions for Medium Dense Condition

- Load Case-3 (eccentric-inclined loading with + load combination (partially compensating)) is the most critical of all the cases. When $D_f = 0$, the bearing capacity was 33.4% and 67.9% less than the concentrically loaded footing (Load Case-1) for the lateral-to-axial load ratios of 0.10 and 0.25, respectively. When $D_f = 0.5B$, the bearing capacity was 45.7% and 44.4% less than the concentrically loaded footing with $D_f = 0.5B$ (Load Case-1) for the lateral-to-axial load ratios of 0.10 and 0.25, respectively.
- Load Case-4 (inclined loading): When $D_f = 0$ the bearing capacity was 42% and 61.8% less than the concentrically loaded footing (Load Case-1) for the lateral-to-axial load ratios of 0.10 and 0.25, respectively. When $D_f = 0.5B$, the bearing capacity was 14.5% and 28.5% less than the concentrically loaded footing with $D_f = 0.5B$ (Load Case-1) for the lateral-to-axial load ratios of 0.10 and 0.25, respectively.

- Load Case-5 (eccentric-inclined loading with – load combination (reinforcing)) generally showed less decrease in bearing capacity than Load Cases 3 and 4. When $D_f = 0$, the bearing capacity was 18.3% and 21.3% less than the concentrically loaded footing (Load Case-1) for the lateral-to-axial load ratios of 0.10 and 0.25, respectively. When $D_f = 0.5B$, the bearing capacity was 6.7% and 8% less than the concentrically loaded footing with $D_f = 0.5B$ (Load Case-1) for the lateral-to-axial load ratios of 0.10 and 0.25, respectively.
- Embedment of 0.5B had marked effect on the bearing capacity of all load cases. Bearing capacity increased by 45% for Load Case-2 (eccentric load). Between tests of Load Case-3 (most critical), there was a 18.2% and 88.6% increase for the lateral-to-axial load ratios of 0.10 and 0.25, respectively. For Load Case-4, there was a 75.2% and 94.8% increase for the lateral-to-axial load ratios of 0.10 and 0.25, respectively. For Load Case-5, there was a 52.3% and 54.6% increase for the lateral-to-axial load ratios of 0.10 and 0.25, respectively.

8.3 Recommendations

Methods to estimate the bearing capacity of the footings tested in this study include those recommended by AASHTO Bridge Design Specifications and existing methods in the literature. These mostly vary on the soil self-weight factor, N_γ, and the inclination factors i_q and i_γ. Depth of embedment factors from Meyerhof and multiple shape factors (Vesić, Meyerhof, and Zhu) compared well with the results and were used in the bearing capacity analysis together with the inclination factors. For the rectangular footing (L/B = 10) on very dense sand, the Hansen N_γ with Hansen i_q and i_γ, the Vesić and Zhu N_γ with Loukidis f_{ie} (factor to account for eccentric-inclined load), and Hansen N_γ with Loukidis f_{ie} resulted in good agreement with most cases tested. For the rectangular footing (L/B = 10) on medium dense sand, the Vesić N_γ with Loukidis f_{ie} and Zhu N_γ with Loukidis f_{ie} resulted in good agreement with most cases tested. For the square footing

(L/B = 1) on very dense sand, the Hansen N_γ with Hansen i_q and i_γ, Hansen N_γ with Vesić i_q and i_γ, and Zhu N_γ with Loukidis f_{ie} resulted in good agreement with most cases tested. For the square footing (L/B = 1) on medium dense sand, the Vesić N_γ with Hansen i_q and i_γ, Hansen N_γ with Vesić i_q and i_γ, Zhu N_γ with Loukidis f_{ie} resulted in good agreement with most cases tested.

REFERENCES

AASHTO (2016). AASHTO LRFD Bridge Design Specifications (U.S. Customary Units), Fourth Edition, American Association of State Highway and Transportation Officials (AASHTO), Washington, D.C.

Bowles, J.E. (1996) Foundation Analysis and Design. 5th Edition, The McGraw-Hill Companies, Inc., New York.

Bowles, J. E. (1997). *Foundation Analysis and Design*. McGraw-Hill, Singapore.

Boyle, S. R., 1995, Deformation Prediction of Geosynthetic Reinforced Soil Retaining Walls, Ph.D. Dissertation, University of Washington, 391 pp.

Bransby, M. F. & Randolph, M. F. (1998). "Combined loading of skirted foundations", *Géotechnique*, 48, No. 5, pp. 637-655

Das, B.M. (2016). Principles of Foundation Engineering (8th ed.). Cengage Learning, Boston, MA.

De Beer, E.E. (1967) Proefodervindelijke bijdrage tot de studie van het gransdragvermogen van zand onder funderingen op staal; Bepaling von der vormfactor sb, Annales des Travaux Plublics de Belgique, 68, No.6, pp.481-506; 69, No.1, pp.41-88; No.4, pp.321-360; No.5, pp.395-442; No.6, pp.495-522

De Beer, E. E. (1970). "Experimental determination of shape factors and the bearing capacity factors of sand", *Géotechnique*, 20, No. 4, pp. 387-411.

DIN 4017 (2006). *Berechnung des Grundbruchwiderstands von Flachgründengen*. Normenausschuss Bauwesen (NABau), Deutshes Institut für Normung e. V., Berlin.

Eurocode (2005) (DIN EN 1997-1). *Geotechnical Design, Part I: General Rules*, Deutsches Institut für Normung e.v., Berlin.

$FDOT_a$ (2017). *FDOT Soils and Foundations Handbook*, Florida Department of Transportation, State Materials Office, Gainesville, FL.

$FDOT_b$ (2017). *FDOT Structures Design Guidelines*, Florida Department of Transportation, Tallahassee, FL.

Fuglsang, L. D., and Ovesen, N. K. (1988). "The application of the theory of modeling to centrifuge studies." *Proceedings of International Conference on Geotechnical Centrifuge Modeling.* Balkema, Rotterdam. The Netherlands, pp. 119-138

Giraudet, P. (1965). "Recherches experimentales sur les fondations soumises a des efforts inclines ou excentres", *Annales des Ponts et Chaussees*, Vol. 3, pp. 168-193.

Gill, J.J. (1988). “Development and testing of a device capable of placing model piles by driving and pushing in the centrifuge”, PhD Dissertation, University of Florida

Gottardi, G. and Butterfield, R. (1993). “On the bearing capacity of surface footings on sand under general planar loads”, *Soils and Foundations*, Vol. 33, No. 3, pp. 68-79.

Hansen, J.B. (1970). “A revised and extended formula for bearing capacity”, Akademiet for de Tekniske Videnskaber, Geoteknisk Institut., Copenhagen, Bulletin No. 28, pp. 5-11.

Ingra, T.S. and Baecher, G.B. (1983). “Uncertainty in bearing capacity of sands”, *Journal of Geotechnical and Geoenvironmental Engineering*, Vol. 109, No. 7, pp. 899-914.

Kimura, T., Kusakabe, O., and Saitoh, K. (1985). “Geotechnical model tests of bearing capacity problems in a centrifuge.”, *Géotechnique*, London, England Vol. 35(1), pp. 33-45.

Ko, H. Y., and Davidson, L. W. (1973). “Bearing capacity of footings in plain strain.”, Journal of Soil Mechanics and Foundations Division, ASCE, Vol. 99, No. 1, pp. 1-23.

Labuz, J.F. and Theroux, B. (2005). “Laboratory calibration of earth pressure cells”, Geotechnical Testing Journal, Vol. 28, No. 2, pp. 1-9.

Ladd, C. C., Foott, R., Ishihara, K., Schlosser, F., and Poulos, H. G., (1977), “Stress Deformation and Strength Characteristic SOA Report,” Proceedings of the Ninth International Conference of Soil Mechanics and Foundation Engineering, Tokyo, Vol. 2, pp. 421–494.

Lambe, T.W., and Whitman, R.V. (1969). Soil Mechanics. 1st Ed., John Wiley and Sons, Inc., New York, NY.

Meyerhof, G.G. (1948). “An investigation of bearing capacity of shallow footings on dry sand”, *Proceedings of the second International Conference on Soil Mechanics and Foundation Engineering*, ICSMFE, Vol. 1, pp. 237-243

Meyerhof, G.G. (1951). “The ultimate bearing capacity of foundations”, *Géotechnique*, London, England Vol. 2, pp. 301-332.

Meyerhof, G.G. (1953). “The bearing capacity of foundations under eccentric and inclined loads”, *Proceedings of the third International Conference on Soil Mechanics and Foundation Engineering*, ICSMFE, Vol. 1, No. 1, pp. 440-445

Meyerhof, G.G. (1963). “Some recent research on the bearing capacity of foundations”, Canadian Geotechnical Journal, Vol. 1, No. 1, pp. 16-26.

Meyerhof, G.G. and Koumoto, T. (1987). “Inclination factors for bearing capacity of shallow footings”, *Journal of Geotechnical and Geoenvironmental Engineering*, Vol. 131, No. 9, pp. 1013-1018.

Molnit, T. (1995). *Centrifuge modeling of laterally loaded large plumb pile groups in sand*, ME Thesis, University of Florida

Muhs, H. and Weiss, K. (1973). "Inclined load test on shallow strip footings", Proceedings, *Eighth International Conference on Soil Mechanics and Foundation Engineering*, ICSMFE, Vol. I, pp. 173-179

Loukidis, D., Chakraborty, T., and Salgado, R. (2008). "Bearing capacity of strip footing on purely frictional soil under eccentric and inclined loads", NRC Research Press website at cgj.nrc.ca, Canada, doi:10.1139/T08-015.

Paikowsky, S.G., Canniff, M. C., Lesny, K., Kisse, A., Amatya, S. and Muganga, R. (2010). "LRFD design and construction of shallow foundations for highway bridge structures", NCHRP Report 651, Transportation Research Board, Washington, D.C.

Patra, C. R., Behara, R. N., Sivakugan, N., and Das, B. M. (2012). "Ultimate bearing capacity of shallow strip foundation under eccentrically inclined load, Part II", International Journal of Geotechnical Engineering, Vol. 6, pp. 507-514

Perau, E. (1995). *Ein systematischer Anasatz zur Berechnung des Grundbruchwiderstands von Fundamenten*, Mitteilungen aus dem Fachgebiet Grundbau und Bodenmechanik der Universität Essen, Heft 19, Hrsg.: Profe. Dr.-Ing. W. Richwien, Essen: Glückauf-Verlag.

Perau, E. (1997). "Bearing capacity of shallow foundations", *Soils and Foundations*, Vol. 37, No. 4, pp. 77-83.

Perloff, W.H. and Baron, W. (1976). *Soil Mechanics: Principles and Applications*, John Wiley and Sons, New York.

Prandtl, L. (1920). *Ueber die Haerte plastischer Koerper*. Nachrichten der Gesellschaft der Wissenschaften, Berichte der mathem.-physikal. Klasse, pp. 74-85.

Reissner, H. (1924). "Zum erddruckproblem", Proceedings of 1st International Congress of Applied Mechanics, Delft, pp. 295-311.

Sokolovski, V.V. (1960). *Statics of Soil Media*, Butterworth, London, pp. 1-237.
Taylor, D. W. (1945). "Review of pressure distribution theories. Earth pressure cell investigations, and pressure distribution data", *Contract Report W22-053 eng-185*, U.S. Army Engineer Waterways Experiment Station, Vicksburg, MS.

Ticof, J. (1977). *Surface footings on sand under general planar loads*, Ph.D. thesis, University of Southampton, UK.

Vesić, A. (1963) Bearing capacity of deep foundations in sand, Highway Research Record, 39, National Academy of Sciences, National Research Council, pp.112-153.

Vesić, A. (1973). “Analysis of ultimate loads of shallow foundations”, Journal of Soil Mechanics and Foundations Division, ASCE, Vol. 99, No. 1, pp. 45-71.

Vesić, A. (1975). “Bearing capacity of shallow foundations”, In Foundation Engineering Handbook, H.F. Winterkorn and H.Y. Fang, eds., Van Nostrand Reinhold, New York, pp. 121-147.

Wack, B. (1961). “Distribution of pressure against a wall, supporting a mass of soil”, Inzh. Sb., Vol. 31.

Yamaguchi, H., Kimura, T., and Fujii, N. (1976). “On the influence of progressive failure on the bearing capacity of shallow foundations in dense sand”, *Soils and Foundation,* Vol. 16, No. 4, pp. 11-22

Zhu, F., Clark, J.L., and Phillips, R. (2001). “Scale effect of strip and circular footings resting on dense sand”, Journal of Geotechnical and Geoenvironmental Engineering, Vol. 127, No. 7, pp. 613-621.

Zhu, M. and Michalowski, L. (2005). “Shape factors for limit loads on square and rectangular footings”, *Journal of Geotechnical and Geoenvironmental Engineering*, Vol. 131, No. 2, pp. 223-231.

APPENDICIES OF MEASURED VERSUS PREDICTED BEARING CAPACITY PLOTS

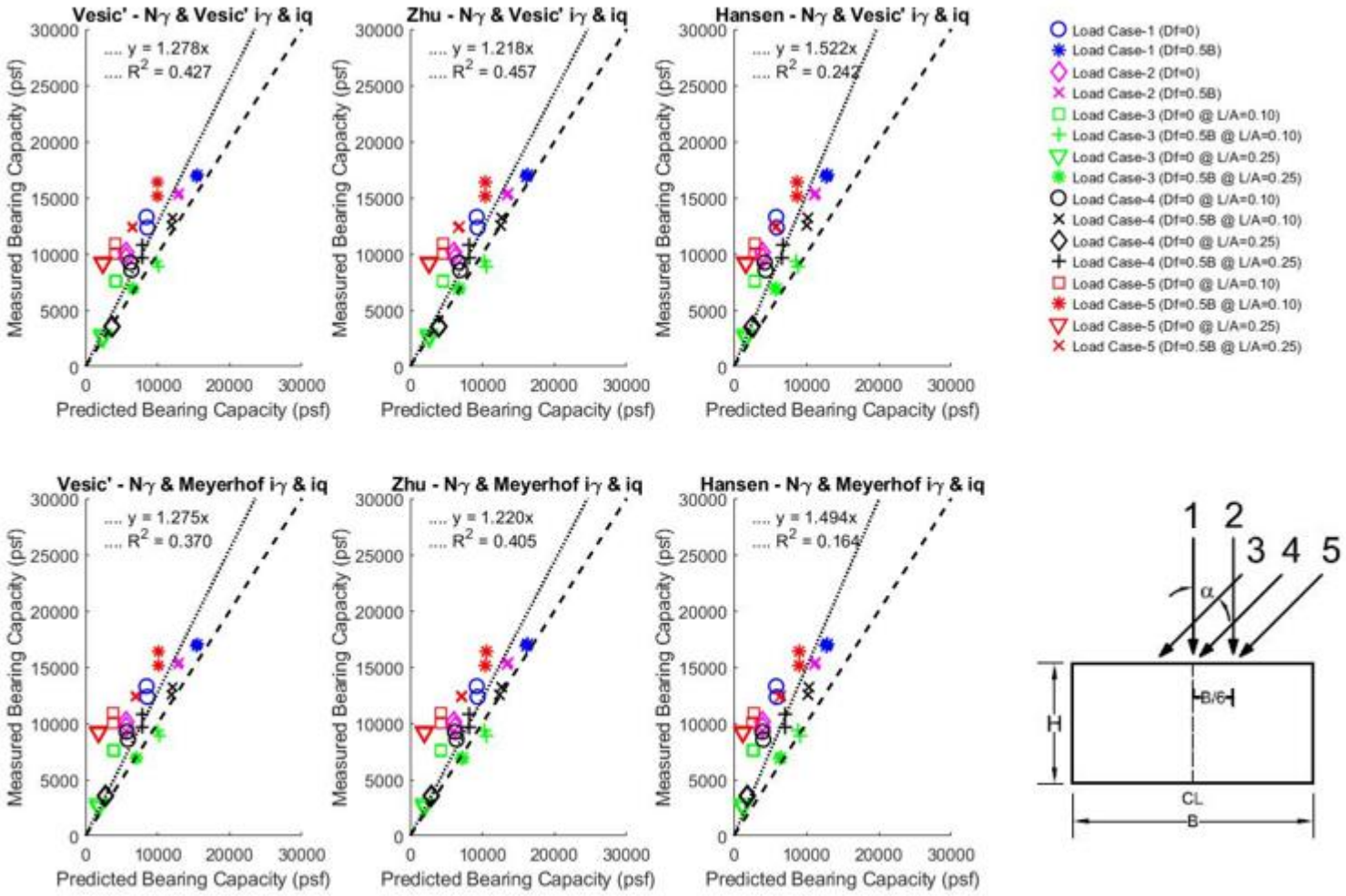

Figure A1 Bearing capacity-q_u bias plots for L/B = 10 medium dense condition with paired design methods using Vesić s_q

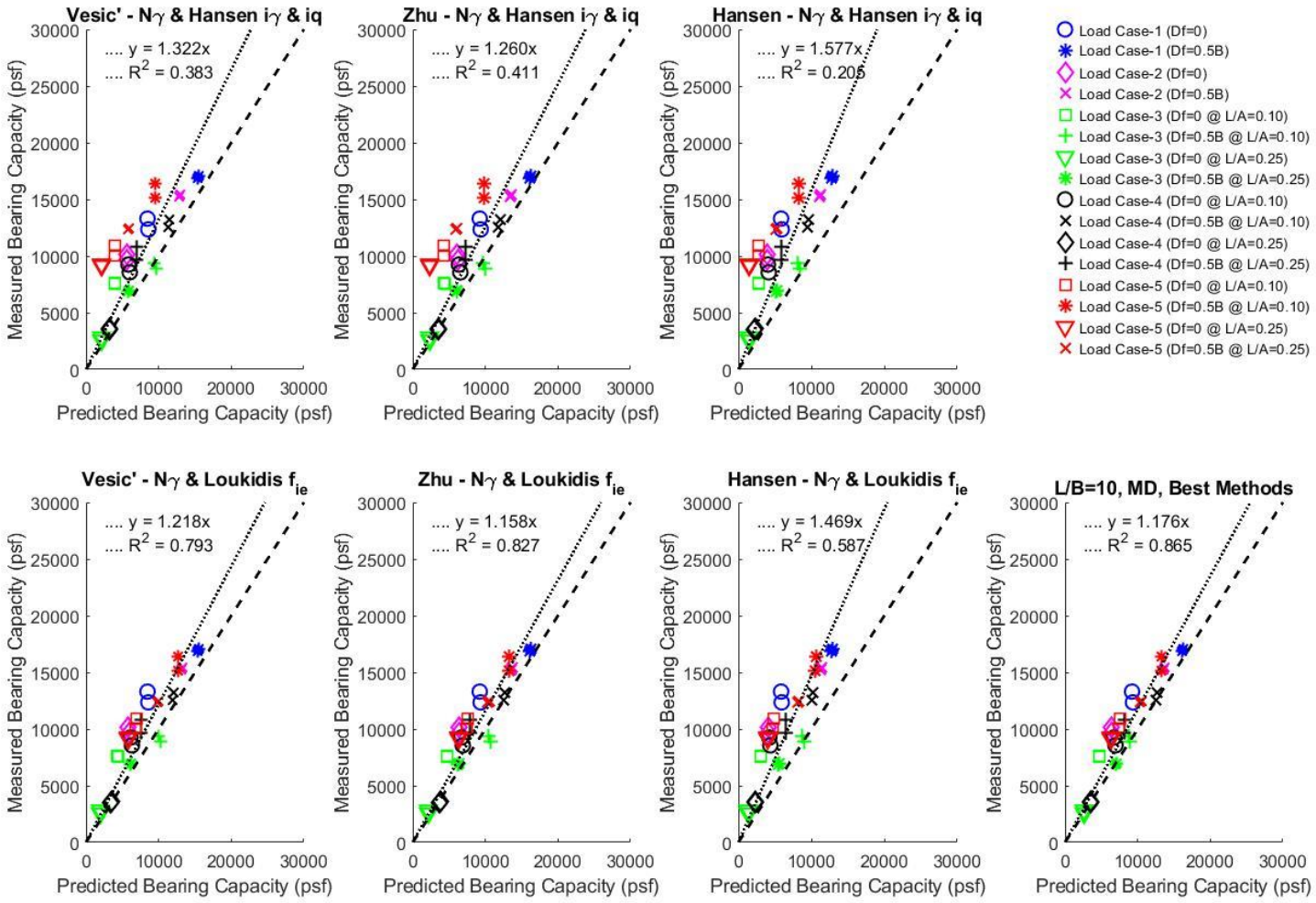

Figure A2 Bearing capacity-q_u bias plots for L/B = 10 medium dense condition with paired and best design methods using Vesić s_q

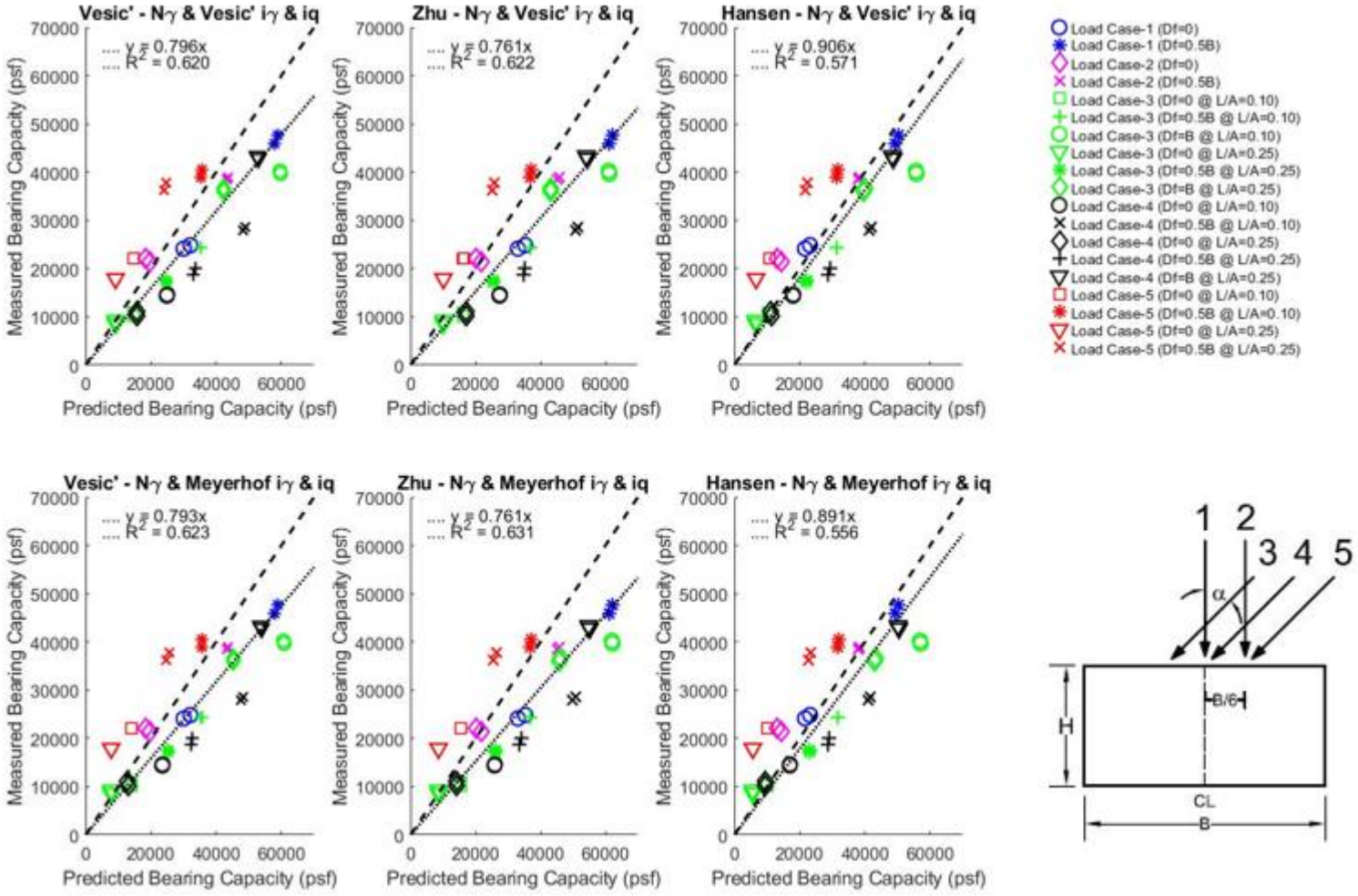

Figure A3 Bearing capacity-q_u bias plots for L/B = 1 very dense condition with paired design methods using Vesić s_q

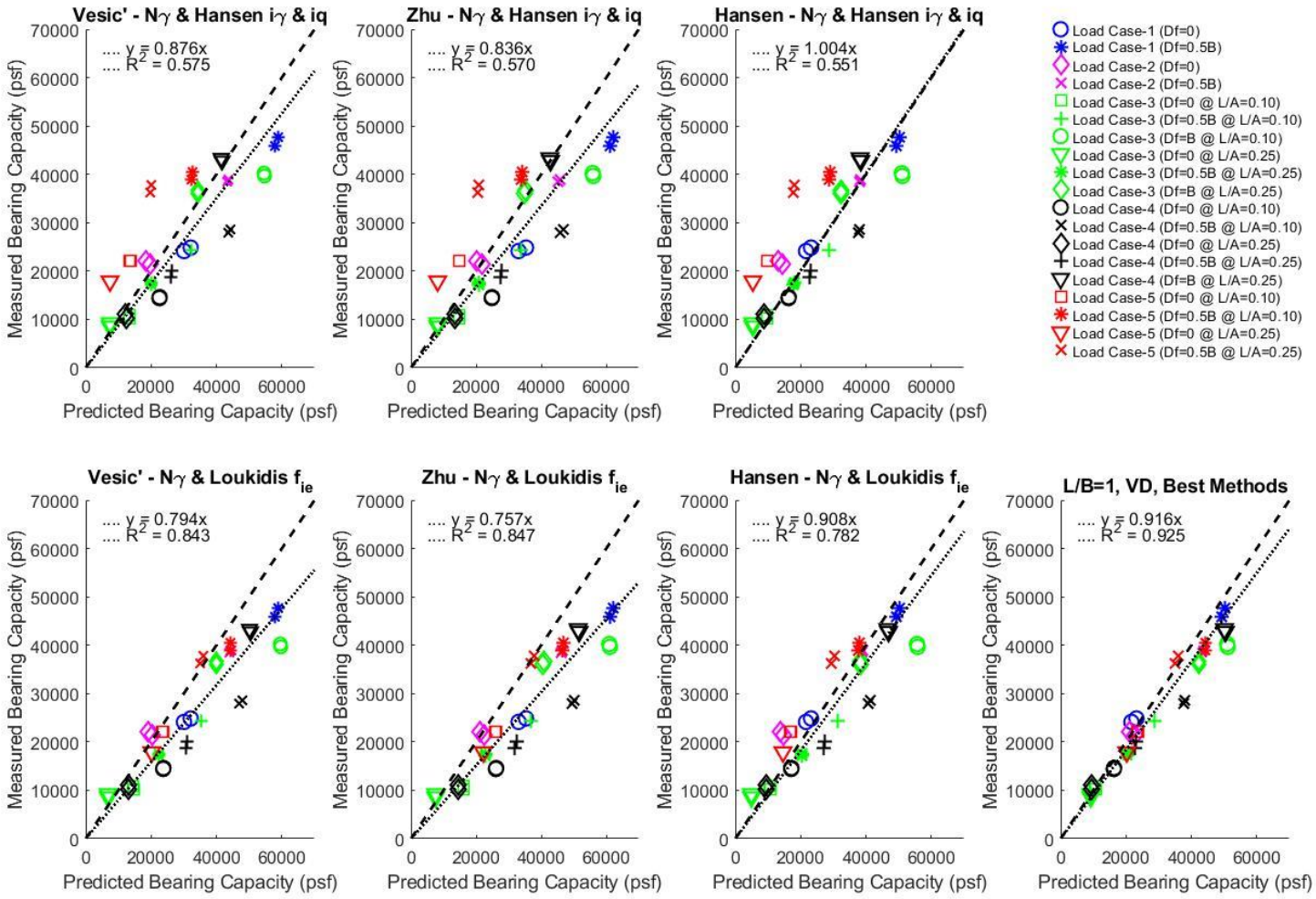

Figure A4 Bearing capacity-q_u bias plots for L/B = 1 very dense condition with paired and best design methods using Vesić s_q

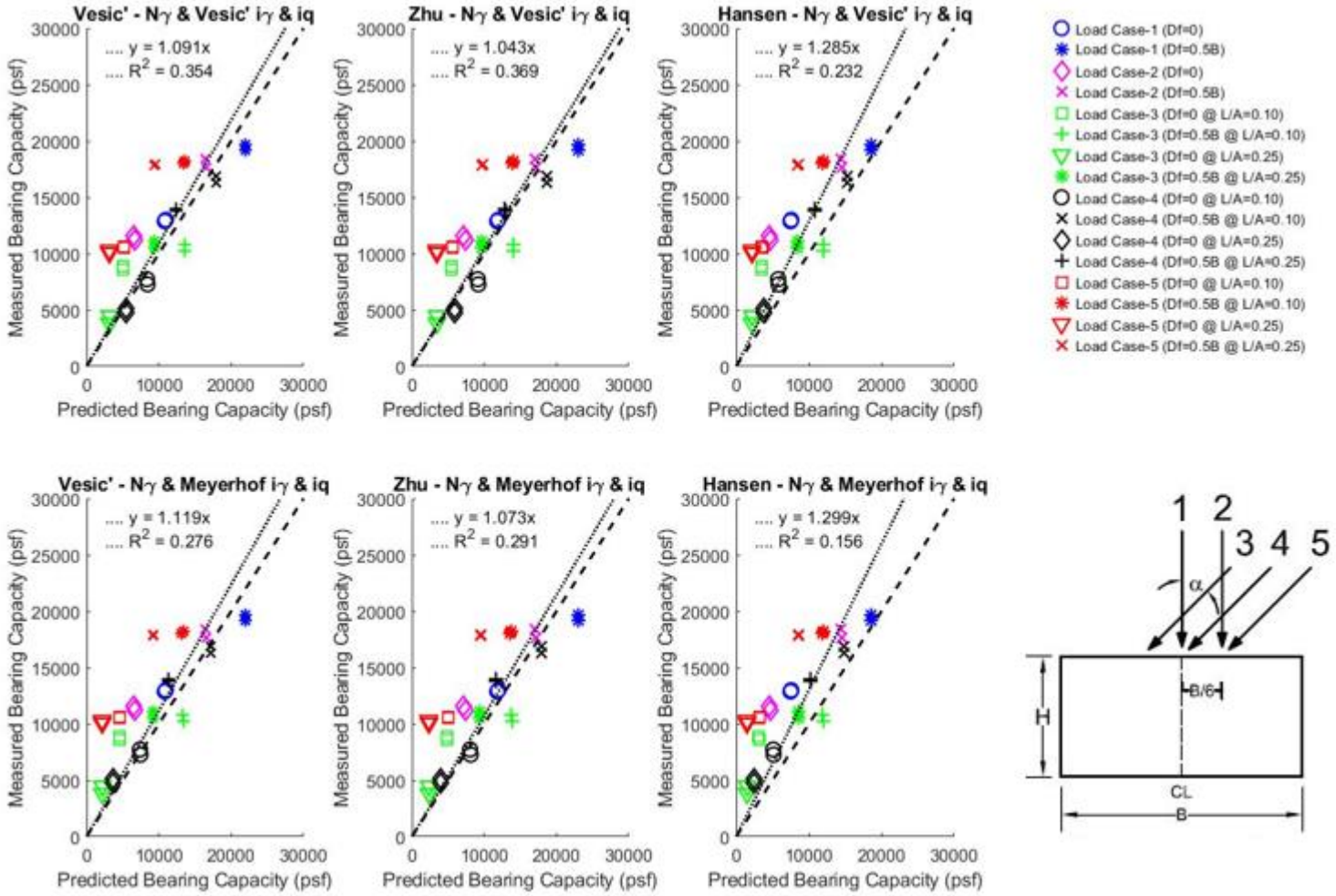

Figure A5 Bearing capacity-q_u bias plots for L/B = 1 medium dense condition with paired design methods using Vesić s_q

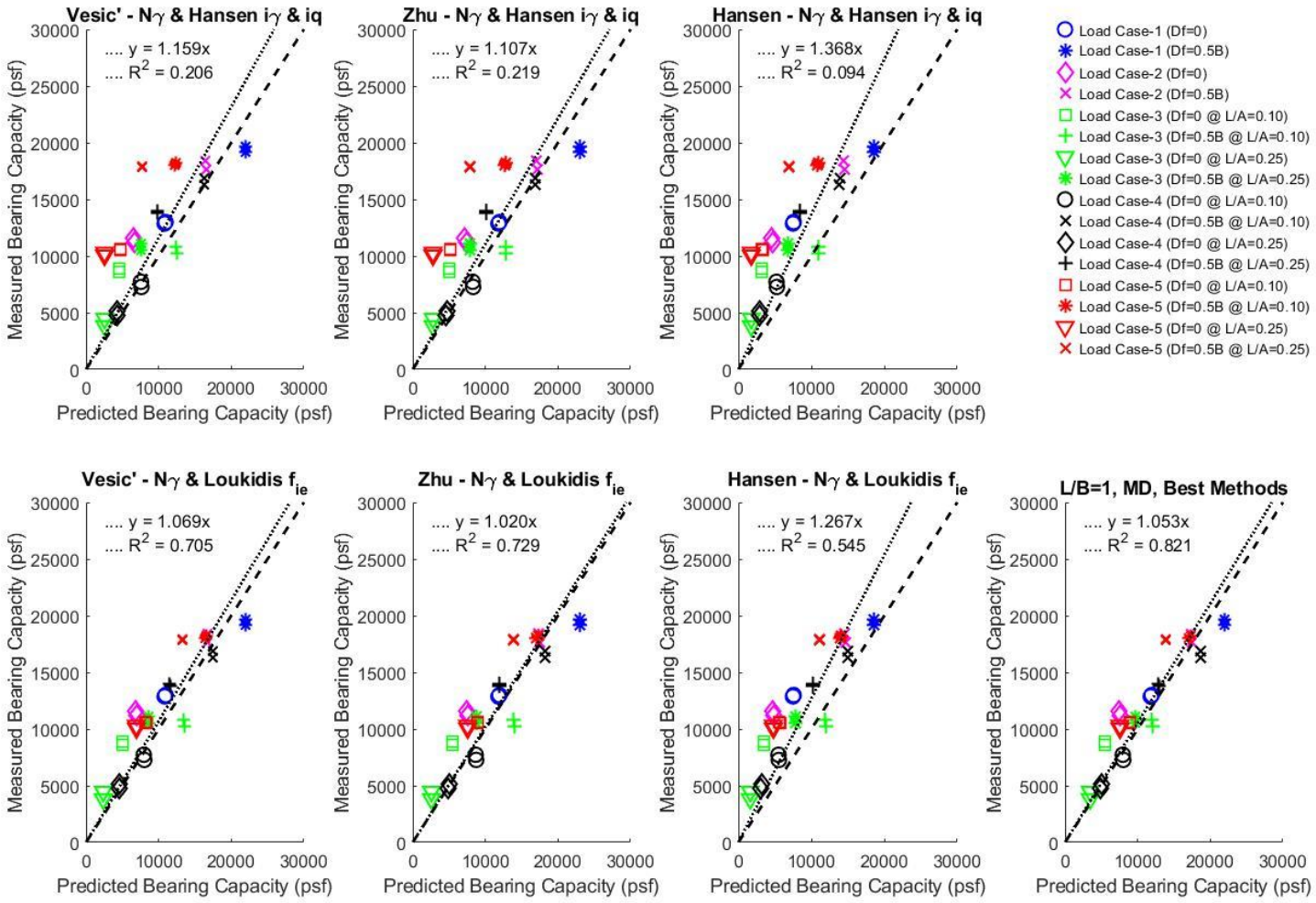

Figure A6 Bearing capacity-q_u bias plots for L/B = 1 medium dense condition with paired and best design methods using Vesić s_q

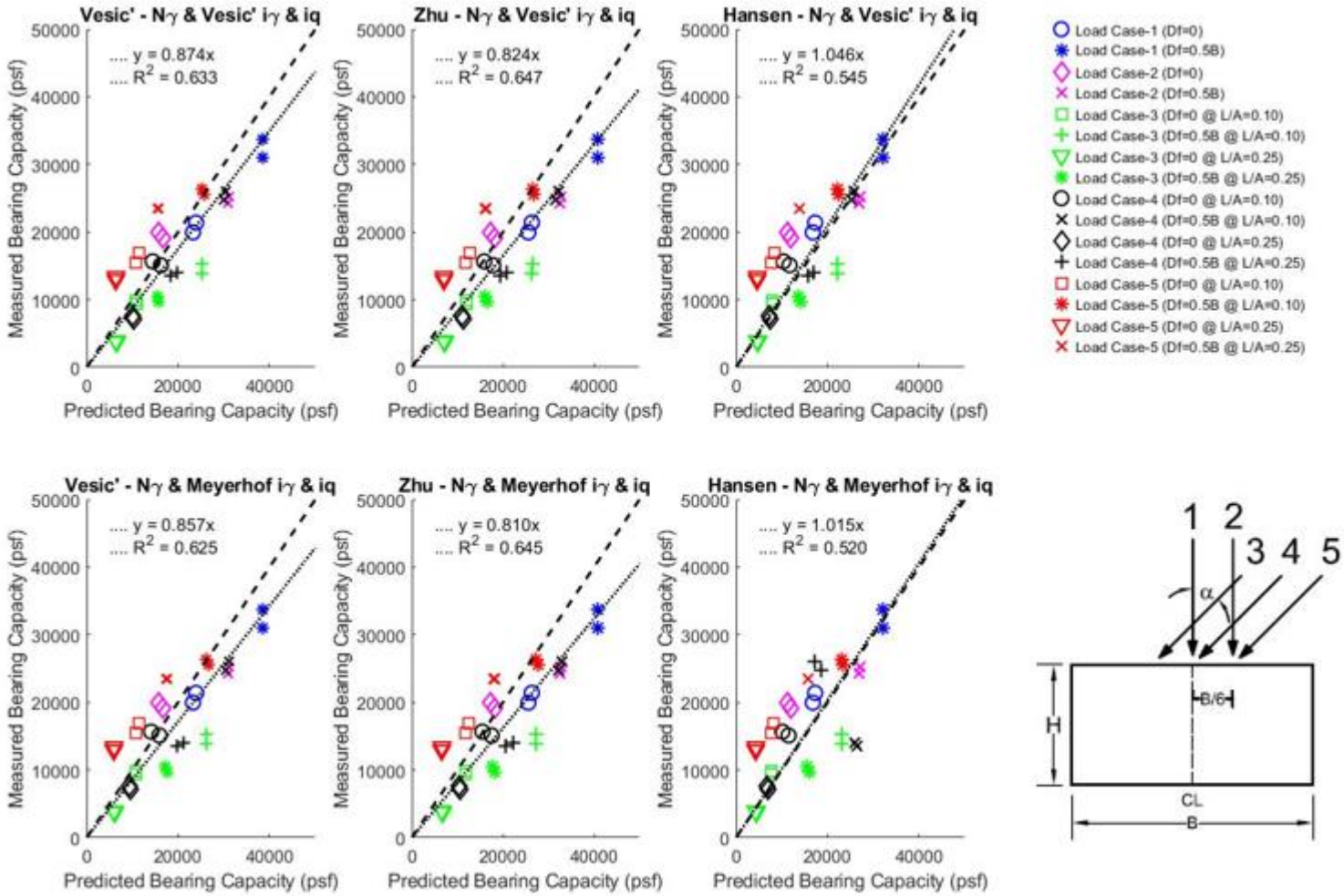

Figure A7 Bearing capacity-q_u bias plots for L/B = 10 very dense condition with paired design methods using Meyerhof s_q

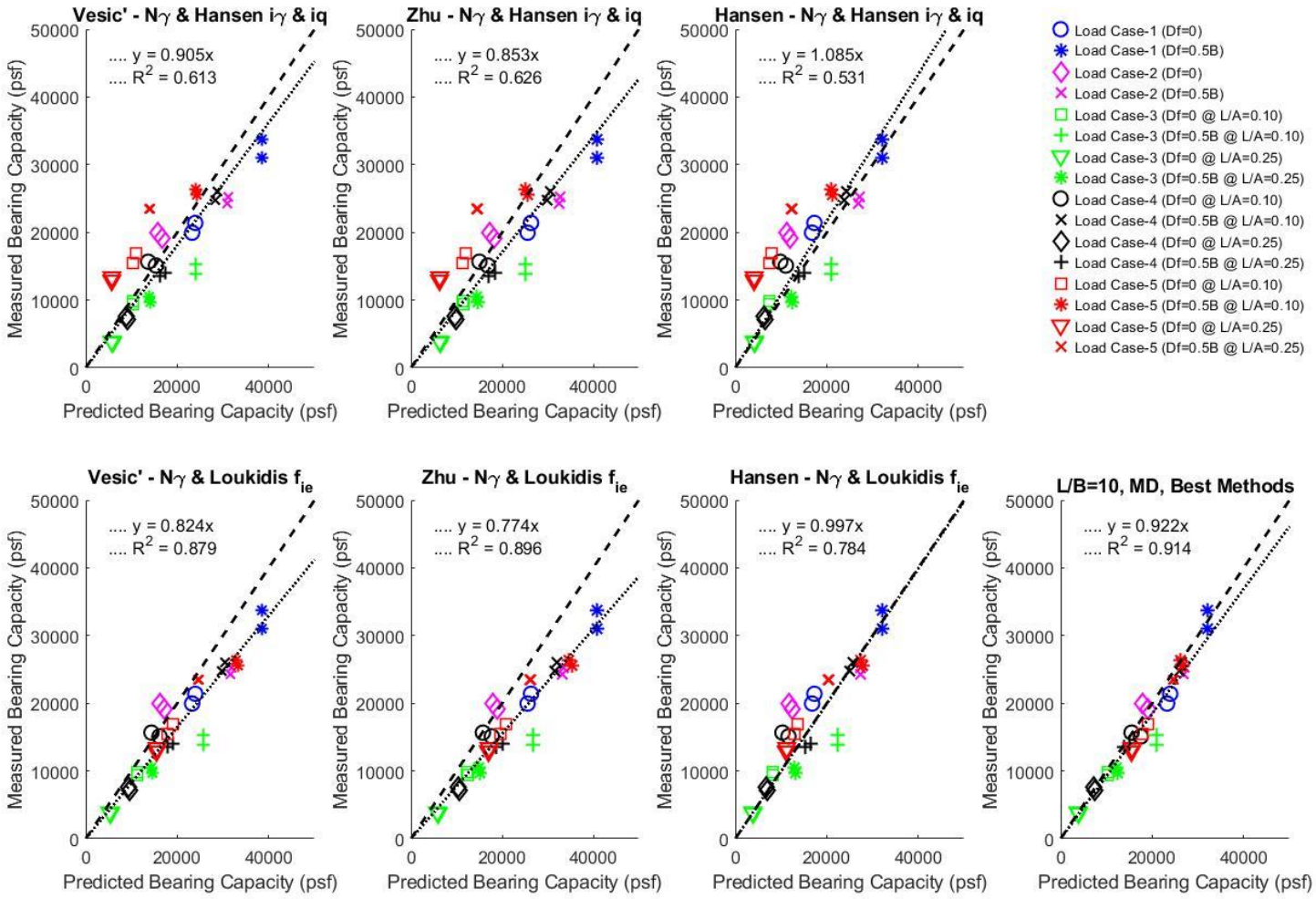

Figure A8 Bearing capacity-q_u bias plots for L/B = 10 very dense condition with paired and best design methods using Meyerhof s_q

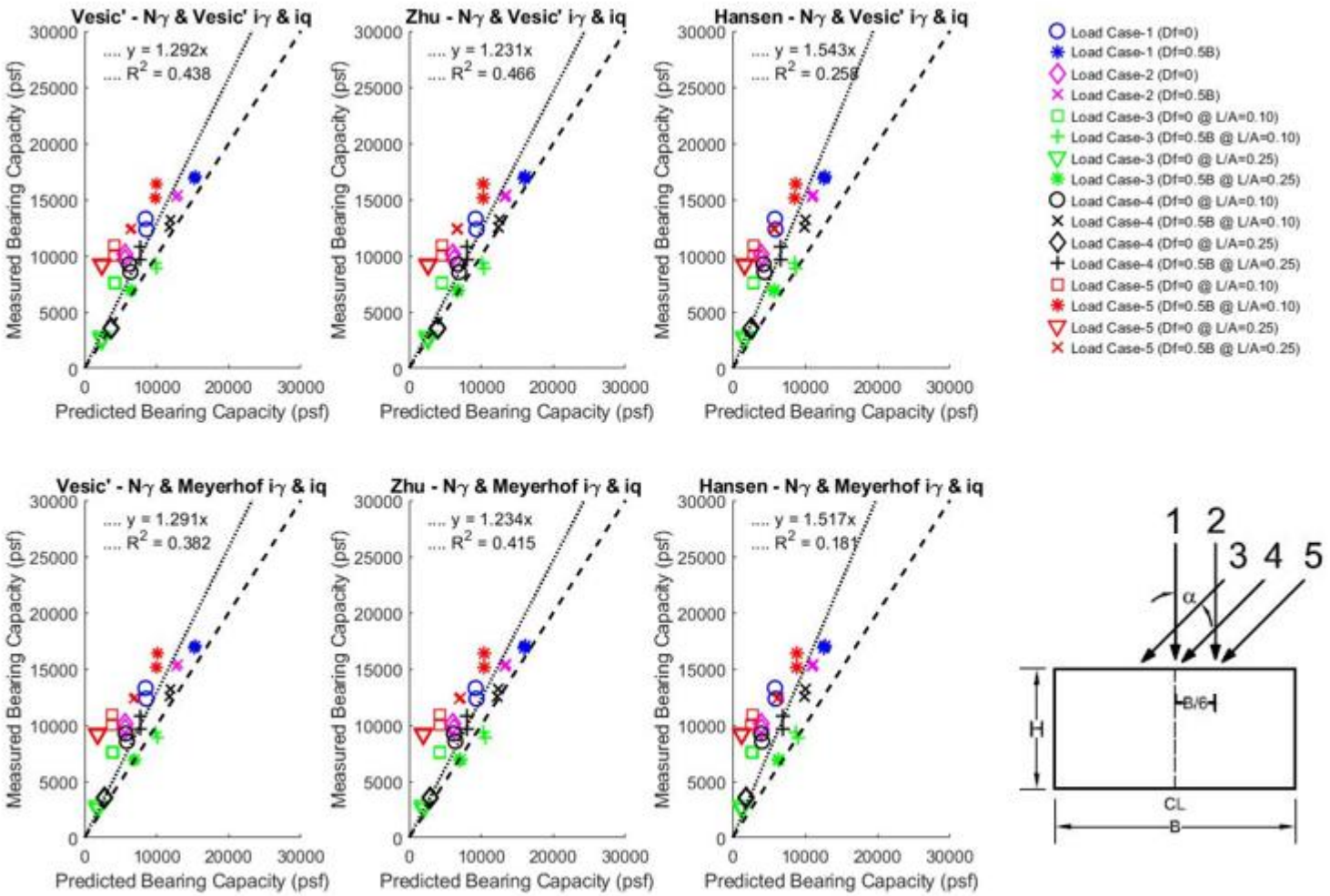

Figure A9 Bearing capacity-q_u bias plots for L/B = 10 medium dense condition with paired design methods using Meyerhof s_q

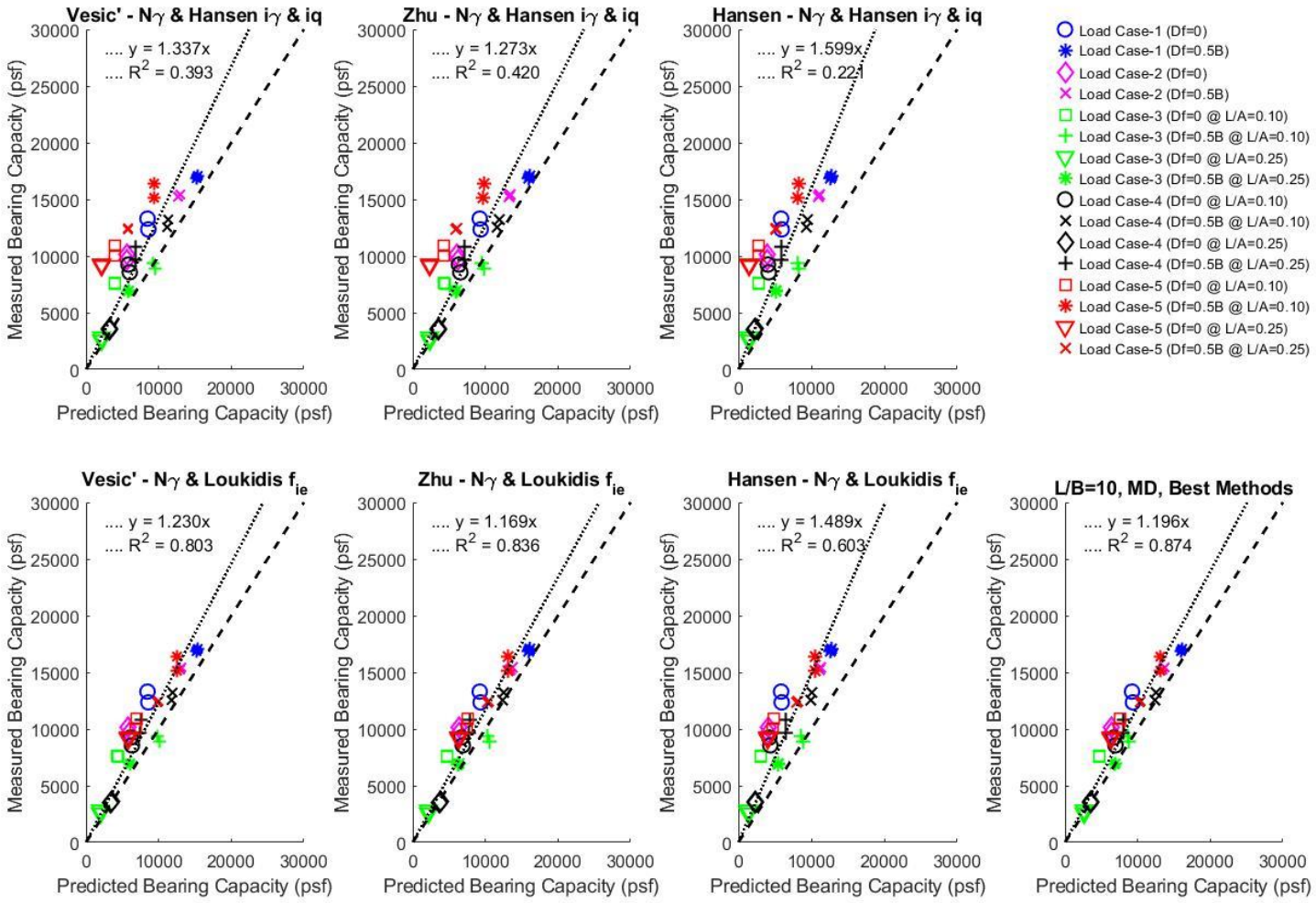

Figure A10 Bearing capacity-q_u bias plots for L/B = 10 medium dense condition with paired and best design methods using Meyerhof s_q

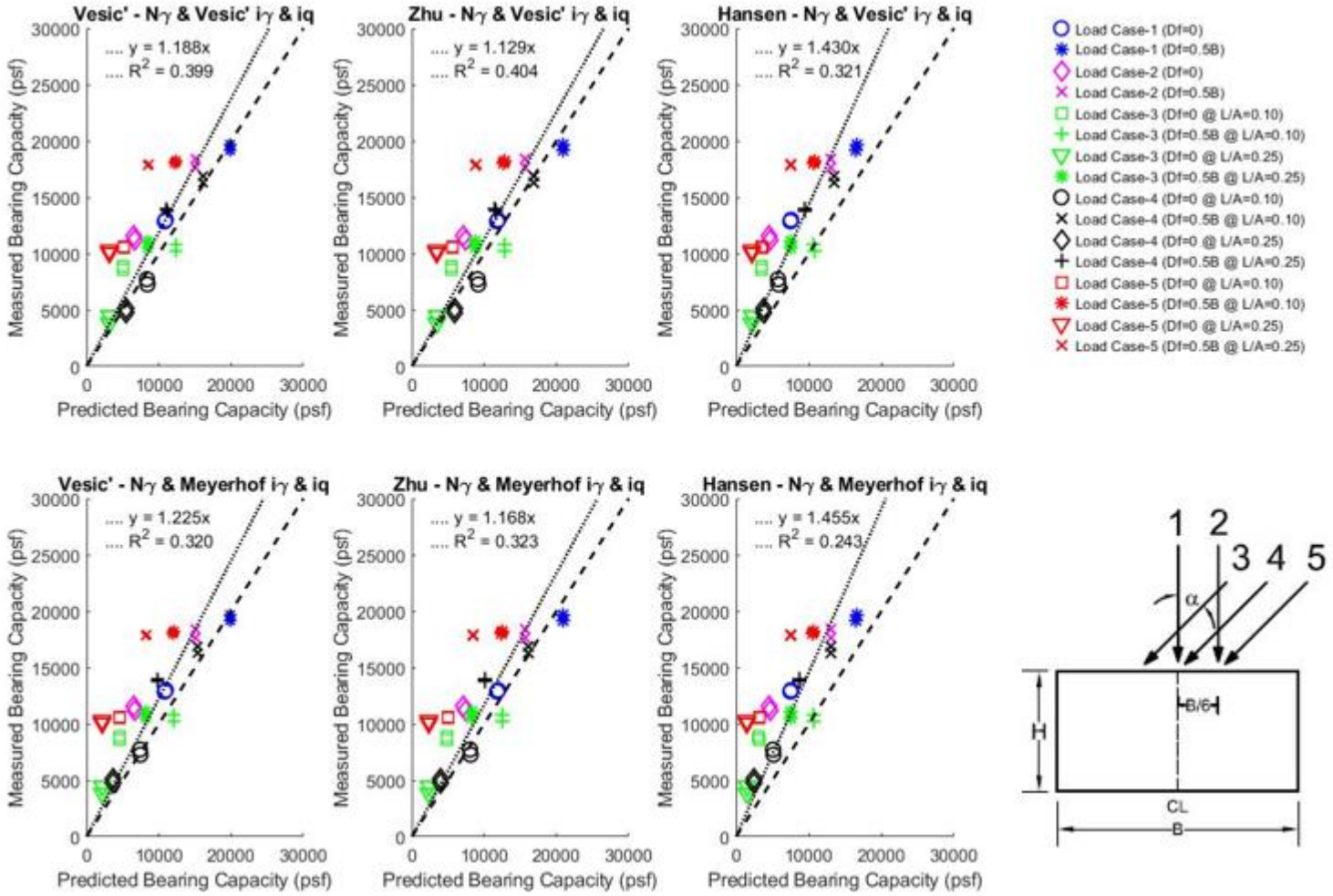

Figure A11 Bearing capacity-q_u bias plots for L/B = 1 medium dense condition with paired design methods using Meyerhof s_q

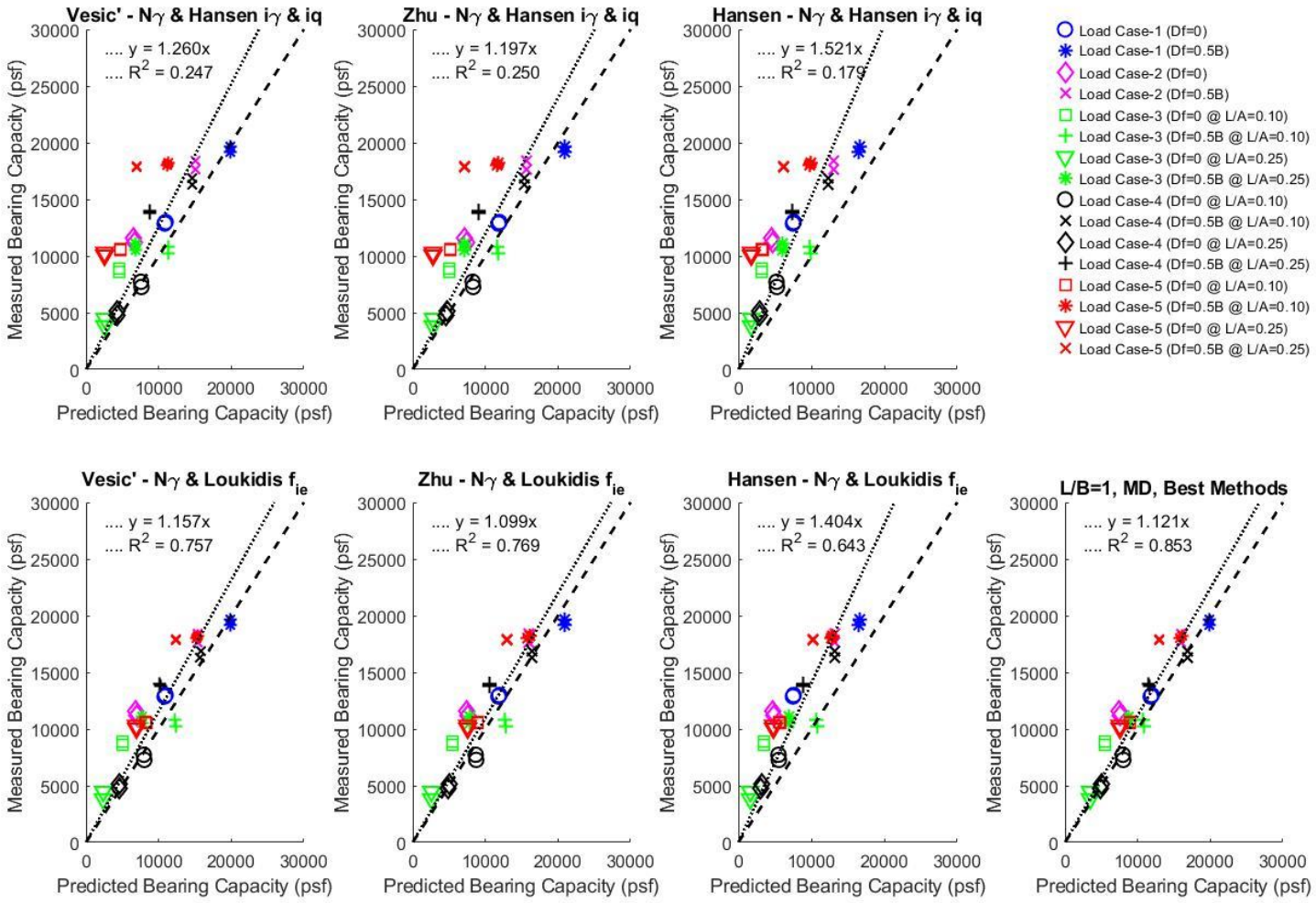

Figure A12 Bearing capacity-q_u bias plots for L/B = 1 medium dense condition with paired and best design methods using Meyerhof s_q

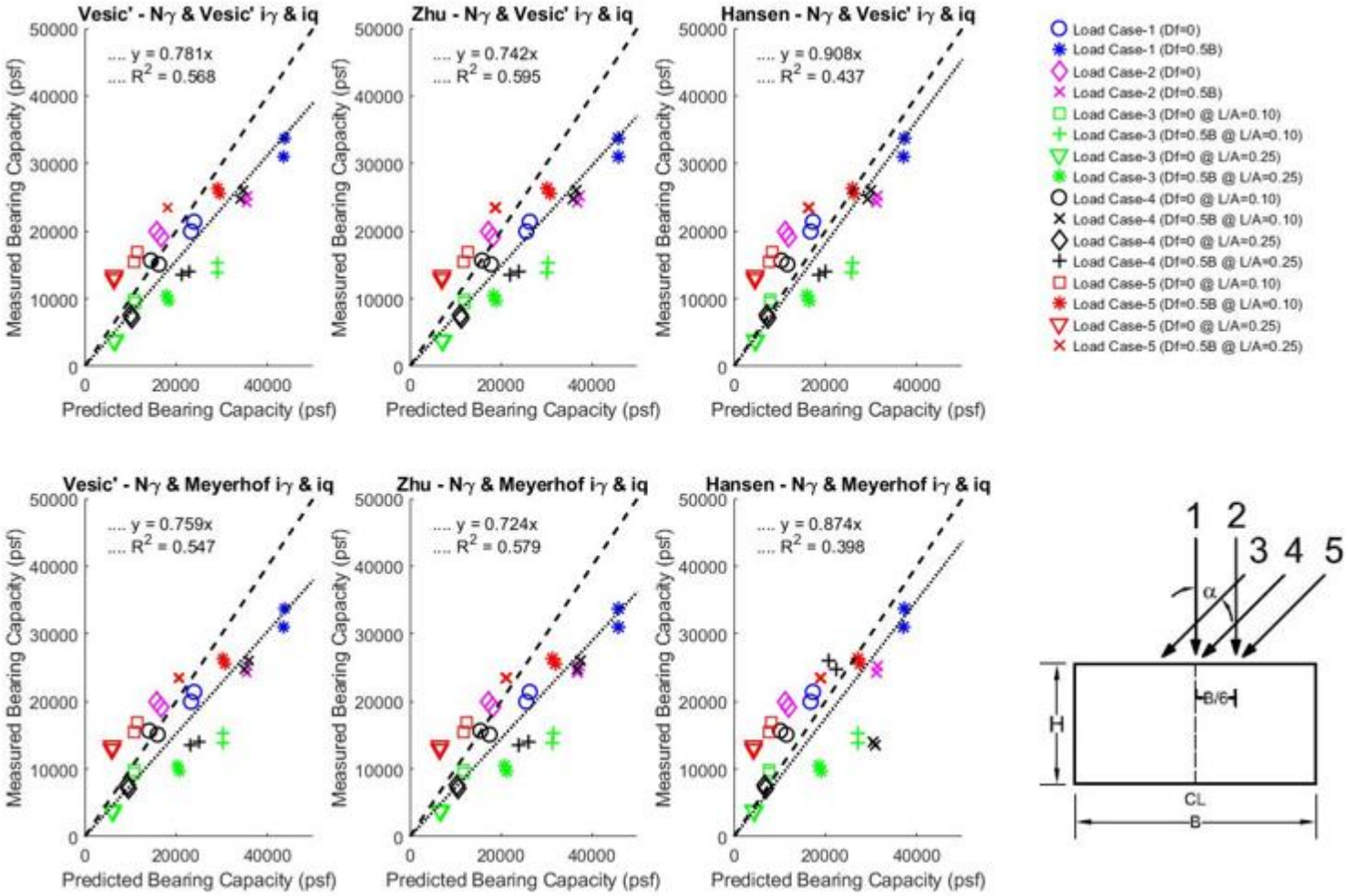

Figure A13 Bearing capacity-q_u bias plots for L/B = 10 very dense condition with paired design methods using Zhu s_q

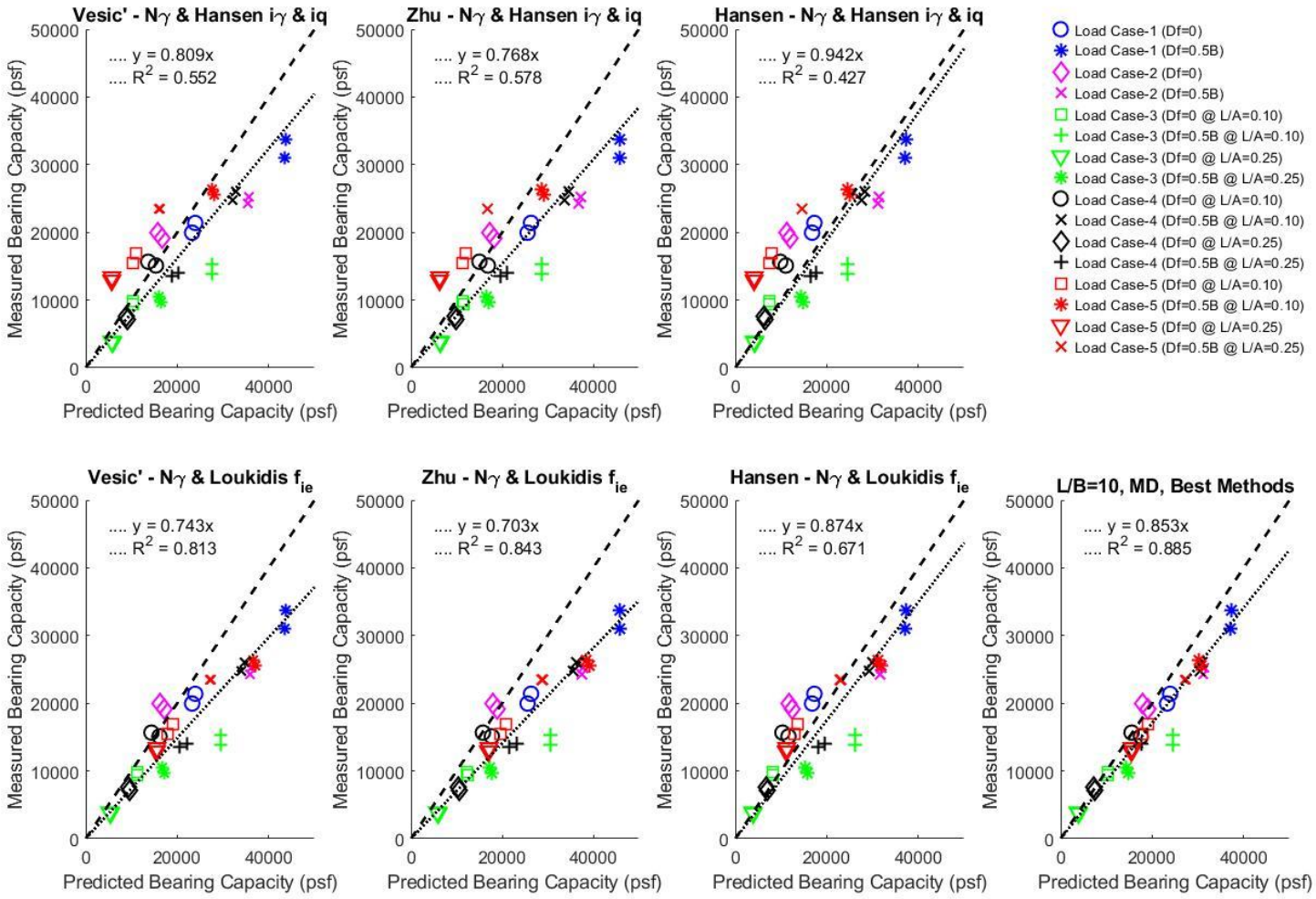

Figure A14 Bearing capacity-q_u bias plots for L/B = 10 very dense condition with paired and best design methods using Zhu s_q

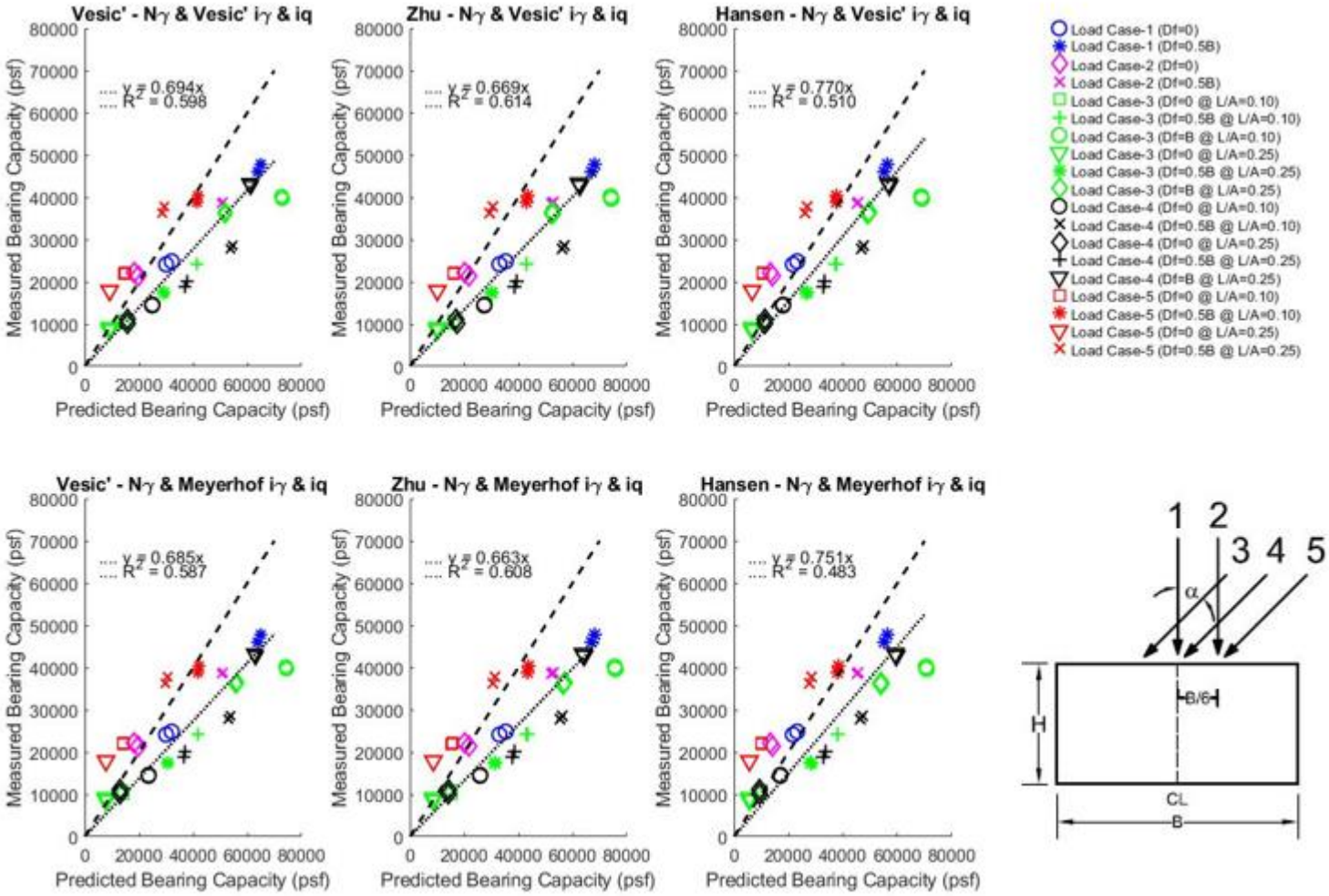

Figure A15 Bearing capacity-q_u bias plots for L/B = 1 very dense condition with paired design methods using Zhu s_q

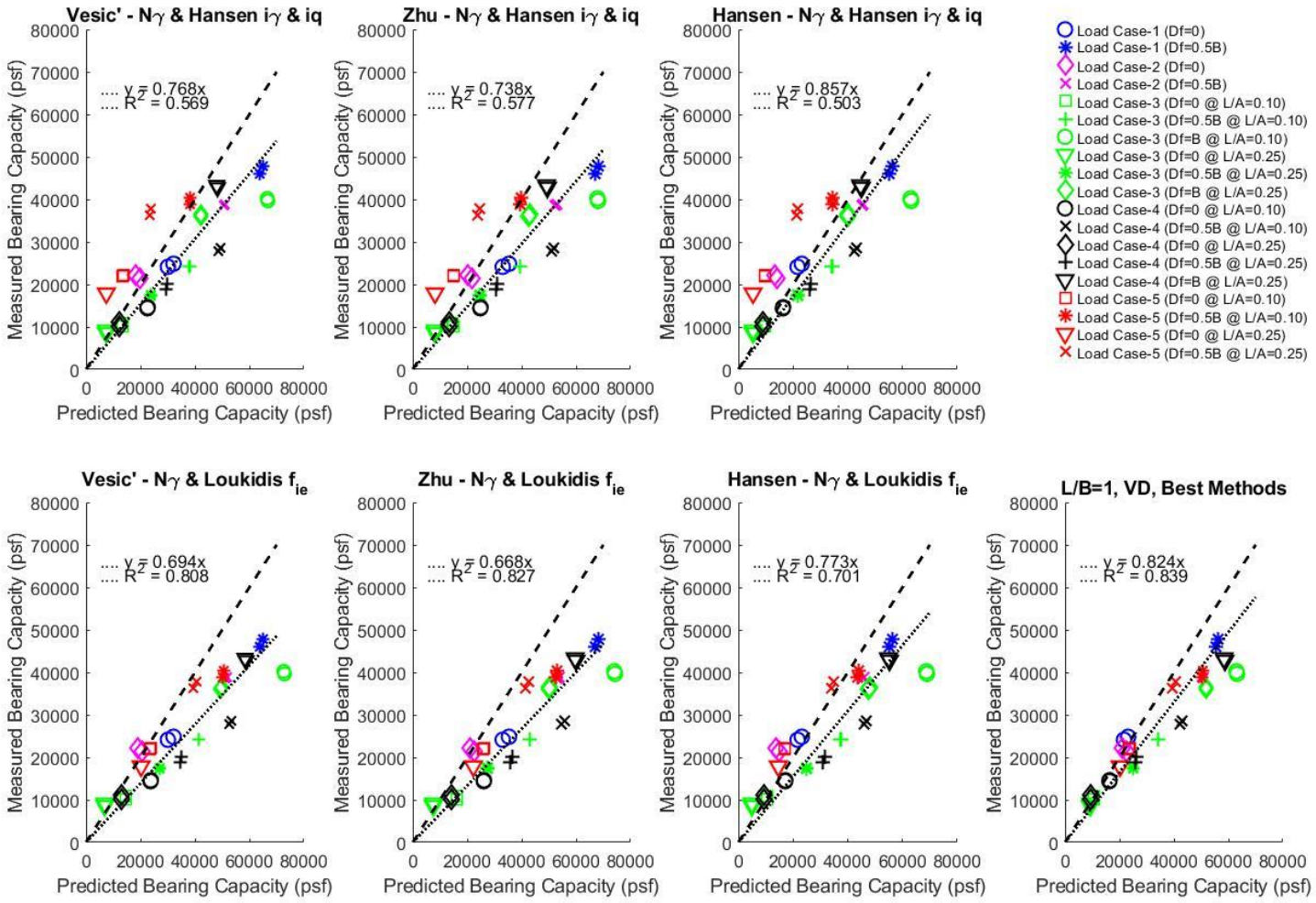

Figure A16 Bearing capacity-q_u bias plots for L/B = 1 very dense condition with paired and best design methods using Zhu s_q